

**Optimising Laser Stereolithography
for Constructing Electronic
Packages onto Novel Substrates.**

by

Robert James Plant

Thesis

Submitted to the University of Nottingham for the
degree of

Doctor of Philosophy

Department of Engineering

2023

Abstract

Additive manufacturing (AM) has matured from its initial concept as a prototyping technique to an established industrial manufacturing process for which compliance with relevant standards is required. Here, we investigate inserting components into geometries constructed directly onto non-standard substrates using stereolithography (SLA), for the purpose of electronics packaging. Silicon nitride is of particular interest as the interfacial material when packaging semiconductors and technologies such as silicon interconnect fabric. Compared to conventional encapsulation processes, SLA avoids elevated temperatures and stresses while permitting much greater flexibility to arrange components in three dimensions. This can enable an increased feature density, optimised packages for confined spaces, functional packaging to complement the operation of the device, and enables rapid production for bespoke applications.

One of the key challenges is the ability to bond the product to the substrate sufficiently to adhere to the industry standard. Additionally, interactions between the SLA process, the photopolymer and the substrate can result in distortion and compromise the ability to deliver products to the required tolerances.

To support this initiative, relevant literature has been reviewed to determine current knowledge and the gaps to be filled through further investigation. From doing so, active adhesion mechanisms were identified and methods to enhance them explored. Moreover, novel experimental processes had to be developed to produce suitable test samples. Characterising the substrate and photopolymer materials allowed potential changes in properties during the curing process to be determined, and comparison with conventional adhesion models. Furthermore, the shear stress generated from shrinkage during post build curing (PBC) has been measured to make a significant contribution to the stress at separation on untreated silicon nitride. The investigation concluded that the application of a TMSPMA monolayer to the plasma treated substrate, combined with PBC, substantially increases the strength of adhesion to an extent compliant with the industry standard and above the cohesive strength of the polymer.

In addition to adhesion, the influences of process parameters are analysed, and their potential to distort the beam and the resulting product. Distorting effects investigated include divergence, ellipticity, refraction, reflectance, over-exposure, and low intensity noise present in the beam. These have been modelled with consideration given to the influence of superposition and the machine architecture. A non-linear relationship between distorting effects and the dimensions of the build area is identified which has implications

for the scalability of production. This allows the extent to which the build area can be increased, until the combined influence of these distorting effects compromises the ability to meet manufacturing tolerances, to be determined.

Further modelling supported by purpose designed experimentation, revealed the potential for significant distortions from refraction and reflectance. If sufficiently energetic, reflections from the substrate can produce spurious curing, and distort the product. Modelling the limits of exposure at which the onset of spurious curing and distortion occurs, allows an operating window to be obtained, within which the construction process can be optimised. This allows for significant savings in construction time with a reduction of 26% demonstrated.

Methods to mitigate distortion by optimising the beam's focal point, the design of parabolic mirror profile, anti-reflective coatings, modulating the laser power, and the potential to modify the photopolymer, are reported.

Lastly, by building on prior work, a process to insert multiple large and complex geometries into the SLA build process, and to connect the installed components electrically for the construction of 3D electronic packages, is demonstrated.

It is concluded, by using the processes described, electronic packages can be constructed directly onto silicon nitride using SLA and meet the required standard of adhesion. Moreover, by applying the tools developed, the process can be optimised for scale and time, while complying with the necessary manufacturing tolerances.

Keywords: Stereolithography, Substrate, Insertion, Adhesion, Distortion

Acknowledgements

There are those who've asked; "What are you doing this for?". The answer is out of interest and passion for a growing technology for which I see an increasing number of applications and huge potential. I consider myself truly fortunate to have the opportunity to study in this field. Special thanks to my supervisors Prof. Tuck, Prof. Hague and Prof. Wildman, for their support and for challenging my work to encourage my understanding and knowledge of stereolithography. I also express my gratitude to Texas Instruments, in particular Sean Chang.

This document reports the findings from a lot of hard work but doesn't include the sacrifices made. These are numerous, but significantly they have also been incurred by people other than myself. Foremost are my immediate family; my wife Nicola, and my two young boys Lachlan and Charlie. I'm looking forward to going on holiday and watching some cricket with you when we finish! I would like to thank the Gladstone family for their unwavering support and only ever offering words of encouragement. Thanks to Reuben Mascarenhas, Matthew Kimbley and Steven Abigail for their good humour and listening to my woes in the pub on a Friday. I wish to thank my fellow university of Nottingham students for their camaraderie and to the lab technicians Mark Hardy and Mark East for keeping the lab running and their good humour. Lastly, I owe my father a great gratitude for his support and advice which was always provided in my best interests.

Dedicated to my father.

John Plant

25-9-1942

to

27-12-2020

“A great guy, and ready-made for tough jobs.”

~ Colonel Ian Currier MBE

Publications

Conference Papers

Plant R, Chang S, Hague R, Tuck C, Wildman R, 2022, Inserting components into geometries constructed onto a non-standard substrate for electronics packaging. In: Bourell D. ed. 2022 Annual International Solid Freeform Fabrication Symposium, 25 – 27 July 2022, Austin: SFF Symposium, pp.1769-1782. Available from: <https://utw10945.utweb.utexas.edu/2022-table-contents>

Conferences Presented

2022 Solid Freeform Fabrication Symposium, Austin: The use of SLA to produce structures onto non-standard substrates.

Table of Contents

Abstract	2
Acknowledgements	4
Publications	6
Abbreviations	18
Glossary of terms	21
Nomenclature	23
Chapter 1	27
1. Introduction	27
1.1. Additive manufacturing	27
1.2. Stereolithography	27
1.3. Industrial application	29
1.4. Motivation	29
1.5. Aim	31
1.6. Chapter content summary	32
Chapter 2	35
2. Literature Review	35
2.1. Packaging electronics using SLA.	35
2.2. Inserting geometries into the SLA process	36
2.3. Building onto wafers and non-standard substrates	38
2.4. Adhesion in SLA	42
2.5. SLA material	55
2.6. Feature size and resolution	58
2.7. Defects and distortion in SLA	60
2.8. Knowledge gaps	64
2.9. Research questions	65
Chapter 3	66
3. Experimental and numerical methods	66
3.1. Reference properties and design tools	68
3.2. Numerical methods for modelling distorting effects and optimisation of the SLA process.	71
3.3. Experimental methodology for investigating distorting effects in the SLA process.	97
3.4. Adhesion experimental methods	104

3.5. Inserting geometries approach and methodology	125
Chapter 4	134
4. Results	134
4.1. Distorting effect results	134
4.2. Adhesion investigation results	153
4.3. Inserting geometries results and observations.	171
Chapter 5	177
5. Discussion	177
5.1. Discussion of distorting effects in the SLA process	177
5.2. Adhesion discussion	221
5.3. Discussion of inserting multiple geometries into the SLA process.	240
Chapter 6.	243
6. Findings and Conclusions	243
6.1. Further work	246
References	248
Appendix A: Texas Instruments HDC302x Gas Sensor Drawing.	265
Appendix B: Relevant standards	266
Appendix C: Supporting adhesion principals.	267
Appendix D: MIL-STD-883K required attachment strength.	269
Appendix E: Securing substrates to a build platform	270
Appendix F: Form 1 default control logic	271
Appendix G: Results data	273
Appendix H: Model inputs and outputs	289
Appendix I: Supporting diagrams.	291
Appendix J: MATLAB scripts	294

List of Figures

Figure 1.1: Monomers, polymerisation, branching and cross-linking.	28
Figure 1.2: Example gas sensor package by Texas Instruments [25]	30
Figure 1.3: Chapter structure.....	32
Figure 2.1: SLA constructed microfluidic-integrated encapsulant with silicon die and partially filled with liquid by Tehrani [36].	35
Figure 2.2: Example of 3D Structural Electronics by Lopes [2]	36
Figure 2.3: Single adaptor piece as described by Kataria et al [13].....	37
Figure 2.4: Insert criterion diagram by Liao [41]	38
Figure 2.5: Deformation attributed to reflectance by Aspar [16].....	40
Figure 2.6: Pendant drop (A) and curved surface (B) by Winkler [64].....	44
Figure 2.7: Crosslinked polymer chain lengths	47
Figure 2.8: Crack propagation with core shell rubber.	48
Figure 2.9: A sessile water droplet on a wafer surface by Okoroanyanwu [96].....	51
Figure 2.10: A Gaussian beam exposure profile.	59
Figure 2.11: Hatch spacing and exposure by Jacobs [9].	60
Figure 2.12: Ellipticity of a beam incident at oblique angles.....	62
Figure 3.1: Form 1 [142] [left] and Form 2 [42] [right] SLA machines.	69
Figure 3.2: The cured line width centralised on the perimeter circumference of the target construction and with line width compensation applied [right].	72
Figure 3.3: Formlabs scan pattern.	73
Figure 3.4: Exposure distance relative to FWHM and W_0	76
Figure 3.5: [left] Cure profile view from a single pass, [right] stepped edge profile from multiple layers.....	76
Figure 3.6: Zone of influence relative to line pass no.	78
Figure 3.7: Example superposition exposure profiles.....	79
Figure 3.8: Example energy gain from repeated laser scans	80
Figure 3.9: Light train of the Form 1+ and Form 2 machines	81
Figure 3.10: Laser path showing the angles of incidence for the Form 1 and Form 2	81
Figure 3.11: An example of the path of laser light through the respective mediums in the Form 2 SLA machine.....	83
Figure 3.12: Divergence of a beam with distance Z as a function of Rayleigh length.	83
Figure 3.13: Ellipticity of a beam	84
Figure 3.14: The process for calculating the CLW with the influence of D&E.	88
Figure 3.15: Process for calibrating the Form 1+ model using the dimensions of measured test pieces.	89

Figure 3.16: Process for calibrating the Form 2 model using the dimensions of measured test pieces.	91
Figure 3.17: Specular and Diffuse Reflection by Pedrotti et al [27].....	94
Figure 3.18: 90mm wide MFS test piece.....	98
Figure 3.19: CAD image of refraction array.	101
Figure 3.20: Laser overshoot.	101
Figure 3.21: [Left] Form 1+ reflectance test sample arrangement. [Right] Reflectance test samples on build platform after construction.	103
Figure 3.22: Flowchart for investigating adhesion.	105
Figure 3.23: Formlabs' cure oven [164].....	106
Figure 3.24: Construction of ASTM D638 test pieces	110
Figure 3.25: Construction of embedded strain gauges.....	112
Figure 3.26: The Form 2 build area as shown in the Preform software.	114
Figure 3.27: Glass [left] and a silicon nitride wafer [right] secured to the build platform using adhesive tape.....	115
Figure 3.28: Adhesion tensile test array on aluminium.....	116
Figure 3.29: CAD drawing of sample piece mounting bracket for tensile adhesion tests..	117
Figure 3.30: Texture Analyser arranged for tensile adhesion tests.....	117
Figure 3.31: Shear test sample secured in TA machine for adhesion testing.....	118
Figure 3.32: MIL-STD-883 test piece on silicon nitride	119
Figure 3.33: Pre-treatment process for silicon nitride with oxy-plasma and TMSPMA coating to promote adhesion.....	120
Figure 3.34: Mounting arrangement to observe interface using optical microscopy.	122
Figure 3.35: [Left] Greyscale test image by lightburnsoftware.com [172], [right] greyscale output showing varied lateral exposure.	123
Figure 3.36: Greyscale shear test pieces for varying lateral cure.....	124
Figure 3.37: Flowchart for constructing test pieces with varied lateral cure.	124
Figure 3.38: [centre] CAD image of piston insert geometry, [left and right] 2-part adaptor piece.	126
Figure 3.39: [top] TI semiconductor package (P82B715DRG4) insert, [bottom] TI chip insert with 2-part adaptor piece.	126
Figure 3.40: [left] Micro-LED before insertion into the SLA package	127
Figure 3.41: A design concept to integrate multiple packages constructed as individual modules.....	127
Figure 3.42: Process for inserting geometries into the SLA construction process	128
Figure 3.43: Package housing for inserting a micro-LED component.....	130
Figure 3.44: CAD of LDR insert housing.	131
Figure 3.45: CAD image of stacked insert housing.	131

Figure 3.46: [Top] CAD image of interconnector piece. [Bottom] CAD image of housing for multiple electrical inserts.....	133
Figure 4.1: The combined area of the FTIR spectra peaks.....	135
Figure 4.2: Measurement of the outer dimensions of the refraction array.....	143
Figure 4.3: Measurement of inner dimensions of the refraction array.....	144
Figure 4.4: [Top] Variation in the measured width of 1mm (design) test pieces.....	148
Figure 4.5: SLA polymer characterisation.....	153
Figure 4.6: Area of FTIR peaks (1637cm^{-1} and 1407cm^{-1}) corresponding to C=C bonds against PBC time.	154
Figure 4.7: Separation force of 1mm^2 test pieces on PC and elastic modulus with cure time.	158
Figure 4.8: Separation force of 1mm^2 test pieces on aluminium and elastic modulus with cure time.	158
Figure 4.9: Footprints from tensile tests on silicon nitride.....	159
Figure 4.10: Frustum shear tests on PC.....	159
Figure 4.11: Frustum test pieces on silicon nitride.....	159
Figure 4.12: Gauge strain (arbitrary units) vs cure time for samples after different periods of PBC.....	160
Figure 4.13: Average and corrected average strain (gauge) vs cure time.....	161
Figure 4.14: Strain vs cure time with temperature compensation samples 1 to 3.	162
Figure 4.15: Strain vs cure time with temperature compensation.....	163
Figure 4.16: Manually measured (method 3.4.2.8) absolute shrinkage and strain with PBC time.	163
Figure 4.17: Optical microscope image of sectioned interface between an SLA construction.....	164
Figure 4.18: SEM images of SLA interface on PC.....	164
Figure 4.19: SEM imaging of SLA product surface.....	165
Figure 4.20: Viscosity vs CSR concentration (liquid FLC photopolymer).....	166
Figure 4.21: Separation force of SLA photopolymer with CSR in shear tests (frustum test piece) on PC against cure time.....	166
Figure 4.22: [Left] SEM image of CSR particles (300x magnification). [Right] SEM image of free-standing CSR particle (800x magnification).....	166
Figure 4.23: SEM image of sectioned SLA sample containing CSR.	167
Figure 4.24: Optical microscope image of sectioned SLA sample containing CSR.	167
Figure 4.25: Optical microscope images from underside of SLA samples containing CSR.	168
Figure 4.26: standard (Form 1+ default machine settings) vs varied exposure (section 3.4.6.3) shear test results (frustum test piece) on glass.	169
Figure 4.27: Tensile test results on TMSPMA treated and untreated silicon nitride.	170
Figure 4.28: Residual footprints from tensile test pieces on untreated silicon nitride.....	170

Figure 4.29 Residual stems parts of tensile test pieces on treated silicon nitride	170
Figure 4.30: Separation force of MIL-STD-883 shear test pieces.....	171
Figure 4.31: Example of stacked modules (left) and compressed to form a package (right).	172
Figure 4.32: [Left] Example of a first layer modulus constructed directly onto silicon nitride,	172
Figure 4.33: [Left] A micro-LED embedded in an SLA package constructed onto a build platform.....	173
Figure 4.34: [Left] SLA construction interrupted and an LDR inserted mid build. [Centre and Right] Completed build with supports.	173
Figure 4.35: [Left] Finished photodiode package (supports removed).	173
Figure 4.36: Example test geometries with 2-part adaptors.	174
Figure 4.37: Demonstration package with two adaptor pieces inserted and stacked vertically.	174
Figure 4.38: SLA construction stages of a structural electronic package.	175
Figure 4.39: [Left] Structural electronic package product.	176
Figure 5.1: Measured and modelled CLW calibrated using E_c , FL and power, against scan speed.	179
Figure 5.2: Form 1+ beam power calibration curve.....	180
Figure 5.3: The exposure profile of parallel line passes and resulting superposition	182
Figure 5.4: The exposure profile of parallel line passes and resulting superposition	183
Figure 5.5: Cured leaser spot and interlayer step size.....	183
Figure 5.6: Measured and modelled part dimensions (Form 1+) at increasing scan speed.	184
Figure 5.7: The modelled (calibrated) and measured CLW against scan speed.	185
Figure 5.8: [Top] Intensity and exposure profiles (50mm/s). [Bottom] Cure profile from the beam exposure (50mm/s).....	186
Figure 5.9: Footprint of cure profile resulting from the increasing exposure at decreasing scan speed.....	187
Figure 5.10: Cure profile from the exposure delivered by the Form 1+	188
Figure 5.11: Menisci formed from a Gaussian beam with repeat scans at 50mm/s and 48mW setpoint power.	189
Figure 5.12: Modelled and measured CLW profile laterally across the Form 2 build area, without repeat scans.....	190
Figure 5.13: Variation in CLW across the build area due to divergence.....	191
Figure 5.14: Variation in CLW across the build area due to divergence and ellipticity	191
Figure 5.15: The modelled variation in the cured line width across the build area due to divergence and ellipticity for the Form 2 at default settings with MFLS (Case D1)...	192
Figure 5.16: Modelled and measured CLW and part width (1mm design) laterally across the Form 2 build area, with repeat scans (Case D1).	192

Figure 5.17: Potential magnitude of spurious cure due to specular reflectance from a silicon nitride substrate on the Form 1+ (Case R1).....	194
Figure 5.18: Vertical and lateral components of exposure due to reflectance.	195
Figure 5.19: Angle of reflectance from the build area substrate.....	196
Figure 5.20: Profile of the total exposure delivered to the photopolymer, with and without reflectance from aluminium at (Case R1) at the centre of the build are (normal AOI).	197
Figure 5.21: [Top] Spurious curing due to the vertical component of reflectance (Case R1) on aluminium and [bottom] silicon nitride.	198
Figure 5.22: Cure profiles models with and without reflectance generated using beam profiler.....	199
Figure 5.23: Potential for LSC due to reflectance from aluminium for Case R2 parameters on the Form 2.....	201
Figure 5.24: The potential for LSC due to reflectance from aluminium, and its variation with penetration depth, on the Form 2.	202
Figure 5.25: Measured and calibrated modelled part width with reflectance ($P_L = 96\text{mW}$, $D_p = 384\mu\text{m}$) to demonstrate the feasibility of reflectance accounting for the distortion measured.	203
Figure 5.26: The modelled magnitude of LSC	204
Figure 5.27: [Top] Gaussian model of LSC resulting from reflectance	205
Figure 5.28: [Top left] Variation in the measured width of 1mm (design) test pieces.....	206
Figure 5.29: Test pieces with and without exposure to reflectance,	207
Figure 5.30: Modelled magnitude of lateral distortion across the build area of the Form 2	210
Figure 5.31: Measured and modelled distortion profiles for the Form 2 and the Form 3 SLA machines with refraction deduced from measurements.	210
Figure 5.32: The increase in beam width due to ellipticity and divergence.....	212
Figure 5.33: Focal length of a laser and optimal point of focus.	212
Figure 5.34: CLW with optimised focus.	213
Figure 5.35: Build time operating window for optimisation using Case R1 parameters....	215
Figure 5.36: Operating window for gas sensor package.....	216
Figure 5.37: Transverse electric and magnetic reflectance of 405nm light incident on a silicon nitride wafer.....	217
Figure 5.38: The profile of a parabolic mirror to maintain a normal angle of incidence for the geometry of the Form 1 machine.	218
Figure 5.39: Beam power correction algorithm for the Form 2.	219
Figure 5.40: Lateral strain from shrinkage and the resulting stress plane.	226
Figure 5.41: Shear stress from shrinkage at the interface with the substrate.	227
Figure 5.42: Process flow to calculate and compare the stresses generated from shrinkage to those generated from applied test loads.	227

Figure 5.43: Gauge strain vs manually measured strain.....	228
Figure 5.44: Strain (%) compensated for temperature and calibrated.....	229
Figure 5.45: Stress recorded by using the strain gauge as a load cell,	231
Figure 5.46: Adhesive vs Cohesive failure.....	238
Figure 5.47: Green stumps after tensile testing on treated silicon nitride.....	239
Figure 5.48: Stumps after tensile testing with 2 minutes PBC on treated substrate.	239
Figure 5.49: Stumps after tensile testing with 8 minutes PBC on treated substrate.	239

List of Tables

Table 3.1: Operating conditions.....	69
Table 3.2: Material properties	70
Table 3.3: Equipment and tools.....	71
Table 3.4: Test methods.....	71
Table 3.5: The influence of superposition	79
Table 4.1: Summary of models.	134
Table 4.2 Measured cured line width on Form 1+ for 90µm test piece at increasing exposures.	136
Table 4.3: Form 1+ modelled (calibrated) diverged elliptical results at 50mm/s.....	137
Table 4.4: Form 1+ modelled (calibrated) diverged elliptical results at 100mm/s.....	137
Table 4.5: Form 1+ modelled (calibrated) diverged elliptical results at 200mm/s.....	137
Table 4.6: Form 1+ measured part width (1mm design) with superposition and MFLS at 50mm/s scan speed	138
Table 4.7: Form 1+ measured part width (1mm design) with superposition and MFLS at 100mm/s scan speed.	138
Table 4.8: Form 1+ measured part width (1mm design) with superposition and MFLS at 200mm/s scan speed	139
Table 4.9: Form 2 CLW at default machine parameters without superposition and with MFLS.....	139
Table 4.10: Form 2 measured part width (1mm design) with superposition and MFLS	140
Table 4.11: Form 2 measured part width (1mm design 5.5mm tall) with superposition without MFLS (Corresponding to case D2 in section 5.1.4.3.).....	141
Table 4.12: Form 2 modelled (calibrated) diverged elliptical results.	142
Table 4.13: Measured and modelled distortion of a 1mm wide (design) part with MFLS and reflectance at different locations across the Form 2 build area.....	142
Table 4.14: Measured outer dimensions (corresponding to Figure 4.2) of the refraction test array on Form 2.....	143
Table 4.15: Average measured dimensions (corresponding to Figure 4.3) of the refraction test array on a Form 2 SLA machine.	144
Table 4.16: Measured dimensions (corresponding to Figure 4.16) of the refraction test array on a Form 3 SLA machine.....	144
Table 4.17: Form 1+ measured part width of 1mm test pieces constructed onto the unreflective surface of PVC backed polycarbonate at 50mm/s.....	145
Table 4.18: Form 1+ measured part width of 1mm test pieces constructed directly onto silicon nitride at 50mm/s.	146
Table 4.19: Form 1+ measured part width of 1mm test pieces constructed onto the unreflective surface of PVC backed polycarbonate at 100mm/s.....	146

Table 4.20: Form 1+ measured part width of 1mm test pieces constructed directly onto silicon nitride at 100mm/s.	146
Table 4.21: Form 1+ measured part width of 1mm test pieces constructed onto the unreflective surface of PVC backed polycarbonate at 200mm/s.....	147
Table 4.22: Form 1+ measured part width of 1mm test pieces constructed directly onto silicon nitride at 200mm/s.	147
Table 4.23: 1mm wide test pieces with and without exposure to reflectance from silicon nitride at 50mm/s scan speed.....	150
Table 4.24: 1mm test pieces with and without exposure to reflectance from silicon nitride at 100mm/s scan speed.	151
Table 4.25: 1mm wide test pieces with and without exposure to reflectance from silicon nitride at 200mm/s scan speed.....	152
Table 4.26: Average difference in CLW due to reflectance at increasing scan speeds (reducing exposure) for the SRT and PRT tests.....	152
Table 4.27: Average contact angle and the standard deviation of water droplets on different substrates.....	155
Table 4.28: IFT, contact angle and WoA of water and resins on substrates.	156
Table 4.29: Surface roughness of substrate materials.	157
Table 4.30: Measured length of the uncompensated test strain test pieces before and after PBC.	161
Table 4.31: Measured shrinkage of uncompensated strain test pieces in order of magnitude	162
Table 5.1: Model calibration parameters for the Form 1+	177
Table 5.2: Form 1+ calibration process output values.....	178
Table 5.3: Form 2 calibration parameters	180
Table 5.4: Form 2 calibration test piece widths.....	181
Table 5.5: Form 2 calibration process output values.....	181
Table 5.6: Comparison of modelled and measured 1mm test piece dimensions	190
Table 5.7: Case R1 parameters for modelling reflectance on the Form 1+.....	194
Table 5.8: Case R2 parameters for modelling reflectance on the Form 2.....	200
Table 5.9: Potential LSC from reflectance on silicon nitride.....	206
Table 5.10: Average difference in CLW due to reflectance at different scan speeds for the PRT test.	208
Table 5.11: Specification for an anti-reflective coating to be applied to silicon nitride.....	218
Table 5.12: Minimum substrate pore size which can be penetrated by FLC photopolymer.	222
Table 5.13: Predicted separation force for 1mm ² SLA test pieces on aluminium and polycarbonate	223
Table 5.14: Maximum adhesive strength recorded in tensile tests after PBC.	225

Table 5.15: Average separation force and stress from testing (MIL-STD-883) and calculated equivalent shear force required to generate the same magnitude of stress. 231

Table 5.16: Average tensile stress calculated from the measured separation force during tensile adhesion tests (1mm²) and the corresponding shear stress calculated using Reedy's equation for different substrates. 232

Abbreviations

AM	Additive Manufacturing
AMB	Advanced Manufacturing Building
AOI	Angle of Incidence
ASTM	American Society for Testing Materials
AU	Arbitrary Units
BARC	Bottom Anti-Reflective Coating
BMF	Boston Microfabrication
CLW	Cured Line Width
CPS	Colorado Photopolymer Solutions
CPW	Co-planer Waveguide
CSA	Cross Sectional Area
CSR	Core Shell Rubber
D&E	Divergence and Ellipticity
DIC	Digital Image Correlation
DLP	Digital Light Processing
DMA	Dynamic Mechanical Analysis
DMD	Digital Mirror Device
DoF	Depth of Focus
DSA	Drop Shape Analysis
DSC	Differential Scanning Calorimeter
EUV	Extreme Ultraviolet
FL	Focal Length (mm)
FLC	Formlabs Clear SLA Resin
FLP	Formlabs Print file
FTIR	Fourier Transform Infra-Red Spectroscopy
FWHM	Full Width Half Maximum

IC	Integrated Circuit
IFT	Interfacial Tension
I/O	Input and Output parameters
IoT	Internet of Things
IPA	Isopropyl Alcohol
ITLM	Image to Laser Moves
LDR	Light Dependent Resistor
LED	Light Emitting Diode.
LEP	Liquid Entry Pressure
LOC	Lab on chip
LPP	Laser Produced Plasma
LSC	Lateral Spurious Cure
LPCVD	Low Pressure Chemical Vapour Deposition
LWC	Line Width Compensation
MATLAB	Matrix Laboratory
MEMS	Micro Electromechanical Systems
MFLS	Multiple First Layer Scans
MFS	Minimum Feature Size
MLT	Maximum Layer Thickness
MSDS	Material Safety Data Sheet
nmRC	Nanoscale and Microscale Research Centre
OCT	Optical Coherence Tomography
PBC	Post Build Curing
PC	Polycarbonate
PDMS	Polydimethylsiloxane
PECVD	Plasma Enhanced Chemical Vapour Deposition
PRT	Parallel Reflectance Test

RDL	Redistribution layer
RMS	Root Mean Squared
SEM	Scanning Electron Microscopy
SFE	Surface Free Energy
SFF	Solid Free Form
SIF	Silicon Interconnect Fabric
SIP	System in Package
SLA	Stereolithography
SOP	System on Package
SRT	Separate Reflectance Test
STL	Standard Tessellation Language
STDV	Standard Deviation
TA	Stable Microsystems Texture Analyser
TEAM	Thermoplastic Extrusion Additive Manufacturing
TMSPMA	(3-(trimethoxysilyl)propyl methacrylate)
TGA	Thermogravimetric Analysis
TI	Texas Instruments
TMV	Through Mould Via
UoN	University of Nottingham
UV	Ultraviolet
VP	Vat Polymerisation
WoA	Work of Adhesion

Glossary of terms

The nomenclature and terminology used in the field of additive manufacturing is still maturing with some variations. In 2015 ASTM 52900:2015 [1] was published, to harmonise the usage of AM terminology. For consistency, the terms used in the current document have been based on those available in that standard. Additional terminology, which is not covered by ASTM 53900:2015 is included below.

Adaptor package. An adaptor (single or two part) containing an inserted geometry or component to allow the insert to possess parallel sides.

Complex geometry. A geometry possessing a varying cross-sectional area along at least one axis.

Contour length. The length of an uncoiled polymer chain between cross-links.

Displacement length. The coiled distance of a polymer chain between cross-links.

Embedded gauge. A strain gauge onto which an SLA slab has been constructed resulting in the gauge being embedded within the construction.

Feature density. The concentration of electronic components per unit area of a circuit board.

Green part. A part which has been constructed without post build curing applied.

Hatch spacing. The distance between parallel line passes in an SLA scan pattern.

Insert criterion value. A value indicating whether an adaptor piece is needed for an insert and the requirements (i.e., single, or double).

Interfacial tension [1]. The adhesive forces between the liquid phase of a substance and either the solid, liquid or gas phase of another substance.

Large geometry. Greater than a single SLA construction layer thickness corresponding to the settings for the specific build.

Line pass (pass). The exposing of a single construction line to the laser, with multiple parallel passes having the potential to generate superposition.

Line width compensation. The spacing applied for the cured perimeter line pass to meet the design boundaries of the STL mesh and corresponds to the radius of cure.

Minimum Line Width. The width of the beam exposure profile equal to E_c , and thereby possessing sufficient energy to solidify the photopolymer.

Normal angle of incidence. Perpendicular to the substrate.

Penetration depth. The distance the incident light travels until it attenuates to a value equal to $1/e$ (approximately 37%) of its original incident intensity.

Perimeter line spacing. The distance between parallel perimeter line passes in an SLA scan pattern.

Photopolymer. A liquid polymer also referred to as resin, which is solidified through the crosslinking process initiated by exposure to UV light.

Reflection coefficient. The reflection coefficient is the amplitude of the reflected wave relative to that of the incident light.

Reflectance coefficient. The power of the reflected wave relative to that of the incident wave.

Separation force. The force (N) to separate two surfaces.

Scan. Scanning an entire SLA layer of a construction pattern, with multiple scans often applied to the first layer.

Specular reflection coefficient. The proportion of a reflected beam's power which is specular, with the remainder being diffuse.

Spurious curing. Unintentional curing of the SLA photopolymer.

Structural electronics [2]. Multiple electronic components arranged in three dimensions and within a single package.

Adhesive strength. The force per unit area (stress) required to separate two surfaces (N/m^2).

Work of Adhesion. The work required per unit area, to separate two surfaces (J/m^2).

Nomenclature

γ	Interfacial tension (surface energy) (mJ.m^{-2})
ν	Poisson's ratio
β	Pore geometry coefficient
σ	Stress (N.m^{-2})
$\dot{\sigma}$	Shear stress (N.m^{-2})
$\bar{\sigma}$	Tensile stress (N.m^{-2})
ε	Strain
θ	Angle (degrees)
λ	Wavelength (nm)
η	Refractive index
Σ	Density of attachment points (m^{-2})
ω_0	$1/e^2$ beam width (μm)
B	Direction of insertion into SLA build
B_a	Direction of insertion into adaptor piece
B_d	As-built dimension
C_{LW}	Cured Line Width (μm)
C_r	Cured line radius
D_p	Penetration depth (μm)
D_d	Design dimension
e	Exponential

E	Elastic modulus (N.m^{-2})
E	Exposure (mJ.cm^{-2})
E_c	Critical exposure (mJ.cm^{-2})
E_{max}	The maximum exposure delivered along a single line pass (mJ.cm^{-2})
E_p	Peak exposure resulting from superposition (mJ.cm^{-2})
E_r	Delivered exposure at beam radius r for a given scan speed (mJ.cm^{-2})
E_v	Valley exposure (mJ.cm^{-2})
h_s	Hatch line spacing (μm)
I_0	Peak beam intensity at centre of the beam (mW.cm^{-2})
I_r	Beam intensity at radius r (mW.cm^{-2})
K_{xt}	Lateral deviation of the incident spot due to refraction (μm).
L_c	Average polymer chain contour length (m)
L_T	Layer thickness (μm)
L_{WC}	Line width compensation (μm)
L_x	Average part length in the x-plane (mm)
L_y	Average part width in the y-plane (mm)
L_z	Average part height in the z-plane (mm)
M^2	Beam quality factor.
M_T	Manufacturing Tolerance
n	Vector normal to the STL mesh

n_L	Number of construction layers
N	Number of lines within the superposition zone of influence
P_L	Laser power (mW)
p_s	Perimeter line spacing (μm)
r_{max}	Maximum pore size of substrate (μm)
r	Radius of a beam which corresponds to a given intensity [I_r] (μm)
R	Zone of influence (μm)
R_{az}	Ratio of cross-sectional area to height
R_{LT}	Required layer thickness (μm)
R_s	Specular reflectance coefficient
R_o	Reflectance from an optically smooth surface
R_r	Surface roughness reflection coefficient
S	Insert criterion value
S_q	RMS surface roughness (μm)
S_s	Step size (μm)
t	Time (s)
t_B	Build time (s)
t_D	Delay time (s)
t_e	Exposure time (s)
U	Chemical bond energy ($\text{J}\cdot\text{m}^{-1}$)
U_T	The total energy of the system (J)

V_s	Scan speed (m.s^{-1})
W_0	$1/e^2$ beam radius of a focussed beam (μm)
W_a	Work of adhesion (J.m^{-2} or N.m^{-1})
W_d	$1/e^2$ radius of a diverged beam (μm)
W_{de}	$1/e^2$ radius of a diverged elliptical beam (μm)
Z	Depth
Z_e	Extension to the laser path from the focal point
Z_L	Lateral distance across the build area
Z_{pc}	Length of the laser path to the centre of the build area
Z_R	Rayleigh length

Chapter 1

1. Introduction

“The Moore’s Law has died. We all are living in a post-Moore age. In the post-Moore age, new technology innovations will no longer be from the traditional front-end process. Instead, new technologies such as wafer level fan-out, and 3D packaging will be the dominant forces for technology revolution. As a result, the focus of the semiconductor industry is shifting to the packaging process [3].”

C. Qingzhou (2020) Founder of Polymer Solutions for Electronics Consulting LLC

1.1. Additive manufacturing

Additive manufacturing (AM) uses a digital source to construct a desired geometry by progressively adding material. This provides the ability to form geometries which are difficult, or even impossible, to construct by conventional, subtractive processes. Additionally, no mould or pattern is required, which lends itself to reduced lead times, product customisation and associated cost savings. Moreover, due to the ability to construct complex parts, a significant reduction in the required number of sub-components can be realised which reduces assembly time, the number of interfaces, and improves reliability. Consequently, AM technologies have become established industrial manufacturing processes encompassing a variety of materials including metals, ceramics, and polymers. The applications for AM polymer products are diverse and include the manufacture of medical implants [4], living cell laden tissue constructs [5], dentistry [6] and electronics. It is the latter which is the topic for the current investigation.

1.2. Stereolithography

Stereolithography (SLA), which is also known as vat polymerisation was first patented by C.W.Hull [7] in 1990. The conventional laser SLA process uses software to convert a CAD image, typically in an STL format (Standard Tessellation Language), to generate a series of planar sections and corresponding command scripts for controlling the movement of galvanometers to which mirrors are attached. Some recent equipment uses an LED as the light source in conjunction with a micro-electric DLP (Digital Light Processing) [8] system. Most commercial machines can be categorised as bottom-up or top-down machines depending upon the direction from which the UV-light originates. Within the build area, a platform attached to an actuator, is precisely positioned within a vat of liquid photopolymer. In a bottom-up process the resin tank contains a UV transparent window through which the

laser is directed. The UV source is then illuminated and guided around the build area by the galvanometer mirrors to form each planar section, or ‘layer’. The photopolymer contains an initiator which, when exposed to sufficiently powerful UV light, initiates a free-radical reaction to form polymer chains which subsequently branch and cross-link [9] (Figure 1.1) to form a solidified product. The threshold energy at which curing of the photopolymer initiates and solidification ensues is termed the critical cure energy (E_c). After the scanning of each layer has been completed, the construction is interrupted, and the photopolymer levelled (top-down process) or the window wiped (bottom-up process) normally using a screed or wiper. The wiper serves to mix the photopolymer, remove failed builds to avoid damage to concurrent constructions and importantly to oxygenate the surface of the resin tank window. The position of the platform is then adjusted along the z-axis, ready for exposing and constructing the next layer.

The process is repeated and the subsequent layer crosslinks with the previous partially cured one, to form a continuous solid product. Once completed, a construction is removed from the platform and washed with IPA (Isopropyl alcohol) to remove residual resin. It is common practice to then place the part into a post build curing (PBC) oven for a period of time to progress the cross-linking process (Figure 1.1) and increase the strength of the part.

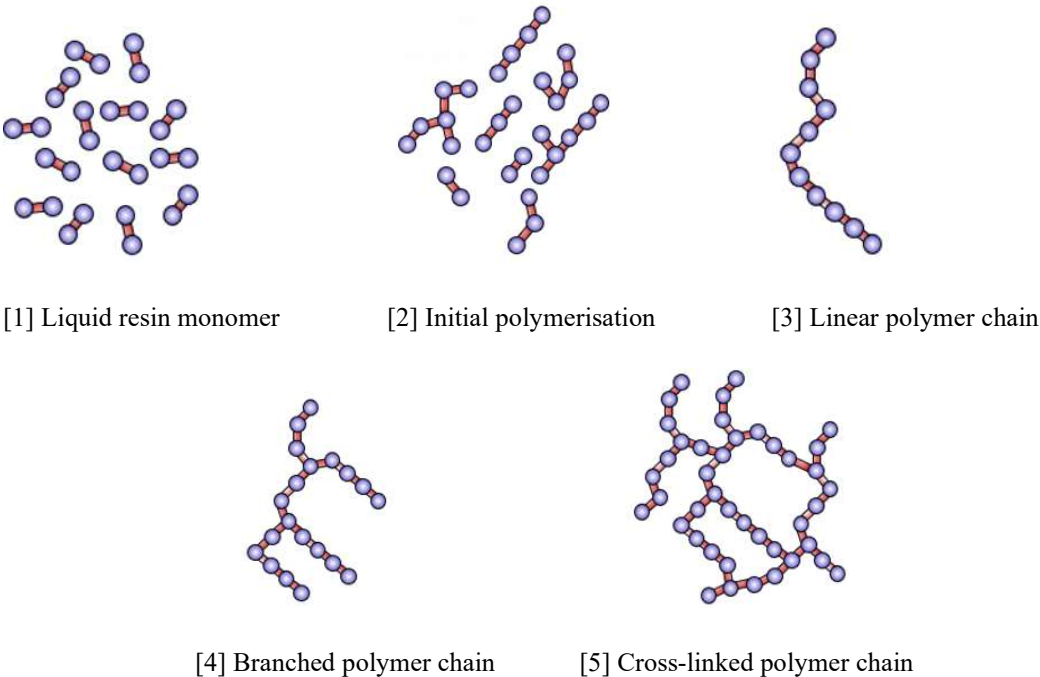


Figure 1.1: Monomers, polymerisation, branching and cross-linking. Generic example of polymerisation from [1] liquid monomers (e.g. ethylene $[C_2H_4]$) undergoing [2] initial polymerisation to form short chain polymers (e.g. polyethylene $[C_2H_4]_n$) and [3] further polymerising to form polymer chains of increasing length ($>n$), [4] branched polymers (e.g. low density polyethylene) and [5] crosslinked polymers (e.g. high-density cross linked polyethylene (e.g. HDXLPE)).

1.3. Industrial application

Potential benefits have been identified in using SLA to construct three-dimensional geometries onto non-standard substrate materials, for the purpose of packaging electronic components. The substrate material of primary interest is silicon nitride (Si_3N_4) for which an industrial need has been identified. This initiative is sponsored by industry and supported by the work reported in this document.

1.4. Motivation

The interest in new packaging solutions is increasing with the advent of the internet of things (IoT) and the increasing demand for low-cost devices. Conventional methods for packaging electronics include potting and injection moulding. Tiedje et al [10] explains how SLA avoids the strict process rules required when removing a casting from a mould. Additionally, SLA offers a potential reduction in production time compared to moulding processes [11], [12]. The conventional process of potting requires the injection of pressurised epoxy resin at high temperature which imposes stress on the product and introduces a failure mechanism. By using SLA and constructing packages incorporating purpose designed cavities, the stresses associated with conventional methods may be reduced or eliminated [10] and improve the reliability when embedding sensitive components such as sensors [2], motors [13] and antennas [14], with the added benefit of reduced energy consumption [15]. Aspar [16] investigated the compatibility of TEAM (Thermoplastic Extrusion Additive Manufacturing) and SLA with substrates of common materials used in electronics including polyimide, silicon dioxide and silicon mono-nitride. Due to the superior adhesion recorded between SLA products and the substrates, and the technology possessing a higher resolution, SLA was identified as the preferred process. Additionally, SLA avoids the high temperatures associated with TEAM. SLA is also preferred to inkjet technology, for the potential to insert, and subsequently encapsulate complex, and large components. Aspar [16] also dismisses inkjet technology for packaging electronics as it does not allow the construction of “complex structures and cavities at the same time”. Consequently, SLA has been chosen in preference to the AM processes of TEAM and inkjet printing.

SLA allows flexibility when constructing complicated geometries and to arrange components in three dimensions while providing a cost-effective alternative to injection moulding [11]. The sentiment expressed by Qingzhou [3] at the beginning of this chapter, describes the focus being placed on packaging in the semi-conductor industry. It is

envisaged that SLA will yield extensive solutions and opportunities in this field. Gordon Moore in his paper [17] which presents his signature law to which Qingzhou refers [3], also mentions the potential for functional packaging and its disproportionate cost. The potential benefits for using SLA technology includes enabling an increased feature density [18] to optimise the use of expensive and long lead time substrate materials; the construction of packages for complex spaces; aid the interfacing for MEMS (Micro Electro-Mechanical Systems); and facilitate rapid production for bespoke applications. Other potential outcomes include the construction onto bare die removing the need to package individual components and the construction of conduits for die-to-die interconnects, and in-package passive components. Additionally, functional packaging to complement the operation of the device, by incorporating microfluidics [12], [19] or SOP (System on Package) technology [20], [21] can also be possible. The ability to construct SLA onto silicon nitride can also be applied to the relatively new technology of Silicon Interconnect Fabric (SIF) [22], [23]. When compared to conventional PCBs, SIF permits a substantially increased density of connections and features in a circuit. This can increase the bandwidth by up to 300 times [22] and reduce the energy per bit by a factor up to a 500. The technology uses silicon nitride [24] as the surface passivation layer which forms the interfacial contact layer with surface mounted semiconductors and their associated packaging. Consequently, it is this material layer which would form the interface with SLA polymer in the current investigation.

However, some concerns regarding the use of SLA to construct electronic packages and building directly onto silicon nitride have also been identified and are discussed below.



Figure 1.2: Example gas sensor package by Texas Instruments [25]

In SLA processes, the achievable manufacturing tolerance is dependent upon the minimum cured line width (CLW) which dictates the side length of the minimum feature size (MFS). The need for precise control of the MFS is demonstrated by the example gas sensor package [25] shown in Figure 1.2. The component requires a MFS of $350\mu\text{m}$ and possesses a minimum manufacturing tolerance of $50\mu\text{m}$ (Appendix A). The quality and consistency when manufacturing fine features in the SLA process is sensitive to inaccuracies, loss in

precision, and distorting effects. Moreover, there is a trade-off between the MFS and build time which needs to be considered for commercial applications.

Reflectance is a concern in the photolithography process when fabricating semi-conductors because it can cause distortions in the product. To mitigate this, it is standard practice in [26], [27] to apply an anti-reflective coating to the surface of the substrate, known as a BARC (Bottom Anti Reflective Coating). Similarly, due to its smooth surface and relatively high refractive index (Table 3.2), potential reflection of UV light from a silicon nitride substrate is a concern [16], [28] when using the material in the stereolithography process. If the reflections are sufficiently powerful, they will have the potential to cause spurious curing resulting in defects.

The strength of the bond between the substrate and the product is of particular interest, due to the requirement for constructions to be sufficiently adhered for industrial applications. Additionally, it is desirable to house multiple components possessing large or complex geometries within a package which would need to be inserted into the SLA build process.

Further work beyond the immediate scope may venture into constructing packages onto flexible substrates and the manufacture of products for moveable, and deformable applications or wearable items.

1.5. Aim

The aim of this study is:

To investigate the production of 3D geometries on silicon nitride for the purpose of packaging electronics, using stereolithography.

To achieve this aim and mitigate the concerns identified in section 1.4, the following objectives have been identified:

Objective 1: Investigate the potential for reflectance from a silicon nitride substrate to generate spurious curing.

Objective 2: Determine factors which influence the strength of adhesion between an acrylate SLA photopolymer and a silicon nitride substrate. Once an understanding of these factors has been obtained, determine how SLA products can be sufficiently bonded to the substrate for commercial application.

Objective 3: Optimisation of the SLA process for build time, while achieving the required manufacturing tolerances.

Objective 4: Develop a process to insert large components and complex geometries, into an SLA build process;

These objectives are reported in the corresponding chapters as summarised in section 1.6. To support these objectives, an understanding of the experience to date using SLA for constructing directly onto silicon nitride is required. Therefore, a review of available and relevant literature was conducted and is reported in chapter 2.

1.6. Chapter content summary

The content of each chapter in this document is summarised below with the chapter structure shown in Figure 1.3. Adhesion, distortion and inserting geometries form the three principal areas of investigation. A review of previous work is reported in chapter 2. Modelling and experimental methods are described in chapters 3 and the corresponding results documented in chapter 4. Those results are then analysed and discussed in chapter 5.

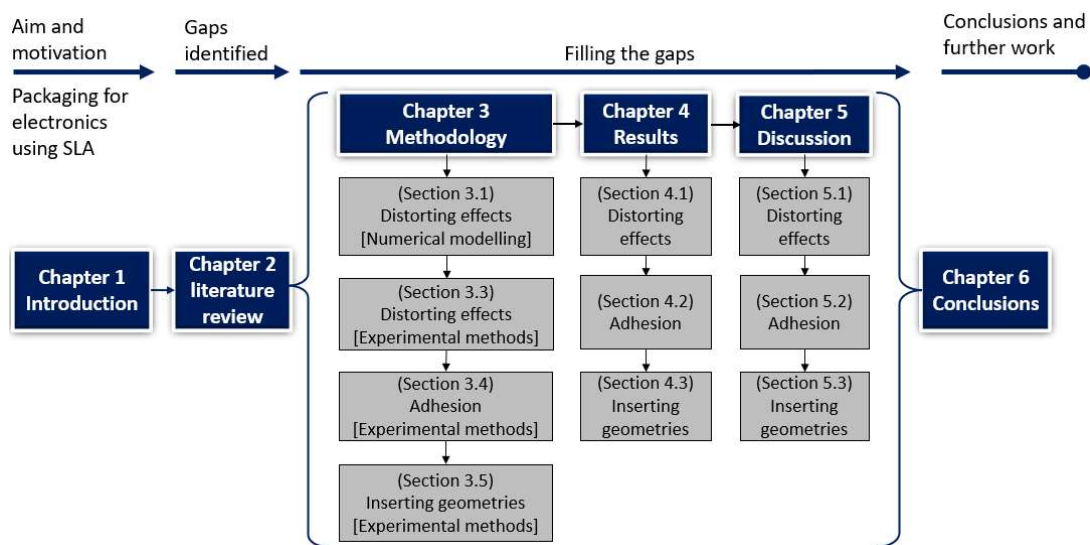


Figure 1.3: Chapter structure

Chapter 2: Literature review

Relevant literature is reviewed to identify the current knowledge of the respective topics being investigated. Due to these being diverse, the review of literature has been divided into three parts: Reflectance and distortion, adhesion in SLA, and inserting components into an SLA process. The gaps in the current knowledge required to achieve the aims of the study are then identified, so they can be filled during the investigation.

Chapter 3: Methodology

The reasoning behind the approach taken to achieve the aims (section 1.5) of the investigation is described. The numerical modelling and experimental methodologies applied are then detailed.

Chapter 4: Results

The results of the experimentation and numerical modelling conducted following the methods described in chapter 3 are documented. These are subsequently analysed and discussed in chapter 5.

Chapter 5: Discussion

The results pertaining to each area of investigation are discussed in their respective subchapters as follows.

Subchapter 5.1: Investigating distorting effects in the SLA process.

A description of numerical modelling using MATLAB™ to investigate the minimum achievable cured line width (CLW), and distorting effects is reported. These include beam noise, ellipticity, divergence, over-exposure, and refraction. The influence of superposition from the Gaussian profile and scan pattern, is considered within the modelling. Resin and substrates properties on refraction, and reflectance are investigated, and experimental methods devised to quantify these distorting effects for comparison with the model, are explained.

The potential magnitude for spurious curing due to reflectance, together with the loss in accuracy and precision due to other distorting influences is reported. Input variables include the photopolymer, substrate, and beam properties, together with the equipment geometry. Measures to mitigate distorting effects are identified, including operating parameters, material adjustment and equipment modifications. By quantifying the operating parameters to meet manufacturing tolerances, the onset of spurious curing due to reflectance, and the required minimum exposure, an operating window can be identified within which to optimise the SLA construction process. Additionally, the scale of construction in terms of the maximum build area which can be utilised before distorting effects preclude manufacturing tolerances from being met, is also determined.

Subchapter 5.2 Adhesion

The strength of adhesion between a commercially available SLA photopolymer and different substrate materials, the failure mechanisms, and methods to promote

adhesion, are investigated. The chemical affinity of the photopolymer with the substrate and the influence of post build curing is explored. Practical methods to enhance adhesion including the addition of core shell rubber and the application of a specific chemical monolayer, are tested and their effectiveness measured. Properties adversely affecting adhesion and causes of inconsistencies are identified. From reviewing laboratory data, the dominant adhesion mechanism between a photopolymer and the substrate is hypothesised and a successful process to promote adhesion between the photopolymer and silicon nitride, is demonstrated.

Subchapter 5.3. Inserting components.

The process to insert large or complicated geometries into a conventional SLA construction is described. This is then developed to incorporate through-mould-vias to allow inserted components to be connected electrically. Relevant design rules are discussed. The process applied to interact directly with a commercial SLA machine to facilitate the inserting of components, and produce a demonstration package featuring stacked components, is explained.

Chapter 6: Conclusions and further work

Conclusions and findings obtained during the investigations and identified in the preceding chapters, together with topics for future investigation are reported.

Chapter 2

2. Literature Review

As will be discussed, the flexibility of SLA lends itself to the integration of components and complex geometries into the build process with the ability for them to be arranged in three dimensions to achieve unitisation and miniaturisation of an integrated package. A review of prior work undertaken to understand the limitations and challenges with using SLA to package electrical components onto silicon nitride, is reported in the following sections.

2.1. Packaging electronics using SLA.

There have been a number of investigations reporting the use of SLA to construct substrates and housings for electronic systems with surface mounted components or system-on-package (SOP) solutions [29], [30], [31], [32], [33], [34]. SLA allows for multiple surface mounted products such as antennas [35] and wireless transceivers [21] to be offset from one another and integrated in a single package. For example, millimetre-wave (mm-wave) technology, provides the benefit of wider bandwidth and smaller antennas, making it attractive for applications such as 5G mobile networks and vehicular radar sensing but suffers from high interconnect losses. The losses can be reduced using highly integrated packages [21] and low loss waveguides. Tehrani [35] used SLA to construct co-planer waveguide geometries to serve as interconnectors and aid the integration of components in confined areas, reducing losses and the overall package size.

Embedded, system-in-package (SIP) solutions, such as microfluidics to allow flow channels to provide cooling, can also be incorporated into an SLA package, as demonstrated by Tehrani [36] (Figure 2.1).

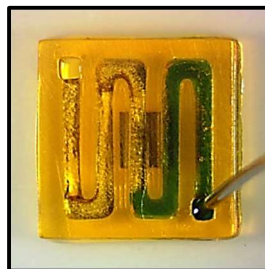


Figure 2.1: SLA constructed microfluidic-integrated encapsulant with silicon die and partially filled with liquid by Tehrani [36].

Similarly, SLA could also be used to encapsulate components such as photosensors which would conventionally have to be located at the surface of a package to allow exposure to environmental light. Instead, optically clear channels could be built using SLA to provide a line of sight to a sensor embedded within the package. Additionally, SLA provides the ability to construct geometries with a high degree of void, allowing the manufacture of complex shapes containing cavities without the need for complex machining. To support this, Gong et al [19] modelled the minimum void which can be fabricated as a function of the penetration depth. Many of the packaging schemes for electronics described in the literature involve hybrid systems which combine SLA with another AM process. Lopes [2] and MacDonald [37] developed particularly advanced hybrid AM systems for encapsulating and interconnecting electronic components in three dimensions. Lopes' proprietary process [2] combines an SLA machine featuring an interrupt function, with a direct print (DP) system for applying conductive interconnects within a single build process. The products from this process have been termed "structural electronics" [2] an example of which is shown in Figure 2.2.



Figure 2.2: Example of 3D Structural Electronics by Lopes [2]

However, as explained by Persad [38], hybrid systems can create issues with process compatibility, and increase complexity, cost and time when switching between processes. Furthermore, proprietary systems possess significantly increased capital and operational costs [38] associated with specialist equipment, materials, and training. Consequently, this investigation is focused on the use of conventional SLA processes.

2.2. Inserting geometries into the SLA process

An SLA construction progresses on a layer-by-layer basis as described in section 1.2. For standard desktop SLA equipment, a typical layer thickness is between $25\mu\text{m}$ and $200\mu\text{m}$ [39], depending on the required resolution in the vertical z-axis. By interrupting the build process between layers, prefabricated components can be inserted and embedded into the construction.

However, as Lopes [2] explains, there are challenges to inserting components such as the component interfering with the SLA process, and the ability to interrupt the operation of the

system. Components greater in height than a single layer thickness are termed ‘large’. Attempting to insert such a component without intervention, will result in a clash [13] with the machine’s equipment. This being either the resin tank in a bottom-up process or the recoating blade in a top-down machine [13].

Tiedje et al [10] used a bottom-up Form 1+ SLA machine to encapsulate a 200µm LED equal in height to a single construction layer and thereby avoiding clashes with the resin tank. The SLA polymer was constructed directly onto the LED to encapsulate a single component. However, this process is limited to encapsulating small components directly onto the substrate. To insert multiple, large components and arrange them in three dimensions, as required to meet the aims of the current study, requires further consideration.

As described by Kataria [13], components possessing a decreasing cross-sectional area (CSA), may not be possible to insert or will result in cavities. These inserts are termed ‘complex’. A solution was identified [13] for inserting complex geometries possessing an inconsistent CSA along a single axis, by using an adaptor piece (Figure 2.3). These accommodate the geometry and convert them to parallel-walled inserts.

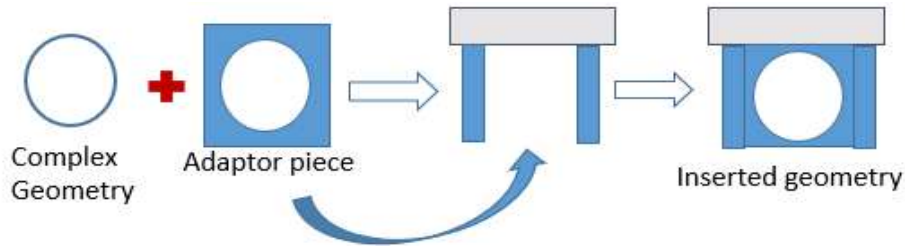


Figure 2.3: Single adaptor piece as described by Kataria et al [13]

The application of adaptor pieces can be developed further, with 2-part adaptors to accommodate inserts with a decreasing CSA in multiple axes. Chiu et al [40] derived an equation to describe the contoured curvature of an SLA construction. Separately, Liao et al [41] applied a similar equation to define the requirement for adaptor pieces using the ‘criterion value’, as a function (Equation 2.1) of the cosine of the angle between; the vector normal to the insert STL surface mesh, and the direction of insertion (Figure 2.4).

$$S = \vec{B} \cdot \vec{n} = |\vec{B}| |\vec{n}| \cos\theta$$

Equation 2.1: Insert criterion value by Liao [41]

Where: S is the insert contour

\vec{B} is the direction of insertion,

\vec{n} is the unit vector normal to the STL surface mesh.

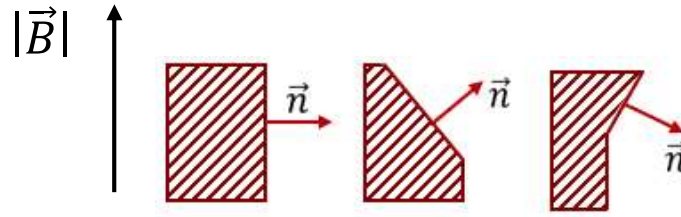


Figure 2.4: Insert criterion diagram by Liao [41]
 [left] $a = 0$, (centre) $b > 0$ and, [right] $c < 0$,

This results in three cases as described by Liao [41]:

- a) “When $\theta = 90^\circ$, $S = 0$, \vec{B} and \vec{n} are perpendicular to each other;
- b) When $\theta \leq 90^\circ$, $S > 0$, \vec{B} and \vec{n} are in the same direction;
- c) When $90^\circ < \theta \leq 180^\circ$, $S < 0$, \vec{B} and \vec{n} are in the opposite”.

The requirement for a single or two-part adaptor piece is then determined as a function of the criterion value relative to the “disassembly line” as defined by Liao[41]. For case [b] ($S > 0$) an adaptor piece may be required if the part can’t be reorientated and the frame receiving the part adapted. It is for case [c] ($S < 0$), when the part can’t be reorientated to satisfy condition [b] to fit in a single adaptor piece (i.e., due to other contours or features), that a two-part adaptor piece may be required.

2.3. Building onto wafers and non-standard substrates

The standard substrate material used in SLA is aluminium [42]. As discussed in sections 2.4.4 and 2.4.5, this provides a durable, sufficiently smooth, non-deformable surface to which SLA polymer will adhere. Alternative substrates have been used in the literature for a variety of reasons, normally to support a specific application. For reasons explained in section 1.4, silicon nitride is the material of interest in the current study. Literature reporting constructing geometries directly onto silicon nitride was searched for but without success which identifies a significant knowledge gap.

Due to the absence of previous work relating specifically to silicon nitride, the literature search was expanded to include that reporting the construction of geometries onto other substrate materials. Materials dissimilar to silicon nitride can provide valuable learning points for incorporating substrates into the build process, investigating reflectance (section 2.3.1) and methods for measuring adhesion (section 2.4.3).

An initial consideration is to identify a means to secure a substrate onto the build platform for the duration of the SLA build process. Malengier [43] experimented with securing substrate samples to a TEAM build area using clamps, glue, and adhesive tape, with the latter being chosen as the preferred method. Grothe [44] also used adhesive 2.7.1 for securing substrate samples in an SLA process. Tiedje et al [10] secured a polyimide substrate, to serve as a redistribution layer (RDL) to a Form 1+ SLA machine with a modified vacuum stage. The thickness of the substrate was compensated for by adjusting the Z-offset of the machine in the control software. However, issues were reported with entrapped gas forming at the periphery of the substrate, possibly due to air and resin being entrained by the vacuum.

2.3.1. Reflectance

For reasons explained in section 1.4, reflectance is a concern when building onto silicon nitride using SLA. Reflectance is described by the Fresnel equations [45]. These show the magnitude of reflectance to be a function of the dissimilarity between the refractive indices of the substrate and the preceding medium through which the incident light travels.

Three studies by Aspar [16], [28], [46], refer to the occurrence of reflectance in SLA processes but do not examine the characteristic in detail. None have quantified the influence on the delivered exposure in an SLA process, or the potential to cause spurious curing.

Sun [46] et al, refer to reflection and recognise its potential to produce adverse effects but without quantifying it. The occurrence of reflectance in their [46] application is mitigated by the arrangement of the experimental setup. Spacers were used to increase the depth of photopolymer and attenuation of the incident light before reaching the substrate to minimise reflectance.

The potential for reflectance to influence the delivered exposure due to a portion of the incident light being reflected by the photopolymer, is mentioned by Lu et al [28]. Their concern being the variation in exposure will also vary the extent of polymerisation and shrinkage, making it non-uniform.

To calculate the magnitude of reflectance in the current application, it is necessary to know the refractive index of the substrate and photopolymer materials. Aspar [16] observed deformation (Figure 2.5) which they attributed to reflectance when constructing 5mm cube test pieces onto silicon oxynitride (SiON). This material's slightly reduced refractive index of 1.96 (Table 3.2) will result in a lower reflectance coefficient than Si_3N_4 when immersed

in an acrylate photopolymer. Therefore, an increased distortion would be expected from silicon nitride.



Figure 2.5: Deformation attributed to reflectance by Aspar [16]

The magnitude of reflectance can also be influenced by interference and the coherence of the incident light. Lasers produce light with a high degree of coherence [47] with a narrow spectral bandwidth (low $\Delta\lambda$). Their spatial coherence is benefitted by originating from a single point source with minimal divergence. Therefore, at normal angles of incidence, the light reflected from the substrate in SLA will be spatially coherent with the incident light resulting in interference. However, in practice, the beam from the laser SLA machines to be used in this study (i.e., Form 1+ and Form 2 machines), only form a normal angle of incidence at precisely the central location of the build area. The extent of interference [45], and whether it is destructive or constructive, at this location is dependent on the respective refractive indices of the substrate and the photopolymer.

Luke et al [48] applied experimentally obtained data to the Sellmeier [45] equation to produce an expression for the refractive index of silicon nitride (Si_3N_4) for wavelengths from 310nm to 5504nm.

$$\eta^2 = 1 + \frac{3.0249\lambda^2}{\lambda^2 - 135.3406^2} + \frac{40314\lambda^2}{\lambda^2 - 1239842^2}$$

Equation 2.2: Refractive index of Si_3N_4 as a function of wavelength [48]

This allows the refractive index of the material to be calculated at the given wavelength of the specific SLA machine to be used.

2.3.1.1. Refraction

The angle of refraction is a function of the angle of incidence as described by Snell's law [45]. The concern regarding refraction in SLA is the potential for the beam to be incident on the substrate at a point removed from the target location. Refraction will occur if the media in the SLA system through which the beam travels possess different refractive

indices. A review of literature did not identify any specific investigations into the potential significance of refraction in SLA. From reviewing the operating manual [42], the material composition of the relevant media and their refractive indices, present in the Formlabs™ SLA machines, have been identified from various sources [49], [50], [51], [52], [53], [54] and included in section 3.1.

2.3.1.2. Surface roughness

The surface topology of a substrate can have an overriding influence on the magnitude of specular reflection which shall be considered when introducing a polished substrate such as silicon nitride into an SLA process. The formation of menisci on smooth aluminium at high exposures was reported by Ackstaller [33]. The cause of the menisci is not identified [33], and the surface roughness of the substrate is not measured but described as “much smoother” than the build platform. It is possible that reflectance from the smooth surface coupled with the low refractive index of aluminium (Table 3.2), may have contributed to the formation of the ‘menisci’ by increasing the overall exposure. The influence of surface roughness on reflectance is described by Trezza et al [55] using the Bennet-Porteus model (Equation 2.3).

$$R = R_0 \exp - \left(\frac{4\pi S_q \cos\theta}{\lambda} \right)^2$$

Equation 2.3: The Bennet-Porteus model [55] for reflectance from a roughened s surface

Where R is the specular reflectance from a rough surface

R_0 is the reflectance from an optically smooth surface,

S_q is the RMS surface roughness.

λ is the wavelength of the incident light.

θ is the angle of incidence.

By dividing Equation 2.3 by the reflectance coefficient (R_0) the surface roughness coefficient (R_r) is obtained in Equation 2.4.

$$R_r = \exp - ((4\pi\sigma.\cos \theta_i)/\lambda)^2$$

Equation 2.4: Surface roughness reflectance coefficient

2.4. Adhesion in SLA

Strong adhesion between the package and the substrate is required to ensure they do not become separated during construction, or commercial application. Consequently, the common adhesion failure mechanism of crack propagation and mitigating measures is reviewed in section 2.4.1. The adhesion mechanisms active in SLA and potential methods reported in the literature to enhance them, are reviewed in section 2.4.2. Prior work into the testing the strength of adhesion in SLA products is reviewed in section 2.4.3. The requirement for an SLA photopolymer to adequately “wet” and thereby achieve sufficient contact with the substrate while in its liquid phase is reviewed in section 2.4.4. Subsequently, after the photopolymer is exposed to UV light and cured, the requirement for the solidified product to be adequately bonded to the substrate for practical use is reviewed in section 2.4.5.

2.4.1. Crack propagation

Adhesion failure at the substrate/SLA interface will result from a crack initiating at the interface [56], which then propagates across the full cross-section of the joint. Conversely, if the crack propagates through the bulk material, this is classed as cohesive failure. Abbott [57] states how "...adhesion is much more about dissipation than it is about ‘strength’". Accordingly, a bonding process providing a high strength of adhesion is undermined without the ability to reliably mitigate failures from cracking. Griffiths law [58] relates the size of a defect in the interface, stress, and crack propagation. Cracks originating from larger defects require significantly less stress than smaller ones to propagate to failure. Moreover, if the defect occurs in a region of high stress, crack failure is more likely to ensue. Lu et al [28] comment that fractures in an SLA process originated from entrapped gas cavities resulting from the re-coating process. Griffith’s law [57] describes how the crack failure stress is proportional to $1/\sqrt{a}$, (where a is the size of the void), so as defects becomes larger, the failure stress reduces. Consequently, it is desirable to minimise the size of defects within the process. Additionally, the inconsistent occurrence and location of entrapped gas cavities introduces some variability into the process.

Griffiths also explains the dependency of crack propagation on energy dissipation as subsequently described by Kendall [59]. Kendall’s equation (Equation 2.5) shows the ability for the crack to propagate in both adhesive and cohesive failure, depends upon the rate at which energy is dissipated, transferred to the formation of the resulting new surface, or stored.

$$\frac{dU_T}{da} > 0$$

Equation 2.5: Crack propagation as a function of the rate of change of the total energy in the system and increase in surface area formed, by Kendall [59].

Where U_T (J) is the total energy of the system in a strained joint of dimension a (m). If the energy at localised stress points is sufficiently high and cannot be dissipated or stored (e.g., the material is not sufficiently elastic to store the energy), then the molecular bonds between the materials are broken and a crack forms. This is the threshold for crack initiation. If there is less energy dissipated or stored by the formation of the new surface than is released during the separation process (Equation 2.5), then the surplus energy will serve to propagate the crack. This continues until the crack energy is dissipated below the propagating threshold (the work of adhesion) or the joint completely fails. Consequently, the elastic modulus of a material and its ability to store energy, can have a significant influence on its adhesive properties.

This is consistent with the work by Gordon [60] into the effect of elastic modulus on polymer adhesion who concluded low modulus materials were less susceptible to crack propagation. Moreover, from a series of shear tests, they [60] found that adhesion / substrate combinations with similar moduli had an improved bond strength. This was attributed to the ability for materials with similar moduli to transfer stresses more effectively [60]. This characteristic was also reported by Newby et al [61], when experimenting with the mechanics of adhesion who state; “In our opinion, the more important source of shear at the crack tip comes from the huge elastic modulus difference between the substrate and the adhesive.”

In addition to dissipation, the elastic modulus and flexibility of a material can influence the quality of the contact between surfaces. Wang et al [62] state: “High elastic modulus (inflexible) materials will not bond well with rough surfaces”, due to their reduced ability to mould to the substrate. That author [62] and several others [57], [59], [62], [63] use the example of the gecko’s foot to explain how the geometry and properties of materials can influence adhesion and promote the mechanism of surface energy. This and other adhesion mechanisms are now discussed in the following section (2.4.2).

2.4.2. Adhesion mechanisms

Kendal asserts [59] that an adhesion theory ‘must take into account elastic and geometric effects’ using energy balances to derive adhesion models. Similarly, Professor Abbott [57], [63] repeatedly reinforces this principle by stating; “Adhesion is a property of the system and not something intrinsic to the interface.” Abbott [63] continues to identify five primary

adhesive mechanisms: surface energy (or interfacial tension); structural interactions; intermingling; chemical bonding and energy dissipation which are now discussed in turn.

2.4.2.1. Interfacial tension and surface energy

Interfacial tension (IFT) is the result of molecules at the surface of a material having fewer interactions with the bulk material compared to embedded molecules.

In a solid this can result in the free bond sites at the surface and in liquids the intermolecular cohesive attractions result in the tendency for suspended liquids to form spheres. A suspended droplet will be distorted by gravity and the affinity of the surface molecules with the surrounding gas. The contours of the resulting pendant shape are indicative of the IFT and described by the Laplace Equation 2.6 [64].

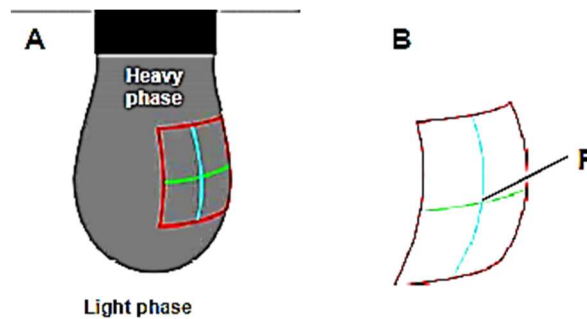


Figure 2.6: Pendant drop (A) and curved surface (B) by Winkler [64]
The radii of the horizontal (green) and vertical (blue) circles of curvature.

$$\Delta p = \gamma_{LV} \cdot \left(\frac{1}{R_1} + \frac{1}{R_2} \right)$$

Equation 2.6: Laplace equation.

Where Δp is the Laplace pressure ($p_{\text{inner}} - p_{\text{outer}}$); σ is the interfacial tension; R_1 and R_2 are the radii of the horizontal and vertical circles of curvature at point P.

Similarly, the surface energy of a solid is the energy available to bond to another material on contact. Surface energy is comprised of two components, these being dispersive and polar. The dispersive fraction is the result of Van der Waals interactions, and the stronger polar interactions are those generated by the attraction between polar molecules.

The strength of adhesion is the force required to separate two surfaces and the distance over which that force must be applied gives the work of adhesion (WoA). Therefore, in the SFE (Surface Free Energy) and IFT mechanisms, the WoA is the energy required to overcome the intermolecular attractions and stretch the bond past the separation distance according to the Lennard-Jones [65] relationship between force and distance. A detailed diagram and explanation of the Lennard-Jones potential by Kendall [65] is included in Appendix C (part

C1) for ease of reference. Due to the separation distance being defined by the type of bond, the WoA at a molecular level, is directly proportional to its separation force (N). However, because “adhesion is a property of the system” [63], at a macro level other influences such as inhomogeneity, and elasticity, result in the maximum adhesive force and the WoA being disproportionate. This is discussed further in section 2.4.5.

2.4.2.2. Structural interactions

The benefit to adhesion from two surfaces with random roughness placed together is considered negligible by Kendall [65] and Abbott [63]. However, the bond strength of a joint can be substantially increased by applying purpose designed features to form interlocking structures [13], [57]. Aspar [16] demonstrated how the adhesive shear strength between an SLA polymer on SiO₂ was increased by nearly nine times by patterning the surface using a diamond saw to lock the surfaces laterally. However, the 50-100µm deep channels cut into the surface of the samples tested by Aspar [16] would compromise the thin (200nm) Si₃N₄ coating [66] used in the current study. Consequently, this and other mechanically destructive methods are undesirable for the current application being investigated.

2.4.2.3. Intermingling and entanglement

Intermingling is the interaction between strands of the adhesive and adherend, such as polymer chains, generating friction which produces a bond. This mechanism contributes to the interlayer adhesion in the SLA process and resulting cohesion of the product.

Entanglement is similar to intermingling but defined [67], by individual fibres or chains crossing the adhesive/adherend interface three or more times and looping around other fibres/chains as they do so. Grothe [44] explored the adhesion of SLA constructions onto textile substrates with the “hairiness” off the material identified as a contributing factor to the strength of adhesion. This characteristic where the fibres protrude into the polymer construction was also identified by Mpofu [68] in a TEAM process and is consistent with the intermingling mechanism [63].

Similarly, Sanatgar et al [69] proposed a theory for liquid polymers in a TEAM process to adhere to solid polymer substrates including, nylon, polyamide, and polylactic acid via polymer chains forming bonds across the interface with the adherend. However, due to the inability for polymer chains to extend beyond the interface and penetrate the surface of silicon nitride, the mechanism of intermingling is considered infeasible for the current study’s application.

2.4.2.4. Chemical bonding

The technical data sheet for Formlabs' clear photopolymer [70] identifies the presence of urethane dimethacrylate ($C_{23}H_{38}N_2O_8$) which polymerises to form polyurethane (PU). PU is known [71] for its adhesive properties. Kim et al [71] conducted detailed modelling of two chemical mechanisms for bonding polyurethanes to hydroxyl groups formed on aluminium oxide. These are included in Appendix C (Figure C2.1) for ease of reference. The mechanisms [71] result in a direct nitrogen-aluminium (N-Al) (ionic) bond with the substrate or an indirect carbon-oxygen-aluminium (C-O-Al) (ionic) bond, which evolve water, and amine respectively.

Modelling of the thermodynamics of the reaction was conducted using quantum chemical calculations [71]. Subsequently, the enthalpy of formation was calculated from which it was concluded that the prevailing mechanism was an exothermic reaction resulting in a N-Al bond with the substrate.

It is suggested that the adhesion mechanism between the urethane component of solidified SLA polymer and the hydroxyl sites on the aluminium surface described by Kim [71] will also proceed at the hydroxyl sites of naturally oxidised silicon nitride, and other substrates. The potential for hydroxyl sites to form under atmospheric conditions on the surfaces of soda lime glass and polycarbonate has been reported by Luo [72] and Tjandraatmadja [73] respectively. Separately to the interface, the methacrylate tail of the urethane will cross-link with an SLA photopolymer during curing to produce a covalent bond. This will bind the molecule with bulk SLA polymer.

2.4.2.5. Energy dissipation

As established in section 2.4.2.1, two different joints can possess the same maximum separation force but with different WoA due to elasticity and other influencing parameters as described by Kendall (2.4.3). To separate a bond in the polymer chain or at the substrate attachment site, it is necessary to stress the whole chain to near the breaking force. The work required to do this will be substantially greater than the dissociation energy of a single bond. Upon failure, elastic energy is released, and if not dissipated or stored elsewhere in the system, will contribute to the crack energy as described in Equation 2.5. Therefore, a system with a higher WoA will be more resilient and less susceptible to crack propagation.

Energy dissipation in polymers primarily results from either the release of heat [61], or by its storage and gradual subsequent release as the material relaxes [63].

Lake and Thomas [74] when investigating the cohesive strength of crosslinked polymers explain that the applied forces are predominantly transmitted via the crosslinks and stored

within the polymer chains between them. The system's resulting WoA can be described by de Gennes general expression shown in Equation 2.7 [63].

$$W_a = \Sigma \times U \times L_c$$

Equation 2.7: De Gennes equation for the work of adhesion

Where, W_a is the work of adhesion, U is chemical bond energy bond per unit length (Jm^{-1}), Σ is the density of the attachment points (m^{-2}) and L_c is the average contour length (Figure 2.7) of the polymer chain (m).

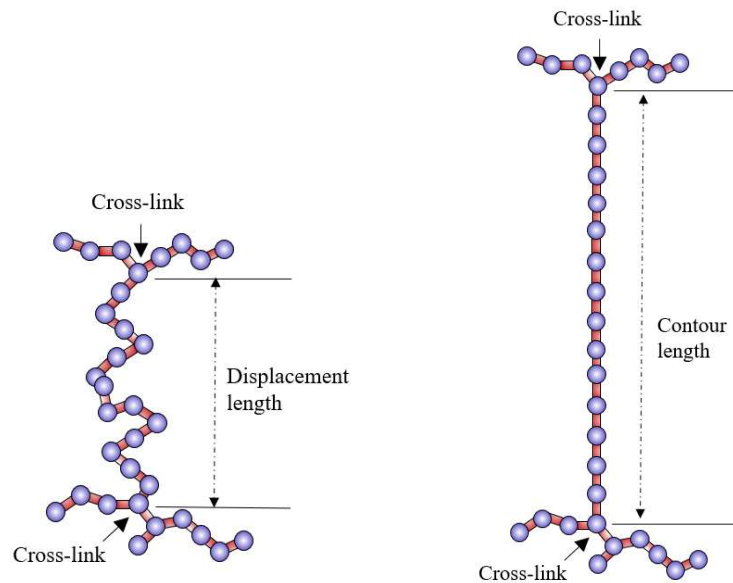


Figure 2.7: Crosslinked polymer chain lengths

Generic definition of [left] displacement length and [right] contour length as can occur in all cross-linked polymers.

The displacement length is the coiled distance between cross-links and the contour length is the length of the uncoiled polymer chain between them. The unravelling of a coiled chain results in energy being dissipated as heat as chains move over one another when the material is stressed. The ratio of contour length to displacement length indicates how coiled a polymer chain is. If that ratio were one (i.e., not at all coiled), the chain's potential to dissipate energy would be much reduced.

The contour length (Figure 2.7) initially increases during the polymerisation process and subsequently decreases with progressive crosslinking and entanglement [57]. This eventually results in embrittlement of the part, a reduction in the WoA, the ability to absorb energy and an increased susceptibility to crack propagation (Equation 2.5).

De Gennes principle (Equation 2.7) indicates a directly proportional relationship between the WoA and density of attachment points (Σ). However, increasing attachment points also

reduces the contour length (L_c) particularly in the near-interface region. Therefore, the WoA can vary with the orientation of the system, making the direction and location of the applied load significant. Consequently, clearly defined boundaries, and information of some properties which are difficult to measure, would be required for the expression (Equation 2.7) to give absolute values. The expression is however useful for explaining the trend in adhesive behaviour (WoA) between cross-linking polymers and a substrate.

Excessive cross-linking leading to brittle failure is the principle by which UV-tape used in the manufacture flip-chip semiconductors operate [75]. The UV-sensitive adhesive on the tape is used to attach and manoeuvre the chips and upon exposure to UV light, the cross-linking and subsequent embrittlement results in the adhesive failing and the chip being released. Conversely, Abbott [63] describes how the WoA and energy dissipation can be promoted by the addition of core shell rubber (CSR). When a crack reaches the rubber (Figure 2.8), its energy is dissipated, and the crack is prevented from propagating. However, it is necessary to contain the rubber within a shell which will bond with the bulk material, or the crack will simply propagate around the material as shown in Figure 2.8.

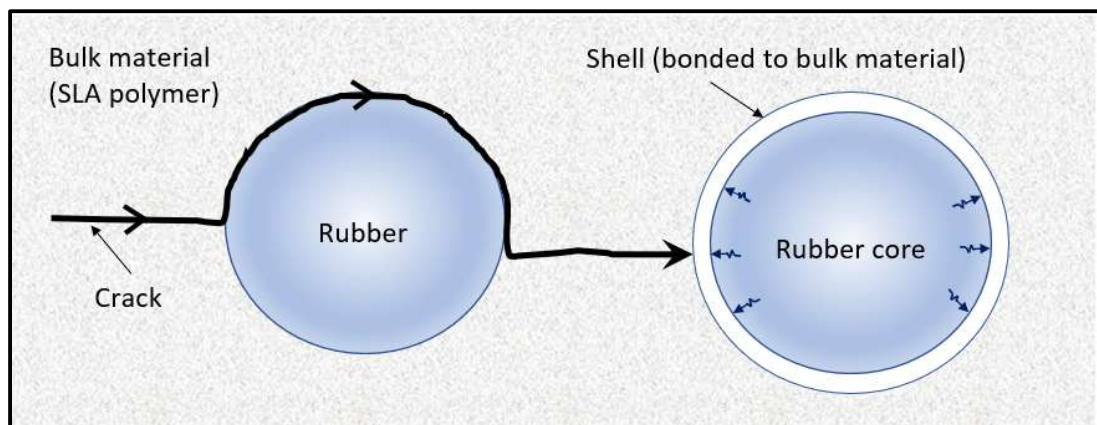


Figure 2.8: Crack propagation with core shell rubber.

Left - The crack propagates around the rubber; Right - the crack is arrested by the rubber being contained within a polymer shell as described by Abbott [1]

An alternative method to promote dissipation was reported by Fitton [76] who varied the elastic modulus across a product's cross-section. A reduction in experimental scatter with low modulus materials was also reported [76]. This was attributed [76] to an increased strain at failure making them "...more tolerant to any cracks or minor flaws in the joint which would lead to premature failure with a stiff brittle adhesive." Similarly, Vu et al [77], experimented with different materials in an AM polyjet system to form a product with varied elastic modulus. When testing the adhesion of these constructions on substrates, it was concluded [77] that their increased deformation improved energy dissipation, reduced crack propagation and thereby enhanced the adhesive strength of the system.

Since the elastic modulus of an SLA product is known to increase with exposure [78] it is possible to tune the elastic properties of the product by varying the delivered exposure laterally. This allows the manufacture [79] of flexible joints or composite textures and stiffness within a single construction. Therefore, if the exposure can be varied laterally across an SLA construction, similar benefits to adhesion as those achieved by Fitton [76] and Vu [77] may be realised.

Following this review, the adhesion mechanisms of dissipation, chemical bonding and surface energy are considered relevant to the application in the current study and will be investigated further. To support this investigation, suitable methods to test the adhesion of SLA products will now be reviewed.

2.4.3. Testing adhesion

There are a number of established processes reported for measuring adhesion [26], [63], [80], [81]. However, the appropriate test method is dependent upon the application and the direction of force to which the product is likely to be subjected when in use. A shear test specifically designed for measuring the adhesive strength of electronic packaging is described by Szeto et al [81]. However, there are relatively few studies reporting adhesion in additive manufacturing and specifically SLA. Those available, together with studies using other polymer-based AM processes (i.e., TEAM), have been reviewed and the test methods used discussed below.

The quality of the adhesion of SLA test pieces constructed onto textiles substrates was measured by Grothe et al [44] by comparing the number which remained attached following the post build washing process. However, the quantifiability and consistency of this method is a concern.

Malengier et al [43] reviewed test methods (shear, peel and tensile) for evaluating the adhesion of polymer AM constructions (TEAM) to textile substrates and concluded the tensile test to be the preferred method. Tiedje [82] and Fei et al [31] also chose to use a tensile test when investigating the adhesion of SLA products (liquid chambers) onto PCBs.

Kendall [65] derives an expression for the tensile separation force required between rigid and elastic materials, from which the influencing parameters of contact area, W_oA , elastic modulus, and Poisson's ratio are identified.

$$F^2 = \frac{\pi W_o A E d^3}{(1 - \nu^2)}$$

Equation 2.8: The Kendall model [65] using the work of adhesion in an energy balance to describe the tensile force required to separate a joint.

The elastic modulus of SLA constructions is known [78] to increase with cross-linking and progressive curing. Consequently, in accordance with Kendall's expression (Equation 2.8) the separation force is expected to increase with PBC and the corresponding change in elastic modulus when adhered to a high modulus / rigid substrate. Therefore, characterising the SLA polymer properties used in Kendall's equation would allow comparison of the model with the results of tensile tests. However, no standard has been identified for the required tensile separation force of electronic packages.

In contrast, Aspar [16] and Lorenz [34] both used a shear test when comparing the adhesion of SLA photopolymers onto a variety of substrate materials. The required shear separation force of electronic packages mounted on substrates, across a range of contact areas, is quantified in test 2019.9 of the industry standard MIL-STD-883K [83].

Therefore, separate adhesion tests to measure the separation force of SLA products constructed onto substrates with tensile, and shear forces applied are to be developed. These will allow comparison with Kendall's model and the MIL-STD-883 standard respectively. The specific test methods to be used are described in sections 3.4.4 and 3.4.5.

2.4.4. Adhesion of liquid photopolymer to substrates

One of the common causes for build failures in SLA is due to the part under construction becoming separated from the platform. This concern is compounded when using non-standard substrates such as silicon nitride. To address this, the chemical affinity of the photopolymer (Formlabs clear) and silicon nitride is reviewed below.

Skliutas et al [84], characterised commercially available photopolymers including Formlabs' Clear as hydrophilic. This makes the photopolymer compatible with the hydrophilic [85] aluminium oxide on the build platform [42] of the Formlabs SLA equipment.

Voyutskii [86] explains polymer-to-polymer adhesion according to M^CClaren's theory of adsorption. The first stage of adhesion with liquid polymers initiates through "micro Brownian motion" [86] of molecules toward to the surface of the substrate. The sorption process [86] occurs during the subsequent stage; "When [the] distance between molecules of adhesive and adherence becomes less than 5 Å, intermolecular forces come into play." These are described [86] as including the "whole 'force spectrum' from dispersion forces to hydrogen bonding. However, the interaction between a photopolymer and silicon nitride will be dependent upon the affinity between the materials. In SLA processes, the adhesion resulting from the interfacial energy, promotes contact between the photopolymer and the

substrate during curing. Consequently, the importance to have a substrate and polymer with compatible hydrophilicity in AM processes to promote wetting and SFE adhesion, has been stated by several authors [44], [87], [88], [89].

There are two common methods [90] used commercially for coating silicon wafers with silicon nitride (Si_3N_4). These being, LPCVD (Low Pressure Chemical Vapour Deposition) and PECVD (Plasma Enhanced Chemical Vapour Deposition). The product of both methods [91], [92] produce a hydrophilic surface. The SFE of Si_3N_4 is reported by Barhoumi et al [93] to be $42\text{mJ}\cdot\text{m}^{-2}$, compared to SiO_2 at $32\text{mJ}\cdot\text{m}^{-2}$. Raider et al [94] explain how silicon nitride can oxidise when exposed to moist air at room temperature onto which hydroxyl (OH^-) groups can form [92], promoting its hydrophilic [95] behaviour.

Due to the hydrophilic nature of liquid SLA photopolymers and silicon nitride wafers, the two materials are expected to have an attractive chemical affinity. The strength of this attraction can be measured by the work of adhesion [96] using the Young-Dupre drop shape analysis (DSA) described by Okoroanyanwu [96].

The shape of the droplet is dictated by the free surface energies between the liquid and the substrate. Wetting can then be calculated using Young's equation (Equation 2.9) relating the contact angle to the solid, liquid and vapour interfaces (Figure 2.9).

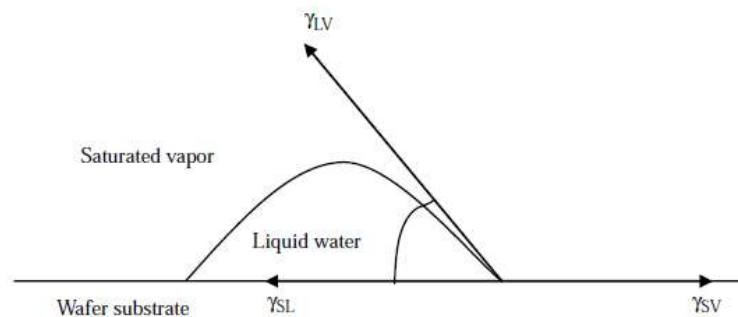


Figure 2.9: A sessile water droplet on a wafer surface by Okoroanyanwu [96]

$$\gamma_{LV} \cdot \cos\theta = \gamma_{SV} - \gamma_{SL}$$

Equation 2.9: Young's equation

Where γ_{LV} is the surface tension at the liquid/vapour interface, γ_{sv} is the surface tension at the solid vapour interface and γ_{SL} is the surface tension at the solid liquid interface and θ is the contact angle.

Okoroanyanwu [96] continues to explain that a completely wetting fluid does not have an equilibrium contact angle. The work of adhesion between a liquid and a solid (W_{ls}) is described [97] by Equation 2.10.

$$W_{ls} = \gamma_{LV} + \gamma_{SV} - \gamma_{SL}$$

Equation 2.10: Work of adhesion by difference of surface tension [97].

Where γ_{LV} is the surface tension of the liquid. By substituting Young's equation (Equation 2.9), Young-Dupre's equation (Equation 2.11) for the work of adhesion between a solid and a liquid can be obtained.

$$W_{oA} = \gamma_{LV}(1 + \cos\theta)$$

Equation 2.11: Work of adhesion

It is possible to accurately measure these parameters using a Kruss drop shape analysis (DSA) 100 machine. This will allow comparison between the WoA on silicon nitride with other substrates. If the WoA is deemed inadequate, methods can be applied to promote wetting by surface treatment.

For instance, the hydrophobicity of a substrate surface can also be modified [95] by binding polar molecules to it. This is one of the actions of chemical adhesion primers of which a variety are available commercially [95]. Adhesion primers work by modifying the surface free energy (SFE) of the substrate surface [96] with the aim to make it similar to the material being bonded. Therefore, by adjusting the SFE through priming, it is possible to under prime or over prime, and potentially causing dewetting [96] of the surface which should be avoided. Barhoumi et al [93] demonstrated the ability to increase the SFE of silicon nitride by approximately 75% using a sulfochromic chemical treatment. Other methods are reported to modify the surface chemistry of substrates. For example, Tehrani et al [36] modified the surface energy of hydrophobic SU-8 material constructed using inkjet printing by exposing the surface to UV light and Ozone (O_3). Similarly, Ko et al [98] changed the surface of SU-8 to hydrophilic using oxygen plasma treatment.

The quality of the contact between a liquid photopolymer depends upon surface roughness. The Wenzel model [99] relates surface roughness and the associated increase in area to the resulting contact angle of a sessile droplet. According to the model, hydrophilic materials result in a decreased contact angle with increasing roughness and the converse for hydrophobic materials. The relative roughness of a material compared to a smooth surface is then represented as a function of the contact angle. However, the Wenzel state assumes that the liquid fully penetrates the pores of a rough surface. In practice this will be

dependent upon the interfacial tension between the liquid and the solid and the width of the pores.

The potential for a photopolymer to penetrate the pores of a substrate is important to adhesion as it dictates whether structural interactions (section 2.4.2.2) will result upon curing. Hydrophobic or more viscous liquids can result in the ‘lotus effect’ [100] where the droplet sits on the peaks of a roughened surface minimising contact. This is described by the Cassie-Baxter model [100], [101] which provides the resulting fractional liquid contact area between the liquid and a solid as a function of contact angle.

Similarly, Rudawska [102] explains the behaviour of droplets on an aluminium surface using parallel grooves tens of microns in width and depth. The droplets exhibited [102] significantly increased contact angles compared to a smooth surface. However, as the pores increase in size beyond the minimum which can be penetrated by a given liquid [103], the Cassie-Baxter [101] contact factor increases. Conversely, the surface roughness can be increased, but if the individual pores are below the minimum penetration size, the contact factor will decrease.

Rezaei et al [103] generated an equation to relate the minimum pore size which can be filled by a liquid to pressure (Equation 2.12).

$$\text{LEP} = \frac{-\beta\gamma_l \cos\theta}{r_{\max}}$$

Equation 2.12: Liquid entry pressure [103]

Where LEP is the liquid entry pressure, γ_l is the liquid surface tension, β is the pore geometry coefficient (ranging from 0 to 1) with a value of 1 being perfectly cylindrical, θ is the contact angle and r_{\max} is the maximum pore size of the substrate.

Due to photopolymers shrinking as they cure, if they penetrate pores in the substrate while in the liquid phase, they will remain there during solidification and PBC subject to potential changes in SFE. However, there is a knowledge gap regarding the influence of curing on SFE which is not reported in the literature. The adhesion of solidified SLA polymer to substrates will now be reviewed.

2.4.5. Adhesion of solidified SLA photopolymer to substrates

It is standard practice in SLA processes to increase the exposure to the first layer to promote adhesion as mentioned by several authors [33], [34], [84], [104], [105], [106]. Livari [106] states that “...the degree of the curing and the cured area are two important factors to determine the pull force.” However, the authors do not investigate the mechanism

generating the increased adhesive strength. When attempting to enhance adhesion using a high exposure, Ackstaller [33] reports the formation of a “meniscus” around the structure’s base. The formation of a meniscus increased the contact area between the construction and the substrate and in doing so compromised [33] the accuracy of adhesion tests.

Several papers report using SLA to construct geometries either on to a silicon wafer directly [12], [46], [107], [108], or subsequently bonding [109], [110] an SLA product on to the substrate material. However, they do not explain the process in detail or measure the resulting bond strength. Choudhury et al [110] successfully attached an SLA constructed resist mask onto a silicon wafer that had been spin coated with SLA photopolymer and described the adhesion as “excellent”, but the strength of the bond was not measured. Tse et al [12] built measurement cells using SLA 7510 photopolymer directly onto a silicon wafer. However, the authors [12] do not review the quality of the adhesion between the two materials. Ackstaller [34], Tiedje [82] and Fei [31] measured the adhesive strength of SLA test pieces onto substrates of aluminium oxide, copper, and printed circuit boards (PCB) respectively, but without investigating the adhesion mechanism.

Gouboult [111] reports the results of a shear test measuring the adhesive strength of an SLA package constructed onto a silicon substrate. The part tested failed [111] when the applied shear stress reached 1.6MPa which equates to $1.6\text{N}\cdot\text{mm}^{-2}$. The 213mm^2 cross-sectional area of the part [111] is beyond the range covered by the MIL-STD-883 standard. However, $1.6\text{N}\cdot\text{mm}^{-2}$ is substantially below the shear stress required of approximately $\sim 10\text{N}\cdot\text{mm}^{-2}$ (Appendix D) by the standard [83] for smaller packages.

Aspar et al [16] conducted an adhesion investigation considered to be the most relevant to the current investigation, by measuring the adhesion of geometries constructed using SLA onto silicon dioxide (SiO_2), Silicon mononitride (SiN) and Silicon oxynitride (SiON). Interestingly, substantial differences in the adhesive strength when applying a shear force were reported despite the materials sharing similar chemical composition, surface topology, and geometry. A potential explanation for this is differences in SFE or the concentration of hydroxyl groups between the substrate materials (section 2.4.2.4). The use of plasma treatment to generate surface hydroxyl groups and improve the adhesion between polymers, and substrates made from compounds of silicon, is reported by Ohkubo [112]. This process was further enhanced by Zips et al [113], with the application of a monolayer who investigated the adhesion of microfluidic chambers onto silicon containing substrates including PDMS and glass. Firstly, oxygen plasma treatment was applied to the substrate to generate OH^- active sites on the surface. The salinized substrates were then coated with TMSPMA (3-(trimethoxysilyl)propyl methacrylate), forming strong covalent Si-O-Si

bonds. The methacrylate tail of the TMSPMA is capable of crosslinking in an SLA process. This results in the mono layer acting as a covalently bonded bridge between the polymerised SLA material and the substrate. The bursting pressure of the chambers on treated substrates was found to be substantially increased following the process.

Due to the absence of information reporting the adhesion of SLA products to silicon nitride and other substrates, experimentation will be required to quantify the strength of the resulting adhesion.

2.5. SLA material

To ensure consistency and compatibility with the SLA equipment, a commercially available photopolymer (Formlabs clear) from the SLA equipment suppliers will be used throughout the experimentation in the current study. This photopolymer is widely used and benefits from having been characterised previously [50], [52], [84], [114]. The penetration depth of the material was shown [50] to vary with wavelength and significantly different values for the penetration depth and the critical cure energy were obtained by the respective authors [50], [52] (Table 3.2) suggesting some variability between the material samples.

SLA polymers with high heat deflection temperature were selected by Lopes et al [2] when constructing structural electronics. The heat deflection of Formlabs clear resin is not known. However, it will be important that the SLA polymer used for commercial use possesses an adequate heat deflection temperature (ASTM D648) [115] for its application to avoid deformation.

2.5.1. Rate of reaction (polymerisation)

For commercial production, the rate of manufacture is critical to the financial viability of the process. Consequently, one of the objectives of this study is to optimise the build time of the SLA process to which there are several approaches. One method would be to increase the rate of polymerisation. The crosslinking of polymers used in SLA, proceeds via two main mechanisms [116]. These being free-radical photopolymerisation and cationic photopolymerisation, activated by exposure of a suitable initiator to UV light.

In 2010, Gibson [116] et al explained that the photopolymerization reaction in SL photopolymers is very complex and that no one had published an analytical photopolymerization model that describes reaction rates. Those reaction rates are largely

controlled by the concentrations of photoinitiators and monomers for which Gibson et al [116] derive an expression applicable for simple formulations.

$$R_p = \frac{-d[M]}{dt} \propto [M](k[I])^{1/2}$$

Equation 2.13: Rate of polymerisation by Gibson et al [116].

Where R_p is the rate of polymerisation, t is time, $[M]$, and $[I]$ are the concentrations of monomer and photoinitiator, and k is a constant that is a function of the radical generation efficiency.

However, the option to adjust the concentration of monomers in SLA photopolymers is limited [116] making the photoinitiator concentration a more common method to adjust the reaction rate. In 2017 Zhang et al [117] developed “high efficiency” ketone based photoinitiators to facilitate faster fabrication speeds.

Oxygen is known to inhibit the polymerisation reaction, especially the polymerisation of acrylates [108] by scavenging free radicals. Dufaud et al [108] identified that the partial pressure of the oxygen in atmospheric above the photoreactor also has a significant influence on the polymerisation process. Cationic photoinitiators are uninhibited by the presence of oxygen and can allow much faster curing times. However, when an SLA photopolymer is exposed to UV light, there is the potential for the construction to adhere to the resin tank window. This can result in damage to the part during the separation process after each layer. Consequently, in commercial SLA systems [42], [118], the principle of oxygen inhibition is often applied via the re-coating process to prevent the photopolymer adhering to an oxygen-permeable PDMS window. This reduces the shear stresses during separation between layers and the risk of damage to the part. Consequently, free-radical initiated photopolymers available are the most common [116] amongst those available commercially.

2.5.2. Fillers

Previous work to support the potential to add fillers such as CSR (section 2.4.2.5) to promote dissipation and adhesion is now reviewed further. Numerous filler materials have been added to SLA photopolymers [119] to modify the mechanical and chemical properties of the product. It is important when adding fillers [119] that any suspended particles are homogeneously dispersed and do not agglomerate or undergo sedimentation during build periods.

In photolithography, the diffraction of light prevents a perfect mapping of the resist image [120] resulting in some unintended exposure of the photoresist in the proximity of the target exposure. This can result in variable exposure and a loss of detail in features at the periphery of patterns. Similarly, the presence of fillers in stereolithography tends to promote scattering of the incident light [121] as it is reflected from the suspended particles, with the potential to reduce the penetration depth. The influence of adding ceramic particles with up to 25 μ m in size to an SLA photopolymer was investigated by Sakly et al [121] using commercial (Bluestone) and customised resins. The wear properties of an SLA product were found [121] to be enhanced but at the expense of penetration depth which raised concern regarding interlayer adhesion for filler concentrations above 20% v/v. Li [122] also addressed the adverse effect on penetration depth when adding CSR particles to a customised SLA photopolymer. Li [122] attributed the reduction in penetration depth and E_c to the dilution of photoinitiator from the addition of the CSR. An equation relating the modified penetration depth resulting from the addition of fillers as a function of the volume fraction in which they are present, their particle size, and refractive index, is derived by Taormina et al [119]. This equation can be substituted into the Beer-Lambert law to quantify the influence which adding a filler will have on the cure depth and consequently the maximum layer thickness.

One of the starting points to investigate the influence of a filler material is the proportion in which it should be added. Taormina [119] explains that filler materials added in only small proportions (1% v/v) can significantly alter the behaviour of the material. Whereas substantially higher filler concentrations have been successfully applied by Leigh [123] and Gurr [124] who used fillers in proportions of up to 25% w/w and 30% w/w respectively. Leigh et al [123], found the construction of products became unreliable as the concentration of the filler (magnetite) increased above 30% w/w. Taormina et al [119] state that when an SLA photopolymer's viscosity is increased above 5 Pa/s (5000 centipoise), its ability to flow will be reduced, impacting the recoating process, and increasing build time. Likewise, when adding SiO₂ particles in high concentrations, Gurr [124], increased the layer build waiting interval by a factor of ten, to ensure recoating of the construction layers due to the resulting increase in viscosity but at the expense of build time. When investigating the influence of CSR on the material properties of epoxies, Tsang [125] also found viscosity to be the limiting factor in which CSR could be added, restricting its concentration to 10 wt%.

This review highlights the need to consider the proportion in which to add particles to the photopolymer, their propensity to remain in suspension, and their impact on viscosity. Another potentially adverse effect from the addition of fillers to SLA resin was identified by Dufaud et al [108] who report light scattering caused by the addition of ceramic particle

fillers impacted the beam diameter and the achievable minimum feature size (“polymerized width”). Conversely, liquids such as dyes, have also been added to SLA photopolymers [126], to adjust the refractive index [119], or increase the critical exposure and thereby the achievable MFS as described in section 2.6.

2.6. Feature size and resolution

The ability to construct products within specified dimensional tolerances is fundamental to the success to any manufacturing process. This requirement is combined with optimising build time in objective 3 (section 1.5).

Two-photon stereolithography represents the current state of the art for high resolution additive manufacturing of polymers. In 1992 Ikuta [127] et al developed a 2-photon stereolithography process with a minimum resolution of 5 μ m. This was subsequently improved four years later to produce a minimum resolution of 2 μ m. 2-photon stereolithography has since evolved further with currently achievable feature sizes [128] of <100nm being produced. However, in the current study, equipment incorporating galvanometers is to be used, the angular accuracy of which dictate the achievable X-Y resolution and is discrete from the much larger MFS. It is therefore the MFS which dictates the ability to achieve manufacturing tolerances (Section 1.4) on the equipment used. The MFS in SLA is defined [129] by the minimum cured line width (CLW).

The [116] intensity profile of a laser beam typically conforms to a Gaussian profile across its width. The laser spot width can be measured as the FWHM (Full Width Half Maximum) or the $1/e^2$ width. The former is the width of the beam when the intensity falls to half its peak, and similarly $1/e^2$ width is that when the intensity falls to $1/e^2$ of the peak intensity (approximately 13.5%).

Therefore, the exposure delivered (mJ/cm^2) is a function of the beam intensity profile and the scan speed. The latter determines the duration for which the laser spot is resident at a given location and the total energy delivered.

Consequently, the CLW and MFS is dictated by the diameter of the beam’s exposure profile which possesses sufficient energy to initiate curing (i.e., equal to or greater than E_c) as shown in Figure 2.10.

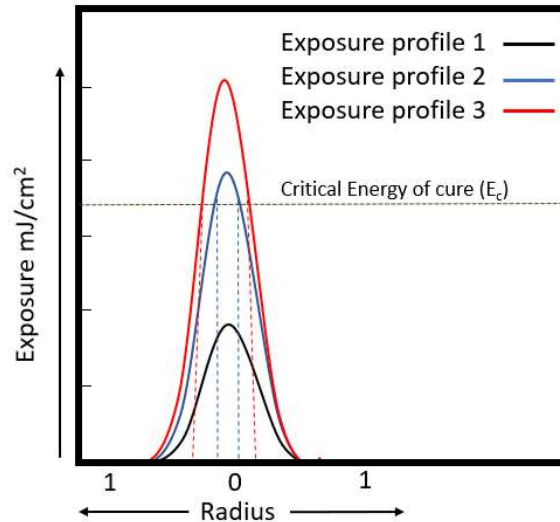


Figure 2.10: A Gaussian beam exposure profile.

[The minimum cured line width corresponds to where the beam intersects the threshold energy (E_c)]

Increasing the photopolymer's critical cure energy (E_c) will achieve a smaller feature size but require a thinner layer thickness, and at the expense of build time. Lu et al [130] explain, that the critical exposure energy is primarily due to oxygen inhibition and therefore can vary.

SLA resolution in the z-plane is dictated by the layer thickness. In turn, the maximum layer thickness is governed by the penetration depth (D_p) [28]. Whereas the minimum layer thickness is usually limited by the control system and the step size of the platform's actuator.

As explained in section 2.7.3, defined scan patterns are applied to SLA constructions to achieve a desired effect. The distance between each pass of the beam in the pattern is termed the hatch spacing. Due to the periphery of each line pass overlapping the previous one, the overall energy delivered to the photopolymer can be significantly increased through the effects of superposition as shown in Figure 2.11 and modelled by Jacobs [9]. Jacob's [9] continues that to avoid issues with surface texture and interlayer adhesion, peak to valley variations in exposure greater than 3% are "not allowed".

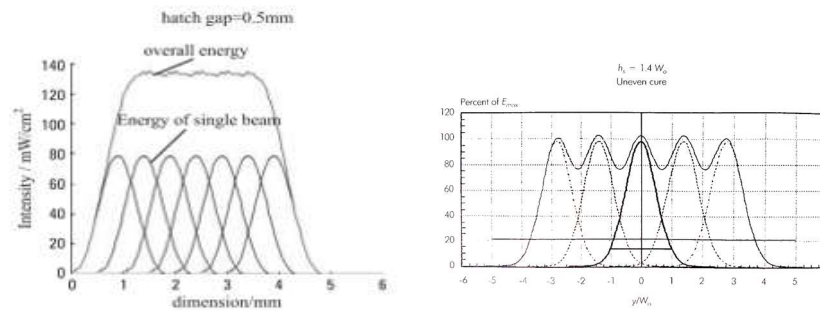


Figure 2.11: Hatch spacing and exposure by Jacobs [9].

Reducing hatch spacing [left] increases the overall exposure, conversely increasing hatch spacing [right] results in uneven exposure and cure.

This guidance supports the findings of LLu et al [28] who attributed defects in an SLA process to variations in cure due to a large layer pitch or hatch spacing. This resulted in cavities or weak areas where the exposure is reduced.

Therefore, it is important to consider the influence of superposition on exposure and the resulting MFS when optimising build time parameters as described in objective 3 (section 1.5). This is necessary to comply with manufacturing tolerances and other requirements (i.e., variation in lateral exposure).

2.7. Defects and distortion in SLA

The ability to comply with manufacturing tolerances can be adversely affected by distorting effects in the SLA system. In addition to reflectance (section 2.3.1) and refraction (section 2.3.1.1), reviewing the literature identified other potential distorting effects relevant to the SLA process.

These include divergence, ellipticity and shrinkage which are now reviewed in turn.

2.7.1. Divergence

A laser has a defined focal length (FL) beyond which the laser spot size will increase [131], and its peak intensity fall as the beam diverges. In SLA this results [132] in a reduced cure depth, increases the MFS and impacts the ability to achieve manufacturing tolerances.

Since divergence is a function of distance, the extent of divergence will vary as the beam is scanned across the build area. Consequently, the width of the beam with sufficient exposure to initiate curing and the corresponding minimum line width will also vary. The

divergence of a beam is defined [133] as the far field cone angle in which the irradiance is greater than $1/e^2$ and described by Equation 2.14.

The depth of focus is defined [134] as double the Rayleigh length which is in turn a function of the spot size. This results in narrow beams possessing a shorter depth of focus and a conflict when selecting the SLA laser equipment between the achievable MFS and the degree of variation in CLW across the build area [131].

For a perfect Gaussian beam at its diffraction limit, the relationship between the angle of divergence and the width of the beam is shown in Equation 2.14.

$$\theta = \frac{\lambda}{\pi\omega_0}$$

Equation 2.14: Divergence of a perfect Gaussian beam [131]

Where λ is the wavelength and ω_0 is the $1/e^2$ beam width.

To compensate for inaccuracies in real beams from the aberration of the lens, a coefficient for the beam quality factor (M^2) is applied. This value is often quoted by the equipment supplier and typically ranges [135] between 1.1 and 1.7 for a low power diode laser as used in desktop SLA equipment.

2.7.2. Ellipticity

In laser SLA systems, the beam is usually directed around the build area by mirrors attached to galvanometers. As a beam from a point-source scans across a planer surface, the incident spot becomes elliptical [136] at oblique angles of incidence. This is due to the far side of the beam travelling a further distance than the near dimension (Figure 2.12). The corresponding X-Y dimensions of the incident laser spot will be transferred into the resulting construction.

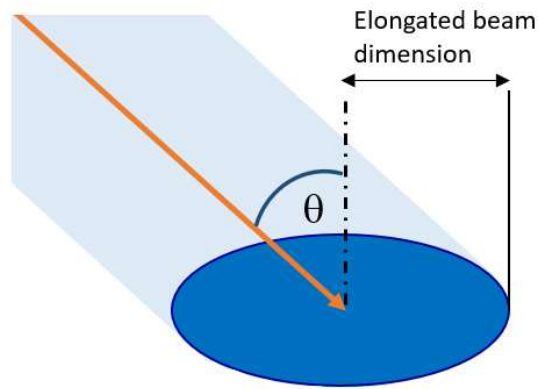


Figure 2.12: Ellipticity of a beam incident at oblique angles.

Therefore, the CLW in the system described will also vary according to the beam's angle of incidence due to ellipticity and in addition to divergence and any reflectance from the substrate.

2.7.3. Shrinkage

Another common cause of distortion in the product is shrinkage. Theuss [137] investigated the influence of stress in electronics packaging and the potential to impact the operation of sensors. It was concluded [137] "A crucial prerequisite for MEMS packaging is low stress packaging not to disturb the device functions." One of the causes of stress identified [137] being shrinkage.

Shrinkage in SLA has been extensively researched, with numerous established methods to mitigate its effects, some of which are programmed into the SLA machine control logic. Depending on the extent, shrinkage may result in parts being out of design tolerance. Shrinkage results from distanced molecules in the liquid phase being more closely packed with relatively short covalent bonds and a reduced occupied volume [116] as the photopolymer solidifies. L.Lu et al [28], consider shrinkage an unavoidable consequence of the polymerisation process and state that a typical degree of shrinkage for photopolymers is up to 8%. Gibson [116] describes how epoxy materials are less susceptible to shrinkage (~2%) than acrylates (5-20%) due to polymerisation opening the epoxy ring. However, increasing the epoxy concentration adversely influences the rate of polymerisation (section 2.5.1).

A number of methods [116], [124], [138], [139], [140] have been used to minimise or compensate for shrinkage and its effects. Excess material can be applied [116] to the appropriate dimension of an artefact, for post build machining but at the expense of additional processing time. Gurr et al [124] discuss how the extent of shrinkage can be reduced with the addition of filler materials such as silicon dioxide.

Rosen et al [116] explain that uniform shrinkage can be compensated for by multiplying the dimensions of the CAD model by an appropriate factor. This process is applied to commercial SLA equipment including Formlabs and AnycubicTM machines used in this study. However, inconsistent shrinkage across a part, can lead to warping. If there are variations in the exposure [28] within the build volume, shrinkage will not occur uniformly, introducing stresses into the build. This can occur with large layer thicknesses and materials with a low penetration depth resulting in different exposures at the at the top and bottom of a layer [28]. Consequently, stresses are often greatest between layers, and at the interface with a substrate which can lead to delamination, curling, and adhesion failure. Moreover, Ebe [75] discusses the potential for shrinkage to cause “microdefects” at the interface which can then be the source of crack propagation (Griffiths law section 2.4.1).

The distortion resulting from these stresses can be reduced by the laser exposure pattern. Common patterns [116] include WEAVE and STAR-WEAVE. These cross-hatching patterns alternate the scan direction and balance lateral stresses from one layer to the next.

Experimentation conducted by Ullet et al [138], to measure the shrinkage of acrylate photopolymers, quoted the maximum linear shrinkage to be “in excess of 2%”. It was concluded [138] that shrinkage could be reduced by 40% by extending the delay time from 1 second to 5 minutes.

A review of patents revealed several other methods to reduce shrinkage in SLA, have been developed. Vinson et al [139] describe a process for reducing curl by curing a balancing layer to counteract the curl in adjacent layers. Guertin et al [7] patented a methodology to reduce shrinkage based upon controlling and varying the delay time between exposing portions across layers. A similar technique was patented by Manners et al [140] to partially cure layers with a subsequent intermediate solidifying step to complete the process.

Although shrinkage in SLA has been investigated extensively, and its potential to cause distortion is well documented, there is a gap in the knowledge regarding its influence on adhesion.

2.7.4. Alignment

Accurate alignment within required tolerances is critical when fabricating parts, with the level of accuracy required normally increasing as the dimensions decrease.

Tehrani et al [36] report a novel process to align a sample being encapsulated in an SLA process, by increasing the wavelength of the first layer projection to reduce UV light and avoid polymerisation. This allowed for the sample piece to be positioned relative to the

projected light which was then reverted to UV for construction. However, this is dependent on the ability to adjust the equipment's wavelength. An alternative approach was used by Choudhury et al [110] who accurately positioned a MEMS device onto a silicon substrate using a 'print mask' which acted as a stencil to align with marks on a silicon die.

2.8. Knowledge gaps

Using SLA as a manufacturing process is well documented [9], [116] with the aspects of previous work relevant to the current investigation reviewed in this chapter. However, specific gaps in the knowledge have been identified when attempting to address the concerns associated with meeting the aims of the current study mentioned in section 1.5.

Significantly, the construction of SLA products directly onto silicon nitride is not reported in the literature. The nearest comparable investigation into the strength of adhesion of SLA products onto silicon dioxide [111] have found it to be inadequate for industrial application. Consequently, concerns regarding reflectance and adhesion to the nitride material remain.

The practice of increasing first layer exposure to promote adhesion is reported in the literature but the associated distortion and the influence of post build curing on adhesion is not. Surface free energy, Poisson's ratio and elastic modulus have been identified to influence adhesion and progressive curing is known to increase the elastic modulus of an SLA polymer. However, the potential variation in Poisson's ratio and in particular surface free energy during curing, are significant to understanding the adhesion in SLA (2.4.4) but have not been investigated in the literature. The topic of shrinkage in SLA is well documented with numerous patents [7], [139], [140] in place for methods to mitigate its effects. However, the influence which shrinkage of SLA polymers may have on adhesion, has not been demonstrated. Moreover, the adhesion mechanism between an SLA polymer and the build platform or substrate has not been established.

The use of SLA in the construction of structural electronics has been identified with the work by Lopes [2] often cited. However, this and other examples reviewed (section 2.1) used hybrid systems or arrange the components into an assembly after construction, with the production of structural electronic devices using the single AM process of SLA (section 2.1) not reported.

The potential for reflectance to cause adverse effects in SLA processes has been referred to in three studies, [16], [28], [46]. However, the magnitude of reflectance and the conditions where it may distort the product through spurious curing have not been quantified. There is

also a gap in the knowledge quantifying the extent to which refraction can reduce the accuracy and precision in a laser SLA process.

This document contributes to the knowledge of the SLA process-material interactions with novel substrates, and their potential to generate distortion. Specific knowledge gaps addressed are the potential for reflections to produce spurious curing and promoting the adhesion between an SLA polymer and silicon nitride.

2.9. Research questions

To support the objectives in section 1.5, and to address specific gaps in the knowledge (section 2.8) identified from the review of literature, the following research questions have been raised:

1. How do SLA photopolymers interact with different substrates?
2. Can the interaction of a photopolymer with a substrate be altered by modifying the respective materials or process parameters?
3. What is the relationship between substrate properties, reflectance, and the extent of distortion in SLA?
4. How is the adhesion of an SLA construction influenced by the process parameters and the properties of a substrate?

Chapter 3

3. Experimental and numerical methods

From reviewing the literature in Chapter 2, reflectance when constructing onto Si_3N_4 is expected to contribute to the first layer exposure and the formation of the menisci as observed by Ackstaller [33]. The use of BARCs have been identified as an effective method to mitigate reflections in photolithographic processes [26], [27]. However, a BARC is unlikely to be suitable for application in SLA. Unlike in photolithography, the BARC will not be etched during subsequent processing and thereby leave a physical layer between the substrate and the SLA construction. This raises concerns regarding compatibility and adhesion. To address the knowledge gaps (section 2.8) associated with reflectance, the characteristic is to be modelled numerically (section 3.2.10) using the Fresnel equations together with the associated refraction. Practical experimentation (section 3.3) will be applied to support the investigation. Reflectance and refraction together with the laser characteristics of divergence (section 2.7.1) and ellipticity (section 2.7.2), are functions of the angle of incidence. Consequently, the latter two properties will also be modelled (sections 3.2.6.2 and 3.2.6.3) to distinguish the extent of potential distortion from each characteristic. The specific concern being the ability to achieve manufacturing tolerances and the potential impact of distorting effects such as spurious curing from reflectance, and the loss of accuracy associated with refraction. These influences will then be used to identify a process window in which to operate and optimise the SLA process with consideration to the orientation of the construction, and exposure, to achieve the required tolerances.

Due to the absence of information in the literature reporting the propensity for liquid SLA photopolymer, and its cured product, to adhere to silicon nitride, these shall be measured directly. The WoA between an SLA photopolymer and silicon nitride will be measured using DSA (section 2.4.4). This will determine whether the substrate surface is sufficiently wetted by the SLA photopolymer to maintain adequate contact during curing to allow the solidified product to bond, or if the use of adhesion promoters (section 2.4.4) is required. The potential change in surface energy as an SLA photopolymer transitions from a liquid to a solid and with subsequent progressive curing, will also be investigated using DSA.

According to McClaren's theory of adsorption as described by Sanatagar et al [69], polar urethane monomers within the photopolymer will migrate to the hydroxyl groups formed

through atmospheric oxidation on the substrate's surface [92], [94]. A potential mechanism by which the solidified photopolymer will then bond to the hydroxyl sites is described by Kim [71] (section 2.4.5). Given the potential for hydroxyl sites to form on silicon nitride (2.4.5), it is hypothesised that the polymerised SLA photopolymer (Formlabs clear) could adhere to the surface of silicon nitride by a similar mechanism. The resulting bonds with the substrate's surface are expected to be N-Si with a dissociation energy [141] of 439kJ.kmol^{-1} compared to 297kJ.kmol^{-1} for an N-Al bond. Consequently, the resulting strength of the individual bonds between the SLA photopolymer and silicon nitride, are expected to be stronger than those on aluminium. By applying the process described by Zips [113] (section 2.4.5) to generate an Si-O-Si bridge with an Si-O bond having a dissociation energy of 798kJ.mol^{-1} , it is anticipated that the resulting adhesive strength could be enhanced further. However, the overall strength of adhesion and the work required to separate the joint, will be dependent upon the number of active hydroxyl sites available and the resulting bond density as described by de Gennes equation (Equation 2.7) [63]. The density of hydroxyl sites which will form on silicon nitride under atmospheric conditions is unknown. This raises concern regarding how effective the bond with the SLA polymer will be. The presence of hydroxyl sites could potentially be promoted by treating the substrate with oxy-plasma [113] [98]. However, no information relating to apply the treatment on silicon nitride has been identified and there is concern regarding its effectiveness given the high bond strength of Si-N.

Other means to promote adhesion (section 2.4.5) shall be explored. To support this, the dominant adhesion mechanism in SLA will be investigated, with the mechanisms of energy dissipation, surface energy, and chemical bonding considered.

As Abbott [63] explains, "adhesion is a property of the system" with one of those properties being elastic modulus as described by Kendall's [65] equation for the tensile separation force. The elastic modulus of SLA constructions is known to increase with cross-linking and progressive curing [78]. Consequently, the extent to which PBC and the corresponding change in elastic modulus of an SLA polymer as it cures can influence adhesion, is of particular interest. A mechanical test (section 2.4.3) will be required to measure the separation force of the solidified SLA polymer on a substrate. To allow comparison with Kendall's equation (Equation 2.8) and following the investigation by Malengier [43], a tensile test will be used in this investigation to investigate the dominant adhesion mechanism and to ascertain the significance of SFE in the adhesion between SLA and silicon nitride. Additionally, the required bond strength of electronic packages to their substrate under an applied shear force, is quantified in test 2019.9 of the standard MIL-

STD-883K [83]. Consequently, a shear test based on the method described by Szeto [81] will also be used in this investigation to determine compliance with the standard.

Reviewing the literature revealed that the ability to accelerate the polymerisation process via photoinitiators is well documented (section 2.5.1). Therefore, optimising build-time to satisfy the fourth objective (section 1.5) of this study, will focus on process parameters, such as part orientation and exposure using commercially available SLA polymers.

Lastly, by building on the work of Tiedje [10] and Kataria [13], the ability to construct structural electronics using the single AM process of SLA will be explored. The intention being to construct a demonstration product to prove the concept.

To support the investigation, relevant reference parameters obtained from the literature are compiled in section 3.1. Specific numerical and experimental methods pertaining to distorting effects and optimisation of the SLA process (section 3.2 and 3.3), adhesion (section 3.4), and inserting geometries (section 3.5) will now be discussed in turn.

3.1. Reference properties and design tools

With consideration to the aims of the study, the following reference parameters and design tools have been defined using findings, manuals and data reported in the literature. These are used for subsequent calculation, modelling and experimentation unless otherwise stated. For reasons explained in section 1, only the single AM process of SLA is being investigated in the current work. The specific SLA machines to be used are the Formlabs Form 1+ and Form 2 shown in

Figure 3.1. The machines are similar constructions. However, the Form 1+ uses a peel process to separate the layer under construction from a PDMS window, applied by tilting one side of the resin tank. In contrast, the Form 2 applies a shear force by sliding the tank laterally. Both machines' lasers operate at 405nm with the Form 2 having a maximum power of 96mW and a 140 μ m (FWHM) beam width, compared to 62mW and 155 μ m respectively for the Form 1+.

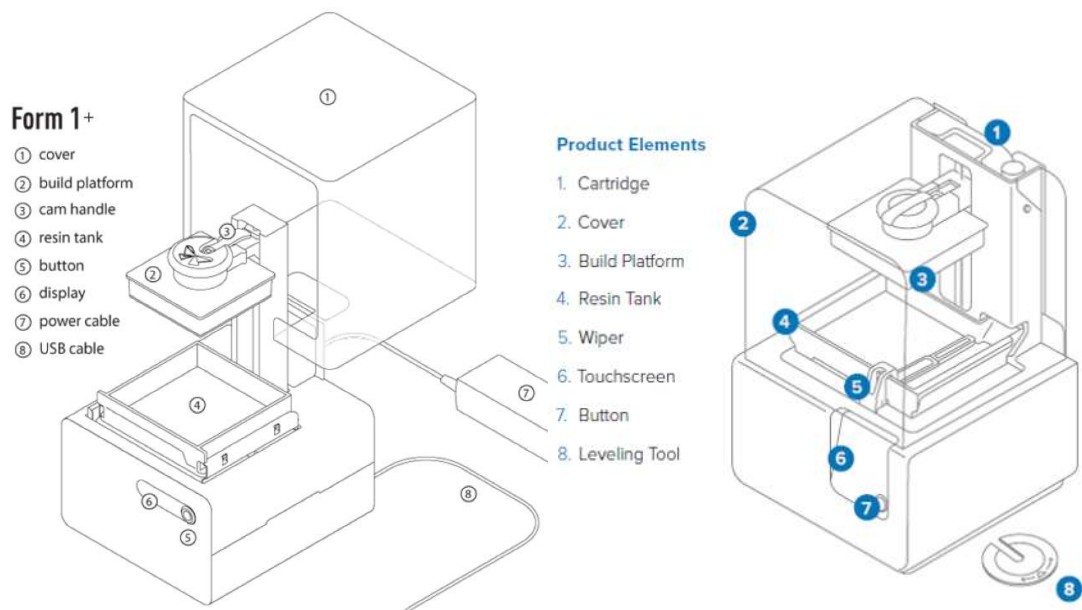


Figure 3.1: Form 1 [142] [left] and Form 2 [42] [right] SLA machines.

By inputting the operating wavelength (405nm) of the SLA equipment to be used in this study (Formlabs Form 1TM, Form 2TM and Form 3TM) into the Sellmeier equation [45] a refractive index for silicon nitride of 2.098 is obtained. Additionally, a list of relevant standards is included in Appendix B.

Operating and process conditions	
Property	Value
Temperature	20°C
Pressure	Atmospheric (1.013 bar)
Post build curing	60°C maximum

Table 3.1: Operating conditions

Material properties	
Property	Value / comment
Glass substrate	Soda lime glass microscope slides, 76mm x 26mm x 1mm.
Polycarbonate substrate	Lexan™ 9030 Polycarbonate thickness = 0.7mm. Samples cut to 76mm x 26mm.
Refractive index of polycarbonate at 405nm [54]	1.61
Polycarbonate elastic modulus [143]	2.3 GPa
Polycarbonate Poisson's ratio [143]	0.38
Aluminium substrate	Aluminium 1050 thickness = 1mm. Samples cut to 76mm x 26mm.
Aluminium elastic modulus [144]	~69 GPa
Aluminium Poisson's ratio [144]	0.33
Refractive index of aluminium oxide at 405nm [54]	1.79
Refractive index of aluminium at 405nm [145]	0.48
Silicon nitride wafer [66] supplied by Inseto™.	
Wafer dimensions	100mm diameter x 0.5mm +/-25µm
Coating	silicon nitride (LPCDV) coated to thickness 200nm, polished one side.
Surface free energy of silicon nitride [93]	42mJ.m ⁻²
Refractive index of silicon nitride at 405nm [48]	2.1
Elastic modulus of silicon nitride [146]	160 GPa
Poisson's ratio of silicon nitride [146]	0.2
Photopolymer	
Formlabs clear penetration depth [50]	192µm
Formlabs clear critical cure energy 405nm [50]	12.6mJ/cm ²
Formlabs clear critical cure energy 405nm [52]	37.5mJ/cm ²
Formlabs clear ultimate strength [70]	65MPa
Formlabs relative density [70]	1.09-1.12
Refractive index of Formlabs clear SLA photopolymer [114]	1.609
Core shell rubber (Paraloid BTA-751U)	
Size range [148]	1.5% w/w retained on 20 mesh (840µm) 5% pass through 325 mesh (45µm)
Relative density [148]	1.06
Refractive index [148]	1.52

Table 3.2: Material properties

Equipment and tools	
Equipment / software tools	Comment or version
AM equipment	Requirement for AM process to be SLA only (see section 1). Form 1+, Form 2, Form 3 and Anycubic photon.
Post build curing oven	Formcure
CAD software	Solidworks 2019 TM
Numerical modelling software	MATLAB TM
SLA machine interfacing software	PreForm TM v2.3.3
Python programming language	Python TM v2.7
Python development tool	PyCharm TM

Table 3.3: Equipment and tools

Test methods	
Adhesion between SLA product and substrate.	Tensile (see section 2.4)
	Shear test (2019.9 MIL-STD-883K) [83]
Elastic modulus	ASTM D638 (see section 2.4)

Table 3.4: Test methods

3.2. Numerical methods for modelling distorting effects and optimisation of the SLA process.

As discussed in Chapter 1, exposing the photopolymer to UV light with sufficient energy to initiate curing (i.e., $>E_c$) will result in solidification of the photopolymer. Jacobs explains [149] that the shape of a single laser cure line determines the minimum feature size and "...is the fundamental "building block" for SL parts." It is reiterated (2.6) that in galvanometer systems, as used in the current study, the minimum feature size (MFS) is discrete from the resolution which is determined by the incremental movement of the laser and the corresponding angular accuracy of the galvanometer.

In practice, the depth of cure and the vertical resolution is limited by the layer thickness. Therefore, it is the radius of the cured line at the perimeter of the part which has the greatest influence on the lateral dimension of the product and compliance with manufacturing tolerances. Consequently, the width of the perimeter cured line is of particular interest in this investigation.

Any factors which influence the delivered exposure or the shape of the beam, may result in spurious curing, or deviation from the design dimensions. The distorting characteristic of primary concern when using silicon nitride as a substrate in stereolithography is regarding

reflectance. Reflectance is a function of the angle of incidence as are the distorting effects of ellipticity, divergence and refraction which makes distinguishing the distortion due to one from another difficult. Although only reflectance will be influenced by the substrate, the significance of the other characteristics mentioned are to be investigated also. This will allow their combined distorting effect to be quantified and that caused by reflectance to be deduced. This investigation into distortion will incorporate numerical modelling to identify the variables of significance, how they change during operation, and the corresponding influence on the output. Once a model has been generated, it can be calibrated using known outputs to compensate for errors in assumptions and to better represent the application. The calibrated model can then be used to predict the influence of changing parameters.

Factors which influence the delivered exposure and the distorting effects of refraction, divergence, ellipticity and reflectance will now be discussed, how they will be modelled numerically, and the calibration of that model for comparison with experimental data. The terminology used is included in the glossary of terms with the distinction between a ‘layer scan’ and a ‘line pass’ of particular importance when describing the modelling process.

Using the equations and numerical relationships described in this chapter, models to quantify the distorting effects discussed (refraction, divergence, ellipticity, reflectance, over-exposure, and step size) and to optimise the SLA process have been generated in MATLAB (script included in Appendix J).

3.2.1. Line width compensation

To allow the accurate construction of borders, SLA machine logic is commonly programmed [9] to target the centre of the beam at a distance one half of the cured line width (CLW) from the external perimeter of the construction as shown in Figure 3.2. This function is called line width compensation (LWC).

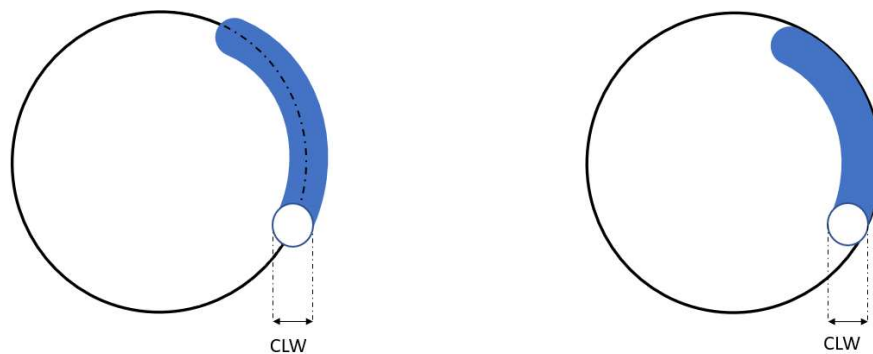


Figure 3.2: The cured line width centralised on the perimeter circumference of the target construction and with line width compensation applied [right].

The relationship between the CLW, the LWC, a part's design [lateral] dimensions (D_d) and the lateral built dimensions (B_d) is shown in Equation 3.1.

$$B_d = D_d + 2 \cdot \left(\frac{C_{LW}}{2} - L_{WC} \right)$$

Equation 3.1: The as-built lateral part dimension as a function of the cured line width, line width compensation and the design dimension.

Consequently, any distortion and deviation in the perimeter CLW will have a corresponding influence on the dimensions of the product. For instance, doubling the line width without adjusting the LWC will result in the product's dimensions being one line width greater than design. Additionally, any variation to functional parameters influencing line width (i.e., exposure) will result in a different line width to that on which the control logic is based and a corresponding distortion to the product.

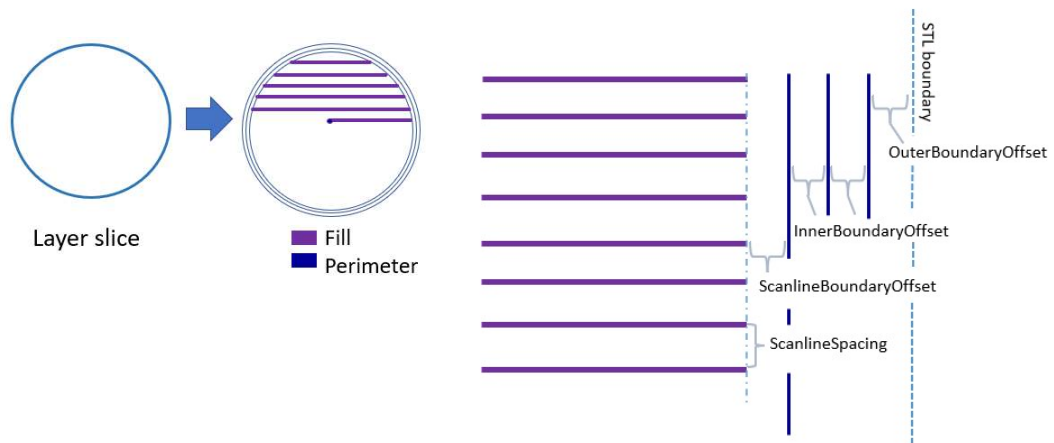


Figure 3.3: Formlabs scan pattern.

In the Formlabs equipment used in the current study, the LWC is set using the OuterBoundaryOffset (Figure 3.3). This has a default design setting of 30 μ m microns [150] for the Form 1 which corresponds to a 60 μ m wide cure line and is assumed to be the same for the Form 2.

3.2.2. Calculation of the cured line width

The CLW is a function of the critical cure energy of the photopolymer, and the diameter of the beam which possesses sufficient energy to initiate curing as explained in section 2.6.

An expression for the radius of the cured line produced from a single pass of a laser is derived in Equation 3.6. The peak intensity of a Gaussian beam occurs at the centre and is described by Equation 3.2 by Siegman [151].

$$I_0 = P_L \frac{2}{\pi \omega_0^2}$$

Equation 3.2: Peak beam intensity by Siegman [151]

The intensity of the beam at a radius (r) is also described by Siegman [151] in Equation 3.3.

$$I_r = I_0 e^{\frac{-2r^2}{\omega_0^2}}$$

Equation 3.3: Intensity of beam at radius r, by Siegman [151].

The intensity of the beam at radius r equals the required intensity to deliver an exposure equal to E_c when:

$$I_r = \frac{E_c}{t_e}$$

Equation 3.4: Condition for the beam intensity to initiate curing.

Substituting Equation 3.4 into Equation 3.3 gives:

$$\frac{E_c}{t_e} = I_0 e^{\frac{-2r^2}{\omega_0^2}}$$

Equation 3.5: Beam conditions to meet E_c as a function of exposure time.

Rearranging Equation 3.5 to find r:

$$\ln\left(\frac{E_c}{I_0 \cdot t_e}\right) = \frac{-2r^2}{\omega_0^2}$$

$$\sqrt{\frac{\omega_0^2 \cdot \ln\left(\frac{E_c}{I_0 \cdot t_e}\right)}{-2}} = r_c$$

Equation 3.6: Radius of the cure line from a single laser pass

Where:

- r_c is the radius of cure and therefore $CLW = 2r_c$;
- E_c is the critical energy of cure, r is the radius of the cure line;
- t_e is exposure time;
- V_s is scan speed;
- ω_0 is the $1/e^2$ width of the beam;
- I_r is the intensity of the beam at radius r;
- I_0 is the beam's peak intensity;
- P_L is the power of the beam at the print plane;
- r is the radius of the beam with sufficient intensity to initiate curing and corresponds to the radius of the resulting cure line.

3.2.2.1. Exposure time

Equation 3.6 is a function of the exposure time which is the duration for which the beam's spot is resident at a point on the photopolymer and is dependent upon the scan distance and speed. The scan speed can vary between SLA machines, with speeds up to 9.5m/s quoted in the literature (3D Systems SLA 7000) [152], and also for different regions within a scan pattern (e.g., the perimeter in Figure 3.3).

Hunziker [153] approximates the exposure time, using the expression in Equation 3.7.

$$t_e \approx \frac{2\omega_0}{V_s}$$

Equation 3.7: Hunziker's exposure time equation 2-6 [153].

However, the exposure time can be calculated more accurately from the general exposure equation [116]. From which, an expression for the maximum delivered exposure (E_{\max}) is derived by Gibson [116] in Equation 3.8.

$$E_{\max} = \sqrt{\frac{2}{\pi}} \frac{P_L}{W_0 V_s}$$

Equation 3.8: Maximum exposure delivered as a function of laser power, spot size and scan speed by Gibson [116].

Therefore, dividing the peak exposure from Equation 3.8 by the peak intensity from Equation 3.2 gives the exposure time (Equation 3.9).

$$\frac{E_{\max}}{I_0} = \frac{J \cdot m^{-2}}{J \cdot S^{-1} \cdot m^{-2}} = t_e \text{ (s)}$$

Equation 3.9: Exposure time as a function of exposure and intensity.

The exposure time can subsequently be used to calculate the corresponding exposure distance $D_s = t_e \cdot V_s$. The resulting exposure distance equates to:

$\sqrt{\frac{\pi}{2}} \cdot W_0 = 1.25 \cdot W_0$ which sits between the beam diameters FWHM and $2 \cdot W_0$ as shown in Figure 3.4.

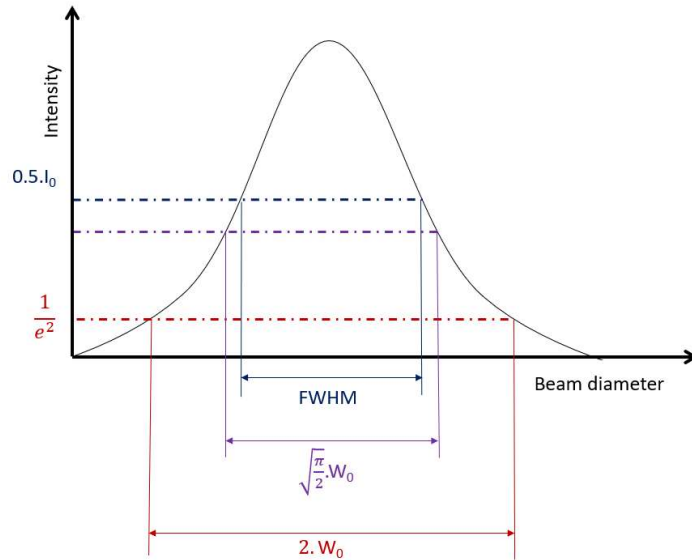


Figure 3.4: Exposure distance relative to FWHM and W_0 .

The exposure time allows the exposure profile and the resulting step size between layers to be calculated.

3.2.3. Step size

The beam is attenuated as it penetrates the photopolymer and, as mentioned in section 3.2, the depth of cure is limited by the layer thickness. This results in the cure profile shown in Figure 3.5. Consequently, when multiple layers are constructed, the stepped edge (Figure 3.5) profile results.

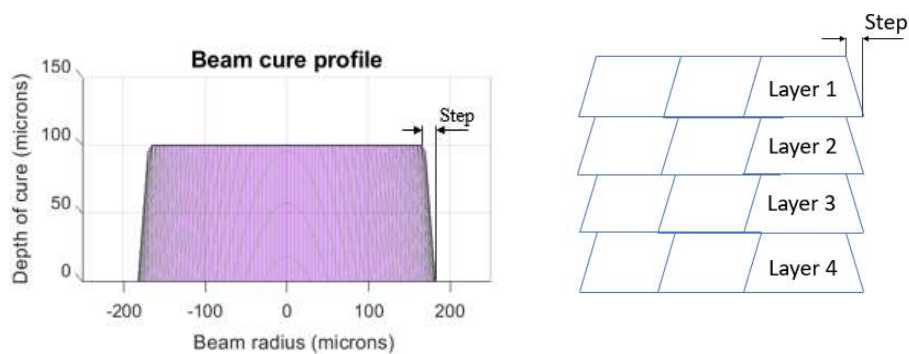


Figure 3.5: [left] Cure profile view from a single pass, [right] stepped edge profile from multiple layers.

The magnitude of the step size between layers is calculated using the Beer-Lambert law [116] and the peak intensity of the beam incident on the surface of the photopolymer from Equation 3.2, to give the intensity at depth Z (I_z) in Equation 3.10.

$$I_z = I_0 e^{-\frac{z}{D_p}}$$

Equation 3.10: Beer-Lambert Law

I_z is substituted into Equation 3.4 and rearranged to find the exposure (E_z) at depth Z .

$$E_z = I_z \cdot t_e$$

Equation 3.11: Exposure at depth Z as a function of intensity.

The radius of the cure line at depth Z (r_{cz}), can then be calculated by inputting E_z into Equation 3.6.

To calculate the step size (S_s) between layers, Z is set equal to the layer thickness (LT) and r_{cz} subtracted from the cured line radius at the surface of the polymer ($z = 0$) using Equation 3.12.

$$S_s = \frac{C_{LW}}{2} - r_{cz}$$

Equation 3.12: Step size equation using cured line width at the surface of the photopolymer and the radius of cure at the bottom of a layer.

3.2.4. Superposition

A Gaussian beam contains energy beyond the dimensions of the spot (e.g., $2 \cdot W_0$ in Figure 3.4). The radius of the beam in which 99.99% of its exposure energy is contained is termed the zone of influence (R) as described by Equation 3.13 [149].

$$e^{-\frac{2R^2}{W_0^2}} = 0.001$$

Equation 3.13: The zone of influence [9], [149]

Where the zone of influence from two parallel line passes overlap, an increased exposure is experienced resulting in superposition. The magnitude of superposition is a function of the number of lines passes (N) which fall within the zone of influence. Therefore, superposition is dependent upon several parameters including line spacing, laser power, scan speed and the beam profile (spot size).

Jacobs [9] derives the following expressions for the exposure resulting from superposition for parallel line passes relative to a centreline in the y plane. This is applicable to the scan pattern applied by the Formlabs equipment (Equation 3.14)

$$E_n(y,0) = E_{\max} \cdot e^{-\frac{2(y-nh_s)^2}{W_0^2}}$$

$$E_{-n}(y,0) = E_{\max} \cdot e^{-\frac{2(y+nh_s)^2}{W_0^2}}$$

Equation 3.14: Exposure delivered to neighbouring lines spaced at h_s by Jacobs [9]

Where E_n is the exposure influenced by the current line pass (E_0) for a given line n orthogonal to y as shown in Figure 3.6, E_{\max} is the maximum exposure along a single line pass, y is the direction of scan and h_s is the hatch spacing.

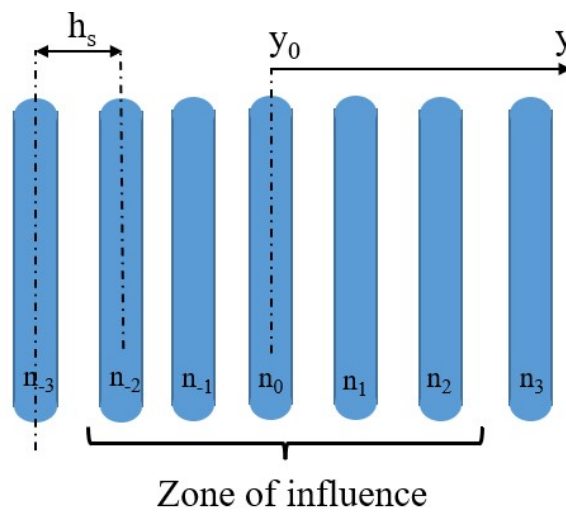


Figure 3.6: Zone of influence relative to line pass no.

$$E_{\text{total}}(y,0) = [E_n(y,0) + E_{n-1}(y,0) \dots + E_{-n+1}(y,0) + E_{-n}(y,0)]$$

Equation 3.15: Total exposure due to superposition by Jacobs [8]

Therefore, the number of line passes which are within 'zone of influence' (R) is governed by the hatch spacing. E_{total} is the sum of the exposures delivered by the respective lines passes within R , and the peak exposure along the centre line of the current pass corresponds to when $y = 0$. Conversely, locations of minimum exposure (E_v) defined as 'valleys' occur at $y_0 + 0.5h_s$, with the average exposure (E_a) being the mid point being E_p and E_v . An example of the influence of hatch spacing on E_a (denoted by the blue bar) is shown in Figure 3.7 and Table 3.5.

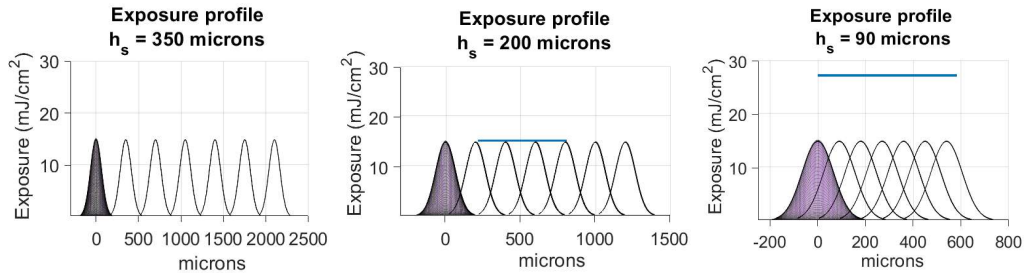


Figure 3.7: Example superposition exposure profiles

The influence of decreasing hatch spacing on superposition [left] $h_s = 350\mu\text{m}$, [middle] $h_s = 200\mu\text{m}$, [right] $h_s = 90\mu\text{m}$.

The influence of superposition			
Example / parameter	Left	Middle	Right
Hatch spacing [h_s] (μm)	400	150	90
Peak exposure [E_p] ($\text{mJ}\cdot\text{cm}^{-2}$)	60.52	65.54	100.24
Peak to valley exposure [%]	100%	16.7%	0.2%
Potential cure depth [C_d] (μm)	301	892	973

Table 3.5: The influence of superposition

As can be seen in Figure 3.7, superposition can significantly increase the delivered exposure (Table 3.5). Decreasing the line spacing also serves to even the exposure distribution between passes by reducing the difference between E_p and E_v . As discussed in section 2.6, the difference in exposure between the two extremes should not exceed 3%.

The maximum exposure delivered (E_{max}) for a centrally located line pass will be E_0 plus the exposure from the adjacent passes either side. In the example shown in Figure 3.6 there are 2 passes either side which will make E_0 equivalent to $E_{-2}+E_{-1}+E_0+E_1+E_2$. Superposition will only influence the CLW width if its outer radius sits within the zone of influence.

Therefore, for a perimeter line pass there will only be two lines in addition to the target line pass within the zone of influence as there will not be adjacent passes beyond the boundary of the part. Therefore, E_{max} for a perimeter line will be $E_0+E_1+E_2$. The spacing between line passes can be different between the hatch spacing (h_s) used to fill constructions and that at the perimeter (p_s) as shown in Figure 3.3. The influence of perimeter line pass parameters (power, speed and spacing) on a part's constructed dimensions (section 3.2), are predominantly of interest in the current investigation. The increase in the radius of cure due to superposition can be calculated using Equation 3.6 (or Equation 3.20 for a D&E beam) by relating E_{max} to intensity (I_0) using Equation 3.9.

3.2.5. Multiple scans

To promote the adhesion of an SLA construction to the substrate, it is common practice to overexpose the first layer with repeat scans as discussed in section 2.4.5. This increases the corresponding CLW for the first layer which often results in the formation of a meniscus (section 2.4.5). However, in practice there will be energy loss between the repeated scans of the laser (Figure 3.8). Therefore, the energy in the system will not simply equate to the number of scans multiplied by the delivered exposure.

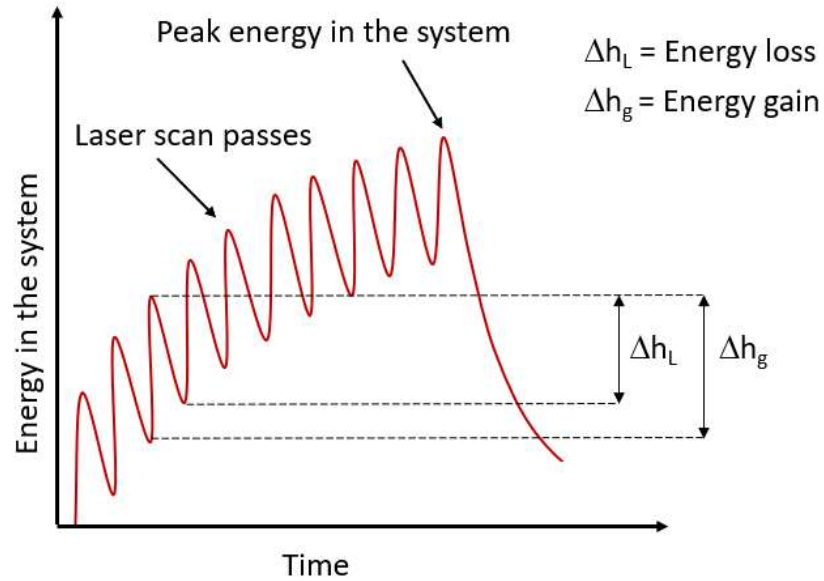


Figure 3.8: Example energy gain from repeated laser scans

The influence of the energy loss during repeated scans can be compensated for by applying a correction factor to the model. The correction factor is determined using the calibration process described in section 3.2.9.

3.2.6. The angle of incidence and distorting effects.

In laser SLA machines, as used in this investigation, an angle of incidence (AOI) is produced by the laser being reflected from the galvanometer and main mirrors as shown in Figure 3.9.

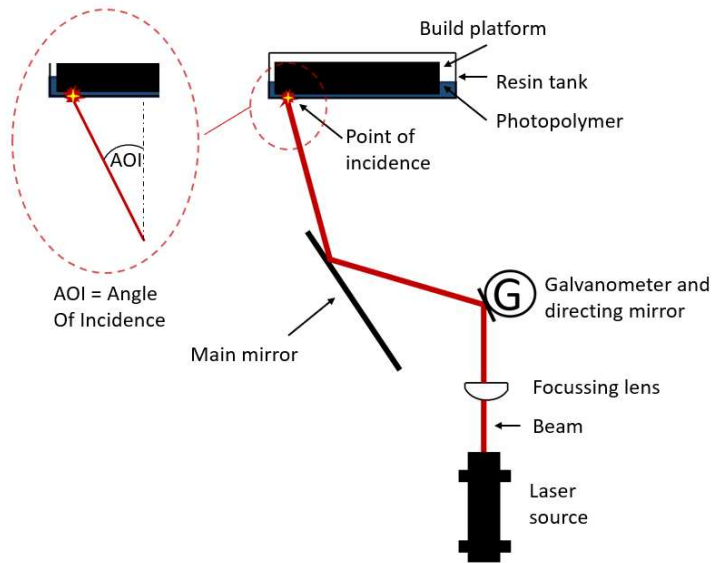


Figure 3.9: Light train of the Form 1+ and Form 2 machines

The AOI is formed between the galvanometer mirror and the point of incidence (POI) in the build area (Figure 3.9). The main mirror serves to extend the light path which allows a smaller AOI than would otherwise be achieved within the confines of the SLA machine housing. Figure 3.10 demonstrates where an equivalent source would be in a linear system (i.e., without the main mirror) where the distance from the galvanometer (Z_a) is equal to Z_b . The AOI then increases with the distance (X) of the POI from the centre of the build area.

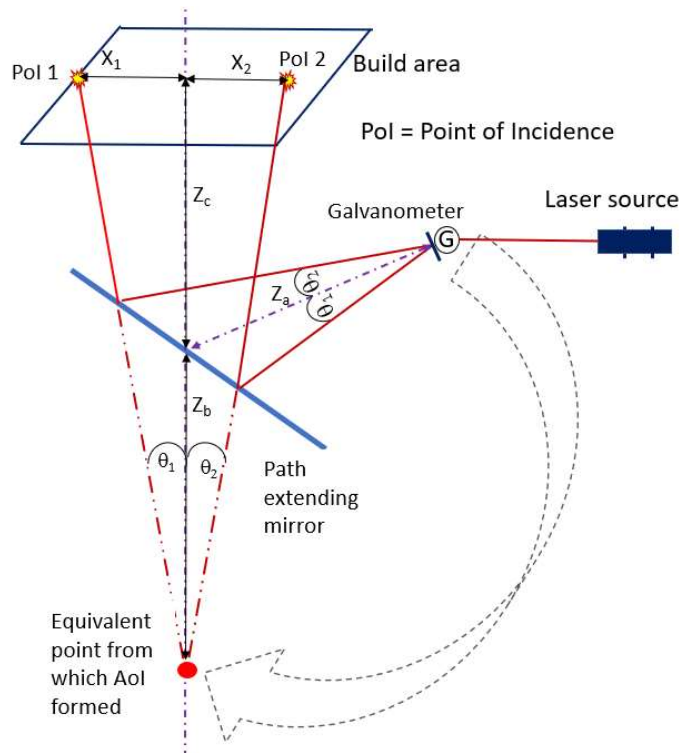


Figure 3.10: Laser path showing the angles of incidence for the Form 1 and Form 2

The path between the centre point of the build area and galvanometer mirrors has been measured to be 300mm on the Form 1 SLA machine and is assumed to be the same on the Form 2. This allows the angle of incidence to be calculated using trigonometry. The angle of incidence produced can cause the distorting effects of refraction, divergence, ellipticity and contribute to reflectance. These will now be discussed in turn.

3.2.6.1. Refraction

Refraction will not produce spurious curing but will impact the accuracy and precision to which cured lines are produced which cumulatively can result in differences between the constructed and the design dimensions of a part.

The beam is refracted as it passes through the different material mediums of the machine as shown in Figure 3.11 for the Form 2 equipment. The resulting transmission angle (Snell's law) from one medium to the next is a function of the dissimilarity in their refractive indices (at 405nm) and varies accordingly. The transmission angle provides the AOI onto the subsequent medium which, in accordance with Snell's law, equals the angle of reflectance. This results in the AOI on the substrate being different to the geometric angle between the galvanometer (Figure 3.10) and the point of incidence in practice.

A model describing this characteristic has been generated (Appendix J) for the material properties (section 3.1) of the Formlabs equipment (Figure 3.11), and the assumptions in section 3.2.13. The model also incorporates the facility to adjust the light path and the dimensions of the build area.

By inputting the geometry of a given SLA process, the model quantifies the lateral distance between the geometric and the refracted points of incidence, to provide the loss of accuracy in the x-plane (δK_{xt} in Figure 3.11).

Four mediums have been considered in the model:

Medium 1: The air between the laser source and medium 2 (Form 2) or medium 3 (Form 1);

Medium 2: The glass window of the Form 2 with an estimated thickness of 3mm. This medium is not installed on the Form 1;

Medium 3: The acrylic base of the resin tank with a measured thickness of 7mm;

Medium 4: The photopolymer with a thickness equal to the layer height of the build (typically 100 μ m).

This model also incorporates the use of the main mirror within the optical train (Figure 3.9).

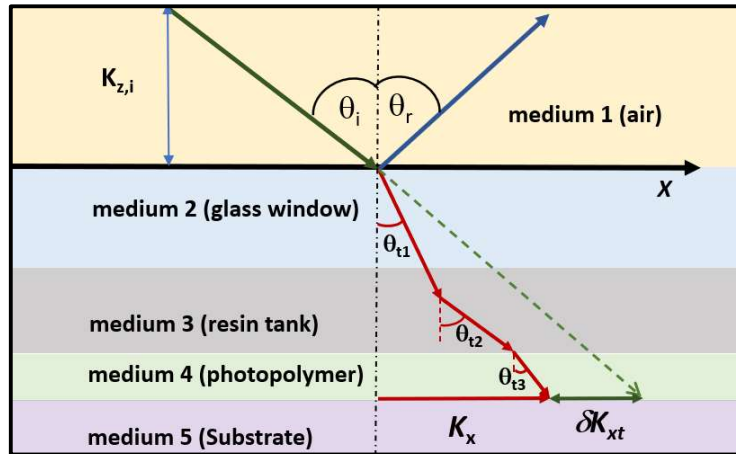


Figure 3.11: An example of the path of laser light through the respective mediums in the Form 2 SLA machine

Experimentation to measure the distortion attributed to refraction, in an SLA construction has been devised in section 3.3.5.

3.2.6.2. Divergence

The beam from a laser will naturally diverge as a function of its wavelength, its waist dimension (W_0 , Figure 3.12), the quality of the beam and the focal lens.

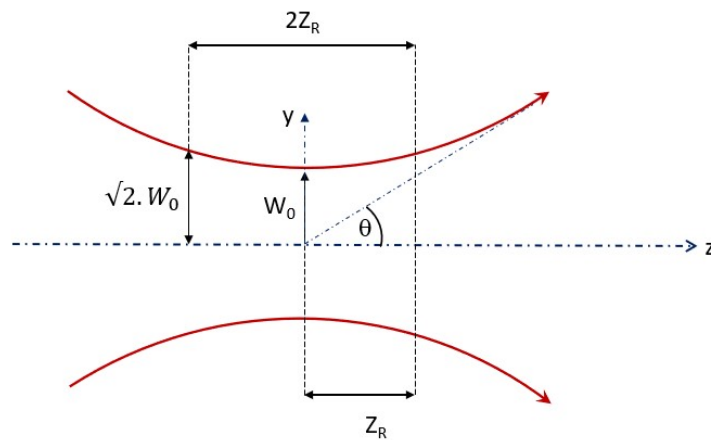


Figure 3.12: Divergence of a beam with distance Z as a function of Rayleigh length.

The diffraction limit is the minimum angle by which the beam will diverge, while its quality is described by the M^2 parameter. This is defined [134] as the ratio of the BPP (Beam Parameter Product) to the diffraction-limited Gaussian beam at a given wavelength. To quantify the M^2 parameter accurately requires direct measurement of the BPP. However, diode lasers, as used on the Form 1 and Form 2 equipment, have a typical range [135] between 1.0 and 1.7 and therefore a mid-range value of 1.4 has been assumed for the current investigation.

The Rayleigh length (Z_R) (Figure 3.12, Equation 3.16) is the distance over which the beam's area doubles and therefore can be used to calculate the radius of the spot at a point relative to the focussed beam (W_0) according to Equation 3.17.

$$Z_R = \frac{\pi\omega_0^2}{M^2\lambda}$$

Equation 3.16: Rayleigh length by Kovalev [134]

$$\omega(z) = \omega_0 \sqrt{1 + \left(\frac{z}{Z_R}\right)^2}$$

Equation 3.17: The beam waist at distance z relative to the focussed dimension by Kovalev [134].

3.2.6.3. Ellipticity

For reasons explained in section 2.7.2, a beam becomes increasingly elliptical as the angle of incidence increases (Figure 3.13).

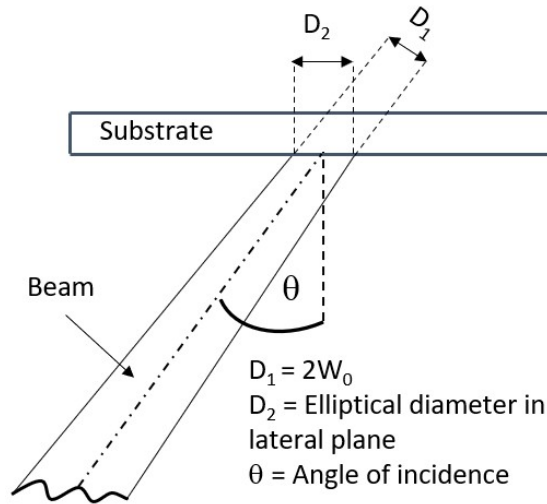


Figure 3.13: Ellipticity of a beam

Temmler [154] simplifies ellipticity by only considering the variation of the beam in a single dimension using Equation 3.18. The same approach is adopted in the current investigation to model (Appendix J) the influence of ellipticity laterally across the build area.

$$D_2 = D_1 \frac{1}{\cos(\varphi + \theta)}$$

Equation 3.18: Equation describing ellipticity in a single dimension by Temmler [154]

Where D_1 is the diameter of the beam at a normal AOI, D_2 is the diameter of the beam at an oblique AOI, φ is the slope of the substrate and θ is the AOI.

For the applications in the current investigation, the φ term equates to zero and can be ignored. Since the beam's absolute power is uninfluenced by ellipticity, the intensity of the beam reduces as the dimension of the beam is extended. Equation 3.18 can be applied to the dimension of the beam incident at the surface of the photopolymer to calculate the influence on the intensity in the lateral dimension, the superposition zone of influence, and the corresponding CLW (section 5.1.4.3).

3.2.7. Tolerances

Without mitigating measures, divergence and ellipticity (D&E) will impact the ability to achieve manufacturing tolerances. Tolerance is dictated by the part's perimeter construction line (section 3.2.1). The relationship between the cured line width and the constructed part's dimension is a function of the line width compensation and the design dimension (D_d) as described by Equation 3.19.

$$T_M (\%) = \frac{C_{LW} - 2 \cdot L_{wc}}{D_d} \cdot 100$$

Equation 3.19: Manufacturing tolerance as a function of the cured line width and its compensation (L_{wc}).

Where T_M is the manufacturing tolerance as a percentage of the design dimension.

Due to divergence and ellipticity both being a function of the AOI (Figure 3.10), the impact of these characteristics is greatest at the extremity of the build area.

3.2.7.1. Tolerance with Divergence

By rearranging Equation 3.19, the maximum CLW permitted to comply with a given manufacturing tolerance can be calculated. By substituting Equation 3.8 into Equation 3.6, the cured line width, as a function of the beam waist, and variables (P_L , E_c and V_s) influenced by the AOI (i.e., ellipticity and divergence) can be obtained in Equation 3.20.

$$r_c = \sqrt{\frac{\omega_d^2 \ln \frac{E_c}{\sqrt{\frac{2 P_L}{\pi \omega_d V_s}}}}{-2}}$$

Equation 3.20: radius of cure as a function of variables independent of the angle of incidence.

Where ω_d is the waist of the diverged beam. For a beam focussed on the centre of the build area ω_d will equal ω_0 .

The maximum cured line width to comply with a given manufacturing tolerance can be obtained by rearranging Equation 3.19. In turn, the maximum diverged beam width (ω_d) corresponding to that CLW can be obtained from Equation 3.20 and the tolerance in the spot size (T_s) for a given T_m , obtained using Equation 3.21.

$$T_s (\%) = \frac{\omega_d - \omega_0}{\omega_0} \cdot 100$$

Equation 3.21: Spot size tolerance

This allows the maximum build area dimensions to avoid exceeding manufacturing tolerances to be determined and the operating limits for optimisation (section 5.1.8).

To calculate the former, the relationship between the beam's POI on the build area and the resulting extension to the path length (Z_e) is needed (Figure 3.10). By equating Z_e to the distance Z , and ω_d to $\omega(Z)$ in Equation 3.17, the divergence of the beam relative to its focussed width (assumed to be at the centre of the build area) can be calculated from the ratio of ω_d/ω_0 . When applied to Equation 3.17 and rearranged, this gives the maximum path extension to comply with tolerances:

$$z_R \cdot \sqrt{\left(\frac{\omega_d}{\omega_0}\right)^2 - 1} = Z_e$$

Equation 3.22: The maximum path extension to comply with manufacturing tolerances.

3.2.7.2. Tolerance with ellipticity

The calculation is extended to incorporate ellipticity by replacing ω_d with ω_{de} (beam waist of a diverged elliptical beam) from Equation 3.18 into Equation 3.17. This gives Equation 3.23 and the maximum proportional increase in the beam waist relative to the focussed beam (ω_{de}/ω_0) to comply with manufacturing tolerances.

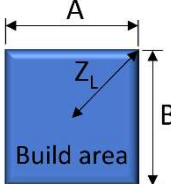
$$\omega_{de} = \frac{\omega_d}{\cos \theta} = \omega_0 \cdot \frac{\sqrt{1 + \left(\frac{Z_e}{z_R}\right)^2}}{\cos \theta}$$

Where θ is the AOI.

$$\frac{\omega_{de}}{\omega_0} = \frac{\sqrt{1 + \left(\frac{Z_e}{Z_R}\right)^2}}{\cos \theta}$$

Equation 3.23: The proportional increase in the beam waist due to divergence and ellipticity.

The greatest increase in the beam waist will occur when Z_e is longest, which will occur at the extremity of the build described by Z_L :

$$Z_L = \sqrt{\left(\frac{A}{2}\right)^2 + \left(\frac{B}{2}\right)^2}$$


Where Z_L is the lateral distance to the extremity of the build platform, and A and B are the lateral dimensions of the build area. The extension to the path length is therefore:

$$Z_e = \sqrt{Z_{PC}^2 + Z_L^2} - Z_{PC}$$

Equation 3.24: Extension to the laser path at the extremity of the build area.

Z_{PC} is the laser path length to the centre of the build area and equal to $Z_a + Z_c$ in Figure 3.10. The angle of incidence can then be calculated in Equation 3.25.

$$AOI = \tan^{-1} \frac{Z_L}{Z_{PC}}$$

Equation 3.25: AOI as a function of the laser path length and the lateral distance from the centre to the extremity of the build area.

The increase in the beam waist (relative to ω_0) due to ellipticity and divergence at the extremity of the build area is calculated by substituting Equation 3.24 and Equation 3.25 into Equation 3.23 to give Equation 3.26.

$$\frac{\omega_{de}}{\omega_0} = \frac{\sqrt{1 + \left(\frac{\sqrt{Z_{PC}^2 + Z_L^2} - Z_{PC}}{Z_R}\right)^2}}{\cos\left(\tan^{-1} \frac{Z_L}{Z_{PC}}\right)}$$

Equation 3.26: The increase in the beam waist (relative to ω_0) due to ellipticity and divergence at the extremity of the build area.

Equation 3.26 can then be applied to determine the maximum build area permissible due to the effects of divergence and ellipticity to comply with manufacturing tolerances. This has been applied to the MATLAB model and the script included in Appendix J.

3.2.8. Combining the divergence, ellipticity, and superposition models

The models (Appendix J) characterising divergence, ellipticity, exposure and the resulting CLW are combined to represent the operation of the Form 1+ machine. Specifically, its geometry including the distance of the galvanometers to the centre of the build platform, the dimensions of the build area, and relevant operating parameters (Table 5.1). The beam will diverge as its path is extended towards the extremities of the build area. The influence of ellipticity is then applied to the diverged spot to generate the beam profile and spot size at any location in the X-Y plane on the build area.

The parameters of scan speed, line spacing and laser power are applied to the superposition model (section 3.2.4) to identify the maximum exposure (E_{max}) delivered and the corresponding CLW (section 3.2.2) calculated. The model is then calibrated for multiple first layer scans (MFLS) with the associated energy loss using the processes described in section 3.2.9.

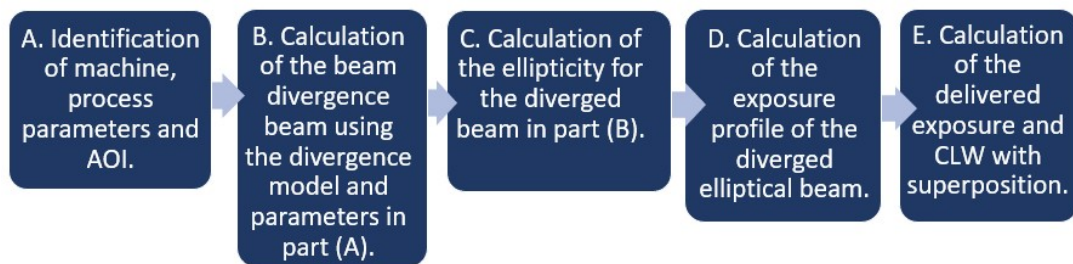


Figure 3.14: The process for calculating the CLW with the influence of D&E.

3.2.9. Model calibration

For the applications in the current study, the extent to which superposition and MFLS increase the delivered exposure and the corresponding influence on the CLW, is not known. Consequently, the calibration processes described in sections 3.2.9.1 (Form 1+) and 3.2.9.2 (Form 2) are applied to the model to account for these influences. The calibration process requires modelling the application with known parameters.

By comparing the modelled output to measured results, a correction factor for the energy lost during MFLS can be determined.

Three parameters which have not been measured directly and can be used for calibrating the model are focal length, the critical cure energy of the photopolymer (E_c), and the laser power at the print plane. It is assumed that the beam is focussed on the centre of the build

area [9] with its path length equal to the beam focal length. The photopolymer used in the current study has been characterised by Bennet [50] with an E_c of 12.6 mJ/cm^2 [$\pm 10\%$].

However, the beam will attenuate as it is reflected from the mirrors in the light train (Figure 3.10) and passes through the various machine media (3.2.6.1). Additionally, diode lasers experience temperature sensitivity and are reported [155] to degrade relatively quickly compared with other electrical devices. Shuttleworth [156] measured the power at the print plane (Y) for a Form 1+ machine to be substantially (56%) lower than the setpoint value. The relationship between Y and the setpoint power in the logic (X) was described [156] by the expression $Y = 0.44X - 0.02$. According to this relationship, the default perimeter power setting (Appendix F) used of 48mW corresponds to 21.1mW delivered.

The extent of attenuation and degradation will vary between specific machines depending upon the extent of fouling and their use. In the model, this is accommodated by adjusting the laser power by following the calibration process described in sections 3.2.9.1 (Form 1) and 3.2.9.2 (Form 2).

For comparison, calibration using focal distance and E_c for the Form 1+ will also be conducted by substituting these parameters for laser power in stage [B] of the process (Figure 3.15). In these cases, laser power at the print plane is set to 21.1mW according to Shuttleworth's curve [156].

3.2.9.1. Form 1+ calibration process

The Form 1+ model is calibrated against the default operating parameters [150] which has a line width compensation of $30\mu\text{m}$. It is assumed this line width is formed with the influence of superposition as it is part of a scan pattern (Figure 3.3).

The Form 1+ SLA machine is calibrated using design data as summarised in Figure 3.15.

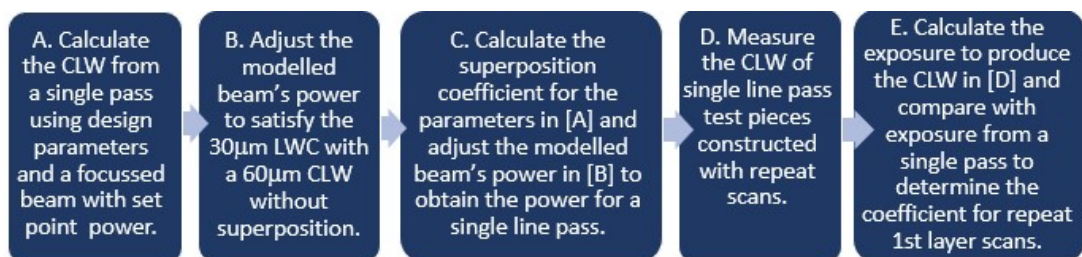


Figure 3.15: Process for calibrating the Form 1+ model using the dimensions of measured test pieces.

- A. The design parameters (section 3.1) of the Form 1+ are entered into the model described in section 3.2.8, with the beam assumed to be focussed on the centre of the build area in accordance with design practice [9]. Therefore, the beam's focal distance is set equal to the measured light path. The CLW corresponding to the setpoint power in the control logic is calculated.
- B. The power of the Form 1+ beam at the print plane is significantly lower than the setpoint [156]. Therefore, the modelled power is reduced until a CLW of 60 μ m at the centre of the build area is obtained, to match the design LWC of 30 μ m.
- C. In practice superposition will be active (section 3.2.4). Therefore, the superposition coefficient is calculated (section 3.2.4) using the operating parameters in stage [A] and applied to the power in [B] to obtain the power at the print plane and exposure for a single line pass (i.e., without superposition).
- D. MFS test pieces are constructed (method 3.3.2) using the operating parameters in [A] and measured. These test pieces are formed from a single line pass and thereby without the influence of superposition but are subjected to repeat scans. This provides the minimum CLW with repeated scans and without superposition. The corresponding exposure required to produce these is then modelled.
- E. The diabatic exposure required to generate the test piece in stage (D) is compared with the theoretical adiabatic exposure delivered. The latter is calculated by multiplying the exposure delivered in a single scan pass in stage [C]. The difference between the two exposures is then used to calculate the energy lost during the repeated scanning process using Equation 3.27.

$$\text{Energy loss (\%)}_{\text{repeat scans}} = \frac{(n \cdot E_{\text{max.[C]}}) - E_{\text{max.[D]}}}{n \cdot E_{\text{max.[C]}}} \cdot 100$$

Equation 3.27: Energy loss during repeat scanning in a diabatic system.

Where n is the number of repeat scans (design = 10), $E_{\text{max.[C]}}$ is the exposure delivered in a single scan pass (i.e., without superposition) calculated in [C], and $E_{\text{max.[D]}}$ is the total diabatic exposure required to form the measured part calculated in [D].

3.2.9.2. Form 2 calibration process

Compared to the Form 1+, relatively few operating parameters are known for the Form 2. This includes the number of first layer scans, and hatch spacing, which are not reported in the literature or the equipment documentation. Therefore, a slightly different process to that used for the Form 1+ (section 3.2.9.1) is applied. The Form 2 model calibration process is based on the ratio of the measured dimensions of parts constructed using the methods in section 3.3.3, to calculate the superposition and MFLS coefficients. The three scenarios used are:

1. Test pieces with MFLS without superposition (section 3.3.3.1);
2. Test pieces with MFLS and superposition (section 3.3.4.2 part A).
3. Test pieces without MFLS with superposition (section 3.3.4.2 part B);

The Form 2 spot size (FWHM) is $140\mu\text{m}$ [42] and is assumed to be focussed on the centre of the build area with a scan speed of 1000mm/s (Table 5.3). By modelling the exposure required to construct the first test piece (no.1) and applying the coefficients for superposition and MFLS determined using the process in Figure 3.16, the corresponding beam power can be calculated. The Form 2 model calibration process is summarised below.

Form 2 calibration process

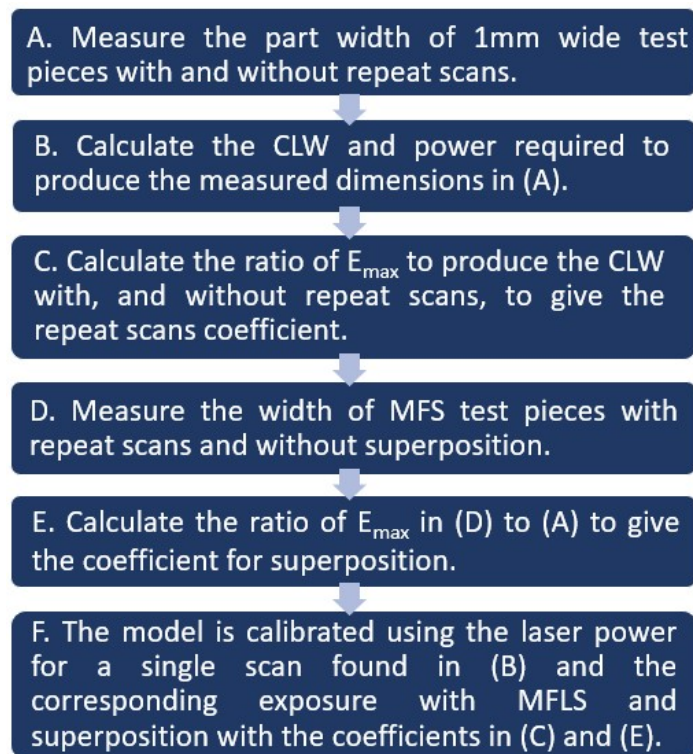


Figure 3.16: Process for calibrating the Form 2 model using the dimensions of measured test pieces.

- A) 1mm wide test pieces are constructed (section 3.3.3) using repeated scans. A second set of 1mm wide test pieces are constructed to a height of 5.5mm to avoid the influence of repeat scans on the upper layers. Each layer of the 1mm test pieces is subject to superposition because they require multiple parallel line passes to construct.
- B) The CLW and corresponding power and exposure (at an assumed scan speed), required to construct the measured dimension in stage [A] is calculated by the model. This provides the laser power at the print plane.
- C) The ratio of the required exposures in [B] to produce the CLW with multiple scans to that without, provides the MFLS coefficient.
- D) MFS test pieces (section 3.3.3.1) are constructed using MFLS and measured. Being narrower than the minimum CLW, the test pieces are constructed from a single line removing the influence of parallel line passes. This provides the MFS with repeated scans and without superposition.
- E) The exposure required to form the measured CLW in [D] is calculated by the model and compared to the test pieces with repeat scans and superposition in [B], to provide the superposition coefficient.
- F) From the above process the model is calibrated using the laser power for a single scan found in [B]. The corresponding power and exposure, with repeat scans and superposition is then obtained from the MFLS coefficient in [C], and superposition in [E].

The calibrated model can then be applied to analyse the potential for reflected exposure energy from substrates to combine with the incident exposure and produce spurious curing (section 3.2.10).

3.2.10. Reflectance model

A model to characterise reflectance in an SLA process, has been written in MATLAB (Appendix J), incorporating the facility to adjust, and input; the beam characteristics; machine geometry (e.g., path lengths and build area); machine operating parameters; the properties of the photopolymer (i.e., E_c and D_p) and those of the substrate (surface roughness and refractive index). The reflection and transmission coefficients of the electric

and magnetic components of light ($\lambda = 405\text{nm}$) at the successive interfaces of the Formlabs SLA equipment (Figure 3.11), and ultimately that from a silicon nitride substrate is calculated using the Fresnel equations [27]. The reflection and transmission coefficients are the amplitude of the respective components relative to the incident light. Whether the reflected light constructively or destructively interferes with the incident light is dictated by its phase and described by the positive (constructive) or negative (destructive) sign of the reflection coefficient. The model was then updated by entering the specific geometric arrangement of the Formlabs equipment and used in the current study (Figure 3.9 to Figure 3.11). This includes the angle and point of incidence on the main mirror to support subsequent potential optimisation (section 5.1.9.1). A full list of the model I/O (input and output) is included in Appendix H.

The reflectance (R), and transmittance (T) coefficients, which relate to the power of the respective waves, are calculated to determine if, and to what extent spurious curing due to reflected light, may occur. The angles of incidence and reflection coefficients at each interface (Figure 3.11) are calculated from their impedance relative to the preceding medium i.e., the photopolymer. The impedance being a function of the material's refractive index. The corresponding angle of transmittance, and the extent of attenuation are calculated according to a material's thickness and extinction coefficient [27]. The beam intensity and exposure profile are calculated following the process described in section 3.2.2. Surface roughness is considered (section 3.2.10.2) using the Bennet-Porteous[55] model.

As explained in section 5.1.5, reflections at oblique angles, delivering an exposure greater than the photopolymer's critical cure energy, will result in spurious curing. Depending upon whether constructive or destructive interference occurs, reflected light from a normal angle of incidence may combine with the incident beam to increase the total exposure delivered. The magnitude of spurious curing is calculated using Jacob's cure depth equation [9] and the corresponding lateral component using the angle of reflectance (section 5.1.5).

3.2.10.1. Secondary reflections

Primary reflections occur at the interface between the photopolymer and the substrate. If this reflection is not completely attenuated in the photopolymer, they will be incident on the interface (Figure 3.11) between the photopolymer and the PDMS window, where a second reflection will occur. The magnitude of this secondary reflection, and its potential to produce spurious curing is dependent upon the reflection coefficient formed between the mediums and is considered in section 5.1.5.5.

3.2.10.2. The effects of gloss.

The topography of a surface has a significant influence on reflectance. Reflections from smooth surfaces will be more specular in nature compared to rough surfaces which will be more diffuse (Figure 3.17) and reflect light across a range of angles.

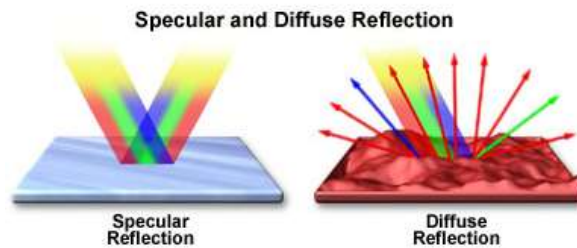


Figure 3.17: Specular and Diffuse Reflection by Pedrotti et al [27].

The extent to which a reflection is diffuse is described by the specular reflectance coefficient obtained from the Bennet-Porteous model [55]. The coefficient is dependent upon the wavelength of the incident light, its AOI, and the substrate surface roughness.

3.2.11. Beam profiling

The beam profile recorded following the experimental method described in section 3.3.7 was transferred into MATLAB, for analysis. To achieve this, the beam's intensity profile is converted into a 2D greyscale image using Spiricon's Beamstar™ software. This is then imported into MATLAB using the 'imread' tool. The resulting matrix is resized in the X-Y plane to correspond to the dimensions of the sample window stated in Beamstar at a ratio of 10µm per matrix unit. The matrix Z-dimension is then scaled to correspond to the peak intensity of the beam calculated (Equation 3.2) from the calibration process described in section 3.2.9.1. The exposure at a given scan speed (Equation 3.8) and the corresponding cure profile for defined photopolymer parameters (E_c and D_p) is then modelled using Jacob's expression for the depth of cure [9]. This profiles the beam and identifies any distortion or noise within it and allows the delivered exposure pattern and resulting cure profile, to be characterised (5.1.4.1).

3.2.12. Build time optimisation.

Parameters influencing the build time of an SLA construction are listed below:

1. The cross-sectional area of the part;
2. The scan speed which dictates how quickly the laser completes the scan pattern;
3. The line and hatch spacing which influences the number of line passes which the laser must travel;
4. The number of layers and the associated delay time between each one to allow for recoating process.

To minimise the number of layers, the part shall be orientated to reduce its height. By describing the part in terms of a ratio between its CSA and its height, allows the parameters (items 1-3) associated with the lateral build time to be related to those in item 4, associated with the vertical build time, for the purpose of calculation.

The scan area = $L_x \cdot L_y$

$$R_{az} = \frac{L_x L_y}{L_z}$$

Equation 3.28: Ratio of cross-sectional area to height

$$\text{Number of layers} = \frac{L_z}{R_{LT}}$$

Equation 3.29: Minimum number of construction layers as a function of the part height and maximum layer thickness.

The width of a line pass is equivalent to the hatch spacing (h_s) and the product of the line pass and the scan speed (V_s) gives the scanning rate ($m^2 \cdot s^{-1}$).

Therefore, the scan time for an individual layer, and the interlayer delay and action time, are added together to give the total build time (Equation 3.30):

$$t_B = \frac{L_x L_y}{V_s h_s} \cdot n_L + t_D n_L$$

Equation 3.30: Total build time as a function of the lateral and vertical operations.

Where t_D is the delay time, R_{az} is the ratio of CSA to height, R_{LT} is the maximum layer height to comply with the MFS in Z plane, and L_x and L_y are the average lengths of the construction in the x and y planes. The average dimensions of complicated geometries can be estimated or calculated using CAD.

Substituting Equation 3.29 into Equation 3.30 and rearranging for t_B gives:

$$t_B - t_D \frac{L_z}{R_{LT}} = \frac{L_x L_y}{V_s h_s} \cdot \frac{L_z}{R_{LT}}$$

Rearranging and dividing through by L_z gives....

$$\frac{\left(R_{LT} \cdot \left[t_B - \frac{t_D L_z}{R_{LT}} \right] \cdot V_s h_s \right)}{L_z^2} = \frac{L_x L_y}{L_z} = R_{az}$$

Therefore:

$$t_B = \frac{\left(\frac{R_{az} L_z^2}{V_s h_s}\right)}{R_{LT}} + \frac{t_D L_z}{R_{LT}}$$

Equation 3.31: Built time equation as a function of hatch spacing, scan speed and Raz.

Equation 3.31, describes the build time in terms of hatch spacing, scan speed and the ratio of the part's CSA to its height. This allows the build time to be related to the geometry and orientation of the part.

Additionally, the corresponding exposure received can be calculated from the scan speed, its associated exposure time, and the peak intensity (I_0) of the beam using Equation 3.9. The influence of superposition can then be applied using the hatch spacing as described in section 3.2.4.

By expanding and rearranging Equation 3.12 (step size) using Equation 3.6 (the radius of cure) and Equation 3.10 (exposure at depth Z), an expression for the maximum layer thickness (MLT) at which manufacturing tolerances (M_T) can be met, is obtained in Equation 3.32.

$$MLT = D_p \cdot \ln \left[\frac{t_e \cdot I_0 \cdot e^{-2 \cdot \left(\frac{(0.5(C_{LW} - M_T))^2}{W_0^2} \right)}}{E_c} \right]$$

Equation 3.32: Maximum layer thickness to comply with manufacturing tolerance.

3.2.13. Modelling assumptions

A list of assumptions used for the modelling is included below:

- The SLA beam is focussed on the centre of the build area;
- The light within the beam and incident light across the spot conforms to a Gaussian profile;
- The light path for the Form 2 is 300mm (equal to the Form 1+);
- The beam quality factor (M^2) is 1.4;
- The beam spot is focussed on the centre of the build area.
- All mediums are homogenous and isotropic;
- The light generated by the Form 2 laser is spatially coherent, circularly polarised and conforms to a Gaussian distribution;

- The surfaces are considered perfectly smooth unless otherwise stated;
- The Form 2 galvanometer mirror is located centrally in the x-y plane and 150mm beneath the glass window;
- The Form 2 build platform is assumed to be 6061 aluminium.

3.3. Experimental methodology for investigating distorting effects in the SLA process.

The following experiments described in sections 3.3.1 to 3.3.7 are designed to support the model calibration process described in section 3.2.9 and to quantify the lateral distortion across the build area. The modelled results can then be compared to the measured distortion to identify the potential for additional distorting effects (i.e., reflectance). In parallel, a separate experiment will be conducted to measure the magnitude of spurious curing due to the increased exposure from light reflected from the substrate. Throughout the experimentation using the Form 1+, the exposure is controlled by adjusting the scan speed (section 3.2.2.1).

3.3.1. Superposition using FTIR.

To verify superposition is active at the machine operating parameters used, a series of FTIR tests were conducted to assess the influence of hatch spacing on cross-linking. During the crosslinking process the C=C bonds in monomers are broken to form C-C bonds. By following the FTIR process described by Chen et al [78], the concentration of C=C (carbon double bonds) which absorb IR light at wavenumbers 1637cm^{-1} and 1407cm^{-1} [78], [157], [158], [159] can be determined.

The carbon oxygen double bonds (C=O) are not affected by the curing process and are therefore indicative of the original concentration of acrylate in the sample being measured. This allows the transmitted spectrum to be normalised [157], [160] using the area of the C=O peak at 1701cm^{-1} .

To vary the influence of superposition, three samples at increasing hatch spacing of $20\mu\text{m}$, $50\mu\text{m}$, $100\mu\text{m}$, $200\mu\text{m}$ and $600\mu\text{m}$, were prepared. These were disc shaped with dimensions $5\text{mm} \times 2\text{mm}$ and constructed from FLC photopolymer on a Form 1+ SLA machine with default settings ([150] Appendix F). The test pieces were constructed directly on the build platform. On completion they were removed with a blade, washed with IPA and wrapped in foil to minimise exposure to ambient light.

The samples were transferred to the Perkins-Elmer FTIR machine with care taken to position the last layer constructed facing the crystal of the machine. The equipment was calibrated by taking a background reading to compensate for the contribution of the environment to the spectrum reading.

The Perkin Elmer™ Spectrum-Quant™ analysis software was used to process the measured normalised profile of absorbance (%) against the wavenumber (cm^{-1}). The area under each C=C peak with the units of percentage absorbance per cm of wavelength ($\text{A}\cdot\text{cm}^{-1}$) can then be calculated by the software. An example graphical output of an FTIR profile for an SLA polymer is included in Figure G1.2 (Appendix G). The relative proportion of C=C bonds remaining in the exposed samples can then be compared to indicate the influence of hatch spacing/superposition on cross-linking. The results of this experiment are included in section 4.1.1.

3.3.2. Form 1+ MFS test pieces (constructed with MFLS without superposition)

To investigate the relationship between exposure and the minimum feature size, an experiment was devised to control the exposure by adjusting the scan speed of the Form 1+ of a test piece constructed from a single line pass to avoid the influence of superposition. A test piece (Figure 3.18) $90\mu\text{m}$ (W) x $100\mu\text{m}$ (H) x $2000\mu\text{m}$ (L) was designed using CAD and converted to an STL file.

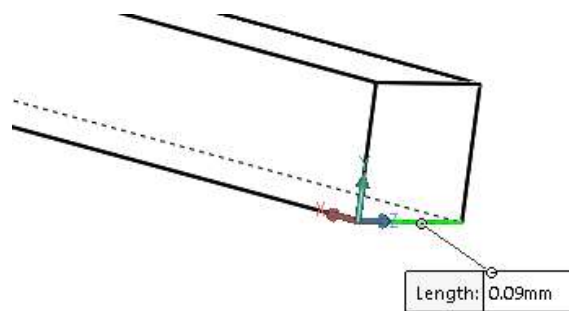


Figure 3.18: 90mm wide MFS test piece.

The design width of the test piece is significantly smaller than the quoted [39] minimum feature size for the equipment of $300\mu\text{m}$ and the $120\mu\text{m}$ line spacing in the control logic [150]. The height of the test piece is designed to equal a single layer thickness and thereby be constructed from a single layer scan to avoid the influence of interactions from additional layers. The test pieces were constructed directly onto the build platform at a central position to achieve a normal AOI and minimise the distortion from reflectance, divergence and ellipticity. The test pieces were constructed at speeds of 50mm/s , 100mm/s , 200mm/s ,

400mm/s, 600mm/s, and 800mm/s, with a laser power setpoint of 48mW, by adjusting the settings in the control logic.

Three test pieces were constructed at each speed and washed with IPA upon completion. Due to the size of the build platform and to avoid damage during transfer to a microscope slide, the test pieces were each measured at three locations using digital callipers (accuracy $\pm 10\mu\text{m}$). The results of these measurements are reported in section 4.1.2.

3.3.3. Form 2 calibration test pieces

Three sets of test pieces were used for calibrating the Form 2 model (3.2.9.2). A dedicated set of test pieces were constructed for the case with MFLS without superposition as described in section 3.3.3.1 below. The centrally located (0mm) test pieces constructed as part of the lateral distortion tests in section 3.3.4.2 were used for the two additional cases. These being with MFLS and superposition (section 3.3.4.2 part A), and single layer scan with superposition (section 3.3.4.2 part B).

3.3.3.1. Multiple first layer scan test piece without superposition

Three MFS test pieces ($90\mu\text{m} \times 100\mu\text{m} \times 2000\mu\text{m}$) shown previously (Figure 3.18), were constructed using a Form 2 SLA machine at default settings and measured following the process for the Form 1+ (section 3.3.2). Upon completion, the test pieces were washed with IPA and measured using digital callipers and the results included in section 4.1.3.1.

3.3.4. Lateral distortion tests

Lateral distortion tests were conducted on the Form 1+ (3.3.4.1) and Form 2 (section 3.3.4.2) SLA machines to quantify the influence of distorting effects as the beam's AOI changes across the platform. A series of test pieces were constructed using each machine to allow comparison of the lateral distortion predicted by the calibrated model with that generated in practice.

3.3.4.1. Form 1+ lateral distortion test with multiple first layer scan test piece with superposition

Test pieces 1mm (W) x 0.1mm (H) x 20mm (L) were designed in CAD. The test pieces were arranged for construction at locations 20mm, 40mm and 60mm either side of the build area's centreline and built directly onto a polycarbonate (Lexan™ 9030) substrate to ease removal and subsequent measurement of the array. The polycarbonate was washed with IPA, wiped with a lint free clothe and allowed to air dry before use. Polycarbonate was

selected due to it possessing the same refractive index [54] of 1.61 to the photopolymer [114] to avoid reflections being generated at the interface of the two mediums and allowing reflections from the build platform to be transmitted into the photopolymer. The polycarbonate was secured to the build platform using PVC tape and a 0.7mm vertical Z-offset was applied in the operating system to compensate for the thickness of the substrate. Three sample arrays were sent for construction at scan speed settings of 50mm/s, 100mm/s, 200mm/s, 300mm/s, 400mm/s, and 800mm/s. Upon completion the substrate was removed from the platform, the test pieces washed with IPA, and the array measured on the substrate using an optical microscope. The results of these tests are presented in section 4.1.2.2 and discussed in section 5.1.4.

3.3.4.2. Form 2 lateral distortion tests

To measure the lateral distortion across the Form 2 build area, two sets of test arrays were constructed as described in Part A and part B below. Both test arrays were washed with IPA and measured using optical microscopy. The microscope calibration was checked at the beginning of each measurement batch and the results included in section 4.1.3.2 and used for analysis in 5.1.4.3.

A. Lateral distortion tests with multiple first layer scans and superposition.

An array of 1mm (W) x 0.1mm (H) x 20mm (L) test pieces that were arranged at locations 15mm, 30mm, 50mm and 70mm, either side of the build area's centreline. The array was constructed and measured using default machine settings with 100µm layer thickness. A polycarbonate substrate was used for the reasons explained in section 3.3.4.1 and applying the same method to accommodate the material.

B. Lateral distortion tests with single layer scans and superposition

To avoid multiple first layer scans, while maintaining the influence of superposition, an array of test pieces 1mm (W) x 5.5mm (H) x 20mm (L) was designed in CAD. These were constructed onto polycarbonate at the same locations as in part A, with default settings (100µm layer thickness). The last layer of construction at the top of the test pieces was then examined under an optical microscope.

3.3.5. Refraction

To measure the distortion due to refraction, an array of 21 x 21, 3mm diameter buttons pitched at 3mm with a total design width of 123mm x 123mm was generated in CAD (Figure 3.19).

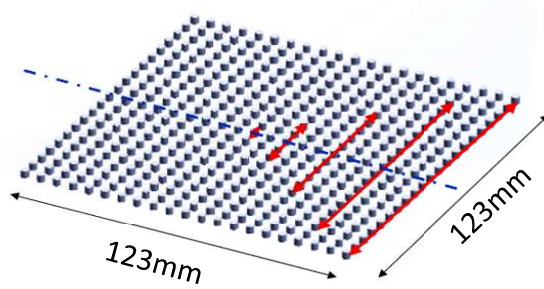


Figure 3.19: CAD image of refraction array.

The array was constructed onto polycarbonate with default settings with a 0.7mm Z-offset applied using a Form 2 and a Form 3 SLA machine. By spacing the test pieces, the cumulative effect of shrinkage is avoided. The substrate allows removal of the entire array from the build platform for ease of measurement and storage. The constructed array was then measured as described in section 4.1.3.5 together with the results which are discussed in section 5.1.6.

3.3.6. Reflectance

It has been identified through modelling in section 3.2.10 and reported in 5.1.5.3, that reflectance on the Form 1+ will only produce significant spurious curing on silicon nitride, at the exposures produced with scan speeds below 200mm/s. Consequently, experimentation is only conducted up to this speed. At these high exposures, and with light incident at oblique angles, there is the risk of laser overshoot. This occurs when the beam passes through the construction and cures residual resin on the substrate (Figure 3.20). This is not normally a concern as SLA parts are typically constructed onto supports.

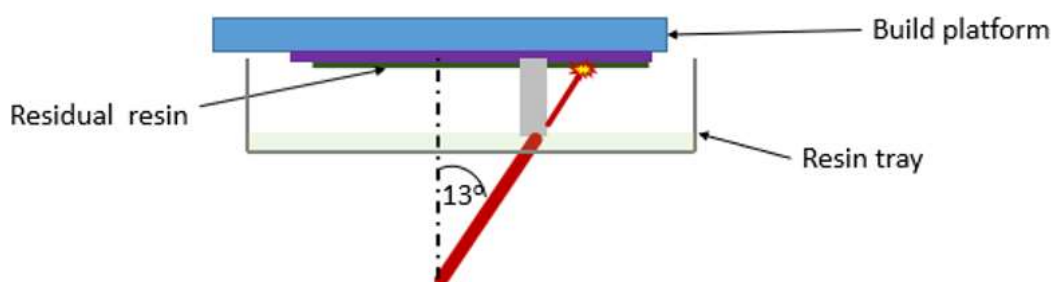


Figure 3.20: Laser overshoot.

However, the first layer of construction is the most likely to experience the effects of reflectance due to MFLS and reflections being rapidly attenuated by the photopolymer, and consequently is of the greatest interest for this investigation. There is concern that any spurious curing from laser overshoot will be difficult to distinguish from that caused by

reflectance. Therefore, to avoid laser overshoot, a test has been devised using samples less than 100 μm tall (i.e., 1 layer thickness) by 1000 μm wide and 2000 μm in length.

3.3.6.1. Form 1+ reflection experiment settings

The reflectance experiments described in sections 3.3.6.2 and 3.3.6.3 are performed on the Form 1+ SLA machine. The experiments are conducted default machine settings except for the perimeter line spacing and power settings being adjusted to 90 μm and 62mW to be consistent with the settings for the fill pattern (Figure 3.3). This allows uniform superposition to be applied for the purpose of modelling. Other settings adjusted are the Z-offset and the scan speed to vary exposure as stated in the respective sections.

3.3.6.2. Experiment with and without reflection

This experiment was devised to allow constructions onto the reflective surface of silicon nitride to be compared with an unreflective surface. To reduce the potential variance due to the inconsistent surface of the build platform an unreflective substrate was prepared. This was achieved by backing polycarbonate (refractive index [54] of 1.61) with pigmented (black) PVC (refractive index [54] of 1.56). Due to the refractive index of the photopolymer [114] (1.61), the polycarbonate and PVC being almost identical, the beam will be transmitted through the interfaces with minimal reflectance and attenuated by the pigmentation in the PVC. This serves to shield the photopolymer from reflections. A polycarbonate window of thickness 0.7mm is prepared by cutting a 130mm (L) x 20mm (W) section, washing with IPA and allowing to air dry. The polycarbonate is then placed directly onto the build platform with the PVC adhered to the underside to provide a smooth surface on which to construct the 1mm (design) wide test pieces as described in section 3.3.2). These are position at lateral locations; -60, -40mm, -20mm, 0mm (centre), +20mm, +40mm and 60mm relative to the centre of the build area. The Form 1+ build platform is adjusted to a 0.8mm Z-offset to accommodate the thickness of the sample (PC and PVC). In parallel, the 1mm wide test pieces are constructed directly onto silicon nitride strips prepared as described in section 3.3.6.3 and a 0.5mm Z-offset applied.

3.3.6.3. Experiment with and without reflection in parallel.

At scan speeds up to 200mm/s used for investigating reflectance (section 3.3.6) the beam is susceptible to distortion (section 5.1.4.1). Additionally, the distorting effects of divergence, ellipticity, and reflectance are all a function of the AOI. These characteristics are difficult to separate to determine the spurious curing produced from reflectance alone. Moreover, the experiment conducted on individual test pieces (section 3.3.6.2) may be susceptible to changes in environmental conditions or fouling of surfaces in the light train (Figure 3.9).

Therefore, to reduce the potential for variance, the experiment in section 3.3.6.2 was developed further to capture spurious curing on samples, with and without reflectance, simultaneously.

A silicon nitride wafer is cut into strips approximately 7mm wide by 20mm long using a diamond scribe, to serve as substrate samples. The substrate pieces are washed with acetone, followed by IPA (identified in 0), and allowed to dry in air. These are secured with PVC tape at intervals across the build platform at the same lateral locations described in section 3.3.6.2, as shown in Figure 3.21.

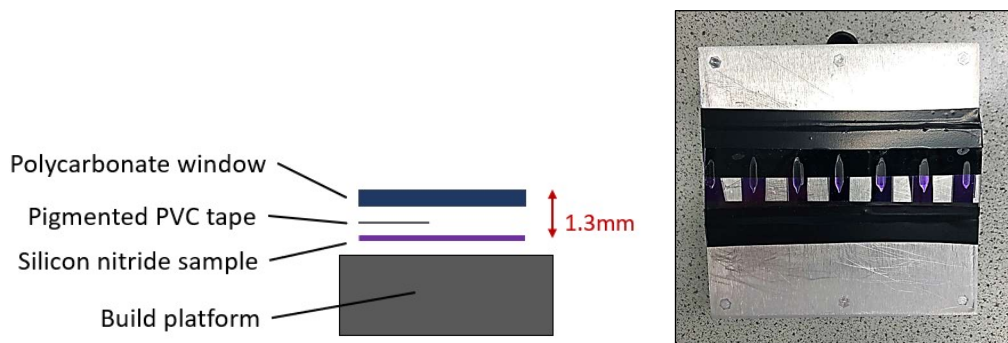


Figure 3.21: [Left] Form 1+ reflectance test sample arrangement. [Right] Reflectance test samples on build platform after construction.

A 10mm wide strip of pigmented (black) PVC is adhered to the underside of a 0.7mm thick polycarbonate strip cut to 130mm (L) x 20mm (W), washed with IPA and allowed to air dry. The PC is then located on top of the silicon nitride test array, so the individual samples overlap the PVC in the vertical plane as shown in Figure 3.21. As previously (section 3.3.6.1), this is done with the PVC on the underside to avoid a lip and produce a smooth surface for construction. The total thickness of the substrate materials in combination (Figure 3.21) is 1.3mm and greater than the maximum Z-offset permitted within the machine's standard operating options of 1mm. Consequently, to set the desired Z-offset, a python script [161] was downloaded and applied using a personal computer connected directly to the Form 1+ machine, as described in section 3.4.6.3, using a USB link.

The 1mm wide SLA test pieces described in section 3.3.6 are then constructed directly onto the polycarbonate surface. As explained in section 3.3.6.1, the photopolymer, polycarbonate and PVC positioned in-series produces an unreflective surface. Both portions of the test pieces are exposed to the influences of D&E to the same extent. Therefore, the effects of D&E can be discounted with the measured difference in the CLW attributed solely to reflectance from the substrate.

The constructed test pieces are then measured at consistent points at 100 μm and 200 μm , either side of the transition point (Figure 5.29) of the PVC and an additional measurement of the exposed portion at 700 μm . By using the PC backed with PVC, the portion of the test pieces constructed above the silicon nitride samples will be exposed to any potential reflections and associated spurious curing. This can be quantified by direct comparison with the portion constructed above the unreflective PVC. The process is conducted at construction scan speeds of 50mm/s, 100mm/s, and 200mm/s. An example of the constructed test pieces with spurious curing evident is shown in Figure 5.29. The results from the separate (3.3.6.2) and parallel reflectance tests are presented in sections 4.1.4.1 and 4.1.4.2 and discussed in section 5.1.5.3.

3.3.7. Beam profiling

To characterise the distortion present in the beam (section 5.1.4.1), the intensity profile generated by the specific Form 1+ machine used for the current investigation was recorded. This was achieved using a V-PCI Ophir beam profiler attached with an attenuating 0.2 Neutral Density filter. The profiler was positioned centrally within a clean resin tank, with the lens facing downwards towards the optics of the SLA machine. A diagnostic function within the Form 1+ control logic was run to produce a laser spot located centrally within the build area and where the profiler was positioned. The profile of the beam was recorded using Spiricon's Beamstar software and transferred into MATLAB following the process described in section 3.2.11. The recorded beam profile is discussed in section 5.1.4.1 and used to support analysis of the reflectance experiments in section 5.1.5.3.

3.4. Adhesion experimental methods

To identify an effective process to promote the adhesion of SLA products on to silicon nitride, the active adhesion mechanisms, and methods to enhance them, are to be investigated. The five adhesion mechanisms identified by Professor Abbott [63] have been considered in the review of literature (section 2.4.2). The intermingling/entanglement mechanism is discounted due to the inability for polymer chains to penetrate the surface of substrates to be used in this study (i.e., polycarbonate, glass, aluminium, and silicon nitride). The remaining mechanisms of SFE, dissipation, structural interactions and chemical bonding will be explored to identify which is dominant and where there is potential for them to be enhanced.

The preferred method will then be applied to bond an SLA polymer to a silicon nitride substrate and tested for compliance with the industry standard MIL-STD-883K [83]. The steps followed in this investigation are summarised in Figure 3.22.

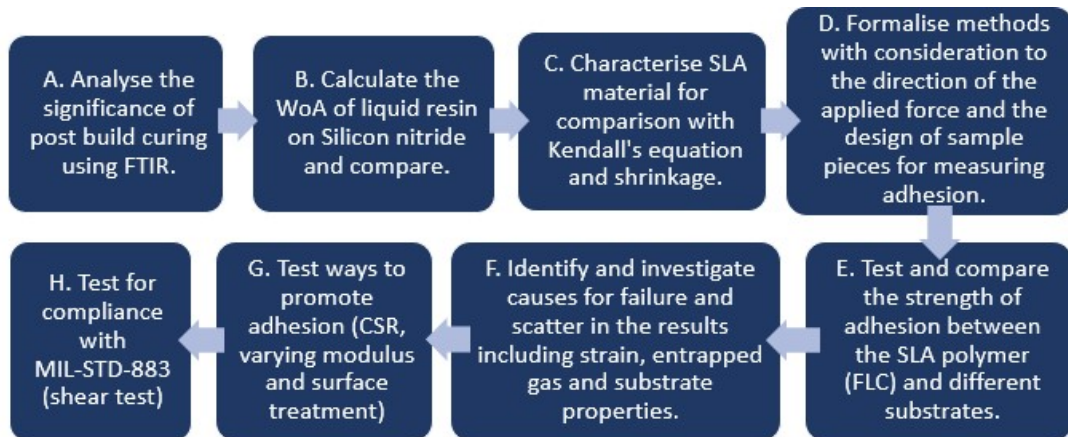


Figure 3.22: Flowchart for investigating adhesion.

- A. Analyse the influence of post build curing on the presence of C=C double bonds using FTIR to verify that there is significant variation from the PBC process used;
- B. Calculate work of adhesion of liquid photopolymer on silicon nitride and onto build platform for comparison;
- C. Characterise relevant properties (Poisson's ratio, elastic modulus and SFE) of the SLA photopolymer. Using Kendall's equation, calculate the significance of the SFE mechanism and determine whether it is an effective means to promote adhesion for compliance with the MIL-STD-883 standard;
- D. Develop suitable test methods for testing adhesion in SLA and for comparison with the aforementioned standard;
- E. Using the methods identified in stage D, measure and compare the strength of adhesion of SLA test pieces constructed onto silicon nitride and other substrate materials;
- F. Identify and investigate causes for failure and scatter in results including entrapped gas, substrate consistency and in particular the influence of strain;
- G. Devise and test methods to enhance adhesion including using CSR and varying the elastic modulus to promote dissipation. Other methods to be considered include the promoting chemical bonding through surface treatments;
- H. Test compliance of the preferred method identified in stage G. with the MIL-STD-883 standard.

3.4.1. Post build curing

The influence of shrinkage (2.7.3) and exposure (exposure 2.4.5) have been identified to influence both distortion and adhesion. As per stage A of Figure 3.22, the objective of this exercise is to validate the use of the Formlabs' cure oven as a reliable process to control the extent of cross-linking (cure) after construction. This will be measured using FTIR as described in section 3.3.1.

5mm x 2mm sample discs were constructed from Formlabs' clear photopolymer using a Formlabs Form 1 SLA machine. Following construction, the samples were washed with IPA to remove residual resin, air dried and wrapped in aluminium foil to prevent exposure to environmental light. Four samples were then positioned on a microscope slide which was placed on a wire frame within a Formlabs' 405nm cure oven (Figure 3.23). To minimise variations due to temperature [162], the PBC temperature recommended by the photopolymer supplier [163] of 60°C was used. Each batch of samples was cured for durations of 0, 4, 8, 12, 15 and 30 minutes. The samples were transferred to a Perkins Elmer FTIR for analysis. The process described in section 3.3.1 was then followed to obtain the relative area of the peaks recorded at wavenumbers 1637 and 1407.



Figure 3.23: Formlabs' cure oven [164]

3.4.2. Characterising the SLA photopolymer

Kendall's [65] model (Equation 2.8), will be used to determine the significance of the SFE adhesion mechanism. The model is derived [59] from the deformation of the material interface under load and an energy balance between the elastic energy stored by the deformed material, the W_oA , and the potential energy of the applied load. This determines when the requirement for separation is satisfied according to Equation 2.5 and demonstrates an increasing separation force with modulus.

Each of the material properties; WoA (section 3.4.2.3), Poisson's ratio (3.4.2.6) and elastic modulus (section 3.4.2.5) required to apply the model will be characterised for the SLA photopolymer under test (Formlabs clear). Additionally, methods to characterise the shrinkage and corresponding strain produced during curing in the Formlabs cure oven (section 3.4.1) are described in sections 3.4.2.8 and 3.4.2.7 respectively.

When a liquid changes phase to a solid, its surface energy can increase because the free space between the molecules reduces and so the density increases as does the concentration of active free sites (bonds) at the surface. Additionally, the change in geometry has an influence because internal cohesive forces within a liquid causes the free energy at the surface (the surface area for a given volume) to be minimised causing droplets to possess a characteristic pendant shape. Whereas solids which have molecules locked in position, can have a much higher surface area. Consequently, the surface energy of the SLA photopolymer is expected to increase when transitioning from a liquid to a solid during curing. Further curing a solidified photopolymer (i.e., during PBC) may influence the availability of active surface sites at the surface. Any change in surface energy (section 2.4.5) as a photopolymer transitions from a liquid to a solid and subsequently during PBC will influence the attractive force and the strength of adhesion. Consequently, the potential for SFE to change during solidification and progressive PBC is to be measured using the method described in sections 3.4.2.2 and 3.4.2.4. Similarly, the change in the elastic modulus of the SLA photopolymer with progressive PBC will also be characterised as described in section 3.4.2.5. These and the measured WoA (section 3.4.2.3) and Poisson's ratio (section 3.4.2.6) together with the tensile separation force (section 3.4.4), then allow comparison with Kendall's model (Equation 2.8) as discussed in section 5.2.4.

3.4.2.1. Consistency of substrates

Both the Wenzel and the Cassie Baxter liquid contact models (section 2.4.4) are a function of contact angle. Therefore, DSA can be used to indicate the consistency of the substrate's surface, as described in the following method. In turn this allows effective ways to prepare different substrate materials for subsequent experimentation, to be identified. The results of the DSA testing are presented and analysed in section 0.

Substrates of polished aluminium (3.4.3.1), polycarbonate (Lexan™ 9030), silicon nitride, and glass were prepared with 10 minutes of sonification in acetone and then manually washing with IPA. A separate batch of glass substrates were used as-received. Three additional batches of polycarbonate substrates were prepared; the first with the supplied protective film removed immediately prior to the DSA test, a second manually washed with

detergent and rinsed with water and the third with 10mins of sonification in IPA alone. All substrate samples were manually dried with a lint free cloth.

Samples of solidified photopolymer were prepared by constructing free-standing 20mm x 7mm x 1.5mm slabs on supports using a Form 2 machine with default machine settings and 100 μ m layer thickness. A separate batch of these samples were constructed directly (i.e., without supports) onto a smooth glass substrate secured to the build platform using adhesive tape and a Z-offset of +1mm applied to compensate for the thickness of the glass. The sample pieces were removed from the substrate using a blade and the underside of the samples which were in contact with the glass, used for subsequent analysis of surface energy (section 3.4.2.4).

TMSPPMA treated samples of soda lime glass were also prepared (method 3.4.6.1) to measure the consistency of the coating process. A series of six 10ml droplets of deionised water were deposited at regular spacing across the surface of each substrate sample using a 1.25mm OD / 0.95mm ID needle and the contact angle measured using a Kruss DSA100S machine. The contact angle was recorded using the Kruss imaging software and the standard deviation (STDV) between the samples calculated.

3.4.2.2. Interfacial tension

The surface energy of the liquid SLA photopolymer was measured to allow subsequent calculation and comparison of the work of adhesion on the aluminium build platform, and silicon nitride.

DSA (Drop Shape Analysis) was performed using a Kruss GmbH DSA100S machine. 10 μ l pendant droplets of Formlabs' clear photopolymer and water for comparison were suspended from a 1.25mm OD / 0.95mm ID needle. The IFT measurement procedure described in Kruss operating manual [165] was then followed. The dimensions of the droplet were measured using the Kruss imaging software and the IFT calculated by Kruss DSA software using the Laplace method.

3.4.2.3. Work of adhesion (liquid)

10 μ l droplets of Formlabs' clear photopolymer and water were deposited on glass slides and the polished surface of a silicon nitride wafer. The left and right sessile droplet angles formed with the substrate were then measured using the Kruss imaging software. Examples of the measurement process for sessile and pendant droplets, are shown in figure I1 (Appendix I). The work of adhesion for the liquid photopolymer onto substrates of glass, PC, and aluminium (plate) and silicon nitride was calculated using the Young-Dupre method [96].

3.4.2.4. Surface free energy

A 30mm x 7mm slab (FLC photopolymer) was constructed onto a glass substrate using the method described in section 3.4.2.1, using a Form 2 SLA machine and Formlabs clear photopolymer. The default machine settings, with 100 μ m layer thickness and a 1mm positive z-axis offset were applied to compensate for the substrate's thickness. The sample pieces were then removed from the substrate with a blade, washed with IPA, air dried and wrapped in aluminium foil to minimise additional exposure. Each sample was individually placed on a transparent glass microscope slide and positioned in a Formlabs cure oven (Figure 3.23) preheated to 60°C on top of wire frame brackets. The samples were then cured for periods of; 0, 4, 8, 12 and 15 minutes. 10 μ l droplets were deposited on the smoother and more consistent (3.4.2.1) underside of the slab which had been in contact with the substrate. The Owens-Wendt [166] method was then applied to calculate the SFE of the surface using liquids (ethylene glycol and deionised water) of known polar, and dispersive components.

3.4.2.5. Elastic modulus

Sample pieces (Figure 3.24) consistent with ASTM D638 [167] were constructed with Formlabs clear photopolymer, using a Form 2 SLA machine with default material settings, and 100 μ m layer thickness. Upon completion, the samples were washed for 20 minutes in an agitated bath of IPA and air dried. A recommended number of five samples (ASTM D638), were then cured in a Formlabs cure oven on a purpose made platform (Figure 3.24), for 0, 4, 8, 15 and 30 minutes at 60°C. Immediately after curing, the samples were stored in aluminium foil to minimise exposure to light. The relevant dimensions [167] of each test piece were measured using callipers before being clamped in a Stable Microsystems Texture Analyser (TA) machine (Figure 3.24). The TA machine was then programmed to measure the stress and strain of the test pieces at 0.2mm/s (ASTM D638) of travel until breakage.

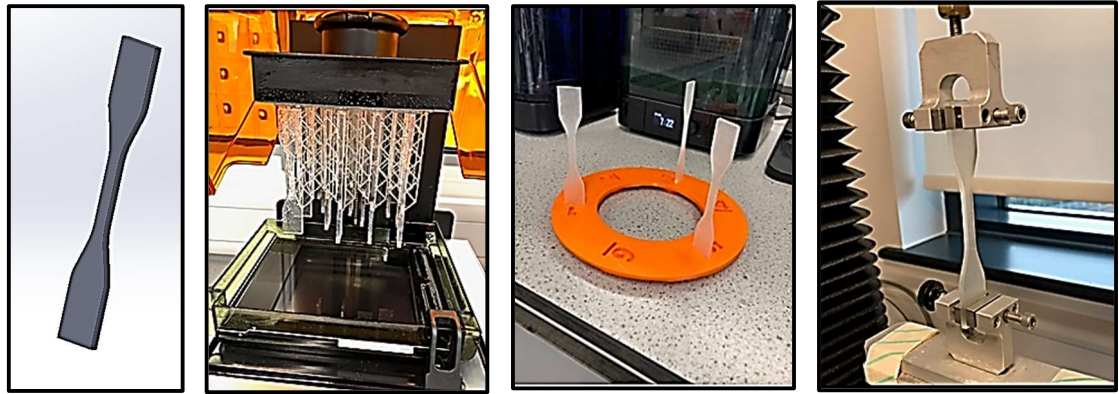


Figure 3.24: Construction of ASTM D638 test pieces

[Left to right] A: ASTM D638 test piece in CAD; B: test pieces constructed on a Form 2 SLA machine; C: a purpose made stand for curing ASTM D638 test pieces; D: A D638 test piece being tested in a Stable Microsystem Texture Analyser machine.

3.4.2.6. Poisson's ratio

The Poisson's ratio of the SLA polymer was measured using an Imetrum gauge optical extensometer with 3 test pieces at each of the cure durations: 0, 4, 8, 15, and 30 minutes.

ASTM D638 Test pieces (Figure 3.24) were clamped into the equipment and a digital image taken of the sample piece. The extensometer was then programmed to travel in the vertical direction at a rate of 0.2mm/s. An optical sensor then tracks a grey scale pattern relative to a reference point in the X-Y axes on the sample. The vertical and horizontal distortion is measured to provide the strain and Poisson's ratio respectively by the proportional change in the pixel co-ordinates of the targets. The maximum tensile force which the sample withstands before breaking, is also recorded.

3.4.2.7. Shrinkage and strain

As described in section 2.7.3, the free volume of an SLA photopolymer decreases during crosslinking and PBC resulting in shrinkage. This shrinkage imposes a lateral force at the interface with the substrate, resulting in stress and strain. To quantify these characteristics generated by shrinkage during PBC, and its potential influence on the strength of adhesion, the following suite of experiments were devised.

The default shrinkage allowance in the Form 1+ control logic for the FLC photopolymer used is 0.8% [150] (Appendix F). Consequently, a BF350-3AA (350 ohm) strain gauge with an operating range of 2% strain as quoted by the supplier's technical data sheet, was selected to measure the strain due to shrinkage during PBC.

A strain amplifier module (type HX711) was connected to an Arduino Uno processor (Appendix I Figure I3.1) together with a BME 280 (Appendix I Figure I3.2) to measure temperature, pressure, and humidity. The Arduino unit was powered by a USB 2.0 type

A/B which also allows direct connection to a laptop computer. Data obtained by the Arduino unit is stored on an SD card reader and connected as shown in Appendix I Figure I3.5 and can be displayed via the connected computer.

The Arduino unit is programmed using C++ programming language. Standalone programmes to operate single strain gauge, BME280 chip, SD card, gauges arranged in a Wheatstone bridge, and to calibrate the active gauge were downloaded from the Arduino [168] libraries. The programmes were then manually integrated and compiled to form a functional parent programme.

A glass substrate was secured to a build platform using adhesive tape (Figure 3.25). The strain gauge was detached from the amplifier and the enamel coating on the gauge's tail wires removed with a blade to aid electrical contact. The gauge was then adhered to the substrate by IFT with a droplet of liquid photopolymer dispensed with a pipette.

A 7mm x 20mm x 1.5mm slab with a 3mm diameter eye (Figure 3.25) to allow connection to a force meter, was constructed directly onto the strain gauge. After construction, the slab with the embedded gauge, was then removed from the substrate, using a blade, and manually washed with IPA to give a test piece shown in Figure 3.25.

The HX711 calibration programme was uploaded to the Arduino processor and ran with a known force of 10N applied to the test piece via the connecting eye (Figure 3.25) and the calibration coefficient adjusted in the programme until a value of 1000 was obtained.

The turntable was removed from a Formlabs cure oven and the amplifier module, embedded active gauge and the BME 280 chip were placed within the cure oven. Grease (Magnalube™ PTFE) was applied to the contacting faces of the sample pieces to ease their motion and avoid residual photopolymer from adhering to the cure oven floor. The processor board was connected to a PC via the USB interface and the cure oven operated for a prolonged period. Data was logged locally on the SD card and displayed via the PC.

The results from the gauges operated individually are included and analysed in section 4.2.4. These show the heat generated by the operation of the cure oven causing thermal expansion of the test piece which counteracts the strain due to shrinkage. Consequently, the same process was used to construct a reference SLA slab with three embedded strain gauges to serve as the compensating legs of a Wheatstone bridge. That slab was subsequently cured for 60 minutes to substantially cure the photopolymer, and the embedded gauges soldered to a stripboard (RS™) in a bridged arrangement (Appendix I Figure I3.3). The connecting wires of the active strain gauge were then connected via the stripboard to the amplifier (Appendix I Figure I3.4) to complete the Wheatstone bridge, and in turn to the

Arduino processor (Appendix I Figure I3.3). The reference slab (with the compensating legs embedded) and the test slab (with the active gauge embedded), were again greased and placed in the cure oven with the associated equipment as previously.

Construction stages of strain test pieces

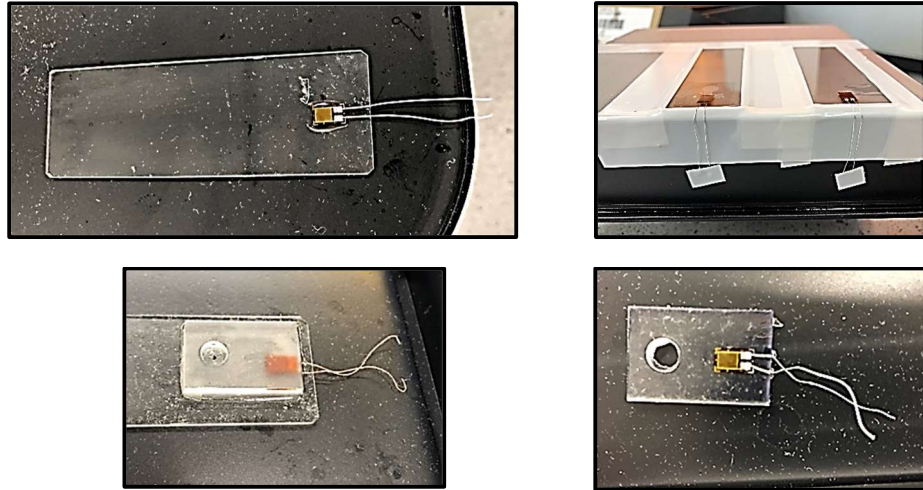


Figure 3.25: Construction of embedded strain gauges

[Top left] (left) Strain gauge on a glass substrate adhered with photopolymer, [Top right] Strain gauges adhered to a glass substrate which are in turn secured to a build platform using adhesive tape. [Bottom left and right respectively] An SLA test piece with strain gauges secured onto the surface before and after removal from the substrate.

Two sets of strain tests were conducted as follows:

- a) A series of tests using an embedded strain gauge without temperature compensation at progressively longer periods of cure from 2 to 12 minutes in increments of 2 minutes, and cured at ambient temperature (i.e., with the cure oven heater turned off). The gauge output from these tests could then be related to the shrinkage measured manually before and after PBC using the method described in section 3.4.2.8.
- b) Due to the tests conducted in part a) being heavily influenced by temperature (section 4.2.4), three further tests were conducted using the Wheatstone bridge arrangement. These were performed continuously for a minimum of 20 minutes. The resulting strain data (section 4.2.4) is discussed and compared with manually measured shrinkage in section 5.2.7.1.

3.4.2.8. Manually measuring shrinkage

In addition to automated continual measurement of strain described above, the longitudinal dimensional change due to shrinkage was also measured. Test pieces with dimensions 24mm x 16mm x 3.2mm and the same thickness as the ASTM D638 (modulus) test pieces were constructed on a Form 2 SLA machine using default settings and 100 μ m layer

thickness. These were then greased (Magnalube PTFE) on the contacting face and placed in the Formlabs cure oven (section 3.4.1) with the heater turned off. The test pieces were then removed from the cure oven, after periods of 2, 4, 8, 12, 15 mins and in increasing increments of 5 minutes thereafter, up to 45 minutes. Upon removal, the samples were stored in the dark to cool, after which their length was measured at 5 locations. The same process was applied to measuring the shrinkage of a series of embedded gauges in section 3.4.2.7 test set a). The shrinkage measured is reported in results section 4.2.4 and related to the measured gauge strain in section 5.2.7.2 to obtain the stress profile during PBC. This is discussed in section 5.2.7.1 and compared with the stress at separation measured in sections 3.4.4 (tensile) and 3.4.5 (shear).

3.4.3. Building onto substrates

Following the characterisation of the FLC polymer and substrate materials, the process of constructing SLA products onto non-standard substrates is investigated. In addition to the cleaning practices discussed in section 3.4.2.1, other necessary substrate preparation methods are described in section 3.4.3.1. Practical considerations include alignment discussed in section 3.4.3.2 and securing the substrates for construction (section 3.4.3.3). Lastly, a method to section samples to examine the SLA/substrate interface is described in section 3.4.3.4.

3.4.3.1. Substrate preparation

Substrate materials used during this study include soda lime glass, aluminium (grade 1050), silicon nitride, and polycarbonate, the properties of which are detailed in section 3.1. For consistency, ease of handling and compatibility with the test equipment, aluminium and polycarbonate substrates were cut to the same width and length as the glass substrates (26mm x 76mm). Unless otherwise stated, samples of silicon nitride were cut from 100mm diameter wafers using a diamond scribe to widths of 26mm while the length is dictated by the profile of the wafer.

No mechanical polishing of polycarbonate, silicon nitride or glass substrates was performed. Rudawska [102] explains that; "Currently, there exists no European Standard for surfaces preparation with wet abrasive methods." Therefore, nine aluminium sample pieces were adhered to a metal block (100mm x 40mm x 40mm) using crystal bond mounting wax, (Buehler.GmbH). The substrates and block were heated on a hot plate set to 100°C, a thin layer of wax applied, and the block and substrates contacted together and cooled. Samples were first manually polished using a with a coarse grit to even the surface

and subsequently polished using Kamet rotary table mounted polishers with 6 μ m and lastly 1 μ m grit size. The substrate was then washed with detergent and cotton wool.

As described by Rudawska [102], roughness will influence the quality of contact and the corresponding adhesion. Therefore, the surface roughness of the respective substrates was then measured using an Ametek Zygo 8300 coherence scanning interferometer and included in section 4.2.1.4.

3.4.3.2. Alignment

Following the review of literature (section 2.7.4) a manual measurement method was considered the most effective to align the construction and the substrate and avoids the need to modify the equipment. To determine the relative position of the build platform and the software's build area, the build platform was measured using callipers to be 144.5mm x 144.5mm. The Preform™ software divides the x-y area of the build platform into a build area of 14 x 14, 10mm squares (Figure 3.26). Thereby leaving a total margin of 4.5mm in the X and Y dimension of the platform. To centralise the build area relative to the build platform, a small slab was designed using CAD software and converted into an STL file. This was positioned in the extreme top left of the Form 2 build area (Figure 3.26) using the Preform software as shown in Figure 3.26. The margin distances in the X and Y dimension between the edge of the slab and the build platform was measured using callipers and the X and Y offset of the machine adjusted. Once this margin had been calculated and the build area centralised, substrates can then be precisely located relative to the laser's point of incidence, using a ruler or callipers.

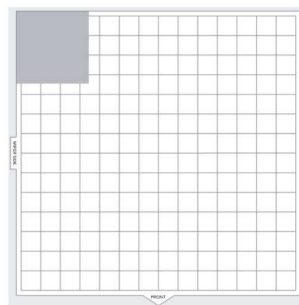


Figure 3.26: The Form 2 build area as shown in the Preform software.

3.4.3.3. Securing non-standard substrates for construction

Soda lime glass microscope slides 26mm x 76mm x 1mm, as described in section 3.1, were identified for use as a test substrate. To accommodate the thickness of the glass and avoid potential clashing between the sensitive coated surface of the resin tank and the slide, a +1mm offset in the z-plane was applied to the Form 2 machine to compensate. An array of

test pieces consistent with the geometries described by Tehrani [36] were designed using Solidworks™ CAD and converted to an STL file.

Due to the issues observed and discussed in section 2.3, a vacuum chuck, as used by Tiedje [10] to secure a substrate to the build platform has been discounted. Other methods were considered as reported in Appendix E with the process of securing substrates to the build platform using adhesive tape (Figure 3.27), similar to the method described by Malengier [43], being preferred.

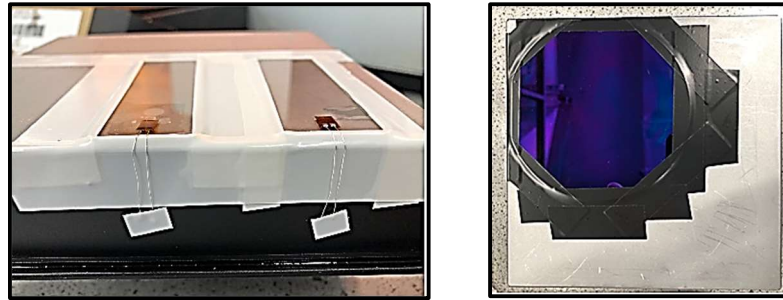


Figure 3.27: Glass [left] and a silicon nitride wafer [right] secured to the build platform using adhesive tape.

The build platform was prepared by washing with acetone, a +1mm Z-offset applied and adhesive tape used to adhere the slides to the build platform. The machine was operated with default settings and initially 100 μ m layer thickness and subsequently 25 μ m. The products were then observed using an optical microscope.

The test pieces were then constructed directly onto a silicon nitride wafer (section 3.1) with the polished surface exposed, using the same process with an appropriate Z-offset. The wafer was attached to the build platform with adhesive tape, and the vertical layer resolution set to 100 μ m. On completion of the build, the wafer was easily removed from the build platform, and both were cleaned with acetone and IPA. The test pieces were washed with IPA in an agitated isopropyl bath for 10 minutes.

3.4.3.4. Sectioning

For the purpose of examining the interface between an SLA polymer and a substrate, SLA slabs (10mm x 10mm x 2mm) were constructed onto PC using a Form 2 SLA machine and sectioned using a guillotine. The samples were then stud mounted so the cross-section could be viewed using an optical microscope. Subsequently, the samples were sputter coated with gold and examined using SEM, the resulting images of which are included in section 4.2.7.1.

3.4.4. Automated adhesion test rig (tensile tests).

An adhesion test was devised to measure the tensile separation force of SLA test pieces on different substrate materials. The rate at which energy can be stored or dissipated by a material will have a corresponding influence on the rate at which it is transferred to the interface. Therefore, as described in tensile test standards such as ASTM D1623-17 [169], the rate of travel of the ‘cross-head’ or lifting beam is kept constant to maintain consistency between tests. Consequently, to test the influence of PBC on adhesion, tensile tests were conducted using a Stable Microsystems +C Texture Analyser (TA) (Figure 3.30) to provide automated and controlled movement of a lifting beam, and record the applied force. The TA equipment was arranged with a 750kg load cell, the calibration of which was checked each test day, and operated in tensile mode with a travel of 0.2mm/s and a target distance of 10mm.

Test arrays consisting of five pieces (Figure 3.28) designed with lifting eyes, with a 1mm² (design) contact area and spaced at 10mm, were constructed onto aluminium, polycarbonate, and silicon nitride. The geometry of test pieces was kept consistent [102] to maintain a consistent transfer of stress to the interface. Following construction, the test pieces were washed manually with IPA using cotton swaps. The substrates, with the test arrays attached were then placed in a Formlabs cure oven (Figure 3.23), in an inverted position a wire frame platform, to maintain a consistent location and avoid pooling of any residual photopolymer at the base of the test pieces. The arrays were cured at 60°C for durations between 0 minutes (green), and 30 minutes. After curing, the test arrays were transferred to a sealed non-transparent storage container to avoid exposure to ambient light.

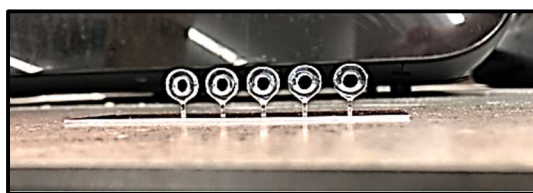


Figure 3.28: Adhesion tensile test array on aluminium

The TA sample mounting arrangement was modified (Figure 3.30) using threaded desk clamps to accommodate a bracket for holding the sample arrays. The bracket was designed using Solidworks CAD (Figure 3.29) and constructed using SLA on a Formlabs Form 2 machine.

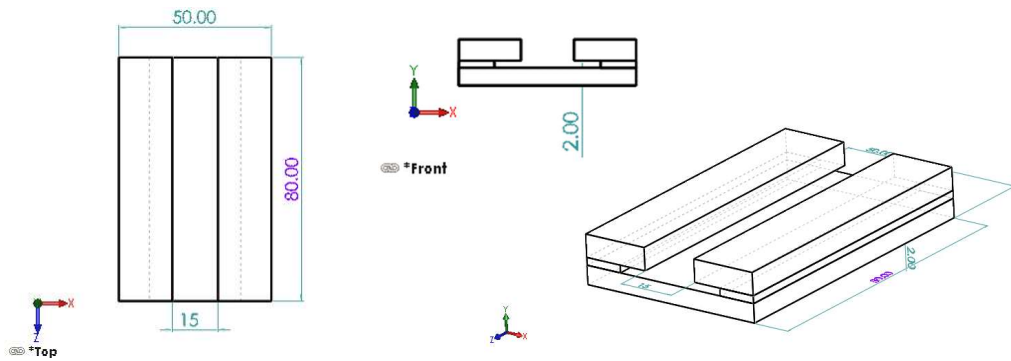


Figure 3.29: CAD drawing of sample piece mounting bracket for tensile adhesion tests.

The location of the bracket was set relative to the mounting plinth and marked to maintain consistency. It is important that tensile test pieces are aligned with the direction of force else torque or bending moments will result in imbalanced stress concentrations and premature failure. Alignment of the bracket with the lifting eye was set using a plumbline and again marked accordingly. The substrates are free to move along the length of the bracket (Figure 3.30) to allow the alignment of each test piece. The test pieces were connected to the lifting eye of the TA machine using a 2mm S-bolt (Figure 3.30 right). The force (N) at separation was then recorded in the equipment's Exponent™ software and included in the results section 4.2.2.

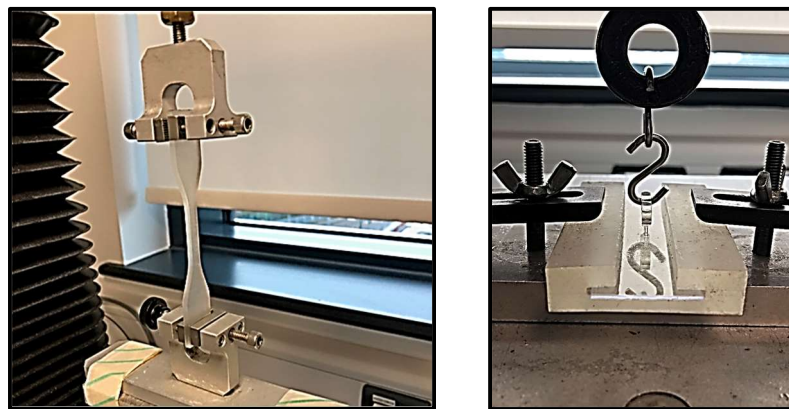


Figure 3.30: Texture Analyser arranged for tensile adhesion tests.
 [Left] Stable Microsystems TA.HD +C Texture Analyser with ASTM D638 modulus test piece
 [Right] Sample bracket and connection to TA machine for tensile adhesion test.

3.4.5. Shear tests

A shear test using the texture analyser equipment (Figure 3.30) was devised. A two-piece bespoke bracket was designed using CAD and constructed with SLA.

The bracket consists of a 100mm x 50mm x 5mm cover plate (Appendix I figure I2.1) and a 50mm x 80mm x 3mm back plate with a 0.5mm recess back plate (Appendix I Figure I2.2) to receive the sample substrates. A flip cap test accessory supplied by Mecmesin Ltd was

used as the test contact tool and connected to the load cell with using an adaptor coupling with an M12 thread. The bracket was stiffened using an aluminium backing plate through which 5mm through holes were drilled for 4mm, threaded bolts. The backing plate was made with a 20mm overhang to secure in a clamp with a micro thread. One side of the clamp's thread was adjusted to its limit of travel to maintain a consistency between tests and the clamp was secured to a purpose made adaptor plate using threaded couplings. The adaptor plate had 6mm holes drilled at pitch of 12mm to allow the offset between the contact tool (Figure 3.31) and the substrate to be adjusted and maintained at a constant distance once selected.



Figure 3.31: Shear test sample secured in TA machine for adhesion testing. [Left] Test bracket clamped on adaptor plate and secured to base plate, [Right] frustum test shear test piece on PC in place for testing.

Frustum and MIL-STD-883 test pieces described in sections 3.4.5.1 and 3.4.5.2, were constructed with their centreline at approximately 25mm from the end of the substrate to allow clearance for the frame of the bracket. A test sample and substrate were placed in the recess of the bracket with the cover plate secured using bolts and wing nuts (Figure 3.31). The bracket was then secured in the clamp and the height of the lifting beam adjusted to allow a few mm of clearance between the contact tool and the test piece. The lifting beam travel speed was then set to 0.1mm/s consistent with the process described by Szeto [81]. The force applied and distance travelled was recorded in by the equipment's exponent software. The results of these tests are presented in section 4.2.3 and discussed in 5.2.5.

3.4.5.1. Frustum test pieces

Frustum shaped test pieces consistent with the geometry described by Szeto [81] with a 9mm and 11.4mm diameter top and base respectively, 6mm high were designed in CAD and constructed directly onto substrates using the process described in section 3.4.3. Single test pieces were constructed onto polycarbonate, aluminium, and silicon nitride substrates. Silicon nitride substrates were cut to a maximum of 76mm length to fit in the recess of the bracket. The substrates were secured in the test bracket described in section 3.4.5.

3.4.5.2. MIL-STD-883 Test pieces

To be within the limit of the contact area covered by standard MIL-STD-883K test 2019-4 [83] of 5.5mm^2 , a test piece with dimensions $2.25\text{mm} \times 2.25\text{mm} \times 3\text{mm}$ to give a contact area of 5.1mm^2 was designed using CAD. To comply with the standard, a construction possessing this contact area is required to withstand a shear force of 49N (Appendix D). Test pieces were constructed using Formlabs clear photopolymer with default machine settings and $100\mu\text{m}$ layer thickness. Silicon nitride substrates were cut to a maximum length of 76mm, and the bracket lined with an EPDM gasket material to prevent the substrate from cracking. Shear tests were then conducted in sample batches of three and cured for 2 minutes, 8 minutes and the third left without post build curing.

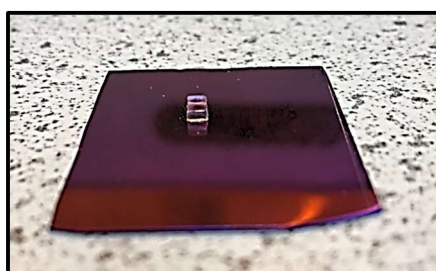


Figure 3.32: MIL-STD-883 test piece on silicon nitride

3.4.6. Enhancing adhesion

Methods identified to potentially enhance adhesion including the application of a monolayer (section 3.4.6.1), the addition of core shell rubber (section 3.4.6.2) and varying the elastic modulus laterally (section 3.4.6.3) are now explained in turn.

3.4.6.1. Application of a monolayer

As mentioned in section 2.4.5 the first layer in SLA constructions is often repeatedly scanned to increase exposure to promote adhesion. This may be influenced by the increase in elastic modulus or SFE with progressive curing as discussed in section 3.4.2.

Alternatively actinic interactions with the polymer may be progressing to form chemical bonds with the substrate. The potential to enhance adhesion by promoting the formation of covalent bonds between the SLA polymer and a silicon nitride substrate, via the chemical bond mechanism described by Zips [113] (section 2.4.5) is investigated. This was achieved by applying a monolayer to the substrate initially using glass samples as described in Table 3.2. These were prepared by washing with acetone followed by IPA and dried before being placed in a metal rack to allow increased exposure. The samples and rack were then positioned in a Diener plasma chamber. The chamber was purged with an oxygen flow, maintained at low pressure, and the system power set to 50W. The samples were then

exposed to plasma for 10 minutes and the chamber purged with air. On removal from the chamber, the samples were immediately immersed in a solution of 2% vol 3-(Trimethoxysilyl) propyl methacrylate (TMSPMA) in dry toluene, prepared at 50°C and stirred for 24hrs. The samples were then washed in acetone and dried at 50°C in a vacuum oven for a minimum of 24 hrs, where they were stored until use.

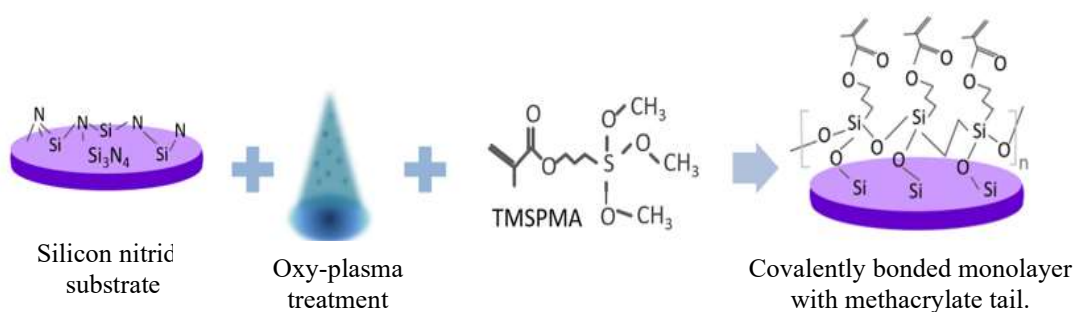


Figure 3.33: Pre-treatment process for silicon nitride with oxy-plasma and TMSPMA coating to promote adhesion.

Three coated samples were then adhered to a Form 2 SLA build platform for use as substrates onto which arrays of five, 0.85mm (CSA = 0.57mm²) adhesion test pieces were constructed. After construction, the arrays were manually washed with IPA using cotton swabs. Following the same curing procedure described in section H an array was cured for 4 minutes, a second for 8 minutes and a third was left without post build curing. For comparison, three separate arrays were constructed onto untreated glass, prepared by washing with the acetone, and cured for the same durations as the coated samples.

The strength of adhesion of all the test arrays was measured using a Solid Microsystems Texture Analyser following the procedure described in section 3.4.4. The results from this testing are presented in section 4.2.7.3 and discussed in section 5.2.8.3.

3.4.6.2. Core shell rubber

To explore the influence of the dissipation mechanism (section 2.4.2.5) on the adhesion between an SLA polymer and a substrate, core shell rubber will be added to Formlabs' clear (FLC) photopolymer using the method described in this section. The modified photopolymer was then used to construct frustum test pieces tested according to the process described in section 4.2.3, with the results included in section 4.2.7.1 and discussed in 5.2.8.1.

By adding CSR into the photopolymer, it is intended to increase the material's ability to dissipate crack energy. This is expected to be of greatest significance at higher levels of cure when the SLA polymer is more brittle.

The review of literature identified viscosity and the associated impact on recoating as a common limiting factor to the proportions in which filler materials (section 2.5.2 and specifically CSR [125] can be added to photopolymers. To characterise the influence of CSR on the SLA photopolymer viscosity, rheology measurements of the resin with increasing concentrations of CSR will be taken. The influence on adhesive strength will be measured using shear tests with incrementally increasing concentrations of CSR.

The volume of photopolymer used during construction in a Formlabs Form 2 resin tank was measured at 200ml by dispensing the contents into a 500ml measurement beaker. A range of 7.5% to 25% v/v was chosen to provide a similar range of filler concentration as used by others [123], [124] (section 2.5.2). The required volumes of paraloid BTA-751 CSR particles supplied by Dow Chemicals, to achieve the selected concentration range were then measured into a second measurement beaker and added to the 220ml of liquid photopolymer. This was manually stirred using a spatula for 3 minutes. Samples were deposited on the lower plate of a cone geometry in standard rheology machine (Kinexus Pro Malvern Instruments) in sufficient quantities to fully coat the plate with the gap closed to 0.15mm with any excess material removed with a cloth. The machine was operated in oscillatory shear mode with a shear rate sweeping through 0.01 to 1000 s⁻¹ and carried out at the SLA machine's (Form 2) operating temperature of 31°C and a total test time of 22 mins.

Suspension

The ability for the CSR particles to remain in suspension was assessed using the Navier-Stokes law applied to the settling velocity [170] (Equation 3.33).

$$V_t = \frac{gd^2}{18\mu} (\rho_p - \rho_m)$$

Equation 3.33: Stokes' law applied to settling velocity [170].

Where g is acceleration due to gravity, ρ_m is the density of the medium, ρ_p is the density of the CSR particle, μ is the viscosity of the medium and d is the particle diameter.

Due to the relative lower density of the CSR particles [148] to the photopolymer (section 3.1), the motion of the particles will be upwards. By inputting the material properties listed in section 3.1 the model indicates that the larger particle size range of 841 μ m (20 mesh) will move approximately 1 mm per minute (0.017mm/s). Given the build duration of the test pieces is approximately 40 mins, separation of the CSR in suspension could be expected without intermittent mixing.

Therefore, operating the SLA machine in open mode avoids automatic refilling of the resin tank with neat photopolymer and diluting the CSR mixture but also disables the wiper

function. Consequently, the machine will be operated in the standard closed mode to promote mixing during the construction to maintain the CSR in suspension. To avoid dilution of the CSR, the machine will be operated with an empty resin cartridge to pass the interlock and with a slightly overfilled resin tank to avoid the level sensor tripping the construction due to low resin.

Constructing with CSR in SLA

Three polycarbonate substrates were washed with IPA and secured to the build platform (section 3.4.3.3). Additional CSR/SLA photopolymer mixtures in proportions of 5%, and 15% v/v were formulated and dispensed into clean Form 2 resin tanks. These were inserted into the machine and 3 off frustum test pieces (3.4.5.1) constructed at each CSR concentration (5%, 7.5%, 15% and 25% v/v). Shear tests on the samples were then conducted following the method described in section 3.4.5.1.

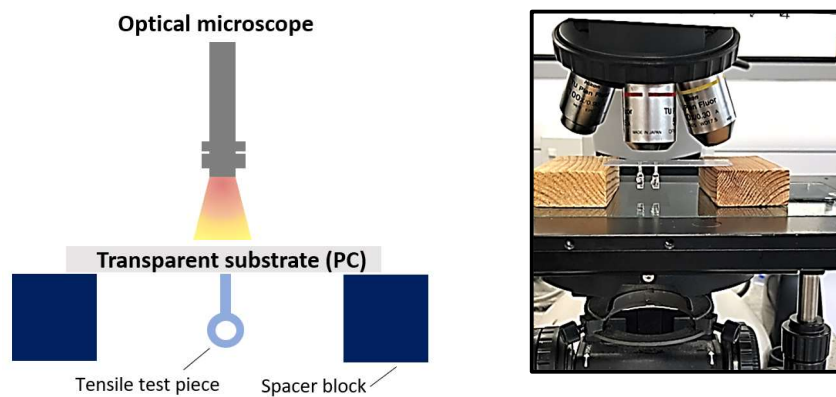


Figure 3.34: Mounting arrangement to observe interface using optical microscopy.

Sectioning

Frustum test pieces were constructed with 25% by volume CSR, cured for 30 minutes and wrapped in foil. A scalpel was used to score the samples across their diameter, which were then suspended in a polystyrene container with 1 litre of liquid nitrogen for 10 minutes. Upon removal, an impact force was applied to the wrapped samples with a chisel along the scored line and the sectioned samples examined under an optical microscope. The samples were then mounted on a pin stub with adhesive carbon tabs, sputter coated with gold for 15 seconds in a nitrogen atmosphere and examined under a scanning electron microscope (Hitachi TM3030).

3.4.6.3. Constructing shear test samples with varied cure

Test samples were constructed using varied lateral exposure by following the process summarised in Figure 3.37. Initially a python script (Image_to_laser_moves.py (ITLM.py) [171]) was imported into PyCharm editing suite for debugging and correcting compatibility

errors. A virtual environment was then generated for housing the script with connection to an appropriate operating structure and USB interfaces. The script (ITLM.py) varies the SLA laser power in each voxel in the build file to correspond to the contrast of the pixels in the 2D input image, for a single layer. The output was tested using a greyscale test image by lightburnsoftware.com [172] to produce a corresponding greyscale product (Figure 3.35). This demonstrates the increasing exposure delivered corresponding to the shading of the cell.

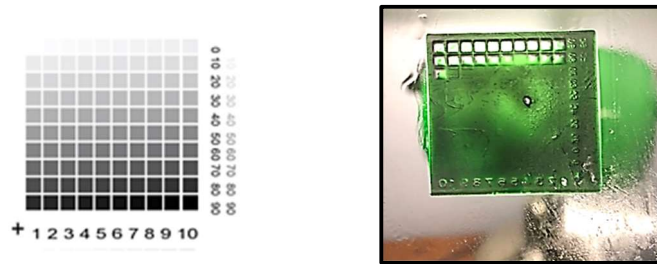


Figure 3.35: [Left] Greyscale test image by lightburnsoftware.com [172], [right] greyscale output showing varied lateral exposure.

A 2D image of a shear test piece with contrasting sections (Figure 3.36) was then generated in 3D Paint™. Black was scaled between 0 (black) and 255 (white) to produce the greyscale in MATLAB. The image was then imported, and the grey mid sections (Figure 3.36) set to a value of 64 to correspond to 75% of full-scale white providing a contrast ratio of 1.33:1. The output was then saved as a jpeg file and uploaded into ITLM.py to generate an FLP output file and sent to a Form 1+ machine via USB using a second programme (Print.py) by Ben Franztdale [171]. The product was then measured using callipers and compared with the pixel count in the MATLAB code at 3.5 pixels per mm. The MATLAB script was then scaled to adjust the image to equal the contact area dimension (11.4mm diameter) of the frustum test piece. To allow the same construction to be repeated for each layer, the test pieces were cylindrical as opposed to the frustum shape used previously. The output was then saved as a jpeg file. The ITLM.py programme then uses the jpeg image to generate an SLA build instruction file (.FLP) with 75% laser power (48mW) and 100% laser power (62mW) for the grey and black pixels respectively. This range is consistent with that used in the default control logic [150] and known to initiate curing. The resulting variation in exposure and cure, generates regions with corresponding variations in elastic modulus, with the aim being to promote energy dissipation based on the work by Fitton and Broughton [76] (section 2.4.5). Test pieces without the exposure varied (i.e., jpeg images of pure white) of the same dimensions were constructed in parallel for comparison.

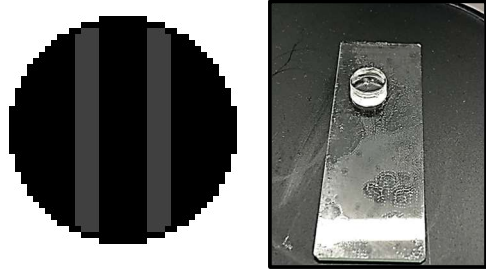


Figure 3.36: Greyscale shear test pieces for varying lateral cure.

A polycarbonate substrate was attached to the build platform following the process described in section 3.4.3.3. A third python open_FL programme (Z_jog) [161] was edited to remove the homing operation at the end of the script and initiate the peel process to begin by separating the build from the resin tank. This permits the position of the build platform to be set at a defined distance and allow the clearance between the substrate and the resin tank to be adjusted between each scanned layer of the FLP file. By resetting and incrementally decreasing the travel of the platform by 100µm between each scan, the corresponding layer thickness can be achieved. This process was repeated to form test pieces 6mm in height, in batches of 3. For consistency, the same geometries (11.4mm x 6mm) were constructed with standard exposure for comparison tests. The shear test procedure detailed in section 3.4.5.1 was then applied to measure the force at separation with the results presented in section 4.2.7.2 and discussed in 0.

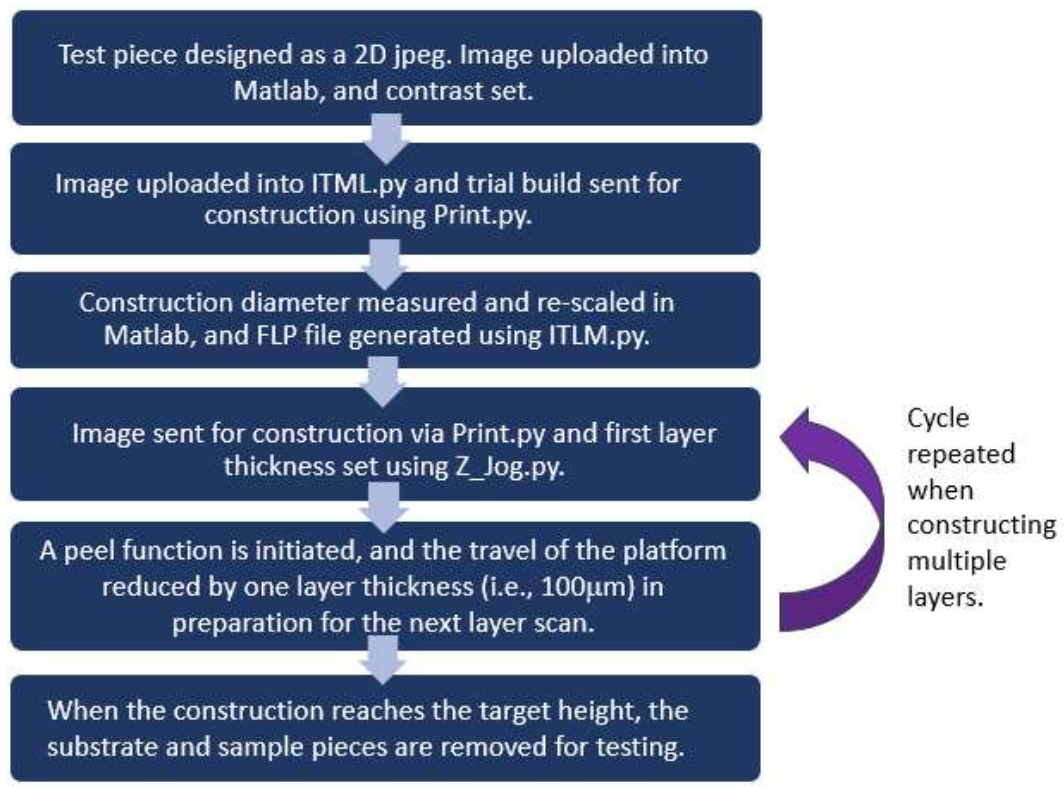


Figure 3.37: Flowchart for constructing test pieces with varied lateral cure.

3.5. Inserting geometries approach and methodology

Here, the ability to insert components into SLA constructions is investigated. When combined with the process to enhance adhesion explored in section 3.4.6. this will allow structural electronic packages to be constructed directly onto silicon nitride.

A process to embed components similar to that described by Tiedje [10] has already been demonstrated in section 3.4.2.7. The low profile (80µm) of the gauges, being less than a layer thickness tall, allowed the SLA part to be constructed directly on top of the component without having to design recesses to accommodate the component. Additionally, due to the component being secured to the substrate, the construction could proceed uninterrupted.

The next progression of the process is the ability to insert large, complex, and multiple components and arrange them in three dimensions. As explained in section 3.1, the process will use a single SLA machine as opposed to hybrid equipment. To achieve this, a direct interaction with the machine operating function with modified instruction code will be applied. The approach adopted draws upon previous work reviewed in section 2.2, in particular the use of adaptor pieces described by Kataria [13] and Liao [41] and expands on that conducted by Tiedje [10] using the same SLA equipment. The development process to insert demonstration geometries is to be approached in the steps described below:

- I. **Review of previous relevant work:** (completed as part of the literature review in chapter 2;
- II. **Identification of test pieces:** Identify and design of suitable adaptor pieces to demonstrate inserting geometries (large, and complex), and electrical components;
- III. **Stacking multiple components:** This step is conducted in two stages as described in stage A and B below with the results and observations presented in sections 4.3.2 and 4.3.3. These are discussed in sections 5.3.1 and 5.3.2.
 - A. **Stacked module concept:** Develop an SLA process to allow components to be stacked by integrating multiple packages.
 - B. **Inserting multiple stacked components:** Devise a method to incorporate large and complex inserts into the body an SLA construction as part of a single construction process;
- IV. **Connecting inserted components to form an SLA structural electronic package:** Design on an interconnector incorporating though vias for wiring, to connect multiple components electrically in an SLA structural electronic package. The results and observations from the associated experiments are presented in section 4.3.3 and discussed in section 5.3.3.

3.5.1. Step II. Identification of test pieces.

There are two requirements for the test geometries to be inserted. The first is to be large and thereby greater in height than a single layer (100 μ m) thickness. This introduces the challenge of designing the SLA construction to with suitable cavities into which large geometries can be inserted and how they are to be secured during the construction process. The second requirement is for them to possess a varied cross-sectional-area (complex). As described in the work by Liao [41] in section in section 2.2, this necessitates the use of suitably designed adaptor pieces. By calculation of the criterion value, the appropriate design of the adaptor piece, whether that be a single or two-part piece, can be identified. A piston geometry (Figure 3.38), and a replica of a TI (P82B715DRG4) semiconductor package (Figure 3.39) were chosen to satisfy these requirements and downloaded from the Stratasys [173] public library. Both inserts fit the criteria for complex geometries with criterion [174] values ($S < 0$), and require a two-part adaptor pieces. These were designed (Figure 3.38 and Figure 3.39) using the mould generation function in Solidworks CAD software.

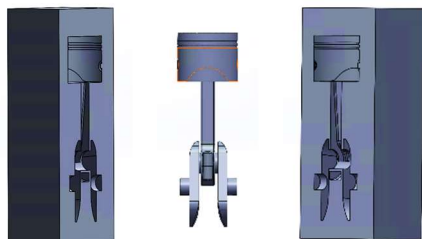


Figure 3.38: [centre] CAD image of piston insert geometry, [left and right] 2-part adaptor piece.

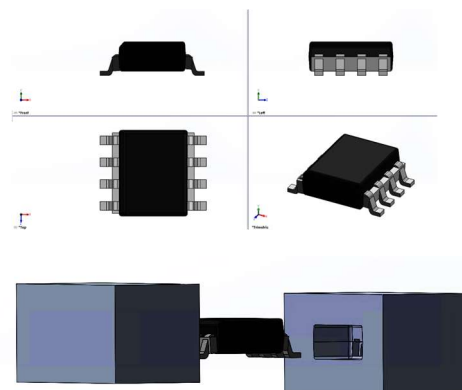


Figure 3.39: [top] TI semiconductor package (P82B715DRG4) insert, [bottom] TI chip insert with 2-part adaptor piece.

The following electrical components have been identified for inserting:

1. Strain gauge (Youmile™ [BF350-3AA 350ohm], 7.2mm x 4.1mm x 0.08mm);
2. Micro-LED (Sourcingmap™ [0402], 1.02mm x 0.55mm x 0.51mm);
3. Large LED (RUNNCI-YUN 12v pre-wired LED, 5.7mm diameter x 9.6mm);
4. Photo-resistor. (Sourcingmap™ [GL5516 LDR (Light Dependent Resistor)], 5.7mm diameter x 2.3mm).

Item 1 is 0.8 μ m tall less than a single SLA layer in height and therefore could be inserted into the construction process (method 3.4.2.7) without modifying the part. The micro-LED,

large LED and photo resistor are 510 μ m, 9.6mm, and 2.3mm tall respectively and therefore require a recess designed into the construction to accommodate the component to avoid clashes (section 2.2).

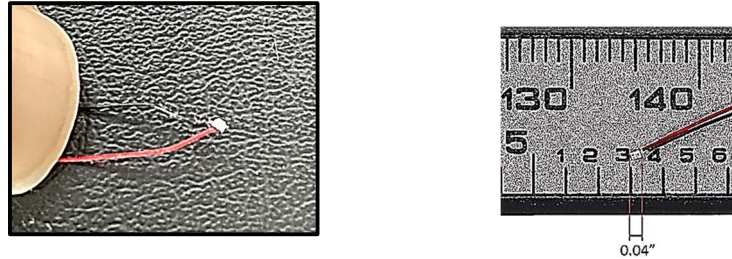


Figure 3.40: [left] Micro-LED before insertion into the SLA package [right] Micro-LED scale image by sourcingmap.com [175].

3.5.2. Step III: Stacking multiple components.

Following demonstration test geometries being identified in step II section 3.5.1, the next action was to develop a package incorporating multiple components arranged vertically (stacked). This increases the potential feature density on the wafer. The method applied to achieve this is described in the following sections (3.5.2.1 and 3.5.2.2).

3.5.2.1. Stage A: Stacked module concept.

An initial concept to stack individual packages in modules, was designed (Figure 3.41). Each module is designed to receive inserts post construction. The modules incorporate through vias to allow wiring connections at the substrate surface level to any given layer. The modules being in individual layers allows access to connect wiring between separate modules before being stacked manually. Depending on the specific component to be inserted, and the thickness of the wire additional lateral vias may be added. The modules were constructed on a Form 1+ SLA machine.

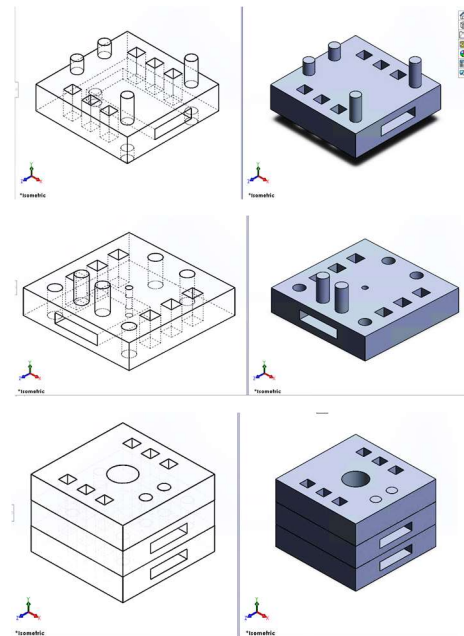


Figure 3.41: A design concept to integrate multiple packages constructed as individual modules.

The design features dowls with a clearance of 60 μ m to achieve a tight fit. The dowls ensure alignment and secure the modules when stacked and compressed onto another (Figure 3.41).

3.5.2.2. Step III Stage B. Inserting multiple stacked components.

A method for embedding a strain gauge between the substrate and an SLA construction was described in section 3.4.2.7. To further this work and enable geometries to be inserted into the body of an SLA construction using the process summarised in Figure 3.42 by establishing a python interaction with a Form 1+ machine via a USB connection.

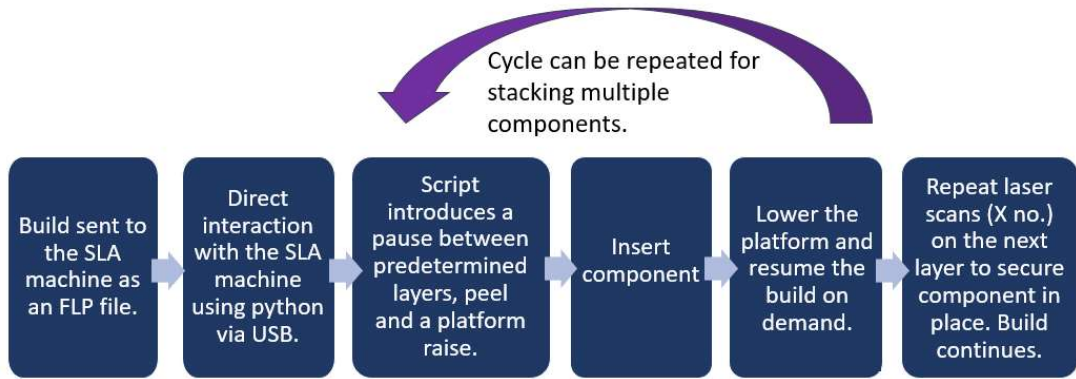


Figure 3.42: Process for inserting geometries into the SLA construction process.

The Form 1+ machine was chosen because its control system will accept open-source operating code. The script below was developed from that originally written by Ben Frantzdale (Formlabs) [171] for embedding materials within a single layer. It was downloaded from the GitHub [176] software hosting website and edited using PyCharm™ development software. The layer(s) at which the construction is to be paused is entered into the fourth line of the script, which is then entered directly into the Windows™ command prompt application.

```
from OpenFL import FLP, Printer
from insert_material_swaps import insert_pause_before

p = Printer.Printer()
layer_i = [160, 240, 308]
flp = p.read_block_flp(layer_i)
flp = insert_pause_before(flp, zJog_mm = 150 - 0.1*layer_i)
flp += [laser for laser in flp
if isinstance(laser,FLP.LaserCommand)]*6
p.write_block_flp(layer_i, flp)
p.start_printing(0,358)
```

The above script calls python subroutines; FLP, Printer, zJog and insert_pause_before from respective folders within the python environment also downloaded from GitHub [176]. In the example shown, the construction will pause before printing layer numbers 160, 240 and 308 of a total of 358. These correspond to when the cavities have been constructed to a sufficient depth to receive the geometry being inserted. A peel is performed as part of the

zJog routine which also initiates the platform to rise when the tilt motor is at its lowest and providing greatest separation with the build to avoid damaging the part. The platform rises to the instructed height above its current level. The height of 150mm used in the example script, corresponds to the platforms start position (maximum height). From this, the preceding build travel, calculated as a function of the layer height and the layer no., is deducted to avoid damage to the machine. The geometry or component can then be inserted into the package and the construction resume on demand. At this point, between being inserted and the platform being lowered, the inserted geometry is held in an inverted orientation and susceptible to becoming detached from the package. To secure the insert, the exposure for the subsequent layer is increased by instructing a repeat number of laser scans, which in the example shown is set to 6. Prior to insertion, the part is manually coated in photopolymer with excess material allowed to flow into the tank. This generates suction between the part and the floor of the cavity, and improves contact for interfacial tension, to secure the insert while inverted until the subsequent layer is formed. The coating also aids the formation of a continuous joint between the insert and the package during post build curing.

Kataria et al [13] states design clearances of 0.006 (150 μ m), 0 μ m, and -0.006" (-150 μ m) to achieve a minimum clearance, transition and interference fits respectively in an SLA process. The accuracy of a construction will be specific to the machine architecture, specifically the laser spot size, and the photopolymer material. Therefore, as also stated by Kataria [13], there is the potential for variation when applying such design rules to different machines. For the current application and equipment (Form 1+) a clearance of 300 μ m between the part and its housing in the X-Y plane was identified to provide a suitable fit to hold photopolymer coated inserts, while allowing insertion.

To demonstrate this process, a housing to accommodate a micro-LED was drawn in CAD. The housing features a 1mm high cavity in which to insert the component. The housing was constructed directly onto the build platform and a second construction onto silicon nitride, without supports. A small lateral via was designed to allow the wire tail of the LED to be inserted. The construction was then sent to a Form 1+ SLA machine for construction, the Preform software closed, and the python interaction established. At the designated layer (45), the construction paused, conducted the instructed peel and platform rise for the micro-LED and associated wiring to be inserted. The construction was then continued by depressing a button on the machine's panel. On completion, the package was manually washed with IPA and the LED illuminated to demonstrate its functionality by connecting it to the terminals of a battery.

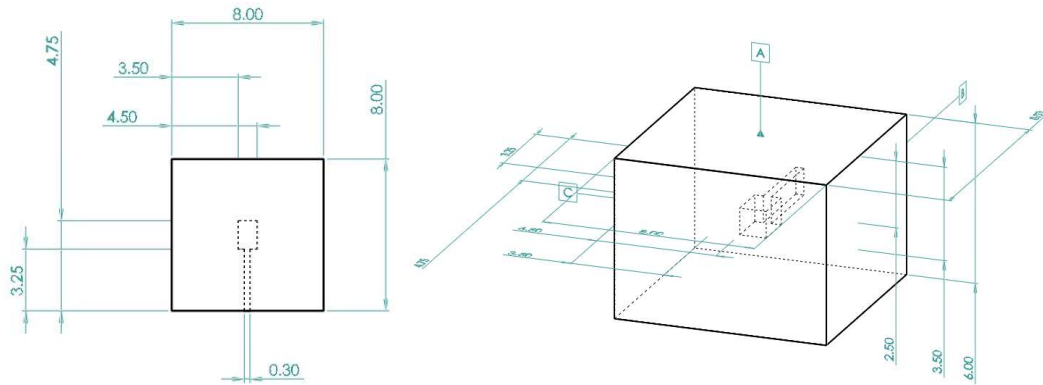


Figure 3.43: Package housing for inserting a micro-LED component.

A second, (15 mm x 15 mm x 10mm) square-based package housing (Figure 3.43) was generated in CAD (Solidworks) to accommodate a larger test component (LDR) with vertical through vias. To facilitate this, the package was constructed on supports which allows the wire tails of the component to protrude from the bottom of the construction for external connection. At the top of the package there is a 2mm deep lofted cut followed by a 1.8mm extruded cut before a 0.6mm thick window above a 2.6mm deep cavity to receive the photoresistor. Two 1mm diameter through vias were designed to accommodate the wire legs of the resistor. Using the CAD dimensions and the layer height, the layer number at which to insert the LDR was calculated to be 56 of the part. Another 70 layers are added to allow for 7mm of supports. This was verified by examining the construction slices in the SLA machine interface software (Preform). The package was then sent to a Form 1+ SLA machine and the python script invoked as described previously (section 3.5.2.2). At construction layer 126, the resistor was inserted, and its wire legs threaded through the vias and supports. The build was then resumed to seal and complete the package, and the supports removed using side snips. The package was manually washed with IPA to avoid IPA penetrating the cavity through the vias. The part was then cured in a Formcure oven for 15 minutes, connected to an Arduino unit using crocodile connectors and tested using a programme (FW1CQYYJ8YRD96J) installed from the Arduino on-line library [168] by exposing the package window to a torch light.

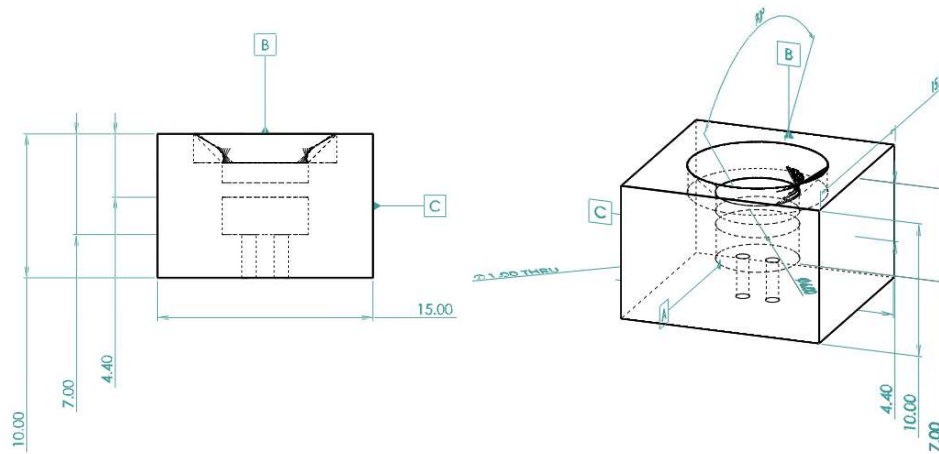


Figure 3.44: CAD of LDR insert housing.

The process described above was then developed to stack large and complex geometries. The piston and semiconductor package geometries described in section 3.5.1 were constructed on an Anycubic™ using default machine settings and green photopolymer of the same brand (Anycubic Photopolymer 09). Corresponding two-part adaptor pieces to accommodate their complex geometries (section 2.2) were constructed on a Form 2 SLA machine. A package housing (Figure 3.45) was designed using Solidworks CAD with two cavities (12mm and 26mm tall) located vertically in-line.

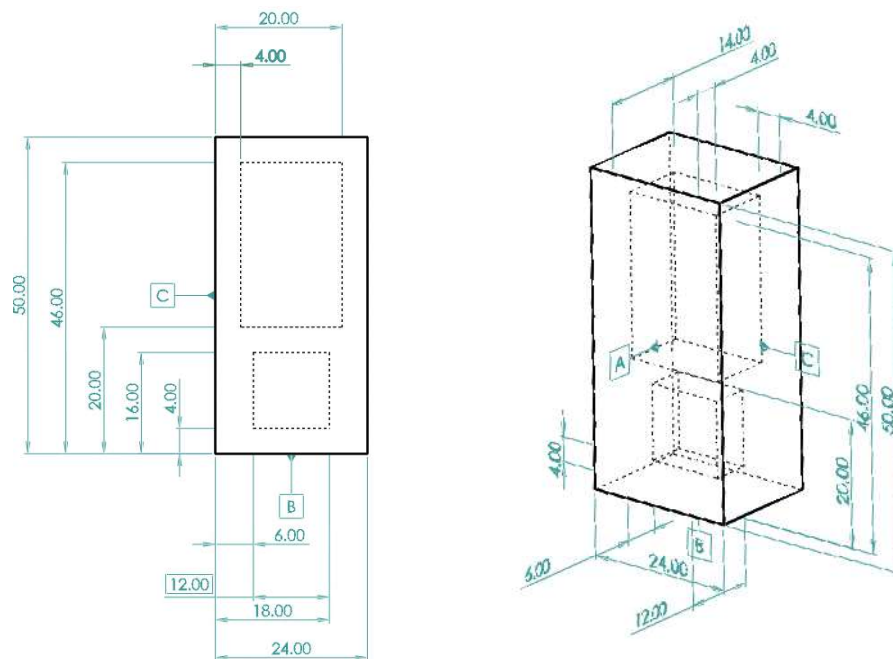


Figure 3.45: CAD image of stacked insert housing.

The geometries were calculated to be inserted at layers 300, and 460, and the python script updated accordingly (3.5.2.2). The housing was constructed on a Form 1+ SLA machine and directly onto the build platform without supports, with a 100µm layer thickness and the

piston adaptor packages inserted by the process described (3.5.2.2). The construction was resumed, and the second (semi-conductor) adaptor package inserted after layer 460. The completed package was then removed from the build platform using a blade and palette-knife, washed in an agitated bath of IPA (Formwash™), and cured for 15 minutes.

3.5.3. Step IV: Connecting inserted components to form an SLA structural electronic package.

An interconnector piece (Figure 3.46) and separate housing were designed in CAD with 300µm of lateral clearance between the two. The interconnector incorporates 1mm wide through vias to allow wire runs to be inserted and a 10mm deep cavity to receive a large LED at layer 190. The wire runs were designed with to be offset, and with wider (2.3mm) orifices at the start and end to accommodate solderless connectors (Molex™ 43030 crimp contacts) to be inserted. The adaptor piece was constructed with supports to allow external connection to the strain gauge and the LED. The components were inserted at the appropriate layers using the python interaction described in section 3.5.2.2. Default machine settings with a 100µm layer thickness was applied. A strain gauge possessing a low profile (0.8µm tall), and consequently not requiring modification to the design, was inserted after layer 204 of the part (274 of the construction allowing for supports). On completion, the construction supports were removed, and the wire tails extended beyond the base of the part using tweezers. Wire with solderless interconnectors were then manually routed through vias prior to the interconnector piece being inserted into the housing.

The housing was constructed on supports using a Form 1+ SLA machine. The python script was updated to facilitate inserts after layers 260 and 300 (330 and 370 of the construction) for the interconnector piece and an LDR respectively. The construction of the housing was completed with the LDR encapsulated beneath a lofted cut window.

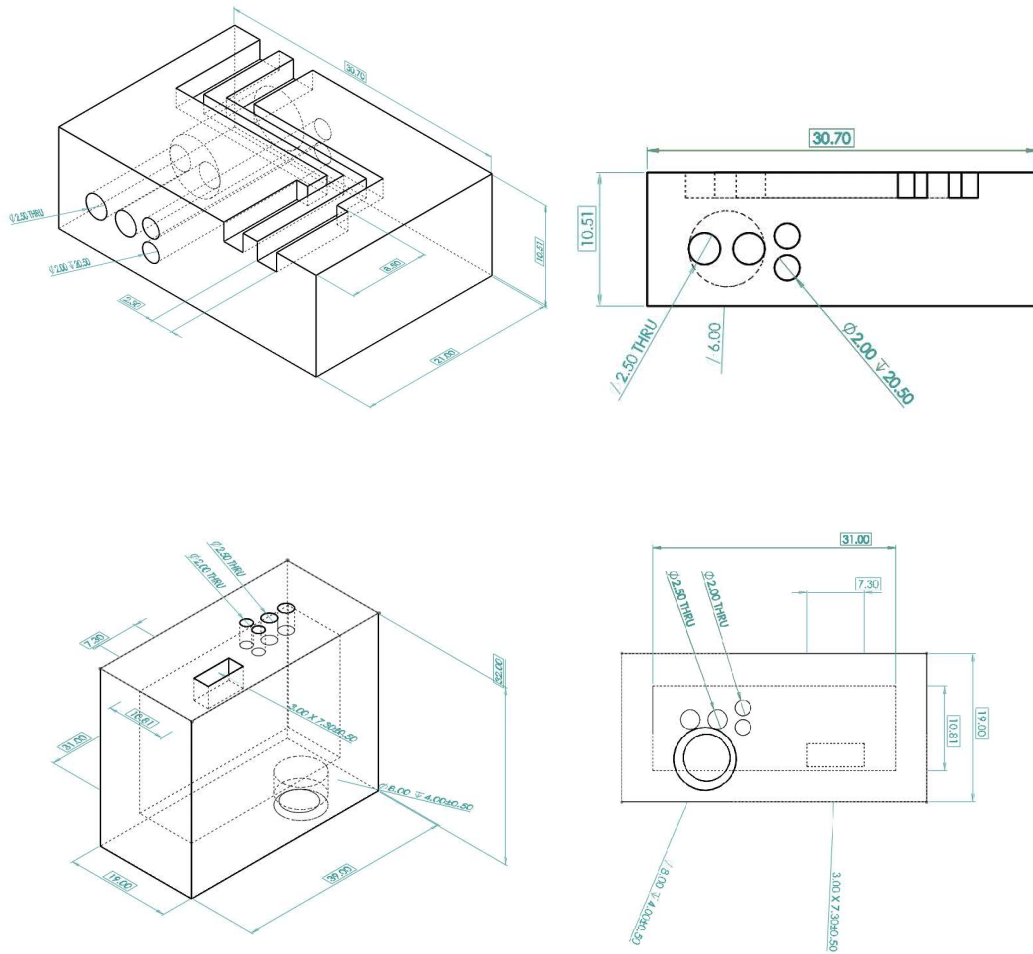


Figure 3.46: [Top] CAD image of interconnector piece.
[Bottom] CAD image of housing for multiple electrical inserts

Chapter 4

4. Results

The results from experimentation pertaining to distortion are reported in section 4.1, adhesion in section 4.2 and inserting geometries in section 4.3. These are discussed in sections 5.1, 5.2 and 5.3 respectively.

4.1. Distorting effect results

The measured results obtained from numerical modelling described in section 3.2 and the associated experimental methods described in section 3.3 are documented in sections 4.1.1 to 4.1.4.2 below. The MATLAB model script is included in Appendix J and summarised in Table 4.1.

Summary of MATLAB model scripts in Appendix J		
Script	Name	Comment
A1	Distortion with divergence and ellipticity.	Calculation of the magnitude of distortion due to divergence and ellipticity.
A2	Characterisation of distortion profiles.	Characterisation of the distorted beam profiles combined with the influence of superposition.
A3	Identification of operating window.	Applies the exposure limits for distorting effect for compliance with manufacturing tolerances to identify an operating window.
A4	Optimisation of SLA process and build time.	Reduces the hatch spacing to defined limits of variance in exposure with superposition and minimises build time.
B1	Refraction with Parabolic mirror.	Calculates the loss in accuracy due to refraction and the profile of a parabolic mirror to maintain a normal angle of incidence.
B2	Reflection	Calculates the magnitude of reflectance and the potential for lateral spurious curing, from a substrate with consideration to the SLA operating parameters, machine architecture, the refractive indices of the media within the light path and the properties of the substrate.

Table 4.1: Summary of models.
(Corresponding script included in Appendix J).

4.1.1. Superposition using FTIR.

Following the method described in section 3.3.1, the readings from FTIR analysis shown in Figure 4.1 were obtained (raw data in Table G1.21 Appendix G).

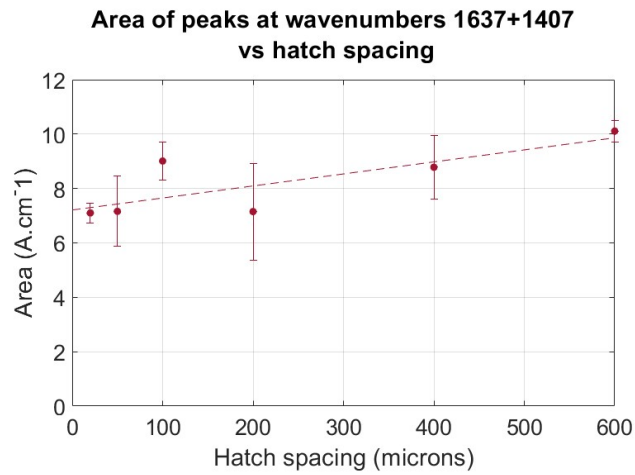


Figure 4.1: The combined area of the FTIR spectra peaks at wavenumbers 1637 and 1407 for SLA samples against hatch spacing.

The results show a reduced presence of C=C bonds in the constructed samples as the hatch spacing is reduced, and indicative of increased cross-linking. This corresponds to an increase in the delivered exposure (section 3.2.4) attributed to superposition and demonstrates the mechanism is active at the applied range of equipment parameters (Table 5.1).

4.1.2. Form 1+ Minimum feature size

The following measurements (Table 4.2) of the CLW constructed at the centre of the build area and at different scan speeds on the Form 1+ were obtained using the method described in section 3.3.2.

Measured cured line width on the Form 1+ at increasing exposures.					
Scan speed (mm/s)	Measurement no.			Average (microns)	Standard deviation (μm)
	1	2	3		
800	240	240	250		
800	250	250	270		
800	280	260	270	256.7	14.1
600	280	280	300		
600	280	290	290		
600	280	270	280	283.3	8.7
400	310	350	320		
400	310	330	310		
400	330	300	310	318.9	15.4
200	610	590	500		
200	540	540	490		
200	540	530	490	536.7	42.7
100	760	750	780		
100	750	760	770		
100	770	780	720	760.0	18.7
50	890	910	930		
50	920	880	850		
50	930	840	860	890.0	34.6

Table 4.2 Measured cured line width on Form 1+ for 90 μm test piece at increasing exposures.

The measurements recorded from the default machine scan speed of 800mm/s are used to calibrate the model following the process described in section 5.1.1. The results also show a disproportionate widening of the cured line width as the exposure increases with reducing scan speed. These are discussed and compared with modelled predictions in section 5.1.4.

4.1.2.1. Modelled (calibrated) results for the Form 1 with an elliptical diverged beam.

The calibrated modelled output (section 3.2.9.1) showing the variation in cured line width across the build area with divergence and ellipticity, for the cases with and without MFLS at scan speeds of 50mm/s, 100mm/s and 200mm/s, is shown in Table 4.3 to Table 4.5.

Form 1+ modelled divergence and ellipticity results for a 1mm (design) wide part at 50mm/s scan speed				
Position	With MFLS and superposition		Without MFLS with superposition	
	CLW	Total part width	CLW	Total part width
-60	410.6	1350.6	321.4	1261.4
-40	406.1	1346.1	318.2	1258.2
-20	403.6	1343.6	316.3	1256.3
0	402.8	1342.8	315.7	1255.7
20	403.6	1343.6	316.3	1256.3
40	406.1	1346.1	318.2	1258.2
60	410.6	1350.6	321.4	1262.5

Table 4.3: Form 1+ modelled (calibrated) diverged elliptical results at 50mm/s.

Form 1+ modelled divergence and ellipticity results for a 1mm (design) wide part at 100mm/s scan speed				
Position	With MFLS and superposition		Without MFLS with superposition	
	CLW	Total part width	CLW	Total part width
-60	378.9	1318.9	279.7	1219.7
-40	374.8	1314.8	277.0	1217.0
-20	372.5	1312.5	275.6	1218.6
0	371.8	1311.8	275.1	1215.0
20	372.5	1312.5	275.6	1215.6
40	374.8	1314.8	277.0	1217.0
60	380.2	1318.9	279.7	1219.7

Table 4.4: Form 1+ modelled (calibrated) diverged elliptical results at 100mm/s.

Form 1+ modelled divergence and ellipticity results for a 1mm (design) wide part at 200mm/s scan speed				
Position	With MFLS and superposition		Without MFLS with superposition	
	CLW	Total part width	CLW	Total part width
-60	344.2	1284.2	230.5	1170.5
-40	340.6	1280.6	228.7	1168.7
-20	338.6	1278.6	227.6	1167.6
0	337.9	1277.9	227.3	1167.3
20	338.6	1278.6	227.6	1167.6
40	340.6	1280.6	228.7	1168.7
60	344.2	1284.2	230.5	1170.5

Table 4.5: Form 1+ modelled (calibrated) diverged elliptical results at 200mm/s.

The diverged and elliptical beam width at a given location is obtained from Equation 3.26. The resulting cured line width, combined with the effects of superposition, was calculated using Equation 3.15 and the process described in section 3.2.4. The angle at which the

beam is incident upon the build platform increases with distance from the centre and has a corresponding effect on the width of the beam. This, combined with the elevated exposure associated with superposition, increases the dimension of the part.

4.1.2.2. Form 1+ lateral distortion measured results.

The measured dimensions of 1mm test parts using the method described in section 3.3.4, for comparison with the modelled values in section 4.1.2.1 at corresponding scan speeds, are shown in Table 4.6 to Table 4.8 and discussed in section 5.1.4. The calculated CLW was obtained from Equation 3.1 using the relationship described in section 3.2.1.

Form 1+ measured part width (1mm design) and calculated CLW with superposition and MFLS at 50mm/s scan speed						
Location (mm from centre)	Average measurement sample no.			Average measured width (μm)	Standard Deviation (μm)	Calculated CLW (μm)
	1 (μm)	2 (μm)	3 (μm)			
-60	3898.56	3945.43	4140.2	3994.73	128.14	3054.73
-40	3868.99	3969.48	4344.49	4060.99	250.61	3120.99
-20	4556.89	4675.99	4622.07	4618.32	59.64	3678.32
0	4591.65	4549.17	4456.48	4532.43	69.12	3592.43
20	4614.52	4602.96	4282.85	4500.11	188.24	3560.11
40	4892.48	5080.42	5066.64	5013.18	104.76	4073.18
60	4020.1	3947.59	4147.27	4038.32	101.08	3098.32

Table 4.6: Form 1+ measured part width (1mm design) with superposition and MFLS at 50mm/s scan speed

Form 1+ measured part width (1mm design) and calculated CLW with superposition and MFLS at 100mm/s scan speed						
Location (mm from centre)	Average measurement sample no.			Average measured width (μm)	Standard Deviation (μm)	Calculated CLW (μm)
	1 (μm)	2 (μm)	3 (μm)			
-60	3197.55	3230.55	3094.45	3174.18	71.00	2234.18
-40	3185.96	3333.60	3359.74	3293.10	93.70	2353.10
-20	3129.18	3225.64	3082.88	3145.90	72.83	2205.90
0	3329.82	3272.96	3310.53	3304.44	28.92	2364.44
20	3310.53	3345.25	3344.29	3333.36	19.77	2393.36
40	3977.21	4008.52	3966.87	3984.20	21.69	3044.20
60	3519.68	3599.10	3522.74	3547.17	45.00	2607.17

Table 4.7: Form 1+ measured part width (1mm design) with superposition and MFLS at 100mm/s scan speed.

Form 1+ measured part width (1mm design) and calculated CLW with superposition and MFLS at 200mm/s scan speed						
Location (mm from centre)	Average measurement sample no.			Average measured width (µm)	Standard Deviation (µm)	Calculated CLW (µm)
	1 (µm)	2 (µm)	3 (µm)			
-60	3027.63	3046.94	3001.86	3025.48	22.62	2085.48
-40	3199.71	3236.16	3247.74	3227.87	25.07	2287.87
-20	2797.12	2756.17	3759.32	2770.87	22.79	1830.87
0	2891.62	2938.86	2957.76	2929.41	34.07	1989.41
20	3045.96	3073.97	3070.11	3063.35	15.18	2123.35
40	3834.73	3848.04	3885.54	3856.10	26.35	2916.10
60	3510.35	3969.90	3909.04	3796.43	249.61	2856.43

Table 4.8: Form 1+ measured part width (1mm design) with superposition and MFLS at 200mm/s scan speed

The measured part dimensions shown in Table 4.6 to Table 4.8, do not demonstrate a consistent relationship with the location on the build platform. This is attributed to distortion in the beam which is discussed further in section 5.1.4.1. The results are compared with the modelled results in section 4.1.2.1 and discussed in section 5.1.4.

4.1.3. Form 2 Distorting effects results

Measurements to support calibration of the Form 2 model are shown in section 4.1.3.1. The calibrated model output for D&E, and reflectance is shown in sections 4.1.3.3 and 0 respectively. The associated measurements of constructions with and without MFLS, and reflectance are shown in sections 4.1.3.2 and 0. These are then compared in chapter 5 to identify the influence of distorting effects.

4.1.3.1. Form 2 CLW calibration test piece results

The measured CLW produced by the Form 2 at default machine parameters and following the method described in section 3.3.3.1 are shown in Table 4.9.

Form 2 CLW at default parameters (without superposition with MFLS)					
Test sample	Measurement no.			Average (microns)	Standard deviation (µm)
	1	2	3		
1	140	140	150		
2	140	140	150		
3	150	150	160	146.6	7.1

Table 4.9: Form 2 CLW at default machine parameters without superposition and with MFLS.

These results (Table 4.9) represent the minimum feature size of construction with MFLS and without the influence of superposition. These are used for calibrating the model following the process described in section 3.2.9.2 and discussed in 5.1.2.

As explained in section 3.3.3, the results from centrally located test pieces (0mm) constructed as part of the lateral distortion tests in section 3.3.4.2 and shown in section 4.1.3.2, were used for other cases. These being with the influence of MFLS and superposition (Table 4.10) and single layer scan with superposition (Table 4.11).

4.1.3.2. Form 2 measured part width (1mm design) and calculated perimeter CLW, with and without MFLS

The measured width of 1mm wide (design) test pieces, constructed with superposition and MFLS, using the method described in section 3.3.4.2 (part A) are shown in Table 4.10. The corresponding results without first layer scans using 5.5mm tall test pieces constructed following the procedure described in section 3.3.4.2 (part B), are included in Table 4.11 and used for comparison with modelled results for discussion in section 5.1.4.3. The calculated CLW was again obtained from Equation 3.1 using the relationship described in section 3.2.1.

Form 2 measured part width (1mm design) and calculated CLW with superposition and MFLS						
Location (mm from centre)	Average measurement sample no.			Average measured width (µm)	Standard Deviation (µm)	Calculated CLW (µm)
	1 (µm)	2 (µm)	3 (µm)			
-70	1282.01	1313.02	1308.75	1301.26	26.98	361.26
-50	1218.93	1232.83	1245.66	1232.47	13.40	292.47
-30	1177.23	1170.81	1202.89	1183.64	16.44	243.64
-15	1155.84	1169.74	1167.61	1164.40	9.49	224.40
0	1147.29	1161.19	1151.57	1153.35	7.01	213.35
15	1152.63	1171.88	1190.97	1171.82	17.25	231.83
30	1164.40	1175.09	1184.14	1174.54	9.04	234.54
50	1218.93	1211.44	1215.90	1215.42	9.32	275.42
70	1241.38	1274.53	1278.92	1264.94	21.58	324.94

Table 4.10: Form 2 measured part width (1mm design) with superposition and MFLS (Corresponding to case D1 in section 5.1.4.3)

Form 2 measured part width (1mm design) and calculated CLW with superposition, without MFLS						
Location (mm from centre)	Measurement no.			Average measured width (μm)	Standard Deviation (μm)	Calculated CLW (μm)
	1 (μm)	2 (μm)	3 (μm)			
-70	1023.72	1039.47	1007.97	1023.72	15.75	83.72
-50	1033.17	1036.32	1039.47	1035.27	3.15	95.27
-30	1036.32	1030.02	1030.02	1033.17	3.64	93.17
-15	1045.77	1052.07	1042.62	1046.82	4.81	106.82
0	1030.02	1033.17	1020.57	1027.92	6.56	87.92
15	1023.72	1036.32	1045.77	1035.27	11.06	95.27
30	1033.17	1042.62	1039.47	1038.42	4.81	98.42
50	1030.02	1036.32	1033.17	1033.17	3.15	93.17
70	1030.02	1036.32	1020.57	1028.97	6.47	88.97

Table 4.11: Form 2 measured part width (1mm design 5.5mm tall) with superposition without MFLS (Corresponding to case D2 in section 5.1.4.3.)

Measurements with the same value can be seen in the results. This is a consequence of the microscope measuring in increments of a single pixel set at $4.916\mu\text{m}/\text{pixel}$. This represents the accuracy of the microscope measurement compared to that of digital callipers of $\pm 10\mu\text{m}$. Therefore, samples with similar dimensions can produce the same microscope measurement. This also emphasises the importance of appropriately calibrating the microscope for a given lens.

There is a contrast in the recorded trend between the measurements in Table 4.10 and Table 4.11. In the former, high exposure case (with superposition and MFLS), the CLW increases with distance from the centre. However, the opposite trend occurs in the case without MFLS and correspondingly reduced exposure. These results indicate that the delivered exposure relative to the centre, is increasing with distance when MFLS are applied. This characteristic and potential causes are discussed further in sections 5.1.4.3 and 5.1.5.

4.1.3.3. Modelled (calibrated) results for the Form 2 with an elliptical diverged beam.

The modelled (calibrated) line width (Equation 3.20) output on the Form 2, with a diverged and elliptical beam (Equation 3.26) using the method described in section 3.2.9.2 at default settings is shown in Table 4.12. The influence of the CLW on the overall dimension of the part is calculated using Equation 3.1 and the process described in section 3.2.1.

Form 2 modelled divergence and ellipticity results for a 1mm (design) wide part				
Position	With MFLS and superposition		Without MFLS with superposition	
	CLW	Total part width	CLW	Total part width
-70	218.02	1158.02	85.28	1025.28
-50	215.54	1155.54	86.72	1026.72
-30	214.08	1154.08	87.50	1027.50
-15	213.50	1153.50	87.79	1027.79
0	213.32	1153.32	87.88	1027.89
15	213.50	1153.50	87.79	1027.79
30	214.08	1154.08	87.50	1027.50
50	215.54	1155.54	86.72	1026.72
70	218.02	1158.02	85.28	1025.28

Table 4.12: Form 2 modelled (calibrated) diverged elliptical results.

The modelled results show the CLW to marginally increase with distance from the centre when MFLS are applied while the converse occurs without them. This trend is consistent with the measured results in 4.1.3.2. However, the magnitude of the increase in CLW with MFLS is significantly greater than that modelled and indicative of an additional distorting effect being active and attributed to reflectance (section 5.1.5.2). These results are now further analysed in section 4.1.3.4 to quantify the extent of distortion.

4.1.3.4. Measured and modelled distortion due to reflectance on the Form 2.

The measured and modelled potential lateral spurious curing (LSC) attributed to reflectance on the Form 2 is compared in Table 4.13.

Measured and modelled distortion of a 1mm wide part with MFLS and reflectance.									
Position	-70	-50	-30	-15	0	+15	+30	+50	+70
a. Measured (Table 4.10)	1301.3	1232.5	1183.6	1164.4	1153.3	1171.8	1174.5	1215.4	1264.9
b. Calibrated modelled D&E (Table 4.12)	1158.0	1155.5	1154.1	1153.5	1153.3	1153.5	1154.1	1155.5	1158.0
c. LSC attributed to reflectance	143.2	76.9	29.6	10.9	0.0	18.3	20.5	59.9	106.9
d. Modelled LSC from reflectance	125.1	94.0	58.4	23.8	0.0	23.8	58.4	94.0	125.1
e. Modelled LSC due to D&E, and reflectance	1283.1	1249.6	1212.5	1177.3	1153.3	1177.3	1212.5	1249.6	1283.1
f. Standard Dev. (Measured vs modelled)	12.8	12.1	20.4	9.2	0.0	3.9	26.8	24.1	12.9

Table 4.13: Measured and modelled distortion of a 1mm wide (design) part with MFLS and reflectance at different locations across the Form 2 build area.

The LSC attributed to reflectance (row c.) is taken as the difference between the measured part width (row a.) and the calibrated modelled values accounting for D&E and overexposure from MFLS (row b.). The D&E modelled values for the CLW (Equation 3.20) calculated from the widened beam (Equation 3.26) were calibrated using the process described in section 3.2.9.2. The reflectance model was run according to the process described in section 3.2.10. to produce the values in row d. The combined influence of D&E and reflectance is modelled in row e. The model can then be calibrated (section 5.1.5.2) to match the average LSC ($125.1\mu\text{m}$) attributed to reflectance (row c) at the edge locations (-70 and +70mm) of the build area, by adjusting the modelled photopolymer penetration depth. These results are further compared and discussed in section 5.1.4.3 (divergence and ellipticity) and 5.1.5.2 (reflectance).

4.1.3.5. Refraction

This section reports the results from an experiment to produce a refraction array (Figure 4.3) using the method described in section 3.3.5.

The full width dimensions (Figure 4.2) of the test array were measured using callipers and shown in Table 4.14.

Measured dimensions of refraction array on Form 2								
Dimension	A (mm)	B (mm)	C (mm)	D (mm)	E (mm)	F (mm)	Avg	STDV
Measurement 1	124.29	124.28	124.39	124.13	123.92	124.21		
Measurement 2	124.17	124.12	124.13	124.03	123.92	124.00		
Measurement 3	124.23	124.08	124.15	124.01	123.97	124.08		
Avg	124.23	124.16	124.22	124.06	123.94	124.10	124.11	0.13

Table 4.14: Measured outer dimensions (corresponding to Figure 4.2) of the refraction test array on Form 2.

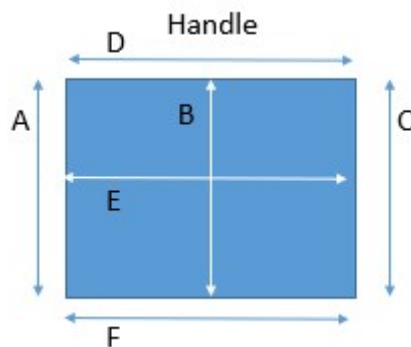


Figure 4.2: Measurement of the outer dimensions of the refraction array.

The measured dimensions (A-F) from the refraction array were consistently measured between 0.94mm and 1.23mm (standard deviation = 0.13) greater than the design dimensions of 123mm.

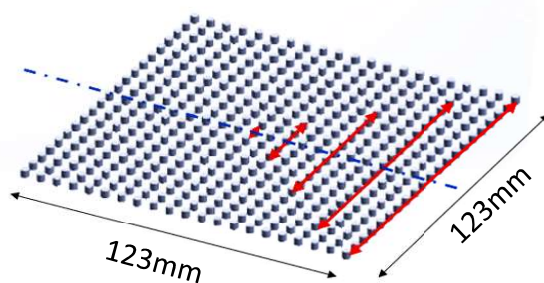


Figure 4.3: Measurement of inner dimensions of the refraction array

To further investigate the potential influence of refraction, two additional test arrays were constructed and measured at dimension A (Figure 4.2), and at intervals inwards and shown in red in Figure 4.3. These measurements are included in Table 4.15.

Measured dimensions of the refraction array on the Form 2					
Design width of measured dimension	123mm [A]	99mm	63mm	27mm	3mm
Measurement 1 (µm)	124.23	100.36	63.83	27.65	3.03
Measurement 2 (µm)	124.64	100.29	63.75	27.39	2.96
Measurement 3 (µm)	124.34	100.21	64.41	27.37	2.98
Avg (µm)	124.40	100.29	64.00	27.47	2.99
Stdev (µm)	0.21	0.08	0.36	0.16	0.04

Table 4.15: Average measured dimensions (corresponding to Figure 4.3) of the refraction test array on a Form 2 SLA machine.

The relationship between the Form 2 as-built $[X_b]$ and the design dimensions $[X_d]$ (linear regression) is: $X_{b2} = 0.0127.X_d$

Refraction arrays (Figure 4.3) were also constructed on a Form 3 SLA machine, the measurements of which are included in Table 4.16.

Average measurement of refraction array constructed on the Form 3.					
Design width of measured dimension	123mm [A]	99mm	63mm	27mm	3mm
Measurement 1 (µm)	124.16	99.92	63.58	27.18	2.96
Measurement 2 (µm)	124.14	99.96	63.59	27.18	2.98
Measurement 3 (µm)	124.17	99.95	63.58	27.21	3.00
Avg (µm)	124.16	99.94	63.58	27.19	2.98
Stdev (µm)	0.015	0.021	0.006	0.02	0.02

Table 4.16: Measured dimensions (corresponding to Figure 4.16) of the refraction test array on a Form 3 SLA machine.

The relationship between the Form 3 as-built [X_b] and the design dimensions [X_d] (linear regression) is: $X_{b3} = 0.0094 \cdot X_d$

Measurements of the test array constructed on the Form 3 (Table 4.16) also show variation from design. However, the Form 3 benefits from the beam maintaining a normal angle of incidence which discounts the potential for refraction. Consequently, the results of the Form 2 and Form 2 test arrays in Table 4.15 and Table 4.16 are compared with modelled results and discussed further in section 5.1.6.

4.1.4. Form 1+ Reflectance tests

The results from the separate and parallel reflectance experiments conducted on the Form 1+ are shown in sections 4.1.4.1 and 4.1.4.2 respectively. These are discussed in section 5.1.5.3.

4.1.4.1. Form 1+ separate reflectance tests on silicon nitride and backed polycarbonate.

The measured part width of 1mm test pieces constructed directly onto the reflective surface of silicon nitride and onto to unreflective PVC backed PC, according to the method described in section 3.3.6.1, are shown in Table 4.17 to Table 4.22.

Form 1+ measured part width for 1mm (design) lines constructed directly onto PVC backed polycarbonate at 50mm/s scan speed							
	Measurement no.						
Measurement (mm from centre)	-60	-40	-20	0	+20	+40	+60
1 (μm)	2740.42	3693.9	4053.03	4581.93	4474.25	3798.49	2796.72
2 (μm)	2686.87	3667.03	4179.00	4601.64	4506.88	3921.15	2759.32
3 (μm)	2671.12	336.61	4135.55	4593.7	4249.83	3957.29	2337.23
4 (μm)	2491.58	3818.92	4826.54	5259.13	5105.91	3992.26	2790.82
5 (μm)	2384.48	3838.69	4830.49	5226.16	5172.22	4108.28	2771.92
6 (μm)	2589.22	3705.01	4810.75	5436.43	5083.99	4179.32	2579.77
Avg. width (μm)	2593.95	3176.70	4472.56	4949.83	4765.51	3992.80	2672.63
STDV (μm)	134.48	1393.11	385.63	398.05	400.09	135.85	183.22

Table 4.17: Form 1+ measured part width of 1mm test pieces constructed onto the unreflective surface of PVC backed polycarbonate at 50mm/s.

Form 1+ measured part width for 1mm (design) lines constructed directly onto silicon nitride at 50mm/s scan speed							
	Measurement no.						
Measurement (mm from centre)	-60	-40	-20	0	+20	+40	+60
1 (µm)	3538.17	5221.78	5023.67	5235.88	4880.90	4537.50	3753.03
2 (µm)	3634.63	5241.10	5120.13	5292.78	5039.10	4414.00	3737.57
3 (µm)	3661.64	5138.71	5304.58	5296.65	5170.91	4444.90	3812.67
Avg. width (µm)	3611.48	5200.53	5149.46	5275.10	5030.30	4465.47	3767.76
STDV (µm)	64.91	54.40	142.73	34.02	145.20	64.27	39.66

Table 4.18: Form 1+ measured part width of 1mm test pieces constructed directly onto silicon nitride at 50mm/s.

Form 1+ measured part width for 1mm (design) lines constructed directly onto PVC backed polycarbonate at 100mm/s scan speed							
	Measurement no.						
Measurement (mm from centre)	-60	-40	-20	0	+20	+40	+60
1 (µm)	2461.98	3451.22	3848.41	3796.51	4020.54	3851.76	1907.09
2 (µm)	2354.26	3468.02	3793.21	3812.3	4040.31	3933.57	2364.17
3 (µm)	2291.48	3498.70	3803.76	3863.01	3992.87	3992.87	2379.93
4 (µm)	1793.71	4147.08	4317.09	3561.95	3629.16	3791.25	2742.55
5 (µm)	2193.04	4447.59	4324.95	3565.91	3748.46	3894.03	2649.80
6 (µm)	2489.89	4483.14	4167.15	3531.22	3724.76	3863.01	2358.33
Avg. width (µm)	2264.06	3915.96	4042.43	3688.48	3859.35	3887.75	2400.31
STDV (µm)	255.08	499.70	255.94	150.48	178.86	69.87	291.93

Table 4.19: Form 1+ measured part width of 1mm test pieces constructed onto the unreflective surface of PVC backed polycarbonate at 100mm/s.

Form 1+ measured part width for 1mm (design) lines constructed directly onto silicon nitride at 100mm/s scan speed							
	Measurement no.						
Measurement (mm from centre)	-60	-40	-20	0	+20	+40	+60
1 (µm)	2501.03	2998.71	3646.53	4271.27	4143.13	4127.95	3095.96
2 (µm)	2541.78	2979.81	4120.79	4266.56	4128.78	4158.87	3120.31
3 (µm)	2589.22	4120.79	4164.38	4278.99	4159.38	4100.89	3135.76
Avg. width (µm)	2544.01	3366.44	3977.23	4272.27	4143.76	4129.24	3117.34
STDV (µm)	44.14	653.36	287.23	6.28	15.31	29.01	20.07

Table 4.20: Form 1+ measured part width of 1mm test pieces constructed directly onto silicon nitride at 100mm/s.

Form 1+ measured part width for 1mm (design) lines constructed directly onto PVC backed polycarbonate at 200mm/s scan speed							
	Measurement no.						
Measurement (mm from centre)	-60	-40	-20	0	+20	+40	+60
1 (µm)	2091.94	2996.63	3134.99	3069.08	3258.67	3337.67	2625.74
2 (µm)	2996.63	3022.21	3186.39	3115.23	3227.07	3584.83	2334.00
3 (µm)	3134.99	2065.13	3278.42	2150.81	3254.72	3648.14	2169.89
4 (µm)	1093.34	3700.32	3392.97	3131.04	3088.83	3403.82	2777.74
5 (µm)	1148.4	3610.21	3391.96	3203.79	3134.99	3467.07	2759.47
6 (µm)	1282.11	3722.24	3285.22	3160.23	3142.90	3716.13	2430.52
Avg. width (µm)	1957.90	3186.12	3278.32	2971.70	3184.53	3526.28	2516.23
STDV (µm)	931.87	640.48	104.98	404.66	71.52	147.24	244.97

Table 4.21: Form 1+ measured part width of 1mm test pieces constructed onto the unreflective surface of PVC backed polycarbonate at 200mm/s.

Form 1+ measured part width for 1mm (design) lines constructed directly onto silicon nitride at 200mm/s scan speed							
	Measurement no.						
Measurement (mm from centre)	-60	-40	-20	0	+20	+40	+60
1 (µm)	2576.62	3469.13	3277.82	3500.12	3422.07	2800.27	2661.67
2 (µm)	2652.22	3444.39	3375.19	3511.74	3444.12	2825.47	2645.92
3 (µm)	2677.42	3479.87	3406.08	3526.06	3459.64	2904.21	2535.68
Avg. width (µm)	2635.42	3464.46	3353.03	3512.64	3441.94	2843.32	2614.42
STDV (µm)	52.458	18.19	66.94	12.99	18.88	54.22	68.67

Table 4.22: Form 1+ measured part width of 1mm test pieces constructed directly onto silicon nitride at 200mm/s.

The SRT results tabulated above are plotted in Figure 4.4 below.

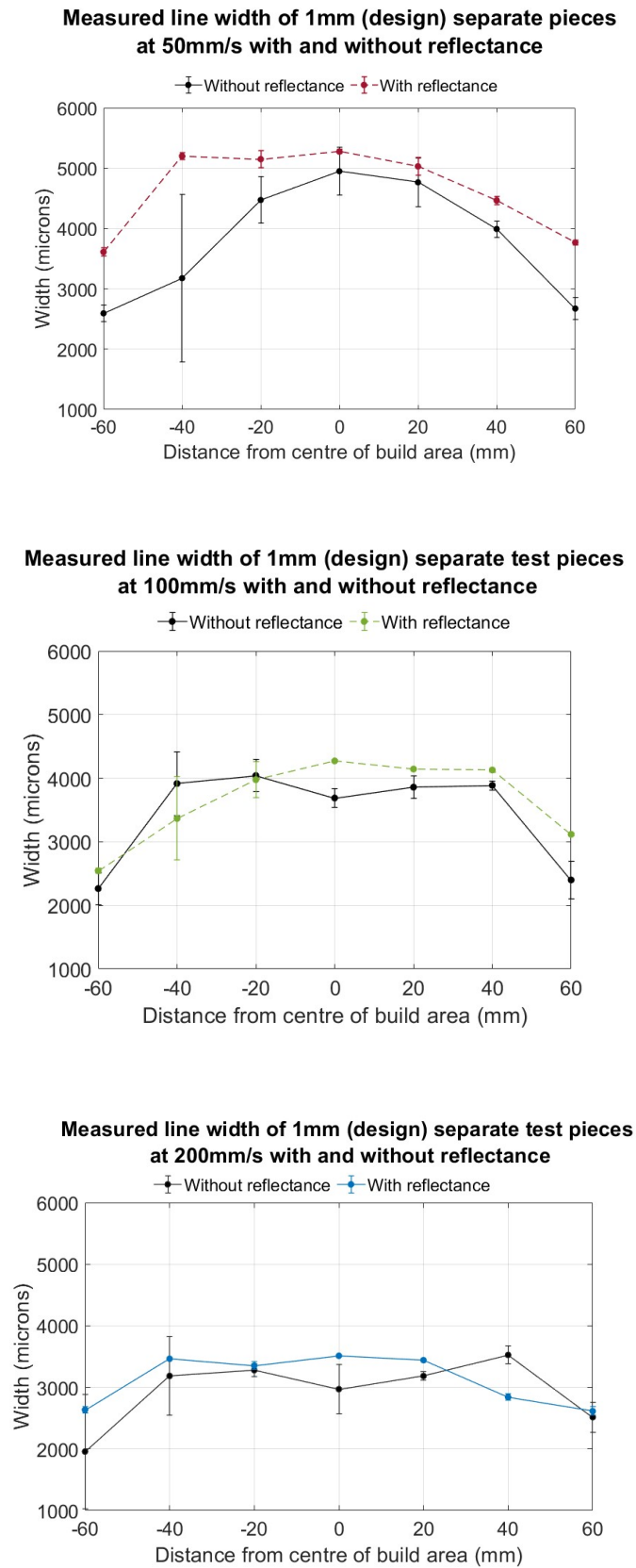


Figure 4.4: [Top] Variation in the measured width of 1mm (design) test pieces constructed on separate samples, with and without exposure to reflectance from silicon nitride at 50mm/s, [Middle] at 100mm/s, and [Bottom] at 200mm/s.

The magnitude of LSC in the reflectance tests (SRT and PRT in section 4.1.4.2) is determined by subtracting the as-built width of the shielded part from that of the part exposed to reflectance. The measured width of the SRT test pieces exposed to reflections at 50mm/s (Figure 4.4) are significantly wider than those shielded from reflections at the same speed in Table 4.17. Except for the -40mm sample at 100mm/s, all the SRT test samples exposed to reflectance exhibit an increased CLW due to spurious curing up to 200mm/s. At this speed the increase in CLW with exposure to reflectance is reduced further and indicates the approximate onset of spurious curing from reflectance. However, the variance in the results is significant (tables Table 4.17 to Table 4.22), and there is some inconsistency between tests conducted with and without shielding test pieces exposed to reflectance being larger than those not (-40mm at 100mm/s and +40mm at 200mm/s). This variance, and inconsistency are potentially due to differences in the environmental conditions between tests. Consequently, to allow test pieces to be constructed with and without exposure to reflectance concurrently, the parallel reflectance test (section 3.3.6.2) was developed, the results of which are included in the next section (4.1.4.2).

4.1.4.2. Form 1+ Parallel test with and without reflectance.

The 1mm wide test pieces single layer test pieces constructed onto polycarbonate with a portion exposed to reflectance from silicon nitride and the remaining portion shielded from reflections (method 3.3.6.1), at scans speeds of 50mm/s, 100mm/s and 200mm/s are shown in Table 4.23 to Table 4.25.

Form 1+ measured part width for 1mm (design) lines constructed onto silicon nitride with and without reflectance at 50mm/s scan speed.					
	Position (DFC)	Measurement (μm from transition point)		Avg	STDV
		100μm	200μm		
W/O reflectance	-60	3294.22	3310.02	3302.12	11.17
With reflectance	-60	3464.07	3479.87	3471.97	11.17
W/O reflectance	-40	4676.33	4684.21	4680.27	5.57
With reflectance	-40	4778.76	4841.79	4810.28	44.57
W/O reflectance	-20	4567.5	4641.53	4604.52	52.35
With reflectance	-20	4835.17	4880.73	4857.95	32.22
W/O reflectance	0	4689.85	4735.5	4712.68	32.28
With reflectance	0	4878.13	4929.48	4903.81	36.31
W/O reflectance	20	4538.27	4578.28	4558.28	28.29
With reflectance	20	4721.17	4761.18	4741.18	28.29
W/O reflectance	40	4684.22	4729.81	4707.02	32.24
With reflectance	40	4843.78	4872.27	4858.03	20.15
W/O reflectance	60	3216.38	3251.9	3234.14	25.12
With reflectance	60	3342.67	3358.45	3350.56	11.16

Table 4.23: 1mm wide test pieces with and without exposure to reflectance from silicon nitride at 50mm/s scan speed.

DFC = distance from centre, W/O = Without reflectance (portion of the sample constructed above backing tape), With reflectance refers to the portion of the sample exposed to reflections from the silicon nitride.

Form 1 measured part width for 1mm (design) lines constructed onto silicon nitride with and without reflectance at 100mm/s scan speed.					
	Position (DFC)	Measurement (μm from transition point)		Avg	STDV
		100μm	200μm		
W/O reflectance	-60	4315.89	4298.76	4307.33	12.11
With reflectance	-60	4481.44	4492.86	4487.15	8.08
W/O reflectance	-40	3751.71	3731.95	3741.83	13.97
With reflectance	-40	3941.47	3901.94	3921.71	27.95
W/O reflectance	-20	5204.41	5198.69	5201.55	4.04
With reflectance	-20	5255.88	5261.6	5258.74	4.04
W/O reflectance	0	4025.14	3996.63	4010.89	20.16
With reflectance	0	4120.1	4105.93	4113.02	10.02
W/O reflectance	20	4846.69	4835.29	4840.99	8.06
With reflectance	20	4926.52	4898.01	4912.27	20.16
W/O reflectance	40	4667.26	4690	4678.63	16.08
With reflectance	40	4752.53	4741.16	4746.85	8.04
W/O reflectance	60	3237.24	3221.47	3229.36	11.15
With reflectance	60	3300.33	3296.39	3298.36	2.79

Table 4.24: 1mm test pieces with and without exposure to reflectance from silicon nitride at 100mm/s scan speed.

Form 1+ measured part width for 1mm (design) lines constructed onto silicon nitride with and without reflectance at 200mm/s scan speed.					
	Position (DFC)	Measurement (μm from transition point)		Avg	STDV
		100 μm	200 μm		
W/O reflectance	-60	2816.28	2804.43	2810.36	8.38
With reflectance	-60	2820.23	2804.43	2812.33	11.17
W/O reflectance	-40	4190.29	4207.42	4198.86	12.11
With reflectance	-40	4196	4213.13	4204.57	12.11
W/O reflectance	-20	5266.1	5271.81	5268.96	4.04
With reflectance	-20	5294.63	5323.16	5308.90	20.17
W/O reflectance	0	3354.5	3358.45	3356.48	2.79
With reflectance	0	3346.61	3362.4	3354.51	11.17
W/O reflectance	20	3079.65	3087.55	3083.60	5.59
With reflectance	20	3095.46	3131.04	3113.25	25.16
W/O reflectance	40	3433.43	3437.38	3435.41	2.79
With reflectance	40	3480.74	3492.63	3486.69	8.41
W/O reflectance	60	2903.18	2922.93	2913.06	13.97
With reflectance	60	2922.93	2926.88	2924.91	2.79

Table 4.25: 1mm wide test pieces with and without exposure to reflectance from silicon nitride at 200mm/s scan speed.

The results of the two reflectance tests (SRT and PRT) are summarised for comparison in Table 4.26.

Average LSC due to reflectance with scan speeds for the SRT and PRT.			
	50mm/s	100mm/s	200mm/s
SRT	839.4	213.1	177.7
PRT	170.7	103.9	19.8

Table 4.26: Average difference in CLW due to reflectance at increasing scan speeds (reducing exposure) for the SRT and PRT tests.

The reducing trend in LSC with increasing scan speed is much more pronounced with the PRT tests (Table 4.23 to Table 4.25) than with the SRT tests (section 4.1.4.1). Additionally, the PRT results are more consistent and possess much reduced variance with a maximum standard deviation of 52 μm at 50mm/s. The PRT test results are further analysed and compared with modelled results in section 5.1.5.3.

4.2. Adhesion investigation results

The following sections (4.2.1 to 4.2.7) present the results from experimentation pertaining to adhesion. The corresponding methodology is described in subchapter 3.4. and the findings of the results are discussed in subchapter 5.2. The results from characterising the photopolymer and the substrates are included in section 4.2.1, followed by tensile (section 4.2.2) and shear (4.2.3) adhesion tests. The results of experimentation to measure shrinkage and strain to determine their influence on adhesion, are included in section 4.2.4. Images taken to examine the interface between the SLA polymer and a substrate are shown in section 4.2.5 and surface images of defects in 4.2.6. Lastly the results of experiments applying potential methods to enhance adhesion are shown in section 4.2.7.

4.2.1. Characterising material properties

The results of material characterisation for elastic modulus (method 3.4.2.5), Poisson's ratio (method 3.4.2.6), maximum force at break (method 3.4.2.6) and surface free energy (method 3.4.2.4) are shown below (Figure 4.5). Additional supporting data is included in Appendix G.

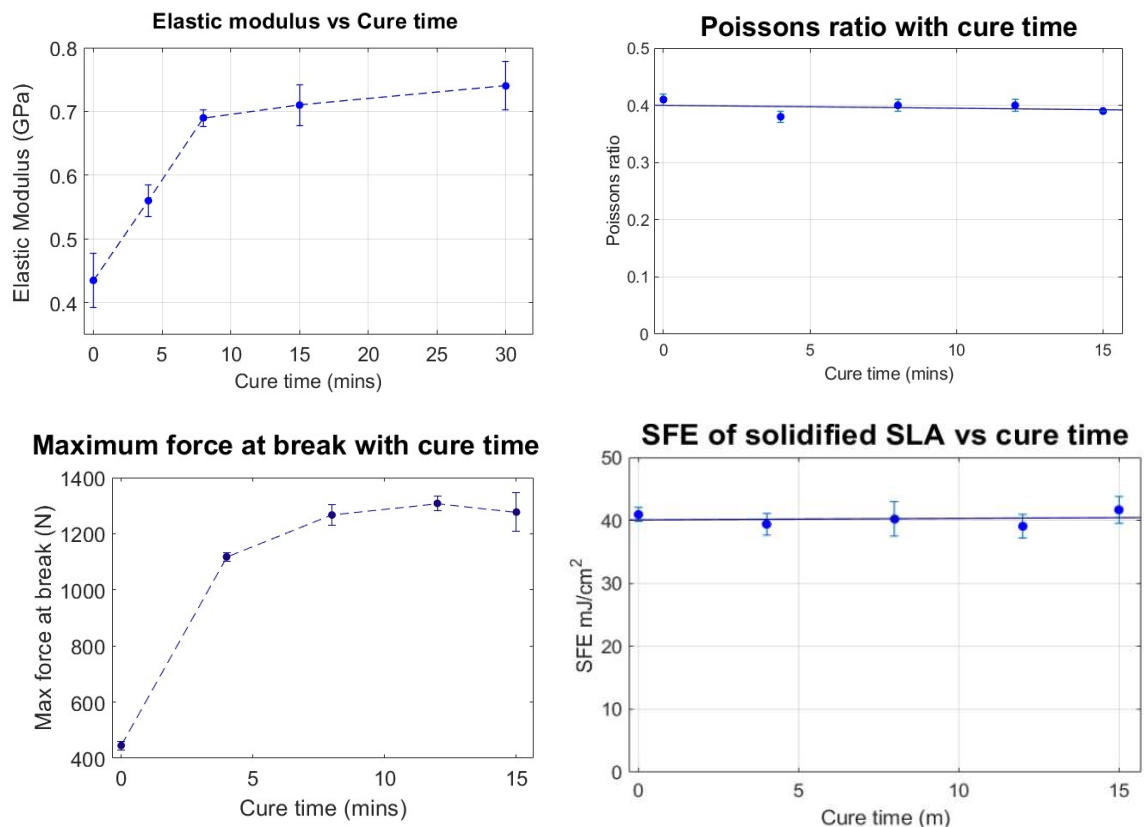


Figure 4.5: SLA polymer characterisation

[Top left] Change in elastic modulus of solidified polymer with cure time. [Top right] Poisson ratio with cure time. [Bottom left]. Maximum break force with cure time. [Bottom right] Surface free energy with post build cure time.

The interfacial tension of liquid FLC resin was measured using the method described in section 3.4.2.2 at $29.93\text{mJ}\cdot\text{m}^{-2}$.

The results (Figure 4.5) of the SLA polymer (FLC) characterisation results show surface free energy and Poisson's ratio to be uninfluenced by post build curing (PBC). In contrast a significant increase in the elastic modulus ($\sim 90\%$) and tensile strength ($\sim 65\%$) of the material with progressive PBC (up to 15 minutes). These properties are discussed further in section 5.2.2. Quantification of these characteristics is also used to support the investigations into the material's adhesion properties and are used for analysis throughout section 5.2.

4.2.1.1. FTIR

The use of FTIR (method H) to measure the relative presence of C=C double bonds and in turn the extent to which the photopolymer has polymerised and cross-linked is shown in Figure 4.6 (raw data in Table G1.20 Appendix G).

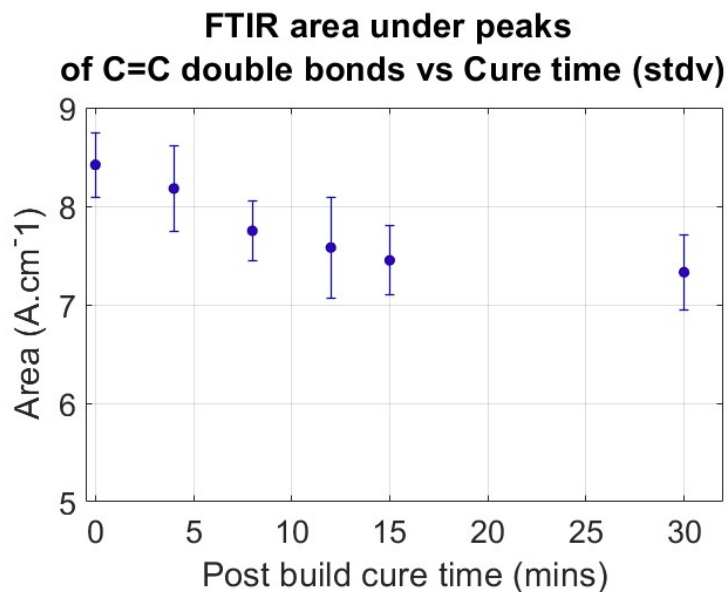


Figure 4.6: Area of FTIR peaks (1637cm^{-1} and 1407cm^{-1}) corresponding to C=C bonds against PBC time.

The C=O area for unexposed liquid photopolymer was measured using the same process at $9.772\text{A}\cdot\text{cm}^{-1}$. Figure 4.6 exhibits a clear downward trend in the presence of C=C bonds with cure time up to 15 minutes. This indicates that the Formcure equipment produces significant variation in the extent of cross-linking during this period. Consequently, the equipment will be used for the investigations into shrinkage and adhesion during PBC.

4.2.1.2. Consistency of substrate measurements

To identify effective sample preparation, the consistency of the substrate was measured by the variation (standard deviation) in the contact angle of multiple droplets deposited across the surface using the method described in section 3.4.2.1.

Consistency of substrate measurements		
Material	Avg Contact Angle	Standard deviation
Silicon nitride as received	58.1	1.4
Silicon nitride washed with acetone and IPA	43.8	0.7
PC (as received)	64.1	3.2
PC washed with acetone	76.9	5.8
PC washed with IPA	76.8	1.5
PC washed with detergent	72.9	2.1
All soda lime glass (as received)	16.2	8.6
Soda lime glass washed with acetone and IPA	31.7	1.0
Soda lime glass plasma treated and coated with TMSPPMA monolayer described in section 3.4.6.1.	40.2	1.8
Solidified photopolymer*	73.8	7.0
Solidified photopolymer* built on glass substrate	59.8	0.5
Alu samples washed with acetone and IPA	62.3	3.7
All polished alu samples washed with acetone and IPA	64.1	3.2

Alu = Aluminium

PC = Polycarbonate

*No post build curing

Table 4.27: Average contact angle and the standard deviation of water droplets on different substrates to indicate the consistency of the substrate surface.

The results of this analysis (Table 4.27) show all the substrates to exhibit some variance in the contact angle, with the most consistent being silicon nitride washed with acetone and IPA (STDV = 0.7) and SLA slabs constructed onto soda lime glass (STDV = 0.5).

Constructing SLA slabs onto glass significantly improved the surface consistency compared with free-standing samples (constructed on supports) (STDV = 7.0). Interestingly, the SLA slabs on glass exhibited a lower variance than the substrate onto which they were constructed (STDV = 1.0). The lotus effect (section 2.4.4) of the photopolymer on the substrate may contribute to this by preventing the resin from entering smaller pores resulting in a more consistent and smoother surface. The improved consistency of the silicon nitride, and SLA polymer samples, identified these techniques as effective surface preparation methods for adhesion testing (methods 3.4.5 to 3.4.6) and SFE measurement (method 3.4.2.4).

Acetone was observed to etch the surface of polycarbonate and consequently decreased the consistency of the surface as shown in Table 4.27. Conversely, washing with IPA improved the surface consistency of polycarbonate samples and was used for preparing the material for subsequent experimentation.

Unlike PC and due to soda lime glass being resistant to acetone, the consistency of the material was substantially improved (Table 4.27) by washing with that solvent followed by IPA. Consequently, this process was applied to prepare the material for subsequent testing.

The adopted method of sequential polishing (method 3.4.3.1.) used prepare samples of aluminium, reduced the standard deviation (Table 4.27) from 3.7 to 3.2.

Additionally, the DSA of soda lime glass (Table 4.27) showed the TMSPMA coating reduced the surface consistency from a STDV of 1.0 to 1.8 but was significantly improved compared the glass as-received and comparable to washed PC (1.5). This provides confidence that the process applies the treatment and monolayer sufficiently evenly for subsequent testing.

4.2.1.3. Work of adhesion and interfacial tension

The interfacial tension and work of adhesion, measured using the methods described in sections 3.4.2.2, and 3.4.2.3 respectively are shown in Table 4.28. IFT and the WoA are calculated using the Laplace (Equation 2.6) and the Young-Dupres (Equation 2.11) methods.

Work of adhesion and interfacial tension.		
Liquid / parameter	Water	Formlabs clear resin
Interfacial tension (mJ/m ²) (Pendant droplet)	72.4	29.9
Average contact angle on glass (degrees)	31.7	35.2
WoA on glass (mJ/m ²)	133.9	54.4
Average contact angle on Aluminium (degrees)	64.1	11.2
WoA on aluminium (mJ/m ²)	-	59.3
Average contact angle on PC (degrees)	76.8	14.0
WoA on PC (mJ/m ²)	-	59.0
Average contact angle on silicon nitride (degrees)	43.7	31.0
WoA on silicon nitride (mJ/m ²)	124.6	55.6

Table 4.28: IFT, contact angle and WoA of water and resins on substrates.
(Raw data included in Appendix G.)

All the substrate materials (i.e., glass, PC, aluminium and silicon nitride) were demonstrated to be hydrophilic with a contact angle <90° (Table 4.28). The work of adhesion calculated for Formlabs clear (55.6mJ/m²) photopolymer on a Si₃N₄ substrate was comparable to that

on a glass substrate (54.4mJ/m²) and 6% less than on aluminium (59.3mJ/m²) and PC (59.0mJ/m²). This provides confidence that the SLA photopolymer is sufficiently compatible with the substrate materials for products to form without surface treatment.

4.2.1.4. Surface roughness

The following results for the surface roughness of the respective substrates were obtained (method section 3.4.3.1) using a Zygo interferometer.

Surface roughness of substrate materials.			
Substrate material	Sa [Arithmetic mean] μm	Sq (RMS) μm	Sz (peak) μm
Build Platform	2.064	2.604	15.307
Glass	Could not measure (could not obtain focus)		
Aluminium plate	0.381	0.524	4.190
Silicon nitride wafer (used)	0.005	0.007	0.145
Silicon nitride wafer (new)	0.001	0.001	0.006
Polycarbonate	0.007	0.016	0.938

Table 4.29: Surface roughness of substrate materials.

These results (Table 4.29) show silicon nitride to be extremely smooth with an average (RMS) surface roughness of 0.001 μm and on the limits of detection. In contrast the surface roughness of aluminium plate, and particularly the build platform, possess a comparably high surface roughness. The implication of the roughness measurements on reflectance, and adhesion mechanisms are used for analysis in sections 5.1.5.3 and 5.2.1. Additionally, the results are used for discussion in 5.2.7.3 (causes of low force failure and variance).

4.2.2. Tensile adhesion tests

The tensile separation force with increasing PBC (method 3.4.4), on PC and aluminium, together with the change in elastic modulus (method 3.4.2.5), are shown in Figure 4.7 and Figure 4.8 respectively. Additional, raw data is included in section 7.5.1 of Appendix G. These results are compared and discussed in section 5.2.3.

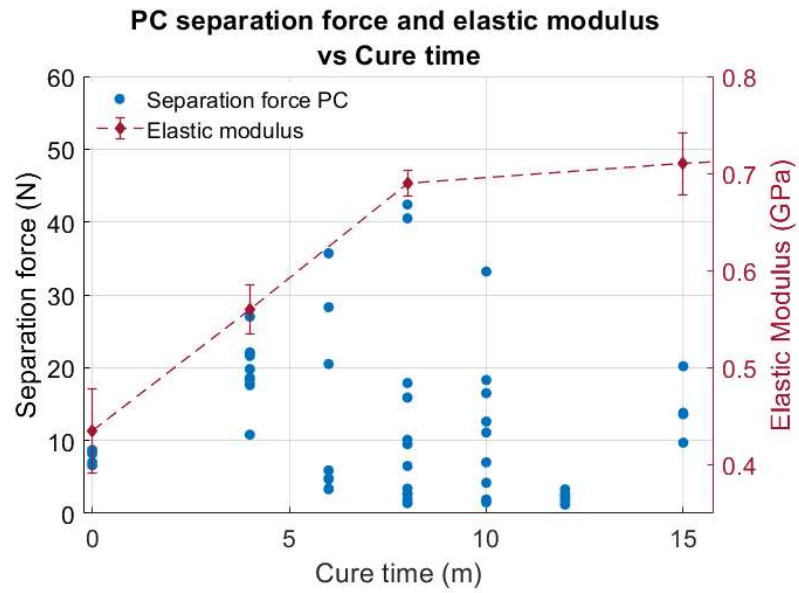


Figure 4.7: Separation force of 1mm² test pieces on PC and elastic modulus with cure time.

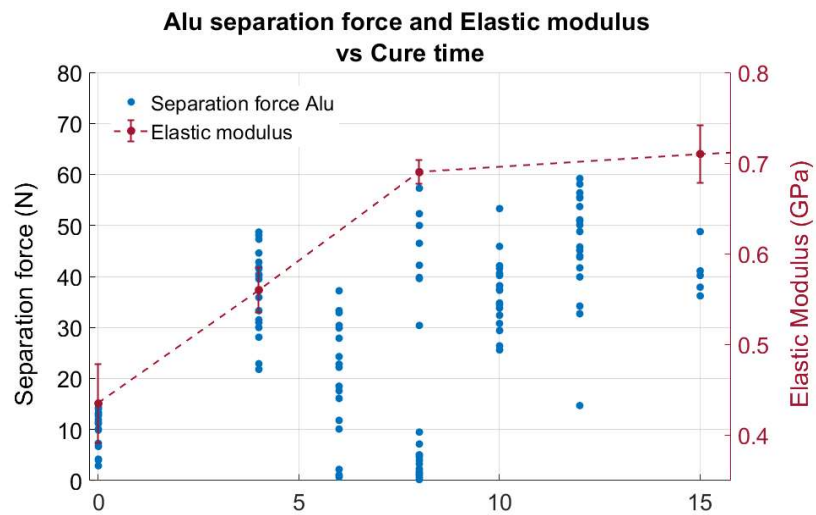


Figure 4.8: Separation force of 1mm² test pieces on aluminium and elastic modulus with cure time.

Tensile test footprints on untreated substrates.

Example, optical microscope images of the residue retained on untreated silicon nitride following tensile tests, after increasing periods of PBC are shown in Figure 4.9. Additional images are included in Appendix G (section 7.5.5).

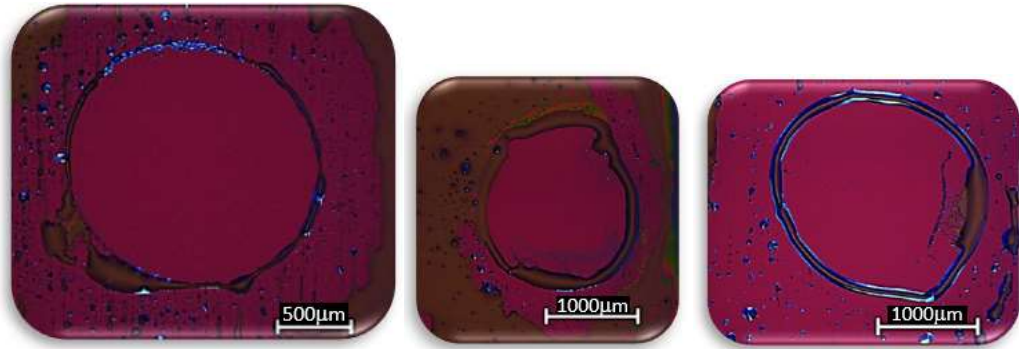


Figure 4.9: Footprints from tensile tests on silicon nitride
 [Left] Footprint of green (no PBC) tensile test pieces on untreated substrate (500µm scalebars),
 [Centre] after 2 mins of curing (1000µm scalebars), [Right] after 8 mins of curing (1000µm scale bars).

The results of tensile tests on PC (Figure 4.7) and aluminium (Figure 4.8), show the peak separation force recorded, to initially increase with progressive post build curing (PBC). This trend flattens after approximately 8 minutes of PBC on aluminium but decreases on PC. However, there is a high degree of variance in the results, which is typical [63] with tensile tests. Consequently, further analysis was conducted using shear tests (section 4.2.3).

4.2.3. Shear tests

The adhesion tests are completed with the results of shear tests using the frustum shaped test pieces and method described in section 3.4.5.1 constructed onto PC and silicon nitride shown in Figure 4.10 and Figure 4.11. Additional, raw data is included in section 7.5.2 of Appendix G.

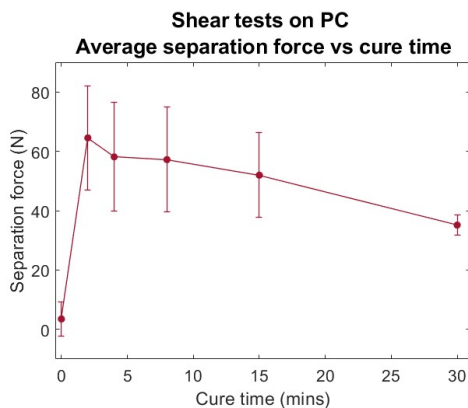


Figure 4.10: Frustum shear tests on PC

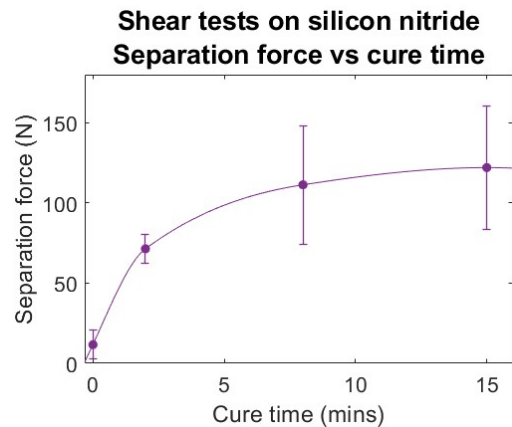


Figure 4.11: Frustum test pieces on silicon nitride

The shear separation force measured on PC (Figure 4.10) and silicon nitride (Figure 4.11) increases by over an order of magnitude with a limited period (2-8 minutes) of PBC. Additionally, the variance in the results of PC (Figure 4.10) is much reduced compared to tensile tests (Figure 4.7). The results of the frustum shear tests results are discussed further in section 5.2.5.

4.2.4. Shrinkage and strain during post build curing

The strain produced by shrinkage during PBC was recorded (Figure 4.12) using embedded gauges with progressively longer periods of PBC and following the method described in section 3.4.2.7. In all tests, the strain generated by shrinkage is eventually counteracted by the thermal expansion due to the elevated temperature of the cure oven, to form a knee point. Direct measurement of the shrinkage (method 3.4.2.8) before and after PBC is included in Table 4.30 for comparison.

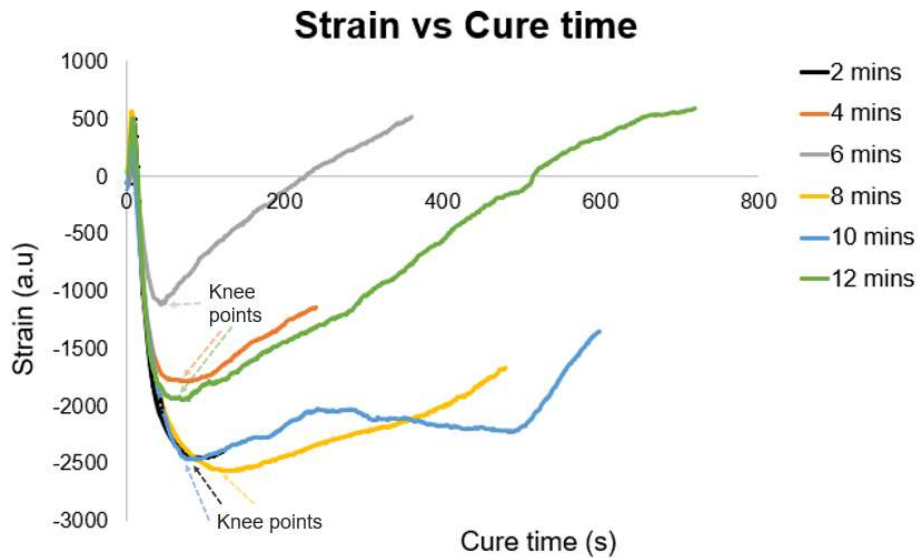


Figure 4.12: Gauge strain (arbitrary units) vs cure time for samples after different periods of PBC.

From these test results (Figure 4.12) have been combined to give an average profile in (Figure 4.13 [left]). However, the differences between each test due to temperature and absolute shrinkage, result in a step change in the profile at the transition points as each test expires (Figure 4.13). To compensate for this step change at the transition times (t_T), a correction value (Equation 4.1) for each transition has been applied.

$$\bar{\epsilon}_{n_6, t_{T1}} - \bar{\epsilon}_{n_5, t_{T1}} = C_{T1}$$

$$C_{T1} + (\bar{\epsilon}_{n_5, t_{T2}} - \bar{\epsilon}_{n_4, t_{T2}}) = C_{T2}$$

$$C_{T1} + C_{T2} + (\bar{\epsilon}_{n_4, t_{T3}} - \bar{\epsilon}_{n_3, t_{T3}}) = C_{T3}$$

$$C_{T1} + C_{T2} + C_{T3} + (\bar{\epsilon}_{n_4, t_{T4}} - \bar{\epsilon}_{2, t_{T4}}) = C_{T4}$$

$$C_{T1} + C_{T2} + C_{T3} + C_{T4} + (\bar{\epsilon}_{n_2, t_{T5}} - \bar{\epsilon}_{1, t_{T5}}) = C_{T5}$$

Equation 4.1: Derivation of correction factors for averaging uncompensated strain tests.

where $\bar{\epsilon}$ is the average strain, n is the number of active readings, C_T is the correction factor, t_{T1} is the time at the first transition.

The correction factors obtained from Equation 4.1 are applied to the raw data shown in Figure 4.13 [left] to obtain the corrected profile in Figure 4.13 [right].

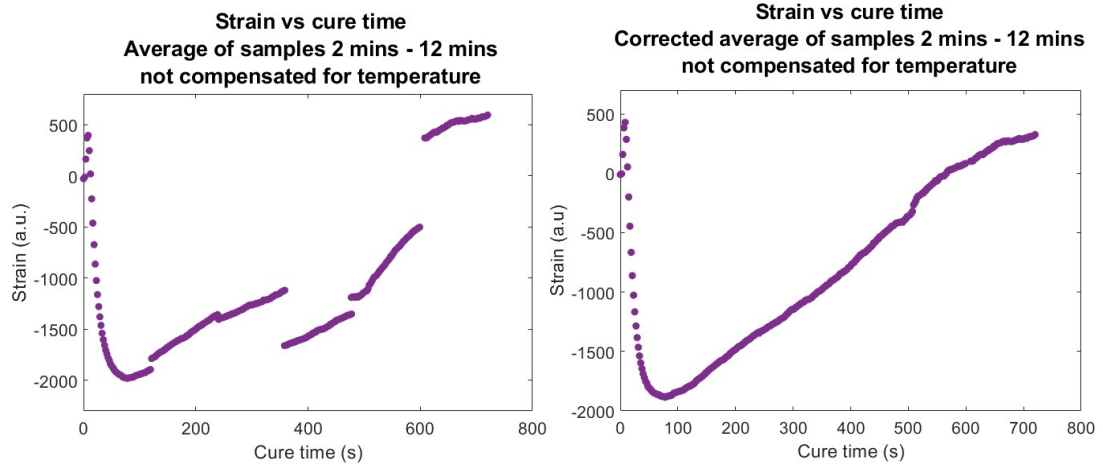


Figure 4.13: Average and corrected average strain (gauge) vs cure time [left] Average for samples 2 mins - 12 mins, [right] corrected average for samples 2-12 mins.

The influence of temperature is apparent at the knee point in these results (Figure 4.12) where the rate of thermal expansion equals shrinkage after approximately 90 seconds.

Table 4.30 shows the manually measured shrinkage (method 3.4.2.8) of the uncompensated strain test pieces after increasing periods of PBC. This is arranged in order of magnitude together with the corresponding strain measured at the knee point in Figure 4.14 for direct comparison in Table 4.31.

Manually measured length of the uncompensated strain test pieces before and after PBC.								
Measurement no. / Cure time.	1	2	3	4	5	Average	STDV	Shrinkage (mm)
2 mins Green (mm)	24.33	24.36	24.33	24.33	24.35	24.34	0.01	
PBC length (mm)	24.29	24.25	24.28	24.27	24.27	24.27	0.01	0.068
4 mins Green (mm)	24.22	24.23	24.20	24.19	24.18	24.2	0.02	
PBC length (mm)	24.18	24.16	24.15	24.18	24.14	24.16	0.02	0.042
6 mins Green (mm)	24.33	24.30	24.31	24.32	24.31	24.31	0.01	
PBC length (mm)	24.28	24.27	24.27	24.27	24.27	24.27	0.01	0.040
8 mins Green (mm)	24.29	24.30	24.29	24.30	24.30	24.30	0.01	
PBC length (mm)	24.23	24.20	24.25	24.23	24.22	24.23	0.02	0.070
10 mins Green (mm)	24.15	24.15	24.14	24.16	24.16	24.15	0.01	
PBC length (mm)	24.08	24.09	24.11	24.10	24.08	24.09	0.01	0.060
12 mins Green (mm)	24.33	24.33	24.30	24.28	24.28	24.30	0.03	
PBC length (mm)	24.28	24.26	24.19	24.2	24.23	24.23	0.04	0.072

Table 4.30: Measured length of the uncompensated test strain test pieces before and after PBC.

The influence of temperature on the recorded strain from shrinkage.				
Measured shrinkage in order of magnitude		Values at knee point (Figure 4.12)		
PBC time (mins)	Shrinkage (mm)	Strain	Time	Temp
6 minutes	0.040	-1100	54	27.5
4 minutes	0.042	-1780	75	23.5
10 minutes	0.060	-2460	91	24.7
2 minutes	0.068	-2450	100	24.5
8 minutes	0.070	-2570	122	23.8
12 minutes	0.072	-1955	71	27.4

Table 4.31: Measured shrinkage of uncompensated strain test pieces in order of magnitude and their corresponding strain, temperature, and time at the knee point (Figure 4.12).

There is some variation between the strain profiles of the individual uncompensated embedded gauge measurements (Figure 4.14) which is attributed variation in the test temperature (Table 4.31). Tests conducted at higher test temperatures (i.e., 6 mins and 12 mins) exhibit disproportionately lower strain values (absolute) and an increased rate of strain after the knee point (Figure 4.12) due to thermal expansion.

To compensate for the influence of temperature, multiple strain gauges were added the circuit and arranged in a Wheatstone bridge (section 3.4.2.7) from which the strain profiles during PBC in Figure 4.14 were obtained. From these, an average combined strain profile was generated (Figure 4.15).

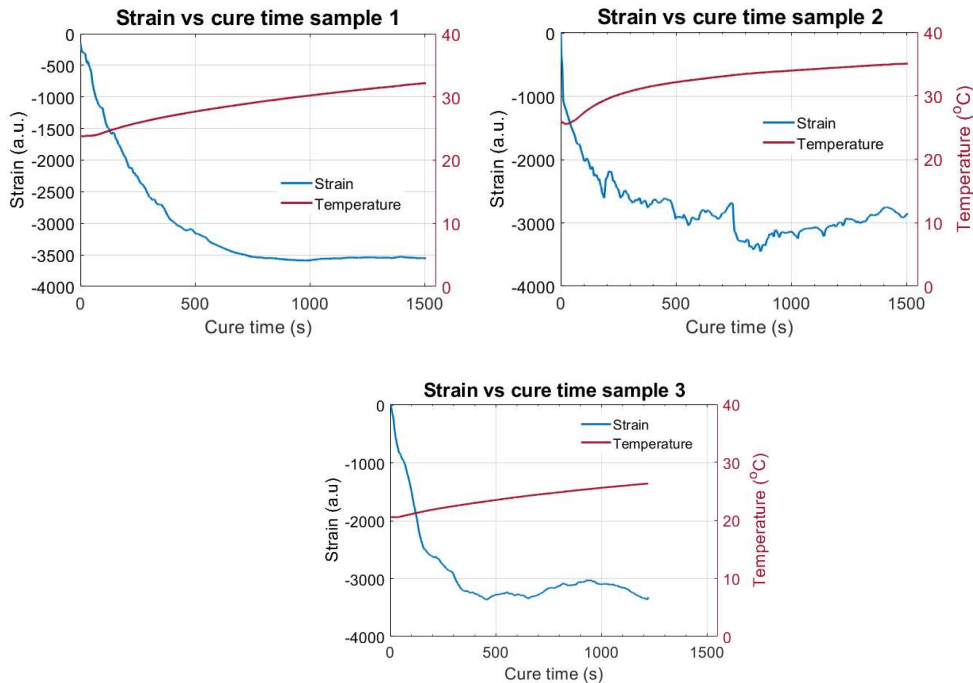


Figure 4.14: Strain vs cure time with temperature compensation samples 1 to 3.

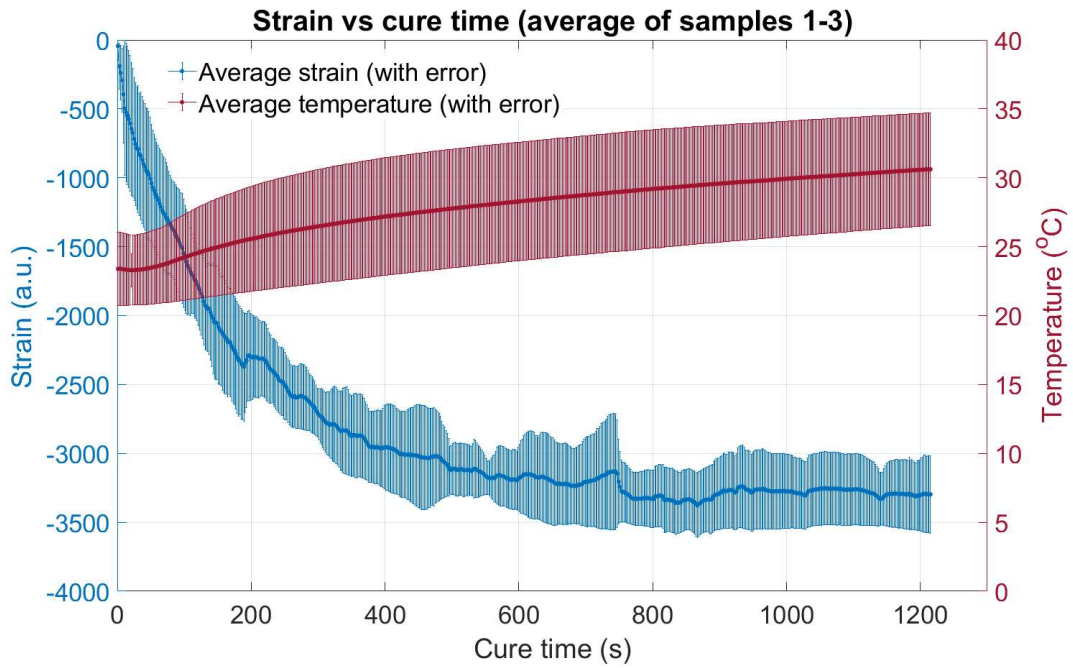


Figure 4.15: Strain vs cure time with temperature compensation (Average of samples 1-3 with error).

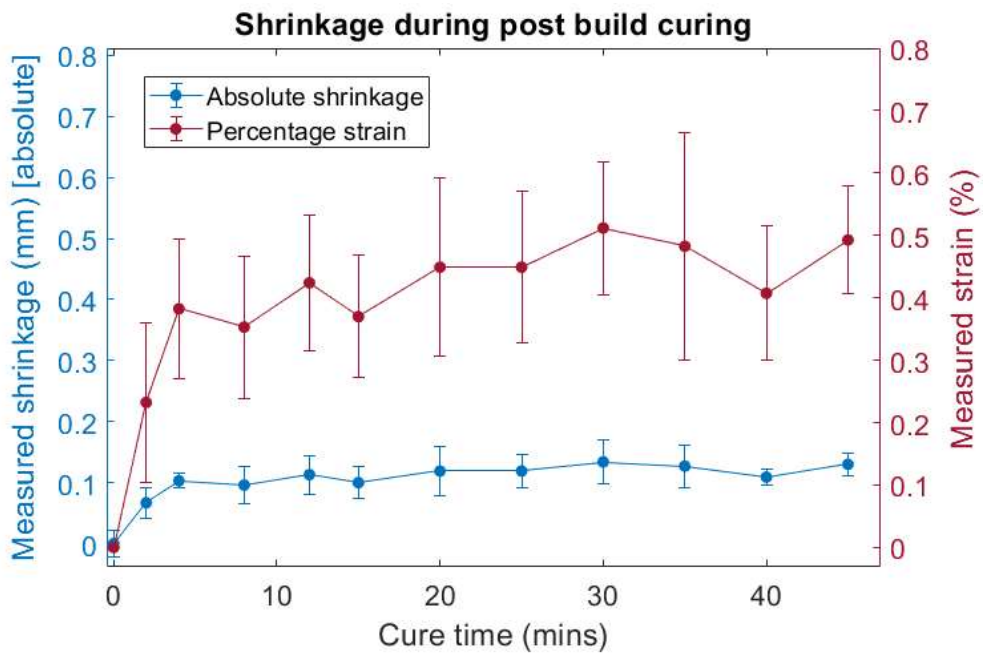


Figure 4.16: Manually measured (method 3.4.2.8) absolute shrinkage and strain with PBC time.

The shrinkage of test pieces measured manually (method section 3.4.2.8) at intervals throughout the PBC curing process is shown in Figure 4.16 (raw data in appendix G, section 7.5.3). This includes the absolute measurement in millimetres and the corresponding strain as a percentage of the original length. The total shrinkage after 45 minutes of cure was measured at 130 μ m (0.49% of the original length). The compensated strain profile (Figure 4.15) and the manually measured shrinkage (Figure 4.16) are compared and discussed in section 5.2.7.1.

4.2.5. Sectioned interface images

To examine the interface for evidence of structural interactions (section 2.4.2.2) or intermingling (section 2.4.2.3) between an SLA construction and a polycarbonate substrate, samples were prepared following the method described in section 3.4.3.4. Optical microscope images (Figure 4.17) and SEM images (Figure 4.18) taken of the sectioned interface are shown below. Additional SEM images are included in Appendix G (section 7.5.6).

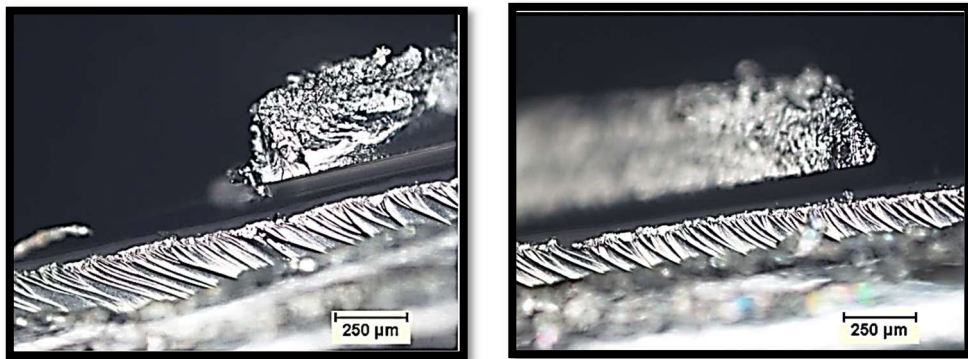


Figure 4.17: Optical microscope image of sectioned interface between an SLA construction (Form 2 default settings 100µm layer thickness) on polycarbonate.

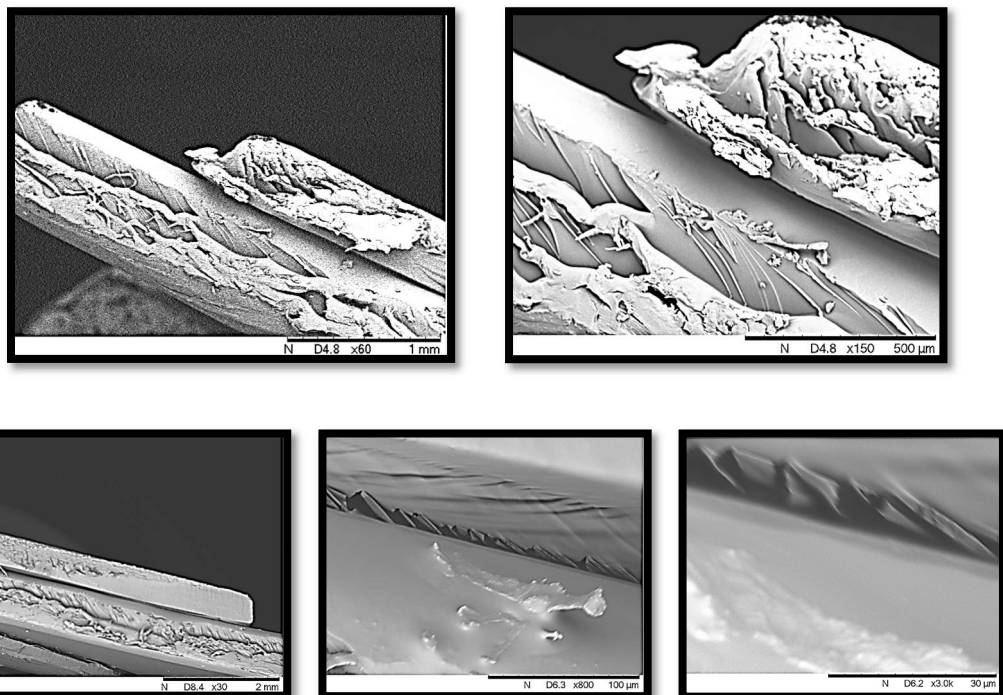


Figure 4.18: SEM images of SLA interface on PC
[Top row] SEM image of sectioned contact (LHS profile) between SLA construction (Form 2 default settings 100µm layer thickness) onto polycarbonate (60x and 150x magnification, left and right respectively). [Bottom row] SEM images of the same SLA sample interface (RHS profile) with SLA onto of PC (30x, 800x, and 3000x magnification from left to right).

Splinters are observed at the interface between the sectioned SLA polymer and the PC substrate (Figure 4.18 bottom row), but the images are inconclusive as to the mechanism of attachment with minimal mechanical interactions identified.

4.2.6. Surface defects (Entrapped gas)

SEM images of SLA samples constructed on a Form 2 using photopolymer after an extended settling period (~14 hours), and immediately following prolonged operation (2 hours), are shown in Figure 4.19.

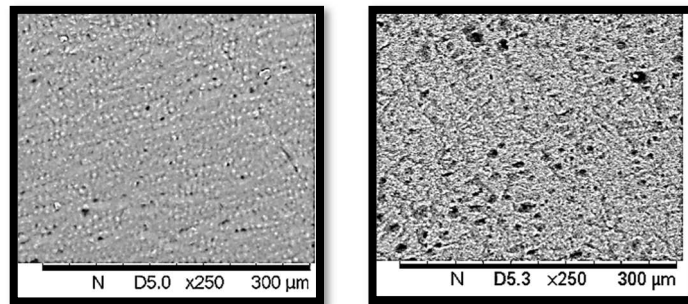


Figure 4.19: SEM imaging of SLA product surface [Left] after a prolonged period of settling (x250 magnification) and [right] after 2 hours of operation (x250 magnification). Samples constructed using Form 2 default settings 100 μ m layer thickness.

A significant increase in the presence of defects from entrapped gas is evident in the image of the righthand sample constructed using photopolymer after prolonged operation. These results are used for discussion in section 5.2.7.4.

4.2.7. Enhancing adhesion

Three methods to enhance the adhesion of an SLA polymer to a substrate were identified from the review of literature in Chapter 2. These include dosing the photopolymer with CSR, varying lateral cure, and surface treatment of the substrate for which experiments were devised in sections 3.4.6.1 to 3.4.6.3. The results of these experiments are shown below in sections 4.2.7.1 to 4.2.7.3 and discussed in subchapter 5.2.

4.2.7.1. Core shell rubber

When adding CSR to SLA photopolymer, the resulting increase in viscosity and potential impact on the reliability of construction, has been identified as a concern (section 3.4.6.2). Consequently, the viscosity profile of the CSR was measured at increasing concentrations up to 25% v/v (Figure 4.20). This showed a linear relationship between the concentration of CSR and the viscosity with a peak of 1.02 Pa.s. which is substantially below the limit for SLA construction quoted by Taormina [119] of 5 Pa.s.

Another concern was the potential deposition of particles from suspension which the analysis conducted in section 3.4.6.2 quantified at approximately 1mm per minute for the larger particles, necessitating the continued operation of the wiper blade to provide intermittent mixing.

The resulting measured shear separation force (method 3.4.5.1) of SLA test pieces (frustum) dosed with increasing proportions of CSR and constructed onto PC are shown in Figure 4.21 and discussed in section 5.2.8.1.

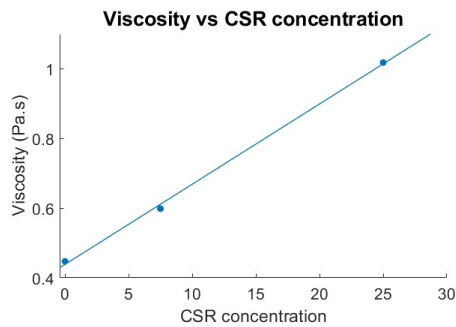


Figure 4.20: Viscosity vs CSR concentration (liquid FLC photopolymer)

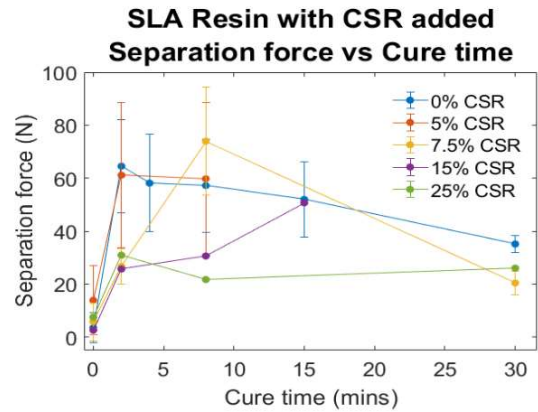


Figure 4.21: Separation force of SLA photopolymer with CSR in shear tests (frustum test piece) on PC against cure time. Constructed using Form 2 default settings (100µm layer thickness).

SEM images of CSR particles are included in Figure 4.22, and of sectioned SLA samples containing CSR (method section 3.4.3.4) in Figure 4.23. The sectioned samples observed under an optical microscope are shown in Figure 4.24.

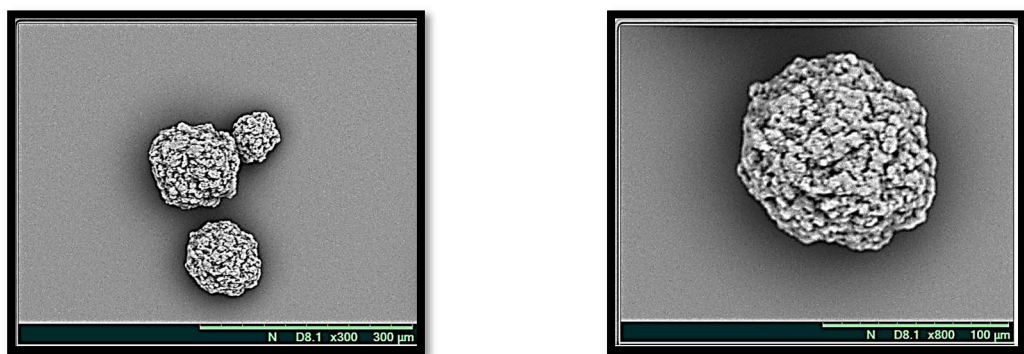


Figure 4.22: [Left] SEM image of CSR particles (300x magnification). [Right] SEM image of free-standing CSR particle (800x magnification).

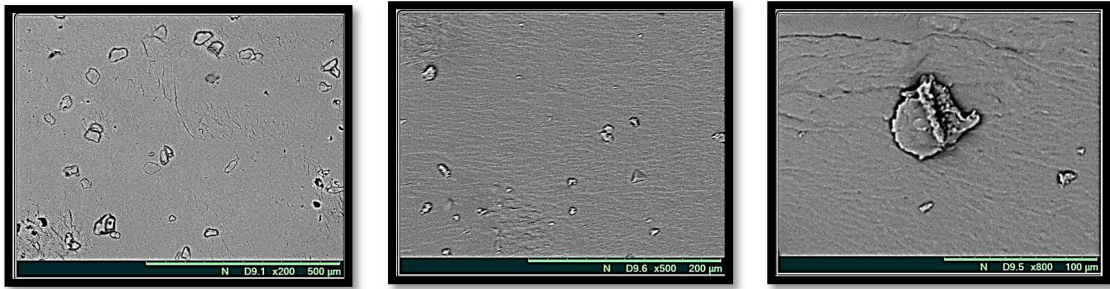


Figure 4.23: SEM image of sectioned SLA sample containing CSR. [Left] SEM image of sectioned sample at 200x magnification, [centre] SEM image of sectioned sample x 500 magnification, [right] sample at 500x magnification. Constructed using Form 2 default settings (100μm layer thickness).

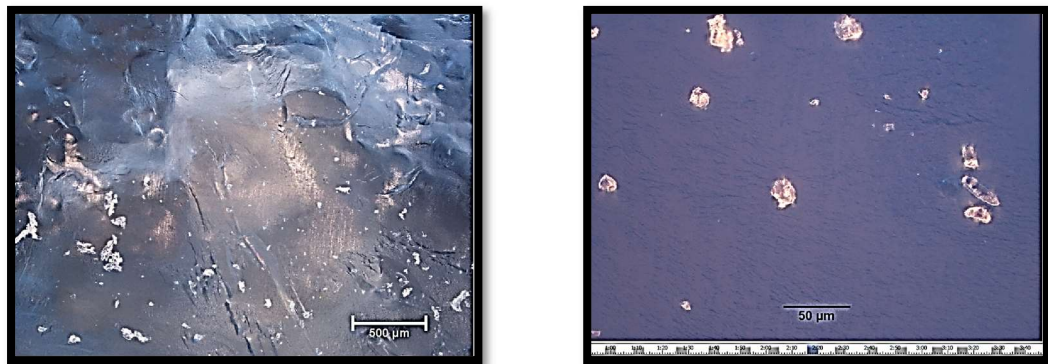


Figure 4.24: Optical microscope image of sectioned SLA sample containing CSR. [Left] Microscope image of sample at 5x magnification. [Right] Microscope image of at 50x magnification. Samples constructed using Form 2 default settings (100μm layer thickness).

The aim of sectioning the CSR samples was to investigate the line fracture around the CSR particles. CSR particles are visible at the surface of the fractured samples shown in Figure 4.23 and Figure 4.24. This indicates that the line of fracture has passed around the particle and the crack has not been dissipated by the CSR particles.

Defects with core shell rubber

Optical microscope images showing the presence of defects at the interface between an SLA construction containing 7.5% and 25% v/v CSR, and a polycarbonate substrate (method section 3.4.6.2) are shown in Figure 4.25.

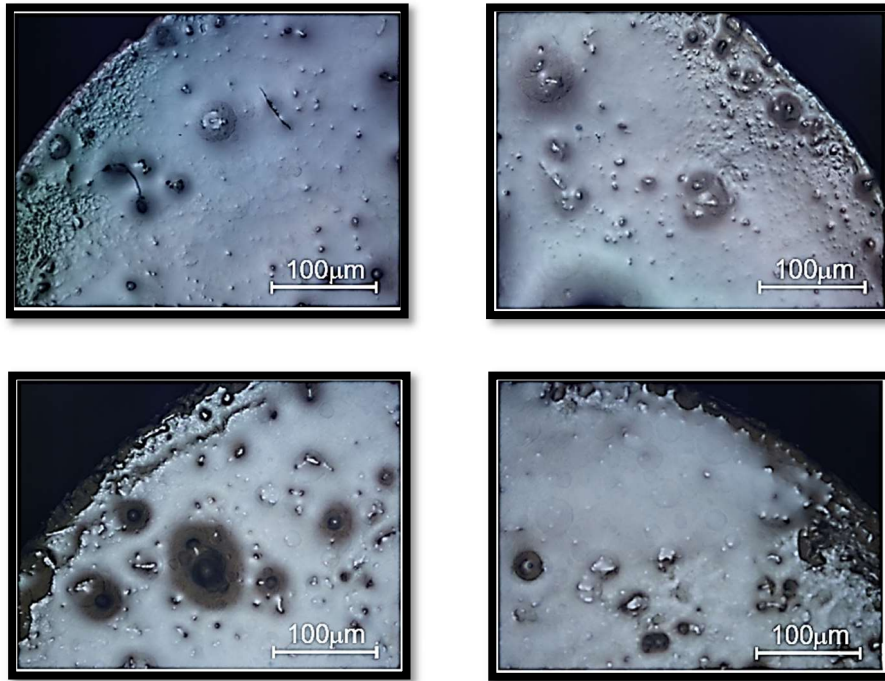


Figure 4.25: Optical microscope images from underside of SLA samples containing CSR. [Top row] Underside of 7.5% v/v CSR tensile test piece on PC. [Bottom row] Underside of 25% v/v CSR tensile test piece on PC. Samples constructed using Form 2 default settings (100µm layer thickness).

The images in Figure 4.25 show a number of defects at the interface between the SLA polymer (dosed with CSR) and the substrate (polycarbonate). These defects are attributed to the presence of CSR particles and consequently are expected to increase with the concentration of CSR particles. This compromises the strength of adhesion with the substrate and is discussed further in section 5.2.8.1.

4.2.7.2. Varying lateral cure.

The exposure was varied laterally across SLA samples using the method described in section 3.4.6.3 with the aim of constructing frustum test pieces possessing a composite modulus.

The influence on adhesion was then measured using a shear test (method section 3.4.5.1). The results of these tests are shown in Figure 4.26 alongside the separation force of test pieces constructed using standard exposure settings for comparison. The raw data is included in table G1.28 (Appendix G).

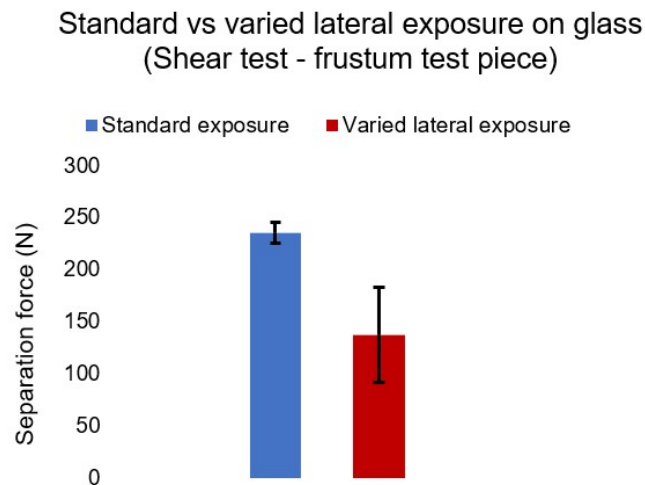


Figure 4.26: standard (Form 1+ default machine settings) vs varied exposure (section 3.4.6.3) shear test results (frustum test piece) on glass.

Figure 4.26 shows a reduced shear separation force (~42%) and increased variance for the test pieces (frustum) with varied exposure applied. These results are discussed further in section 5.2.8.2.

4.2.7.3. Treated silicon nitride.

The third method applied to enhance adhesion was by surface treatment to promote the chemical bonding mechanism. The force required to separate SLA test pieces from treated (method section 3.4.6.1) and untreated silicon nitride in tensile tests (method 3.4.4) and shear tests (3.4.5.2), are shown in Figure 4.27 and Figure 4.30 respectively. Raw tensile, and shear test data is included in tables G1.24.1 to G1.24.2, and G1.27.1 to G1.27.2 (Appendix G), respectively. Optical microscope images of the SLA material retained on the substrate after tensile testing and with increasing periods of PBC are included in Figure 4.29.

Separation Force Coated and uncoated wafer vs Cure time

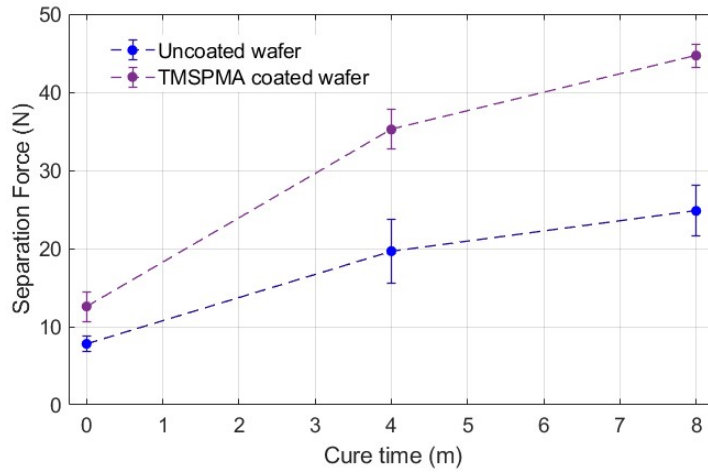


Figure 4.27: Tensile test results on TMSPPMA treated and untreated silicon nitride. Samples constructed using Form 2 default settings (100µm layer thickness).

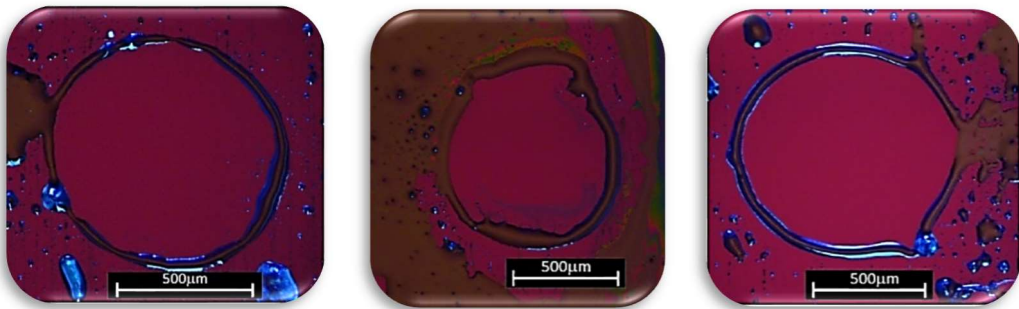


Figure 4.28: Residual footprints from tensile test pieces on untreated silicon nitride [Left] without PBC, [centre] 2 minutes of curing, and [right] 8 minutes of post build curing. Samples constructed using Form 2 default settings (100µm layer thickness).

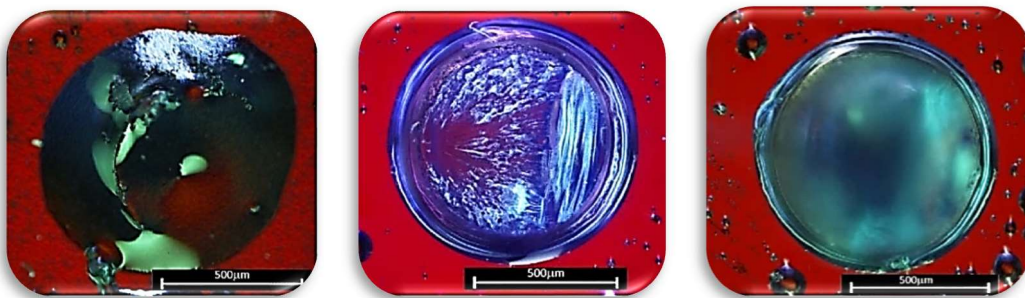


Figure 4.29 Residual stems parts of tensile test pieces on treated silicon nitride demonstrating cohesion failure [left] without PBC, [centre] 2 minutes of PBC and [right] 8 minutes of PBC. Samples constructed using Form 2 default settings (100µm layer thickness).

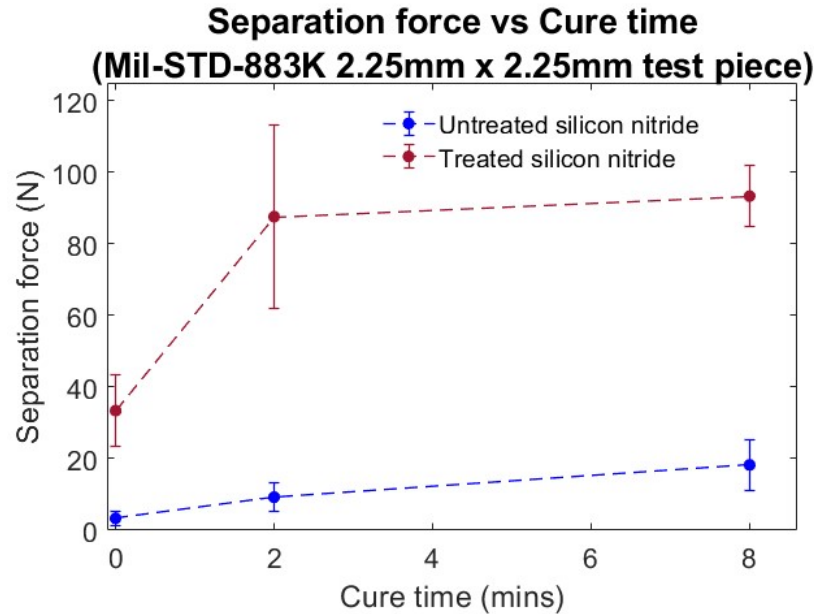


Figure 4.30: Separation force of MIL-STD-883 shear test pieces on untreated and treated silicon nitride.

The separation force of the test pieces with treated silicon nitride is measured to increase after a limited period of PBC (2-4 minutes) in both the tensile (Figure 4.27) and shear tests (Figure 4.30). The strength of adhesion was also substantially increased in both tests by the application of the surface treatment (method section 3.4.6.1). Additionally, the point of separation with the untreated silicon nitride in the tensile tests was at the interface with the test piece (Figure 4.28). In contrast, tensile test pieces constructed onto treated silicon nitride failed in the stem of the constructions (Figure 4.29) which is indicative of cohesive failure. This indicates the application of the surface treatment has promoted the strength of adhesion to an extent above the cohesive strength of the material. These results are discussed in section 5.2.8.3 where they are compared with the requirements of the MIL-STD-883 standard.

4.3. Inserting geometries results and observations.

The first of the 4 steps (section 3.5) to developing an SLA structural electronic package, was to review previous work, and conducted as part of the literature review (chapter 2). The second step was to identify suitable test geometries and components, the output of which is applied to develop the associated constructed methods (section 3.5.2 and 3.5.3). These are applied to construct the demonstration pieces in steps III and IV, the results of which are shown in sections 4.3.1 to 4.3.3. These pieces included a stacked module concept (4.3.1), a concept to insert multiple components (4.3.2), and lastly a structural electronic package with multiple components connected electrically (4.3.3).

4.3.1. Step III Stage A: Stacked module concept

Constructions produced from the method described in section 3.5.2.1 (Step III: stage A) for stacking multiple modules and compressing them into a package, is shown in Figure 4.31. These modulus were subsequently constructed onto silicon nitride and again compressed into a single package (Figure 4.32) and discussed in section 5.3.1.

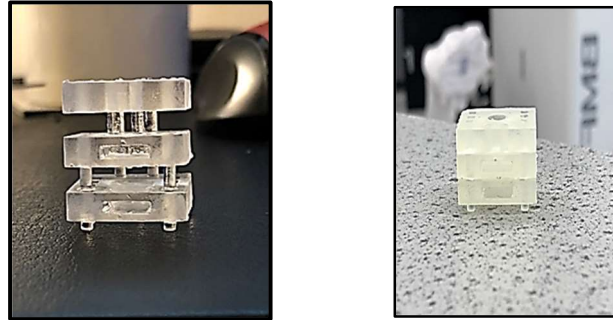


Figure 4.31: Example of stacked modules (left) and compressed to form a package (right).

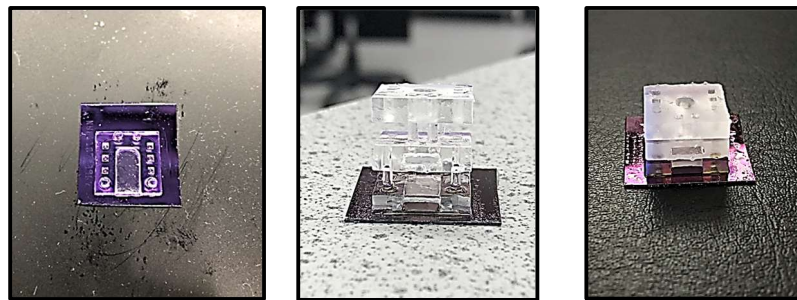


Figure 4.32: [Left] Example of a first layer modulus constructed directly onto silicon nitride, with [centre] subsequent stacked modulus, and [right] compressed to form a package on silicon nitride.

The packages (Figure 4.32) demonstrate the ability to form stacked packages, onto silicon nitride. However, components and wire interconnectors require inserting post construction with associated limitations (i.e., access and sealing). Consequently, the process was developed further to insert components during the build process as described in section 4.3.2.

4.3.2. Step III Stage B: Inserting multiple stacked components.

The package demonstrating the process (Step III: B) of using a python interaction to allow electrical components to be inserted part way through a construction is shown in Figure 4.34 on the build platform, and on silicon nitride in Figure 4.33.

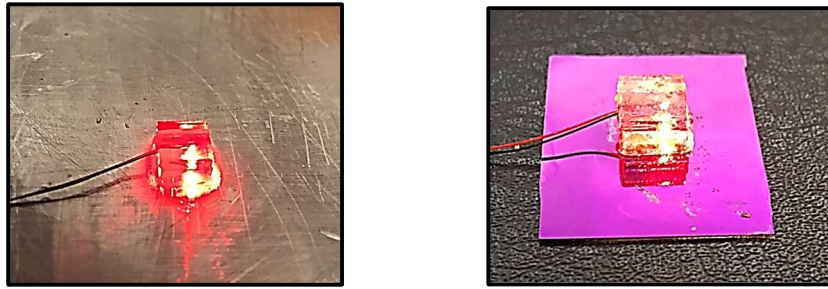


Figure 4.33: [Left] A micro-LED embedded in an SLA package constructed onto a build platform. [Right] A micro-LED embedded in an SLA package constructed onto silicon nitride.

The process was further demonstrated by inserting large geometries (an LDR) into a free-standing package constructed on supports (Figure 4.34).

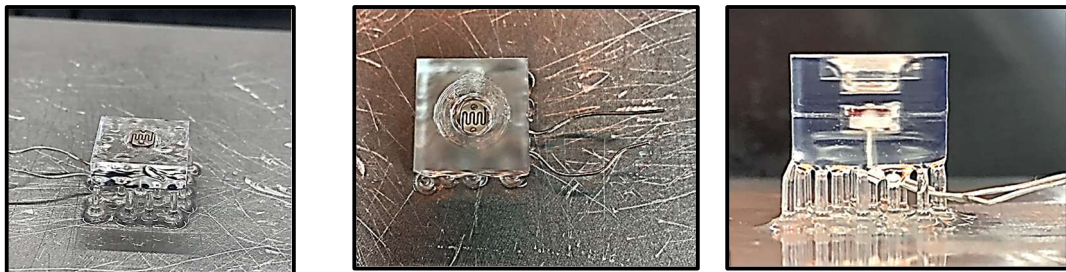
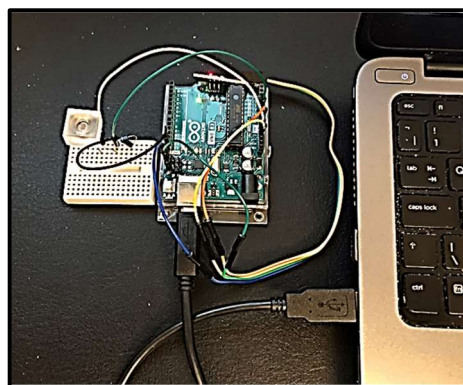
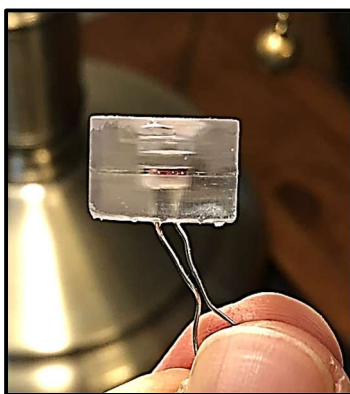


Figure 4.34: [Left] SLA construction interrupted and an LDR inserted mid build. [Centre and Right] Completed build with supports.



Time	Voltage (mV)
20:32:57	80
20:32:57	86
20:32:57	117
20:32:57	201
20:32:57	321
20:32:57	441
20:32:58	529
20:32:58	550
20:32:58	550
20:32:58	542
20:32:58	541
20:32:58	546
20:32:58	545
20:32:58	546
20:32:58	547
20:32:58	545
20:32:59	520
20:32:59	379
20:32:59	208
20:32:59	110
20:32:59	81

Figure 4.35: [Left] Finished photodiode package (supports removed). [Middle] Package connected to an Arduino unit for testing. [Right] Output data from the functionality test showing the change in signal voltage from the photo-resistor as a light is flashed onto it for 1 second before being turned off.

In this application, electrical connections are made by manually threading the wire legs of the LDR through the underside of the SLA construction supports. This is done during the same interruption used to insert the component. The package was then connected to an Arduino unit to test the functionality of the embedded device and example output from the test, are shown in Figure 4.35.



Figure 4.36: Example test geometries with 2-part adaptors. [Left] Example piston and [right] semi-conductor geometry constructed on an Anycubic SLA machine with corresponding 2-part adaptor pieces (constructed on a Form 2 SLA machine).

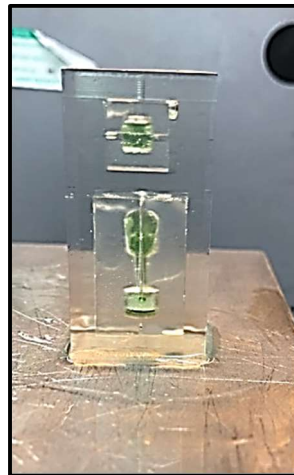


Figure 4.37: Demonstration package with two adaptor pieces inserted and stacked vertically. After demonstrating inserting large geometries into a free-standing package, large complex geometries were constructed with corresponding adaptor pieces (Figure 4.36) and the completed package shown in Figure 4.37. These constructions are further discussed in section 5.3.3. The next evolution of the process was to insert large electrical components arranged in three dimensions with electrical connections as described in section 4.3.3.

4.3.3. Step IV: Connecting inserted components to form an SLA structural electronic package.

The final stage of the process was to produce an SLA structural electronic package as described in Step IV of the method (section 3.5.3). This required the design of an interconnector to insert into the construction which also serves as an adaptor piece. The steps performed to achieve this are shown in (Figure 4.38). The final step (stage G.) shows the device illuminated to demonstrate its functionality.

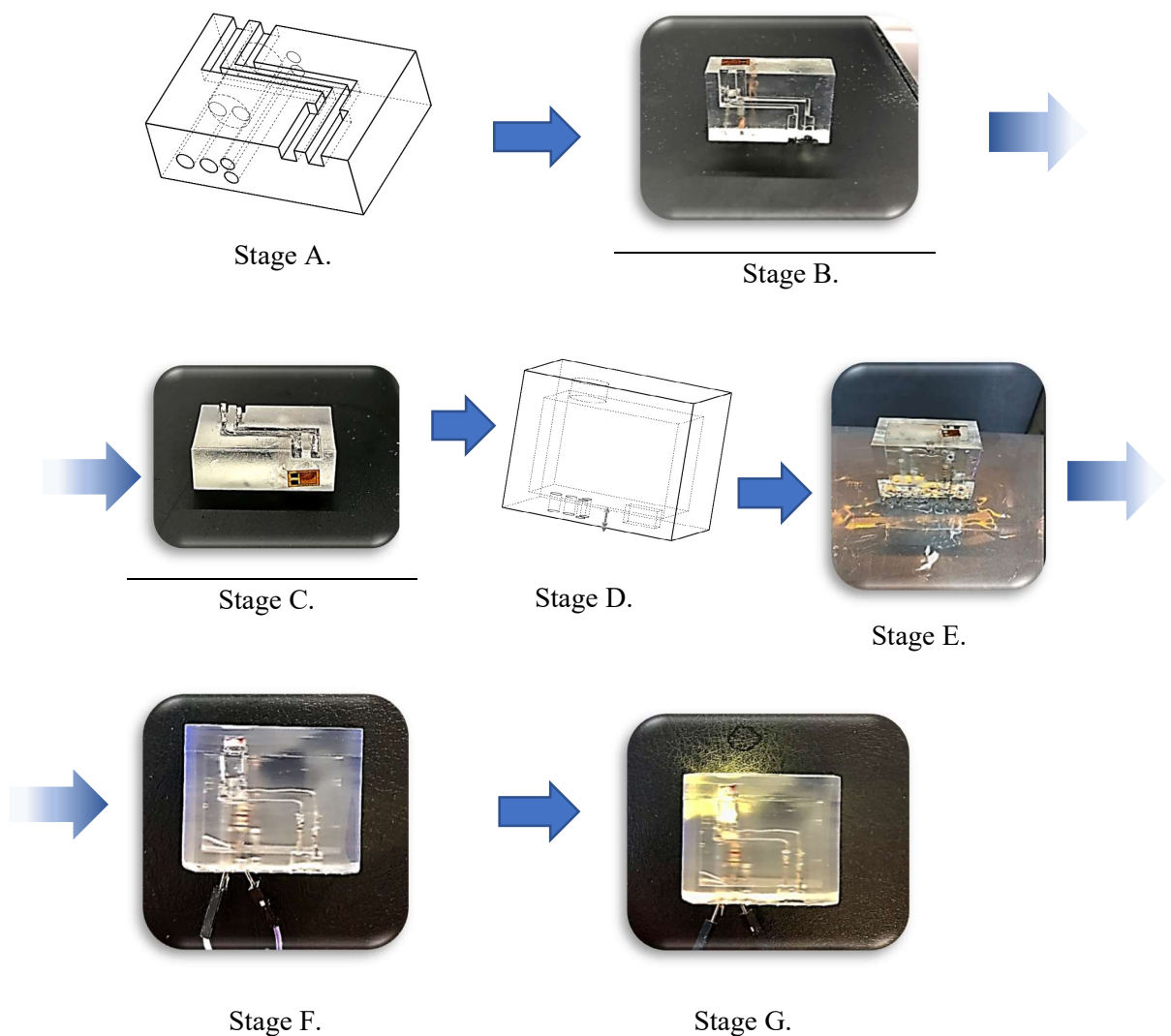


Figure 4.38: SLA construction stages of a structural electronic package. Stage A: CAD design for insert. Stage B: SLA construction of package insert with LED and strain gauge. Stage C: SLA construction of insert with wire interconnects installed. Stage D: CAD design for housing. Stage E: Interconnector inserted into housing mid- construction. Stage F: Demonstration of functionality with illuminated LED.

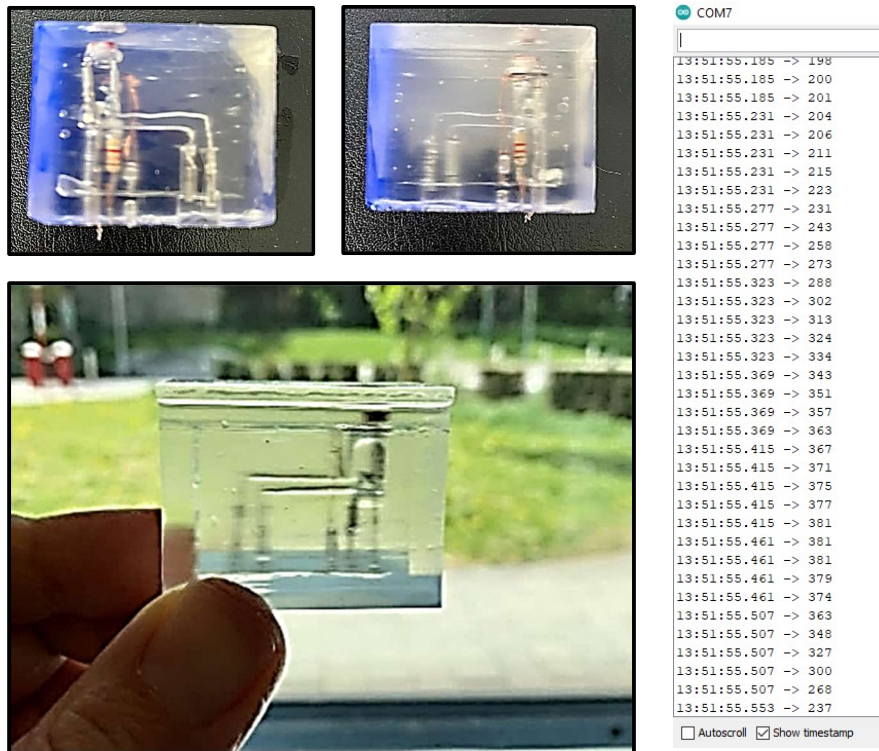


Figure 4.39: [Left] Structural electronic package product.
[Right] Data output to test the electrical connection to the LDR.

Further images of the SLA structural electronic package are shown in Figure 4.39 and example data output from increased light intensity, to test the connection to the LDR. These images show how the components have been arranged in three dimensions and demonstrating the ability to stack and offset multiple components. The findings of these constructions and the associated process are discussed further in section 5.3.3.

Chapter 5

5. Discussion

The results obtained in chapter 3 from experimentation pertaining to distortion in the SLA process, Adhesion, and inserting geometries will now be discussed in sections 5.1, 5.2 and 5.3 respectively.

5.1. Discussion of distorting effects in the SLA process

"To maintain accuracy and consistency during StereoLithographic part formation, the cure depth and the cured linewidth must be controlled with great accuracy. [9]"

Paul Jacobs, (1992), Fundamentals of StereoLithography.

This section discusses the results from modelling distorting effects and the associated experimentation, the methods for which are described in sections 3.2 and 3.3 respectively.

5.1.1. Form 1+ model calibration

The operating input parameters for the Form 1+ SLA machine used to calibrate the model are shown in Table 5.1.

Form 1+ divergence and ellipticity model calibration parameters		
Parameter	Setting	Comment
Line spacing at perimeter	120 μ m	Inner boundary offset parameter in the default logic.
Scan speed	800mm/s	Default logic setting.
First layer scans	10	Default logic setting.
Laser path length	300mm	Direct measurement
Focal length of the laser	300mm	Assumed equal to the laser path length (Z_{pc} section 3.2.7.2).
Line width compensation	30 μ m	Boundary layer offset in the default logic setting.
Laser power setpoint for perimeter line passes	48mW	Default set in control logic. The delivered power will be significantly reduced [156].
Wavelength	405nm	
Spot size (FWHM) [156]	155 μ m	
Laser M^2 value	1.4	Assumed (see section 3.2.6.2)
Critical exposure energy	12.6mJ.cm ⁻²	From Bennet et al [50] for FLC photopolymer

Table 5.1: Model calibration parameters for the Form 1+.

The model was calibrated following the process described in section 3.2.9.1 by adjusting the laser power at the print plane. The outputs from the Form 1+ calibration process are shown in Table 5.2.

Form 1 calibration (beam power) outputs $Z_{pc} = 300\text{mm}$, $FL = 300\text{mm}$, $M2 = 1.4$, $E_c = 12.6\text{mJ/cm}^2$	
[Stage A] CLW with design machine parameters and setpoint perimeter power at the print plane (48mW) from a single layer scan without superposition.	A CLW of 191.7 μm will result from a 48mW beam.
[Stage B] P_L to produce sufficient exposure at 800mm/s scan speed, to produce a CLW of 60 μm with a single scan.	Total $P_L = 18.5\text{mW}$ to construct a 60 μm CLW.
[Stage C] P_L to achieve a 60 μm CLW from a single layer scan with superposition to achieve LWC.	$P_L = 15.7\text{mW}$ to get 60 μm CLW with superposition. This gives a superposition coefficient of 1.18.
[Stages D and E] No. of scans without superposition to get measured line width. (CLW 90 μm design = 256.7 μm measured @800mm/s)	7.2 repeat scans

Table 5.2: Form 1+ calibration process output values

The Form 1+ calibration test piece, constructed with repeat scans and without superposition (section 3.3.2) produced a measured CLW of 256.7 μm at 800mm/s. The calibrated model identified the exposure from 7.2 adiabatic scans are required to produce a line of this width, compared to the 10 MFLS applied in practice. This equates to 28% of the delivered energy being dissipated between repeat scans (Figure 3.8).

Calibration using the alternative parameters of focal length, or E_c , are described in section 3.2.9. These would result in a beam possessing a focal length of 279.6mm and therefore slightly out of focus on the build area at a distance of 300mm, or the E_c of the photopolymer being 14.41mJ/cm².

For completeness, and to understand the extent of variation, the output of the modelled CLW with scan speed for the different calibration parameters are shown in Figure 5.1.

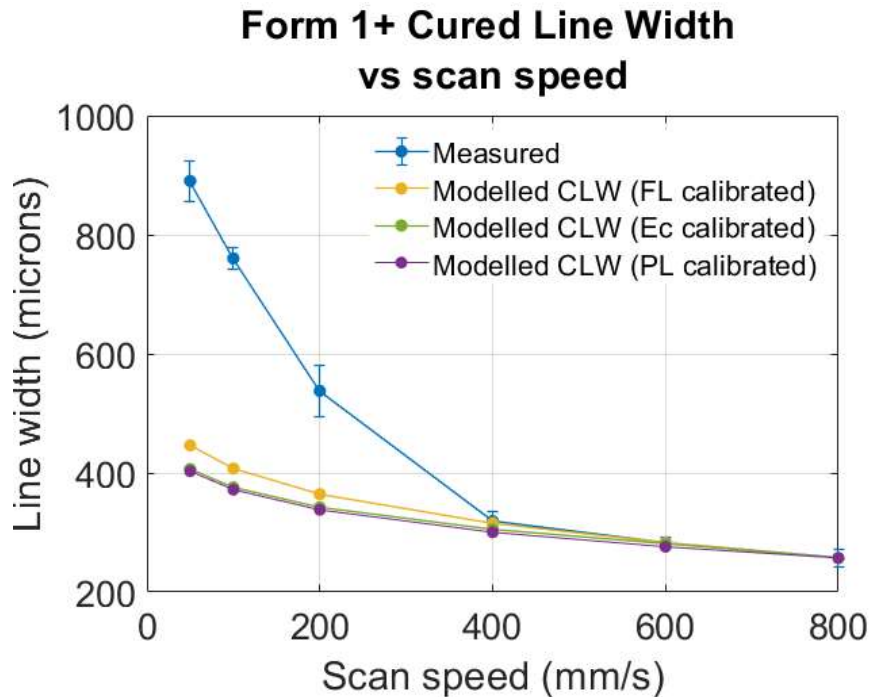


Figure 5.1: Measured and modelled CLW calibrated using E_c , FL and power, against scan speed.

The calibration methods using E_c and the laser power give near identical CLW results (Figure 5.1) and the maximum standard deviation between all three calibration parameters is $24.2\mu\text{m}$ at 50mm/s .

Due to the limited variance between the methods and for reasons explained in section 3.2.9, the laser power parameter will be used for the calibrating the model and subsequent modelling.

The results in Figure 5.1 show the modelled CLW and measured values correlate down to a scan speed of 400mm/s , below which the measured CLW rapidly increases due to distortion in the beam which is discussed later in section 5.1.4.1.

Shuttleworth [156] measured the power at the print plane for a specific Form 1+ machine and recorded a substantially reduced but linear relationship with the power setpoint (section 3.2.9). To account for attenuation in the laser path and degradation of the lasers a calibration curve for the specific Form 1+ machine in the current investigation has been produced in Figure 5.2. This is based on a directly proportional relationship between the beam power calculated from the calibration process (3.2.9), and the setpoint power. The curve allows the power to be extrapolated for modelling scenarios with different power settings.

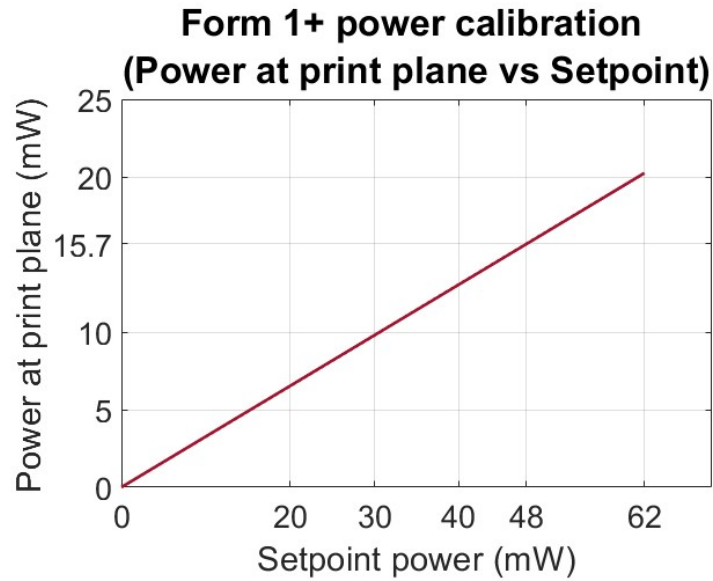


Figure 5.2: Form 1+ beam power calibration curve.

5.1.2. Form 2 model calibration

The Form 2 model was calibrated for the perimeter line pass power against measured part dimensions following the process described in section 3.2.9.2 with the variable input settings in Table 5.3.

Form 2 divergence and ellipticity model calibration parameters		
Parameter	Setting	Comment
Scan speed	1000mm/s	Assumed
Laser path length	300mm	Assumed
Line width compensation	30 μ m	Assumed
Wavelength	405nm	
Spot size (FWHM) [42]	140 μ m	
Laser M ² value	1.4	Assumed (3.2.6.2)
E _c	12.6mJ/cm ²	From Bennet et al [50] for FLC photopolymer

Table 5.3: Form 2 calibration parameters

Only test pieces constructed at the centre of the build area are used for calibrating the distortion models to avoid the influence of D&E. The construction of these is reported in section 3.3.3, with the measured values of those used for calibration summarised in Table 5.4 for convenience.

Form 2 calibration test piece measurements	
Test piece (located centrally)	Measured width (μm)
1mm (design) wide test piece with superposition and MFLS	1153.35
1mm (design) wide, 5.5mm tall, test piece with superposition without MFLS	1072.92
90 μm test piece without superposition with MFLS	146.7

Table 5.4: Form 2 calibration test piece widths

The calibrated model outputs for the Form 2 at the different calibration stages (section 3.2.9.2) are shown in Table 5.5.

Form 2 calibration output	
$Z_{pc} = 300\text{mm}$, $FL = 300\text{mm}$, $M2 = 1.4$, $E_c = 12.6\text{mJ}/\text{cm}^2$	
Measured value and process	Modelled value
[Stages A and B] CLW required to form the measured part dimension with superposition, without repeat scans of 1072.92 μm	87.9 μm
[Stages A and B] CLW required to form the measured part dimension with superposition and repeat scans of 1153.35 μm .	218.8 μm
[Stage C] Repeat 1 st layer scans required with superposition to increase the CLW from 87.9 μm to 218.8 μm .	3.8 first layer scans.
[Stage D] Total exposure (including repeat scans) and P_L required to produce a measured CLW of 146.7 μm from a single line pass without superposition with repeat scans.	Total exposure with repeat scans = 26.8mJ/cm ² $P_L = 10.5\text{mW}$.
[Stage E] Superposition coefficient required to produce the CLW of 87.92 μm (corresponding to the measured part dimension of 1072.92 μm with superposition from a single layer scan).	Superposition coefficient of 2.3 This corresponds to a superposition line spacing of 63.4 μm
[Stage F] The model input P_L at the print plane to deliver the total exposure received on the perimeter line pass of the part for different scenarios with superposition and MFLS.	Without superposition or MFLS = 10.5mW Without superposition with MFLS = 32.3mW With superposition without MFLS = 24.7mW With superposition and MFLS = 76.0mW

Table 5.5: Form 2 calibration process output values

5.1.3. Superposition

The activity of the superposition mechanism at the test parameters (Table 5.1) has been verified experimentally (Figure 4.1) in section 4.1.1.

Superposition was modelled for the Form 1+ for the purpose of the calibration process (section 5.1.1) and the power for a single line pass calculated to be 15.7mW. Figure 5.3 shows the total exposure delivered from superposition with the influence of parallel line passes, on the perimeter of the construction. For the given parameters (Table 5.1), there are two line passes within the ZOI. The orange and blue bars denote the critical cure energy, and the increased average exposure delivered due to superposition (14.1mJ/cm²), respectively. Superposition results in an 18% increase in exposure compared to single line pass. It is noted that the perimeter scans do not deliver sufficient energy (11.9mJ/cm²) to initiate curing without superposition. These results only represent the exposure on the perimeter and demonstrate the reliance on superposition to produce a fine scan line to achieve finer edge detail.

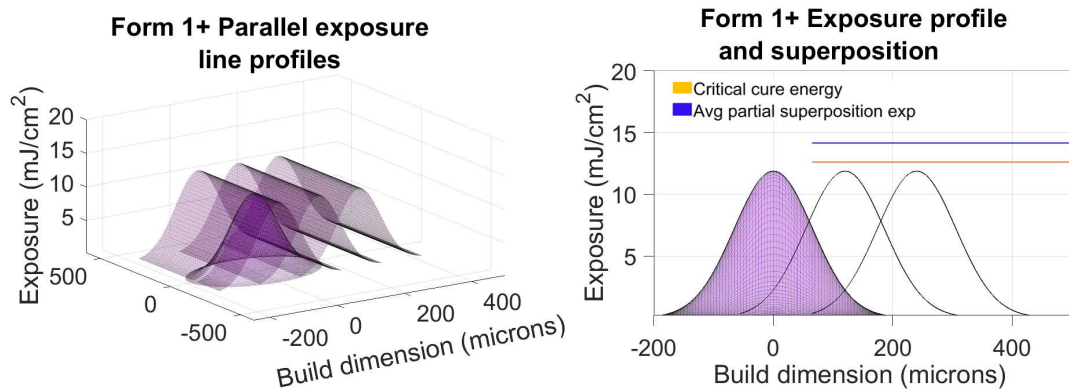


Figure 5.3: The exposure profile of parallel line passes and resulting superposition at the build perimeter, for the Form 1+ parameters (Table 36).

The equivalent exposure delivered is increased further, to 16.4mJ/cm², with superposition for centrally located scan passes denoted by the green bar (Figure 5.4). This is an increase of 38% compared to the exposure from a single line pass. The elevated exposure is due to there now being two parallel line passes, either side of the target line, falling within the ZOI (3.2.4). The peak to valley variation in delivered exposure calculated for these settings was 1.0% and within the recommended 3% (section 2.6)

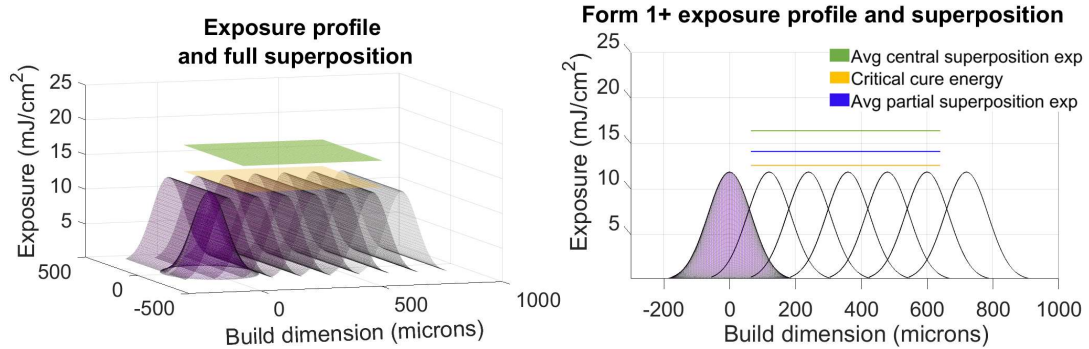


Figure 5.4: The exposure profile of parallel line passes and resulting superposition for the Form 1+ parameters (Table 36).

The above analysis demonstrates the potential for superposition in the equipment used, to substantially increase the overall exposure incident on the photopolymer, and correspondingly on the substrate. Since reflections of incident scan paths will also generate superposition, it is important to consider the characteristic's potential to elevate the reflected exposure.

5.1.4. Form 1+ cured profile analysis

The modelled cured spot and perimeter line profile for the Form 1+ at default settings with superposition and MFLS is shown in Figure 5.5. For a $100\mu\text{m}$ layer thickness, this will produce a step between layers of $20.7\mu\text{m}$ (Figure 5.5).

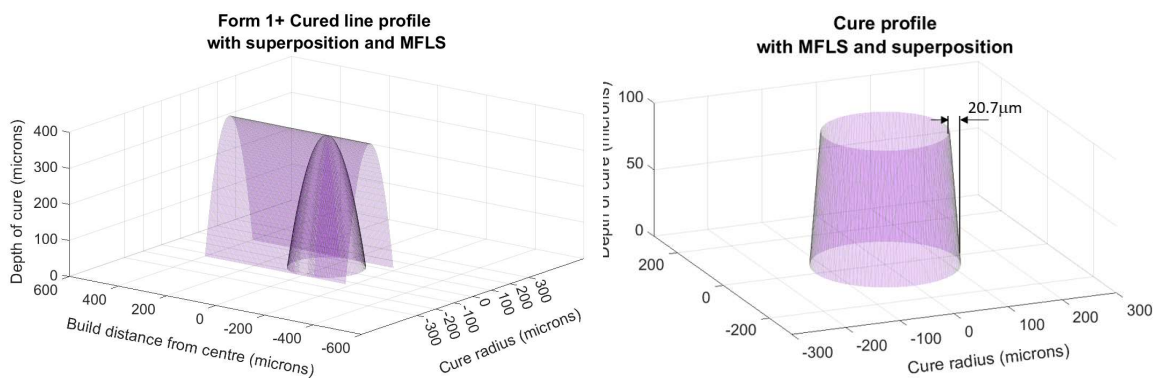


Figure 5.5: Cured laser spot and interlayer step size

[Left] Form 1+ Cured spot and line profile at default settings ($800\text{mm}/\text{s}$) with superposition and MFLS. [Right] Step size resulting from the Form 1+ beam cure profile with a $100\mu\text{m}$ layer thickness.

However, Figure 5.6 shows significant disparity between the modelled part dimensions (section 4.1.2.1) and those measured (section 4.1.2.2) at reduced scan speeds. For centrally located constructions, the difference between the modelled and measured line widths (avg.) were $3190\mu\text{m}$, $1943\mu\text{m}$ and $1651\mu\text{m}$, at $50\text{mm}/\text{s}$, $100\text{mm}/\text{s}$ and $200\text{mm}/\text{s}$ respectively. Additionally, the measured widths of the constructed parts are also substantially greater than the 1mm design width.

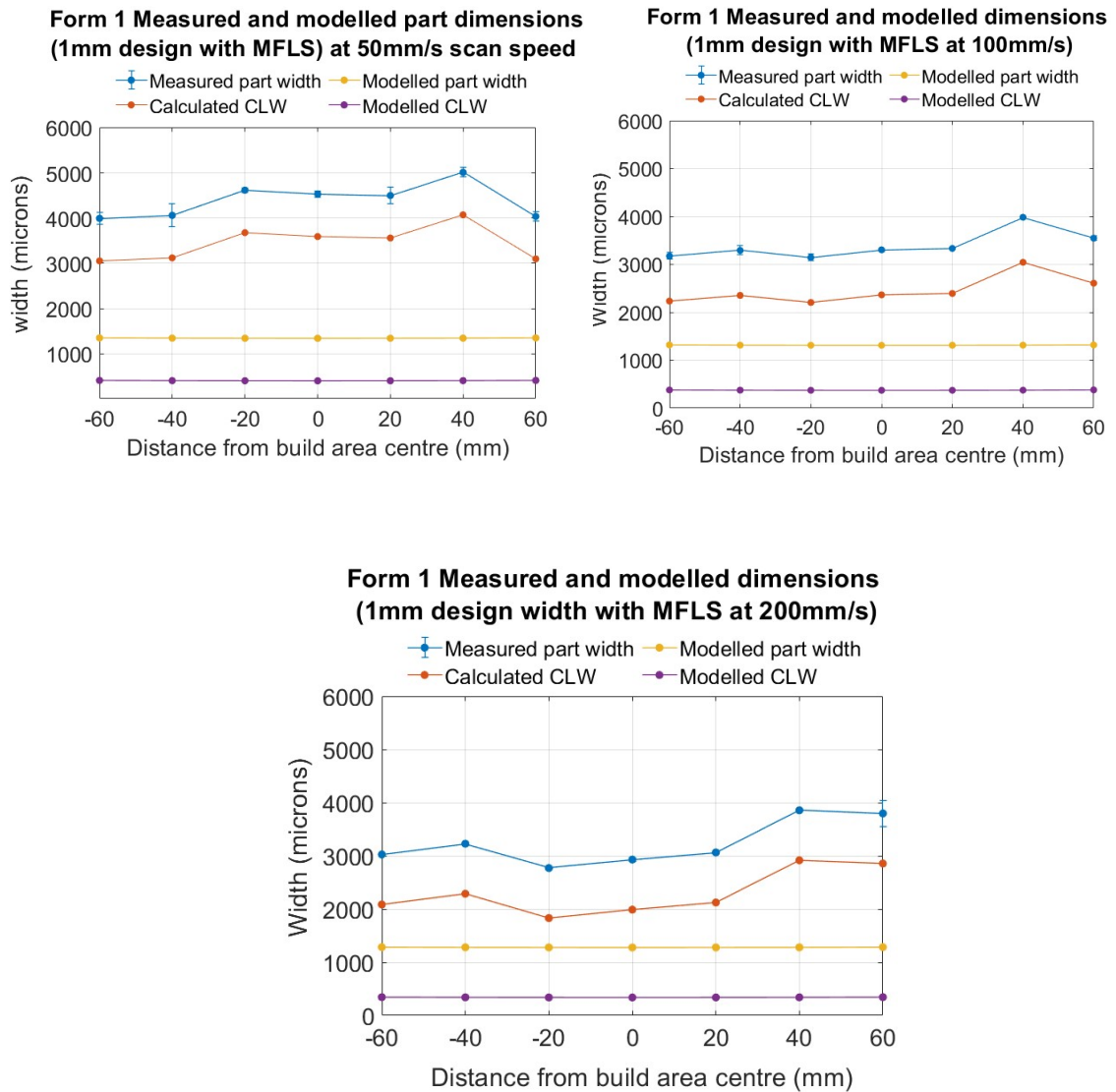


Figure 5.6: Measured and modelled part dimensions (Form 1+) at increasing scan speed. [Top left] Form 1+ Measured and modelled part width (1mm design) and CLW at 50mm/s scan speed. [Top right] CLW at 100mm/s scan speed. [Bottom] CLW at 200mm/s scan speed.

Figure 5.7 shows the calibrated modelled values of CLW to correlate with the measured values as the scan speed reduces from the default setting of 800mm/s, down to 400mm/s. Below this, the measured results rapidly increase in size. This is attributed to distortion in the beam delivering an exposure, which at the default speeds (800mm/s) is less than E_c . However, at reduced scan speeds and in accordance with Equation 3.8, the distortions in the beam deliver an increased exposure which is sufficient to initiate curing producing the excessive curing measured in Figure 5.6. This is discussed further in section 5.1.4.1.

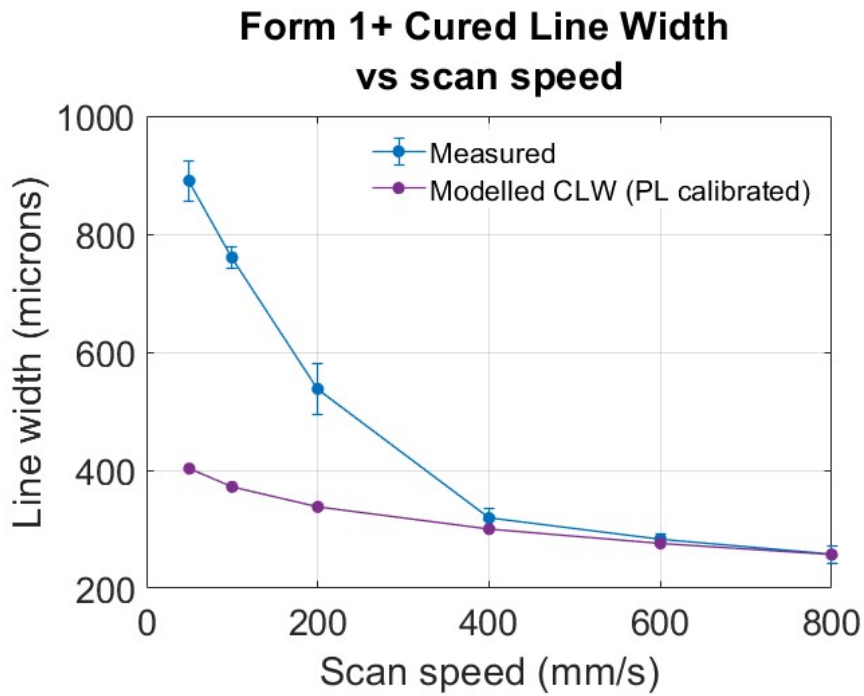


Figure 5.7: The modelled (calibrated) and measured CLW against scan speed.

5.1.4.1. Beam distortion

The beam profile was recorded and processed using the methods described in sections 3.3.7 and 3.2.11.

Figure 5.8 shows the intensity and corresponding exposure profile (at 50mm/s) for the Form 1+ beam at maximum power (62mW setpoint). Highlighted on the exposure profile [top right], is a region of distortion. At the high exposure associated with reduced scan speeds, this manifests as distortion in the cured profile (Figure 5.8 bottom).

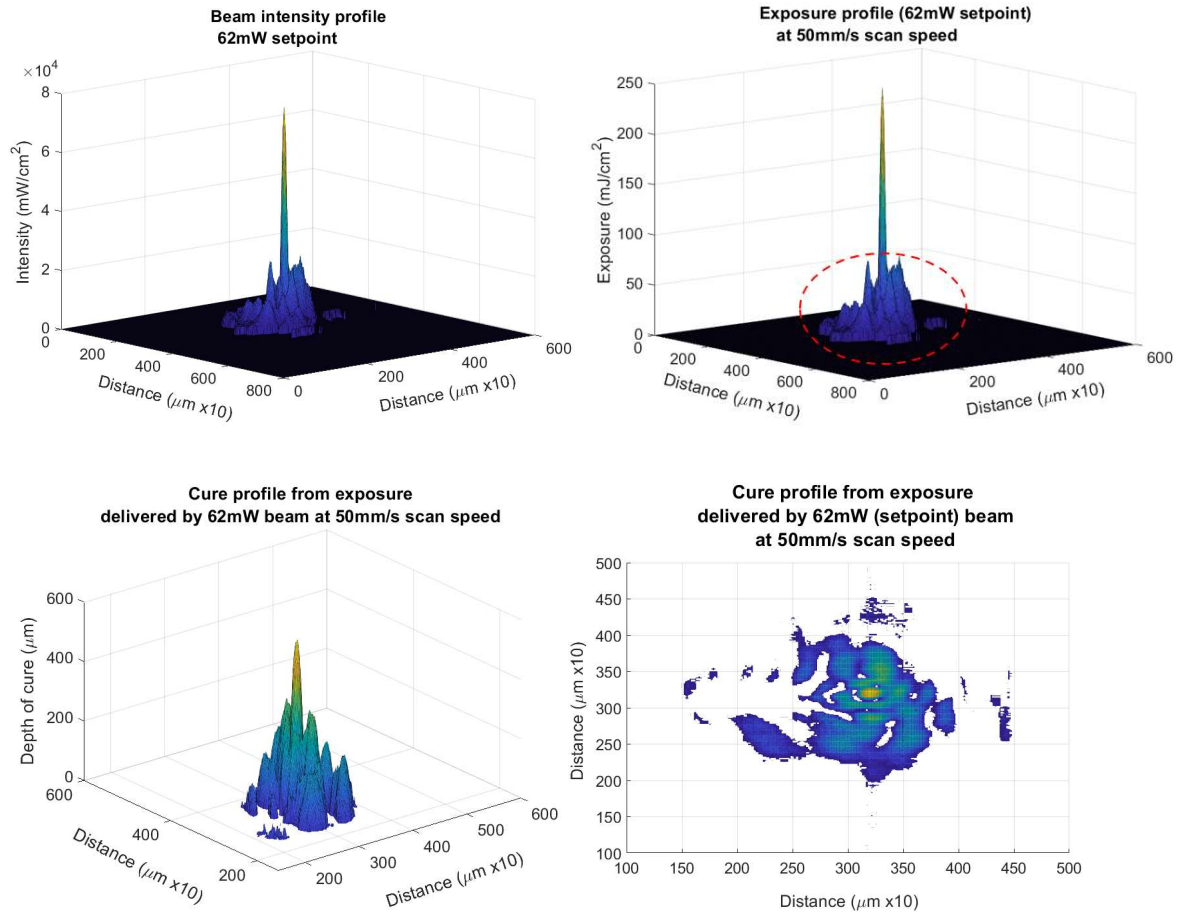


Figure 5.8: [Top] Intensity and exposure profiles (50mm/s).
 [Bottom] Cure profile from the beam exposure (50mm/s).

The distorted area of the beam has relatively low intensity (Figure 5.8). Therefore, at default scan speeds (800mm/s), the beam is not resident at a given location long enough to deliver sufficient exposure for curing to ensue. The point at which the distortion occurs in the product is apparent in Figure 5.7 where the CLW becomes substantially wider at scan speeds below 400mm/s.

Figure 5.9 shows the expanding cure footprint resulting from the increasing exposure delivered at decreasing scan speeds. This is consistent with the relationship between scan speed and the widening of the CLW measured at scan speeds below 400mm/s in Figure 5.7. This characteristic also explains the unusually wide divergence and reflectance test constructions reported in sections 4.1.3.1 and 4.1.4.1. Moreover, the beam intensity profile and measured CLW also demonstrate that the profile of the Form 1+ SLA machine used in the current investigation, ceases to conform to a Gaussian model at these low scan speeds and associated high exposures.

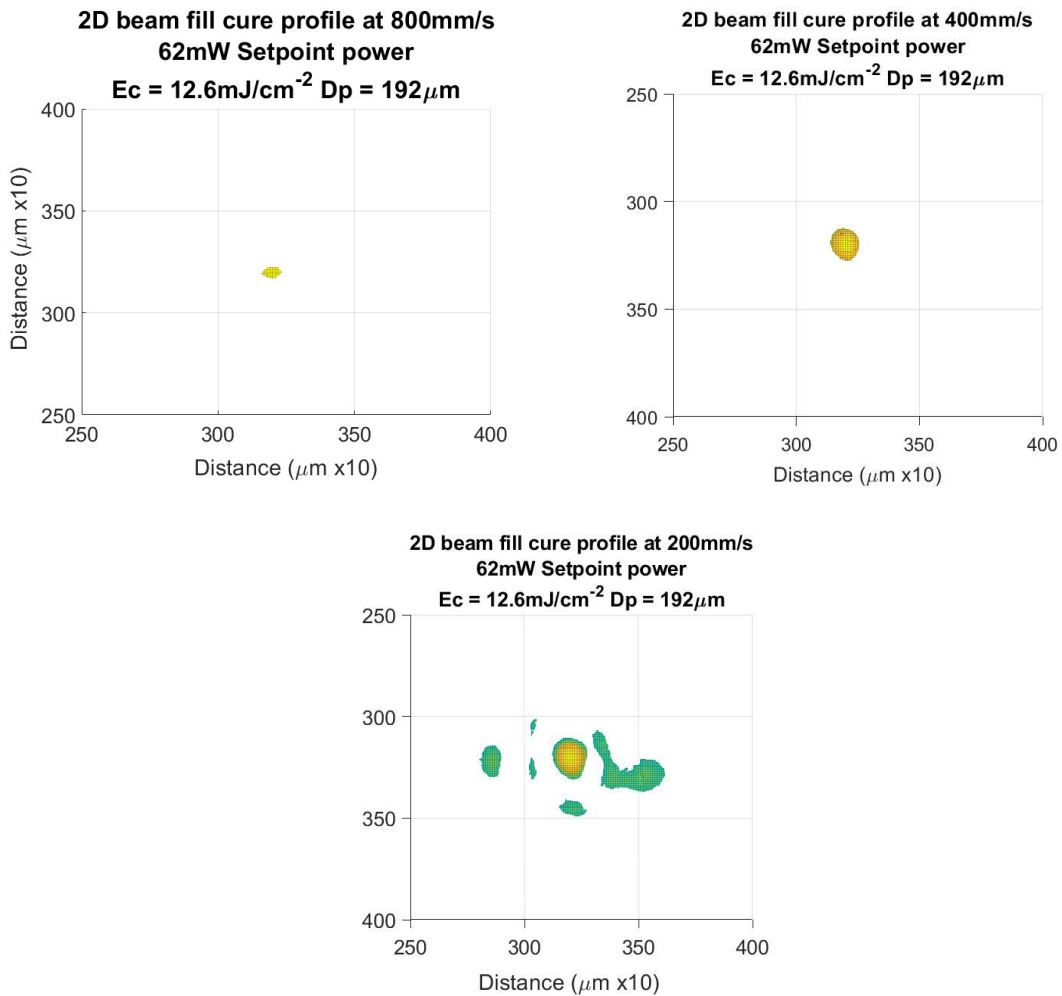


Figure 5.9: Footprint of cure profile resulting from the increasing exposure at decreasing scan speed.

Although the trend between CLW and scan speed using the beam profiler (Figure 5.9) is consistent with that measured in Figure 5.7, there are significant differences between the absolute values, particularly at very low scan speeds below 100mm/s. This is attributed to the greyscale conversions, and the requirement to attach the attenuating filter (section 3.3.7) to the beam profiler which reduces the measurement contrast and the detection of low intensity emissions. Therefore, the beam profile analysis is only applied for qualitative analysis. Additionally, the distortion significantly contributes to the formation of menisci with MFLS, when beam noise which does not impart sufficient energy to initiate curing from a single scan, but does so after repeated scans.

5.1.4.2. Meniscus formation.

The formation of menisci is not normally a concern in SLA because constructions are usually made onto disposable supports which separate the part from the first layer. However, menisci are undesirable for the application being studied where constructions will be made directly onto a silicon nitride substrate. As mentioned in Chapter 2, Ackstaller

[33] identified the formation of menisci in an SLA process which was attributed to reflectance. This is because, Menisci will form when there is a significantly greater exposure on the first layer resulting in a wider CLW than subsequent layers. This can be caused in the current application by reflectance, distortion of the beam or MFLS. An example of the latter two has been modelled using the beam profile method (section 3.2.11) and the parameters in Table 5.1, for the specific Form 1+ machine used in the current study. The cure profile resulting from a single scan of the distorted Form 1+ beam spot at 50mm/s scan speed is shown Figure 5.10. This is compared to the larger footprint resulting from MFLS in Figure 5.10, resulting in a predicted lip of up to $\sim 130\mu\text{m}$. In this example the exposure from low intensity distortions in the beam are multiplied by the repeated scanning resulting those distortions delivering sufficient exposure (i.e., $>E_c$) to initiate curing.

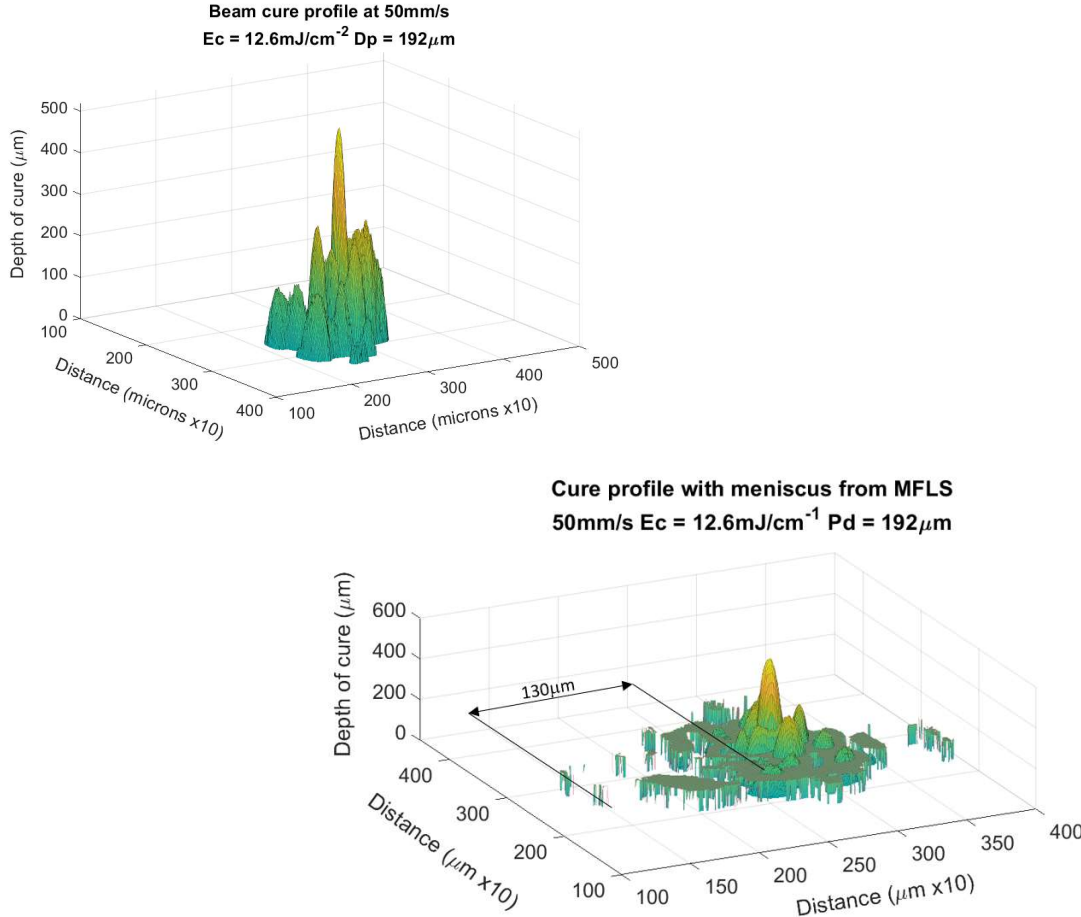


Figure 5.10: Cure profile from the exposure delivered by the Form 1+ [Top] The Form 1+ beam (48mW power (setpoint) and 50mm/s). [Bottom] Cure profile with meniscus from the exposure delivered by the Form 1+ beam at 48mW power (setpoint) at 50mm/s with MFLS.

The above examples (Figure 5.10) are specific to the distortion pattern produced by the Form 1+ machine used in the current study.

The formation of menisci from a Gaussian beam, with the parameters in Table 5.1 at 50mm/s scan speed is modelled in Figure 5.11 and predicted to produce a lip 57 μ m wide.

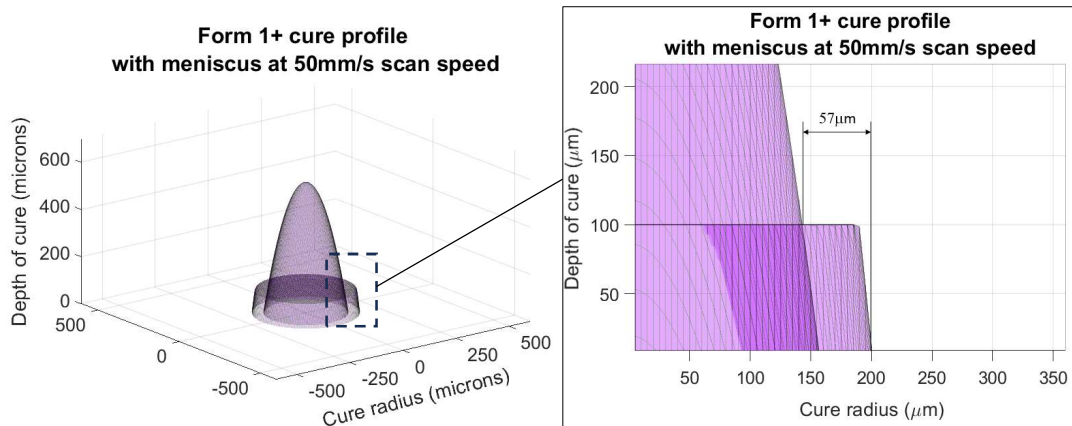


Figure 5.11: Menisci formed from a Gaussian beam with repeat scans at 50mm/s and 48mW setpoint power.

This analysis shows that menisci will routinely form when MFLS are applied and the beam distortion present in the equipment used in the current study can potentially double their size compared to a Gaussian beam. Consequently, the formation of menisci can impact the ability to achieve manufacturing tolerances as discussed in section 5.1.7.2.

5.1.4.3. Divergence and ellipticity

The modelled conditions with and without MFLS apply to two cases:

Case D1: Superposition with MFLS represents a first layer construction directly onto a substrate without supports, as will be the case for first layer constructions in the current study's application to package electronics onto silicon nitride.

Case D2: Superposition without MFLS represents a construction at a layer other than the first one.

The modelled (Case D2) and measured values (section 4.1.3.2) for the lateral variation in the CLW on the form two, are shown for comparison in Figure 5.12.

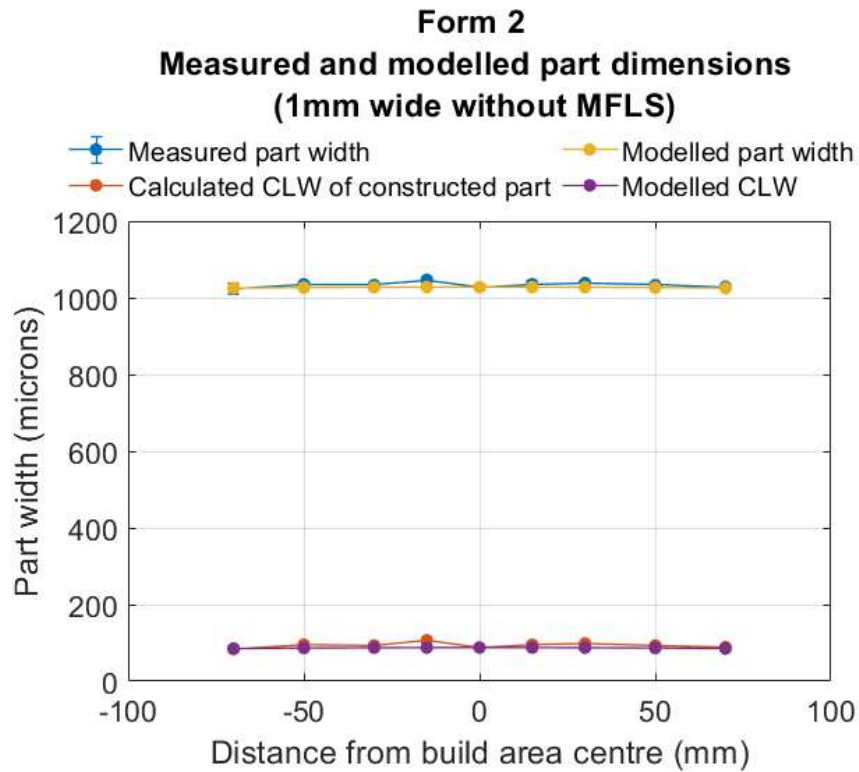


Figure 5.12: Modelled and measured CLW profile laterally across the Form 2 build area, without repeat scans.

The modelled and measured values at the edge of the build area (positions -70mm and +70mm) are included in Table 5.6. This shows for Case D2, without MFLS, the CLW at the edge of the platform predicted from modelling is within 3.1% of the average CLW calculated from measurements.

Form 2 measured and modelled line width distortion attributed to reflectance			
Condition / location	-70mm	+70mm	
Measured part width (Case D1) (μm)	1301.3	1264.9	
Model predicted part width due to D&E (Case D1) (μm)	1158.2	1158.0	
Measured part width (Case D2) (μm)	1023.7	1029.0	
Model predicted part width due to D&E (Case D2) (μm)	1025.3	1025.3	
Calculated CLW from measured part width (Case D2) (μm)	83.7	89.0	
Avg Calculated CLW from measured part width (Case D2) (μm)	86.3		
Model predicted CLW due to D&E (Case D2) (μm)	89.0		
Difference in distortion between modelled and measured values (Case D2 for validation of model) (μm)	-1.58	3.69	
Difference in distortion between modelled and measured values (attributed to reflectance from Case D1) (μm)	143.2	106.9	
Average lateral spurious cure attributed to reflectance (μm)	125.1		

Table 5.6: Comparison of modelled and measured 1mm test piece dimensions at the edge of the build area on the Form 2.

The modelled variation in the CLW for case D2, due to divergence alone is shown in Figure 5.13 for the Form 1+ and Form 2. These show less than $3\mu\text{m}$ change in the CLW across the dimensions of the respective build areas on both machines, and that CLW is relatively insensitive to divergence. The influence of ellipticity has a greater effect on the CLW for the given applications, which combined with divergence (Case D2) is shown in Figure 5.14.

The rate at which the CLW changes, increases on both machines as the beam's AOI increases towards the extremity of the build areas. Consequently, the distorting effects of D&E will ultimately compromise the ability to achieve manufacturing tolerances if the size of the build area were expanded and is discussed further in section 5.1.7.

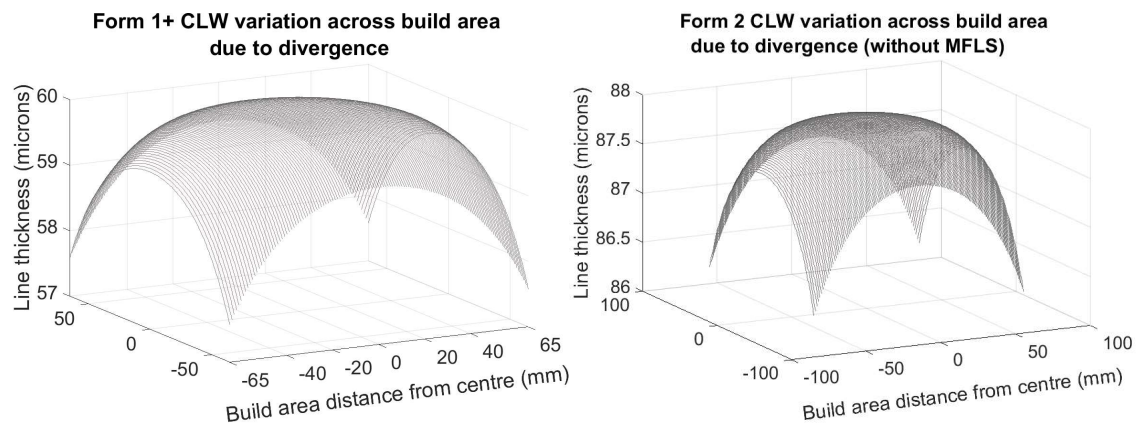


Figure 5.13: Variation in CLW across the build area due to divergence
The modelled variation in the CLW across the build area due to divergence for the Form 1+ at default settings (without MFLS) for the Form 1+ [left] and for the Form 2 [Right].

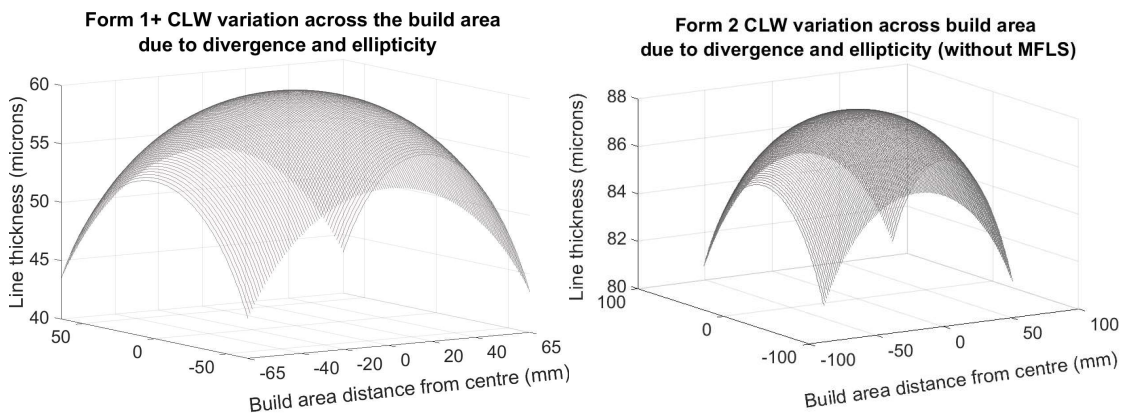


Figure 5.14: Variation in CLW across the build area due to divergence and ellipticity
The modelled variation in the CLW across the build area due to divergence and ellipticity at default settings (without MFLS) for the Form 1+ [left] and for the for the Form 2 [right].

Figure 5.15 illustrates the modelled influence of D&E on the CLW for the Form 2 (Case D1). The profile of the distortion is switched from 'concave-down' for single layer scans to 'concave-up' with the increased exposure from MFLS.

**Form 2 CLW variation across build area
due to divergence and ellipticity (with MFLS)**

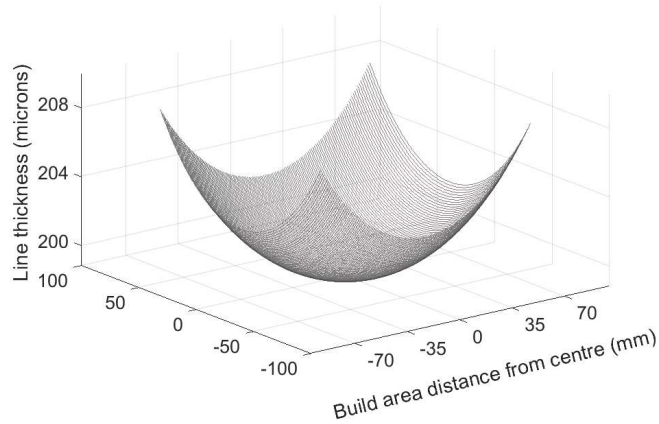


Figure 5.15: The modelled variation in the cured line width across the build area due to divergence and ellipticity for the Form 2 at default settings with MFLS (Case D1).

The corresponding part width (1mm design), at lateral distances from the centre of the Form 2 build area, are shown in Figure 5.16. The modelled part width with the influence of D&E are compared to the measured width (blue) of the constructed test pieces (3.3) and their calculated line width (red).

**Form 2
Measured and modelled part dimensions
(1mm wide with MFLS)**

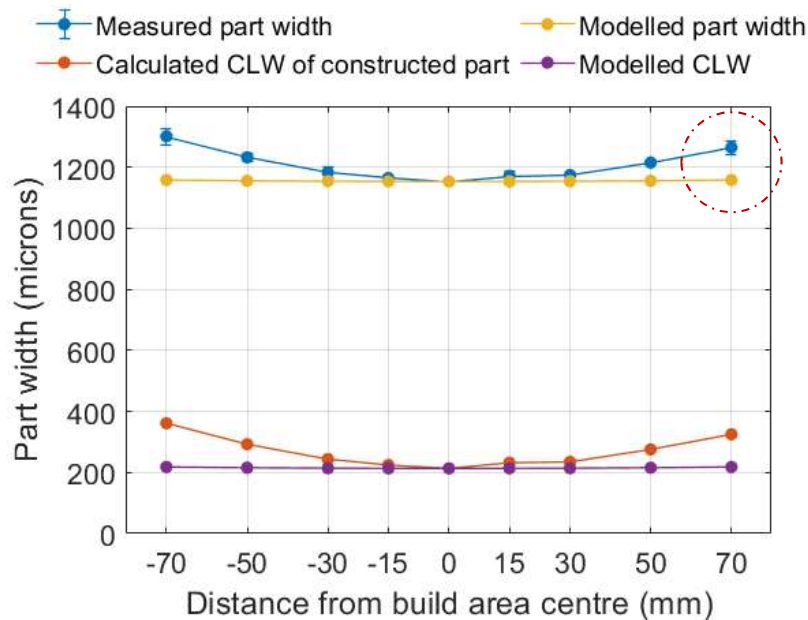


Figure 5.16: Modelled and measured CLW and part width (1mm design) laterally across the Form 2 build area, with repeat scans (Case D1).

As highlighted on Figure 5.16 for case D1, there is an increasing disparity between the modelled and measured results (section 4.1.3.2) with distance from the centre. This indicates that D&E cannot account for the magnitude of measured distortion at the

given parameters (section 3.2.9). The Form 2 model is based on an assumed light path length of 300mm. However, for the distorting effects of D&E to produce the degree of variation measured, the beam's path would need to be reduced to an unrealistic length distance of ~80mm with an AOI of ~41°. The magnitude of the difference between the modelled and measured dimensions suggests an additional distorting mechanism is active. Moreover, the distortion does not occur without repeat scans (Figure 5.12) suggesting it is associated with elevated exposure and the measured profile is a function of the AOI and indicative of reflectance.

5.1.5. Reflectance

By applying the modelling process described in section 3.2.10, the reflected intensity and the corresponding exposure at a given scan speed can be calculated with consideration to the surface roughness (section 3.2.10.2) and the properties of the photopolymer.

The base case parameter settings for the reflectance modelling on the Form 1+ are listed in Table 5.7 and the assumptions in section 3.2.13. Variations to these and specific scenario settings such as scan speed are stated for each modelled scenario.

Case R1 Parameters (Form 1+)	
Parameter	Value
Photopolymer critical cure energy	12.6mJ/cm ²
penetration depth	192μm
Scan power for all sections of the pattern (section 3.3.6.1).	62mW (Setpoint) 20.24mW at the print plane (Figure 5.2).
FWHM beam spot size	155μm
Beam wavelength	405nm
Focal length of beam	300mm
Light path length	300mm
Build area	130mm x 130mm
Exposure delivered by repeated first layer scans.	Equivalent to 7.2 adiabatic scans
Hatch spacing (section 3.3.6.1).	90μm
Parallel line passes producing superposition.	Yes.
Perimeter line spacing (section 3.3.6.1).	90μm
Scan speed	50mm/s
Inter-layer delay time	10 seconds
Manufacturing tolerance	50μm

Table 5.7: Case R1 parameters for modelling reflectance on the Form 1+.

The modelled magnitude of potential cure due to reflectance from silicon nitride at the operating parameters described in Case R1 is shown in Figure 5.17. This is the condition with the highest delivered exposure considered for the Form 1+. It indicates specular reflectance from the first layer of construction on silicon nitride will deliver sufficient exposure to cure to a depth of up to 245.3μm.

Magnitude of spurious curing due to specular reflectance from silicon nitride
Form 1+ with superposition and MFLS at 50mm/s scan speed

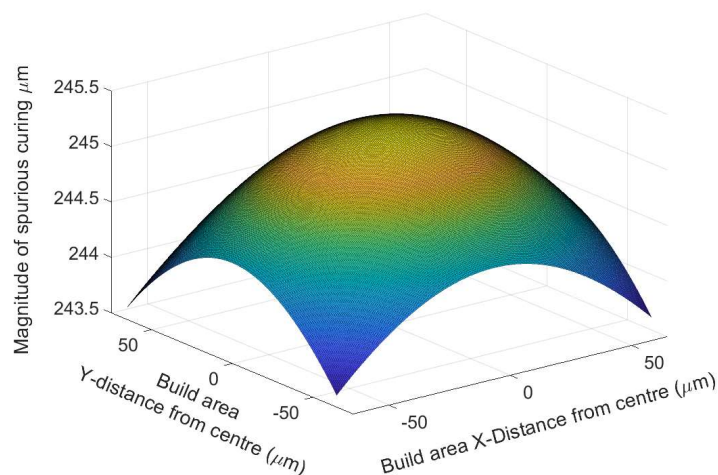


Figure 5.17: Potential magnitude of spurious cure due to specular reflectance from a silicon nitride substrate on the Form 1+ (Case R1).

However, in practice, the depth of cure is limited to a single layer thickness (100µm) by the build platform. Therefore, it is only LSC which will affect the dimensions of the product and the ability to achieve tolerances. To model the potential for LSC, the magnitude of the reflected exposure is resolved into vertical and lateral components (Figure 5.18) using trigonometry and the angle of reflection (AOR) as shown in Figure 5.18.

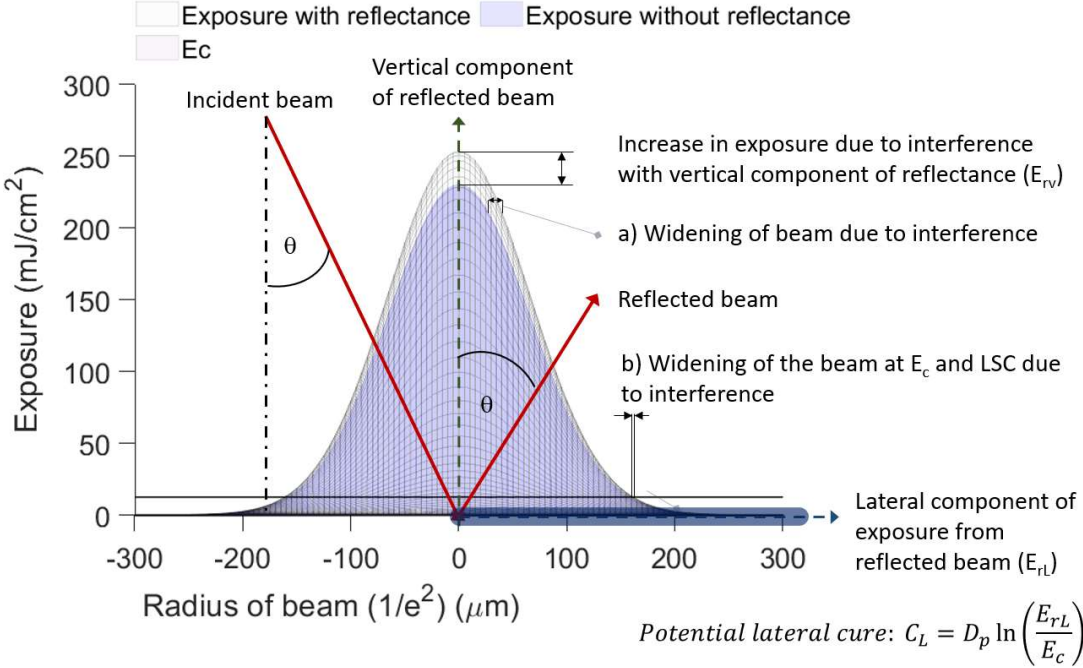


Figure 5.18: Vertical and lateral components of exposure due to reflectance. Where the widening of the beam in a) and b) is due to interference between the incident beam and the vertical component of reflectance.

A map of the AOR (after the influence of refraction) as described in section 3.2.6.1, for the geometry of the Form 1+ machine is shown in Figure 5.19.

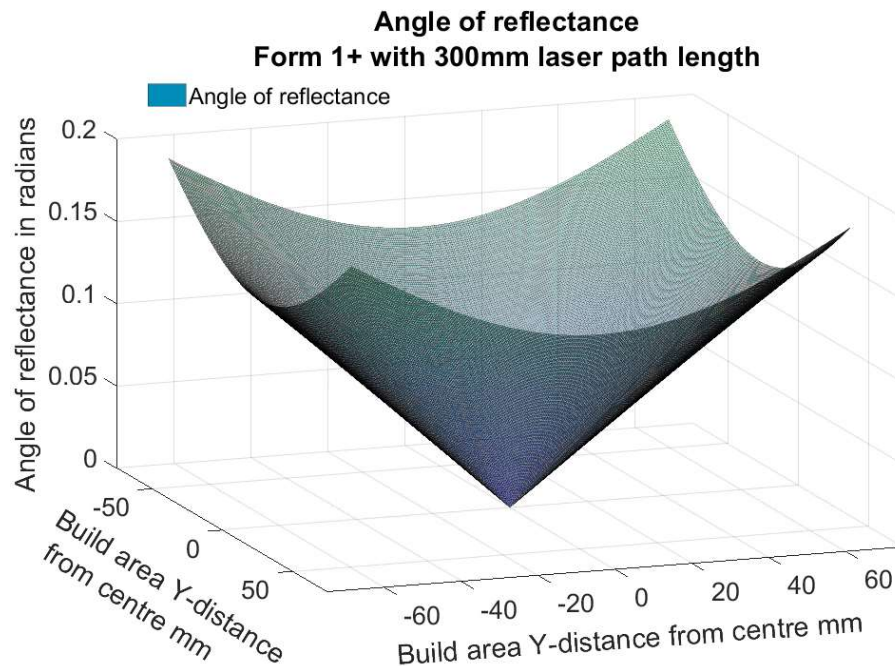


Figure 5.19: Angle of reflectance from the build area substrate for the geometry of the Form 1+ with a laser path length of 300mm.

The reflected vertical component combines with the exposure delivered by the incident beam and widens the CLW via the mechanism described in section 3.2.2. Whereas the lateral component generates spurious cure directly (Figure 5.18). Which of the two components dominates depends upon the angle of the incidence and the reflected energy. The potential for the vertical and lateral components of spurious cure produced in the current application are discussed in turn below.

5.1.5.1. Normal reflectance

The reflected exposure is calculated by applying the modelled (section 3.2.10) reflectance coefficient at a normal AOI, to the exposure incident on the substrate after attenuation through the photopolymer. For this investigation silicon nitride is compared with aluminium from which the Formlabs build platforms are constructed (section 3.2.13). In practice their composition will be a mixture of aluminium and oxide with the potential for aluminium to be exposed by the required frequent and aggressive cleaning. Aluminium is also highly reflective due to its low refractive index ($\eta=0.5$) and provides a severe case for comparison.

The reflected exposure from normal incident light from smooth samples of the two materials has been modelled (Gaussian). This shows specular reflectance from aluminium has the potential to increase the intensity and corresponding exposure (Figure 5.20) by 15.4%, whereas that from silicon nitride would interact destructively with the incident light with the potential to reduce the overall exposure delivered by 1.4%.

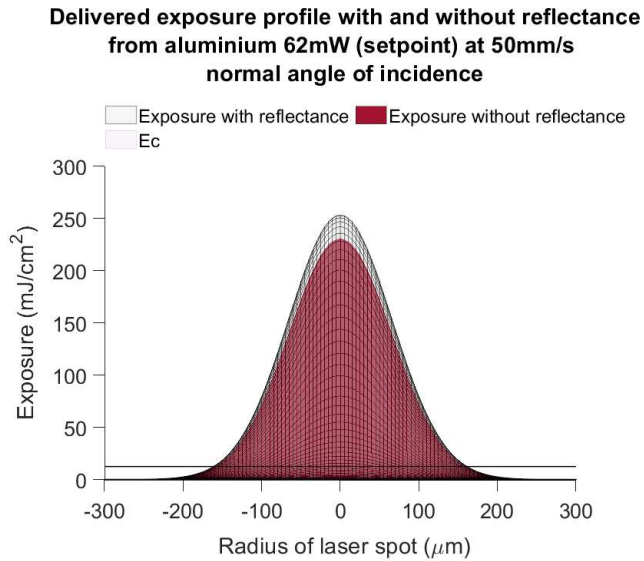


Figure 5.20: Profile of the total exposure delivered to the photopolymer, with and without reflectance from aluminium at (Case R1) at the centre of the build area (normal AOI).

In practice, the majority of the reflected exposure from normal incident light will be absorbed by the polymer solidified by the incident light, thereby reducing the potential for LSC. Additionally, due to the extent of cure being a logarithmic function of the exposure, the magnitude of LSC produced by reflectance is comparatively low.

As the AOI changes across the build area, the corresponding change in spurious curing due to the vertical component of reflectance from aluminium and silicon nitride is modelled in Figure 5.21. This indicates that the magnitude of LSC produced by normal reflections from silicon nitride is minor ($<|1.3\mu\text{m}|$) with little variation (1.3%) across the build area for Case R1. Additionally, the model identifies the reflectance will interact destructively with the incident light, reducing the overall exposure and the CLW, resulting in a negative value of spurious cure (Figure 5.21 [bottom]).

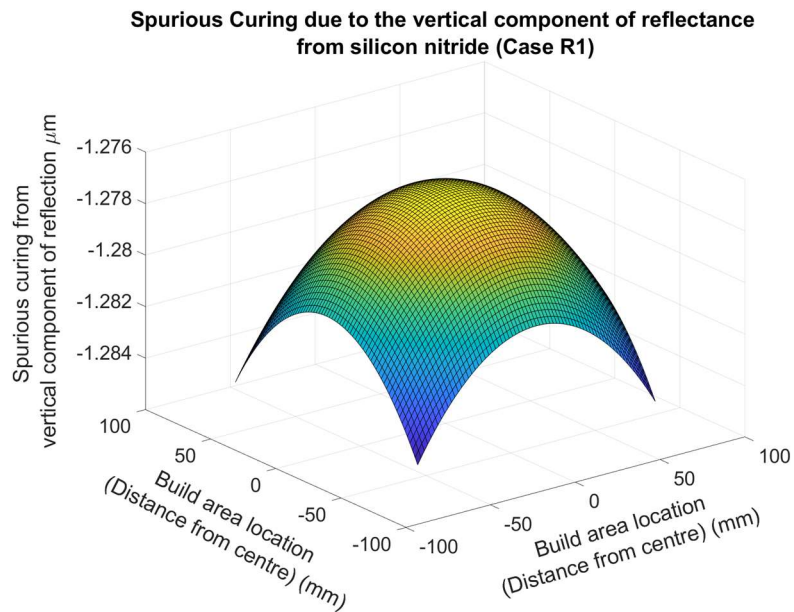
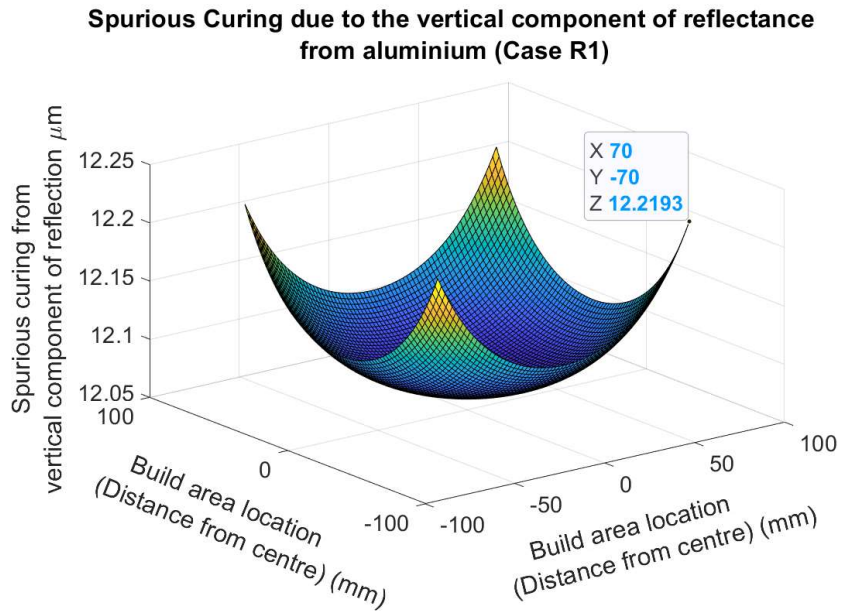


Figure 5.21: [Top] Spurious curing due to the vertical component of reflectance (Case R1) on aluminium and [bottom] silicon nitride.

The potential for the reflected exposure to extend the cure profile (spurious cure), with the distortion present in the Form 1+ beam at low speeds, is investigated using the beam profiling process in 5.1.4.1. This produces the distorted cure profiles with and without reflectance shown in Figure 5.22 for the Form 1+ beam (62mW [setpoint] single pass and scan). The 3D cure profile [left] and the corresponding 2D cured footprint [right] are shown for scan speeds of 50mm/s, 100mm/s, and 200mm/s.

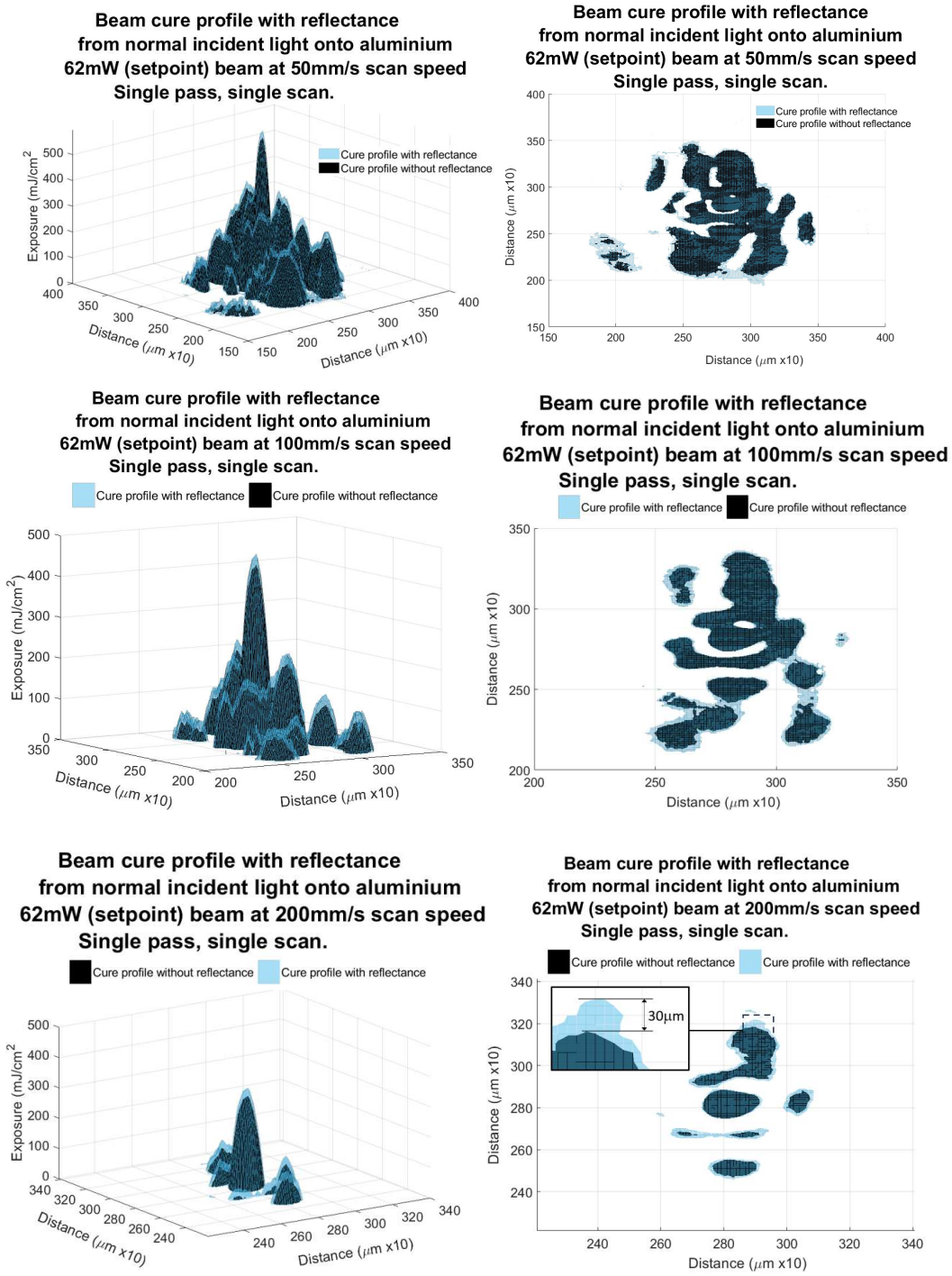


Figure 5.22: Cure profiles models with and without reflectance generated using beam profiler. [Top] Model generated using the beam profiler of the cured profile with and without reflectance from a single pass and scan of a 62mW (setpoint) beam, on aluminium at [top] 50mm/s scan, [middle] 100mm/s, and [bottom] 200mm/s scan speed.

For the given parameters (Case R1) at 200mm/s scan speed, the beam profile analysis in Figure 5.22 indicates up to 30µm of spurious curing will result from reflectance with a normal AOI on aluminium, compared to 6.1µm for the Gaussian model. This is substantially reduced by the lower reflection coefficient of silicon nitride (Table 3.2) for which the beam profile process indicates normal reflectance will produce a

negligible increase in CLW at scan speeds from 50mm/s up to 200mm/s. Similarly, the Gaussian model predicts a minor increase of 0.5 μ m due to the vertical component of reflectance from the material across the same range of scan speeds and parameters (Case R1).

The beam profile analysis (Figure 5.21 and Figure 5.22) is useful when interpreting the measured results of reflectance in section 4.1.4. As discussed in section 5.1.4.1, the profiler has identified the beam increasingly deviates from a Gaussian distribution as the scan speed reduces below 400mm/s. This compromises the applicability of the Gaussian exposure models to the Form 1+ results obtained at these speeds.

5.1.5.2. Spurious curing from reflectance on the Form 2

Further analysis is undertaken to demonstrate the feasibility of reflectance accounting for the measured distortion in the part width across the build area of the Form 2 (Figure 5.25). For reasons discussed later (section 5.1.5.3), diffuse reflections can result in increased spurious cure compared to specular reflections by transcending the perimeter line pass and promoting superposition. Consequently, the in-fill beam power at the print plane of 96mW as quoted in the literature [177] has been used for modelling reflectance (Case R2 in Table 5.8) on the Form 2. Other operating parameters used in the model were obtained from the calibration process (section 5.1.2), the literature review (Chapter 2), and the assumptions listed in section 3.2.13.

Case R2 parameters	
Parameter	Value
Photopolymer critical cure energy	12.6mJ/cm ²
penetration depth	192 μ m
In-fill power at the print plane	96mW [177]
FWHM beam spot size	140 μ m
Beam wavelength	405nm
Focal length of beam	300mm
Light path length	300mm
Build area	140mm x 140mm
Exposure delivered by repeated first layer scans.	Equivalent to 3.8 adiabatic scans
Hatch spacing	63.4 μ m
Parallel line passes producing superposition.	Yes.
Scans speed	1000mm/s

Table 5.8: Case R2 parameters for modelling reflectance on the Form 2.

The modelled output (Case R2) for the magnitude of LSC due to specular reflectance from smooth aluminium ($\eta=0.5$) is shown in Figure 5.23.

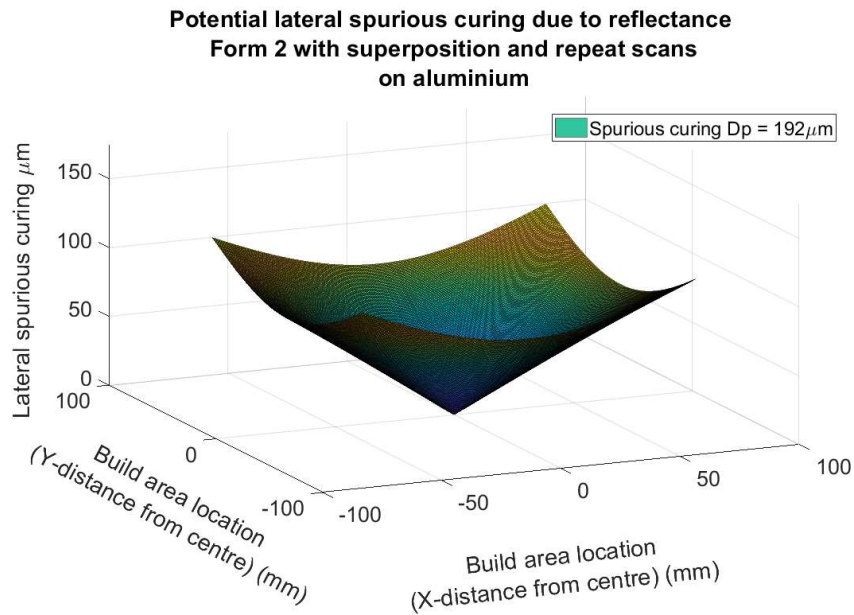


Figure 5.23: Potential for LSC due to reflectance from aluminium for Case R2 parameters on the Form 2.

The ‘concave-up’ profile of the modelled reflectance with MFLS in Figure 5.23 is consistent with the profile of the measured distortion test pieces with MFLS in Figure 5.16 (data in Table 4.10).

The reflectance model is sensitive to the penetration depth of the photopolymer because this determines the extent to which the beam is attenuated by the material before reaching the substrate. Additionally, the penetration depth defines the extent to which the reflected exposure will penetrate the photopolymer and produce spurious cure. Therefore, the difference between the measured distortion and the modelled spurious cure may be attributed to variation in the D_p and other assumed parameters. As mentioned in section 2.5, there is significant variation in the measured D_p between samples of the FLC photopolymer, values of $192\mu\text{m}$ [50] and $318\mu\text{m}$ [52] reported in the literature.

By applying the upper value to the reflectance model, the magnitude (absolute) of potential spurious curing increases significantly, from $375.0\mu\text{m}$ ($D_p = 192\mu\text{m}$) to $687.2\mu\text{m}$ ($D_p = 318\mu\text{m}$). The variation in the lateral component (LSC) is shown in (Figure 5.24) and are now compared with distortion in the measured calibration test pieces (results section 4.1.3.1).

**Potential lateral spurious curing due to reflectance
Form 2 with superposition and MFLS
on aluminium at 1000mm/s scan speed, D_p 192 μm and 318 μm**

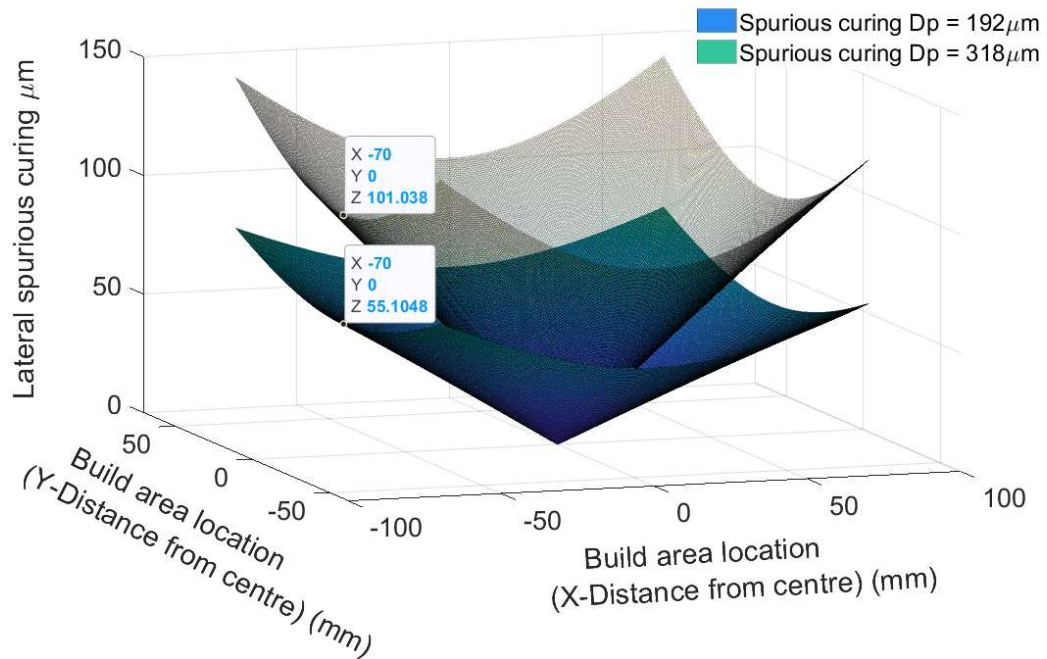


Figure 5.24: The potential for LSC due to reflectance from aluminium, and its variation with penetration depth, on the Form 2.

The 5.5mm tall calibration test pieces (method 3.3.4.2 part B) were shielded from reflectance by the preceding layers so cannot be compared directly with those exposed to reflectance on the build platform and constructed with MFLS. However, this can be accounted for by the calibrated D&E model (section 3.2.9.2). By comparing the measured width of the 5.5mm tall calibration test pieces with the calibrated D&E model values at positions +/-70mm from the build area centre as highlighted in Figure 5.16, the LSC attributed to reflectance is 125.1 μm (Table 5.6). This compares to the reflectance model values of 55.1 μm ($D_p = 192\mu\text{m}$) and 101.0 μm ($D_p = 318\mu\text{m}$), at the same location (Figure 5.24). To generate the measured LSC of 125.1 μm at 70mm (Table 5.6) a penetration depth of 384 μm (Figure 5.25) would be required. In practice several parameters could act to increase exposure and offset the required power and D_p (i.e., reduced hatch spacing, E_c , or scan speed).

For example purposes, using this D_p value to model the extent of LSC corresponding to the points of measurement across the build area (Table 4.13), distortion profile in Figure 5.25 is obtained. This shows that reflectance from exposure within the expected operating range of the Form 2, can produce the magnitude of LSC measured after accounting for the effects of divergence and ellipticity. Moreover, the modelled profile

resembles the measured profile with the standard deviation between the two data sets shown in Table 4.13.

Form 2 measured part width (1mm design) vs calibrated modelled part width with reflectance

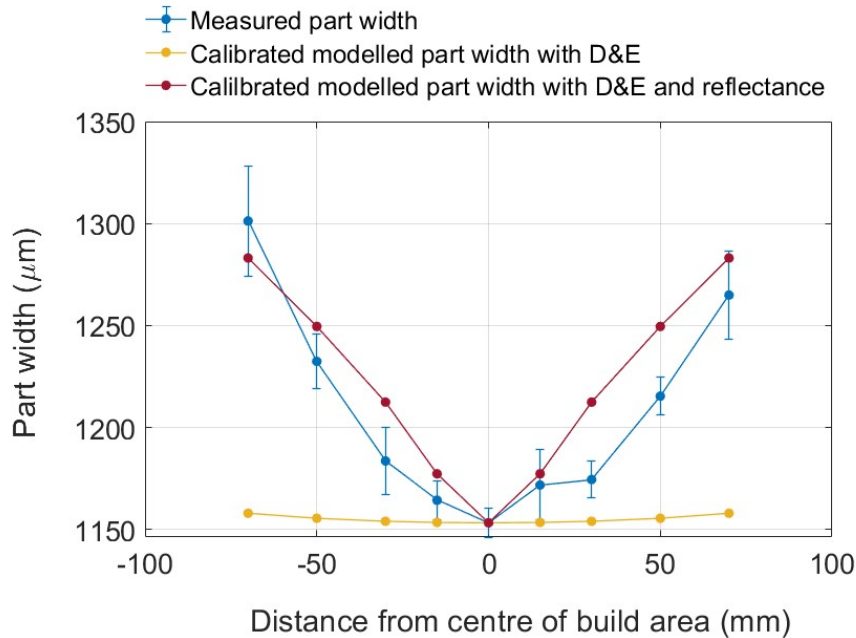


Figure 5.25: Measured and calibrated modelled part width with reflectance ($P_L = 96\text{mW}$, $D_p = 384\mu\text{m}$) to demonstrate the feasibility of reflectance accounting for the distortion measured.

It is stressed that because of the unknown parameters of the Form 2, the modelled output for the Form 2 in Figure 5.25 is purely to demonstrate the feasibility for reflectance to generate the measured extent and profile of LSC. Due to these unknowns, the assumptions required, and the inability to adjust the operating parameters on the Form 2, the reflectance investigation is progressed on the Form 1+ SLA machine. This machine provides the benefit of being open source with the ability to control and vary parameters.

5.1.5.3. Spurious curing from reflectance on the Form 1+

The modelled magnitude of LSC due to reflectance from aluminium at the Form 1+ operating parameters in Table 5.7 is shown in Figure 5.26. For reasons explained in section 5.1.5.2, the model is sensitive to the penetration depth of the photopolymer. Therefore, the model has been run at two reported D_p values of 192mm [50] and 318mm [52] to provide the potential range of spurious cure.

**Potential lateral spurious curing due to reflectance
Form 1+ with superposition and MFLS
on aluminium at 50mm/s scan speed, D_p 192 μm and 318 μm**

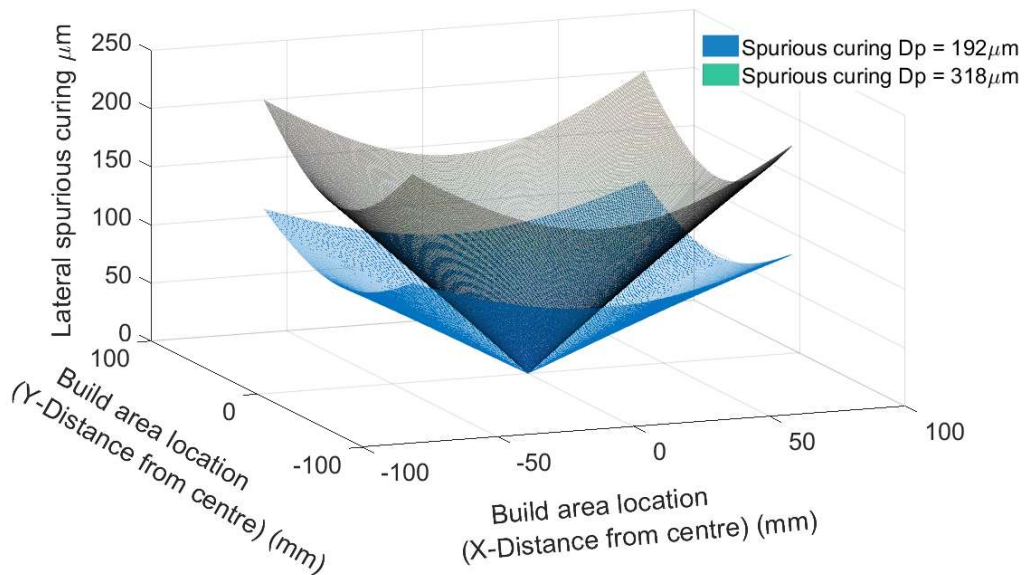
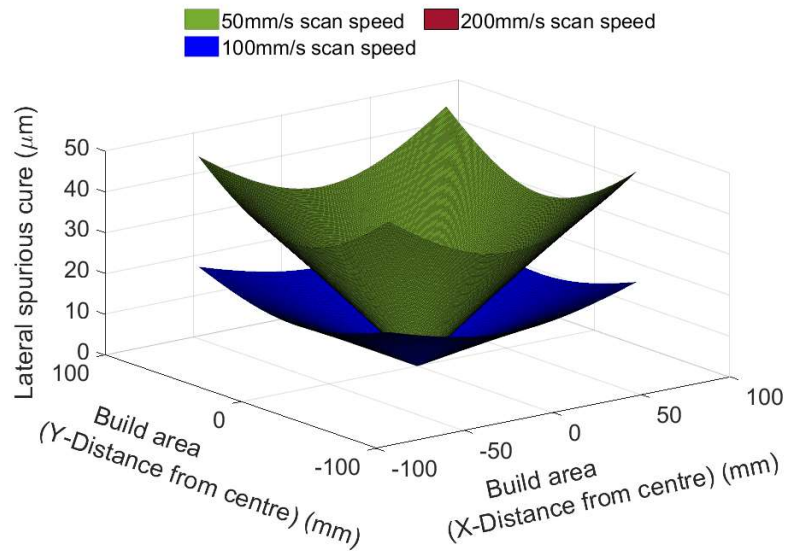


Figure 5.26: The modelled magnitude of LSC for the parameters of Case R1 with $D_p = 192\mu\text{m}$ and $318\mu\text{m}$ and 50mm/s scan speed for Gaussian beam incident at different locations across the build area.

Figure 5.26 shows a comparable magnitude of spurious curing from reflectance of a Gaussian beam on the Form 1+ at a scan speed of 50mm/s to those modelled using the Form 2 parameters in Table 5.8. This is due to the Form 2 beam being more powerful.

By applying the Bennet-Porteous (3.2.10.2) to the measured RMS surface roughness (Table 4.29) of the substrates, together with the AOI, the specular reflection coefficients are obtained. This gives coefficients of 0.00 and 0.99 for the build platform, and the polished surface of silicon nitride respectively. The completely diffuse reflections from the build platform will transcend the incident line passes resulting in a larger zone of influence (section 5.1.5.2) in which superposition occurs. Consequently, the surface (section 3.4.2.1), and specular reflection from silicon nitride will be more reliable for analysis. The modelled potential for LSC for the Form 1+ (Case R1) parameters in Table 5.7, at scan speeds of 50mm/s, 100mm/s and 200mm/s is shown in Figure 5.27, together with a penetration depth of 318 μm .

**Lateral spurious cure due to reflectance
Form 1 with superposition and MFLS
on Silicon nitride at 62mW and 50mm/s scan speed, 192 μ m Dp**



**Lateral spurious cure due to reflectance
Form 1 with superposition and MFLS
on Silicon nitride at 62mW setpoint power
50mm/s, 100mm/s and 200mm/s scan speed 318 μ m Dp**

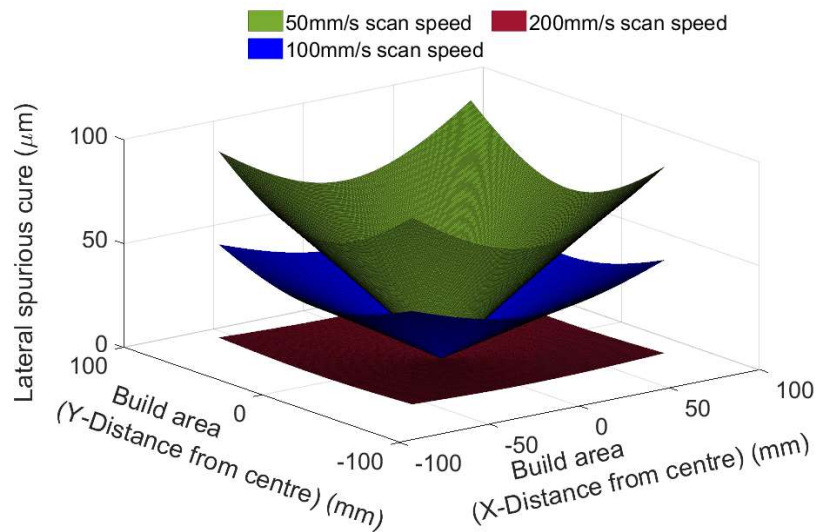


Figure 5.27: [Top] Gaussian model of LSC resulting from reflectance on the Form 1+ beam at 50mm/s scan speed on silicon nitride with penetration depth = 192 μ m and [Bottom] penetration depth = 318 μ m.

The modelling in Figure 5.27 indicates that the reflected beam exposure at scan speeds of 200mm/s or more, will not be sufficiently energetic to initiate any significant curing. Consequently, the investigation on the Form 1+ is conducted at elevated exposures associated with the scan speeds between 50mm/s and 200mm/s. The corresponding exposures for a given beam power setpoint is calculated using the calibration curve (Figure 5.2) and the process described in section 3.2, to apply to different equipment.

The maximum potential LSC for the respective penetration depths (Figure 5.27) at different scan speeds are shown in Table 5.9.

Potential LSC from reflectance with Case R1 parameters on silicon nitride.			
	50mm/s	100mm/s	200mm/s
$D_p = 192\mu\text{m}$	49.5	22.4	0
$D_p = 318\mu\text{m}$	95.8	51.1	6.3

Table 5.9: Potential LSC from reflectance on silicon nitride with Case R1 (Table 5.7) parameters at different scan speeds and penetration depth.

The modelled spurious cure is compared with that measured from experimentation using the parallel reflection tests (PRT) in 3.3.6.3 and tabulated in section 4.1.4.2. For this purpose, the test pieces are constructed with the same operating parameters (Case R1) used for modelling (Table 5.7). The results (4.1.4.2) of the PRT tests (method 3.3.6.3) are plotted in Figure 5.28.

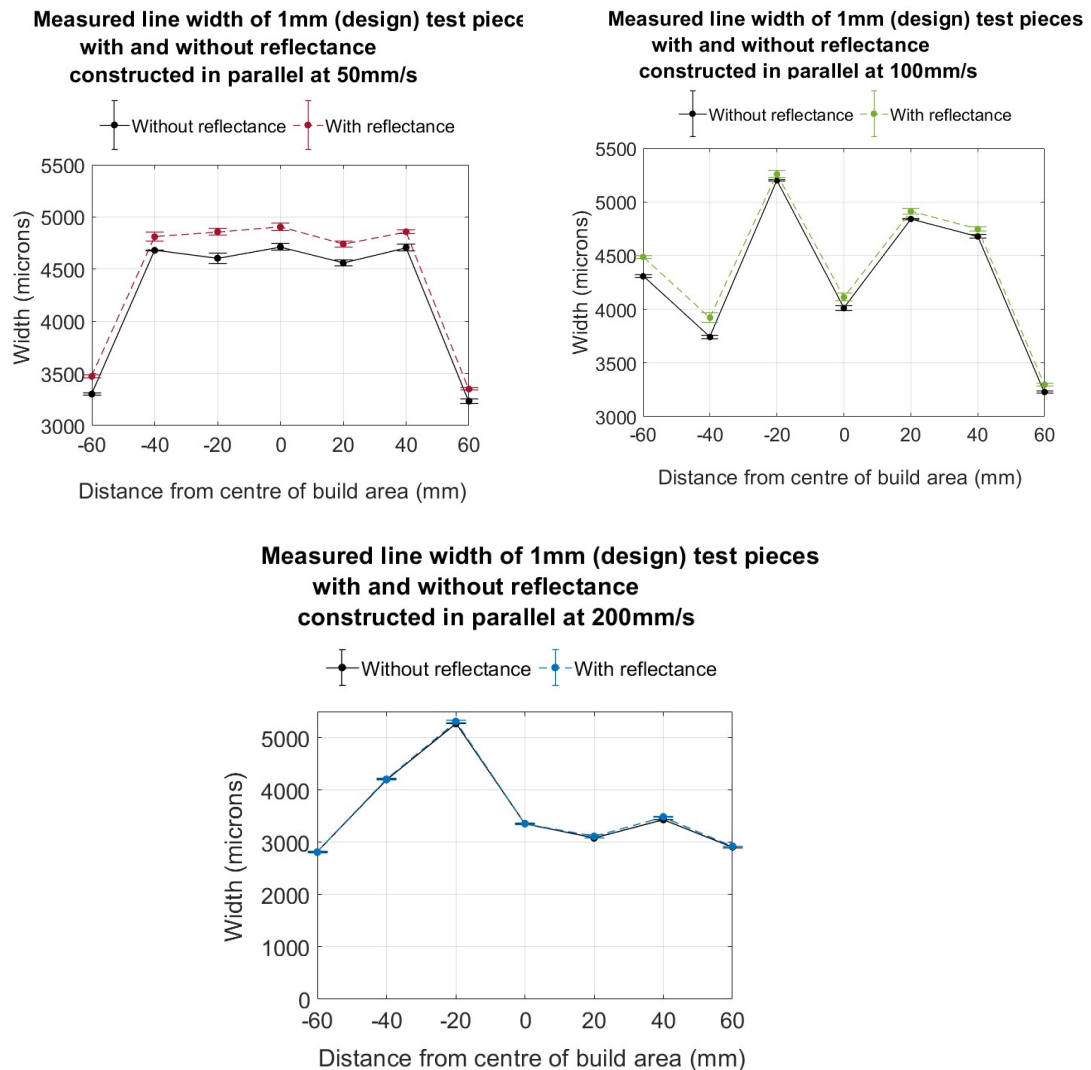


Figure 5.28: [Top left] Variation in the measured width of 1mm (design) test pieces constructed with and without exposure to reflectance from silicon nitride in parallel, at 50mm/s, [Top right] at 100mm/s, and [Bottom] at 200mm/s.

The magnitude of LSC in the PRT test is determined by subtracting the as-built width (Table 4.23 to Table 4.25) of the shielded part from that of the part exposed to reflectance. The results consistently show an increased CLW in the portion exposed to reflectance at all locations and speeds except centrally (0mm) at 200mm/s (inclusive). This is consistent with the measurement point, possessing a normal angle of incidence and at the highest scan speed, where Gaussian modelling predicts exposure from reflectance and the corresponding LSC to be lowest at $0\mu\text{m}$ (Figure 5.27). An example of the spurious curing produced by the PRT samples is shown in Figure 5.29. In this diagram, it is evident from which direction the beam is incident by spurious curing from reflectance formed on the opposite side. Consequently, the PRT test is considered to reliably detect the occurrence of reflectance manifested as spurious cure.

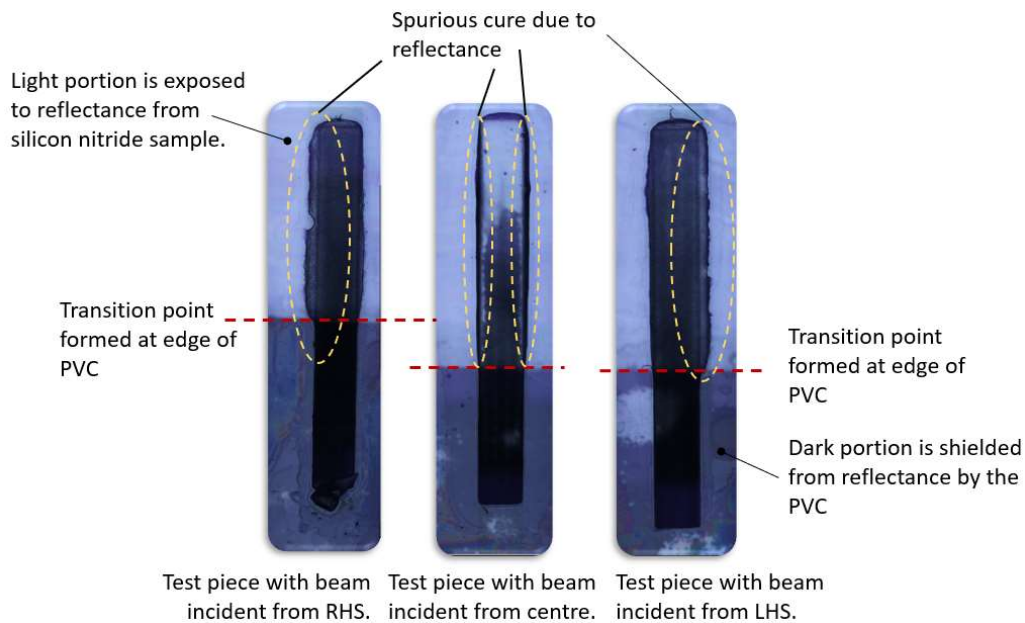


Figure 5.29: Test pieces with and without exposure to reflectance, constructed onto the composite substrate described in section 3.3.6.3.

The PRT tests show a reduction in the average LSC (Table 5.10) with increasing scan speed and the corresponding reduction in exposure. The average measured LSC reduces from $170.7\mu\text{m}$ (50mm/s) to $19.8\mu\text{m}$ at 200mm/s which is consistent with the trend identified by modelling (Figure 5.27).

The average LSC measured at the build area edges ($\pm 60\text{mm}$) at scan speeds of 50mm/s, 100mm/s and 200mm/s was measured (4.1.4.2) at $143.1\mu\text{m}$, $124.4\mu\text{m}$ and $26.6\mu\text{m}$. The measured results are in the same order of magnitude as the modelled (Gaussian) values in Figure 5.27 but the beam distortion (5.1.4.1) prevents a direct comparison between the two from being made.

A slightly elevated D_p would account for the minor LSC measured (Table 5.10) by the PRT tests at 200mm/s as explained earlier in this section. This reaffirms D_p as a parameter by which the Gaussian reflectance model could be calibrated by following a similar process to that applied for the Form 2 (section 5.1.5.2). However, this would not be appropriate with the specific Form 1+ machine used in this application due to the beam not being Gaussian at the range of scan speeds used (section 5.1.4.1).

Average LSC due to reflectance with scan speeds for the SRT and PRT.			
	50mm/s	100mm/s	200mm/s
PRT	170.7	103.9	19.8

Table 5.10: Average difference in CLW due to reflectance at different scan speeds for the PRT test.

5.1.5.4. Destructive interference

Modelling indicates the reflectance from silicon nitride submerged in the photopolymer will interfere destructively (section 3.2.10) with normal incident light. However, this contrasts with the measured results (section 4.1.4.1 and 4.1.4.2) at the central position (0mm) where the beam will have a normal AOI. These results show there to be an increase in the part dimension consistent with constructive interference. This is attributed to the likely incoherence of the incident and reflected beams at high exposures resulting in different interactions to those predicted by the Gaussian model. Additionally, destructive interference will only occur where the vertical component (Figure 5.18) of the reflection interacts with the incident beam. Interference between the lateral components of the incident and reflected beams does not occur due to them being diametrically opposed. Moreover, at oblique angles, and when the reflected exposure is greater than E_c , the lateral component of reflectance will dominate (Figure 5.27 vs Figure 5.21). In a scenario with a normal AOI and reflected exposure is less than E_c , the resulting LSC will be minor. Consequently, the influence of destructive interference and the vertical component of reflectance are considered to have a negligible influence on the LSC in the application discussed.

5.1.5.5. Secondary reflections

If sufficiently powerful, it is possible for reflections from the substrate to be transmitted through the photopolymer and generate secondary reflections from the resin tank window. The potential for these reflections to contribute to spurious curing has been modelled for the geometry of the Form 1+ with a high exposure associated with the parameters in Case R1 (Table 5.7) with superposition, MFLS and a scan speed of 50mm/s. This identified at a point of incidence at the extremity of the build area, the first reflection from the silicon nitride substrate will have an intensity of $17032.8\text{mW}/\text{cm}^2$. This will be attenuated by $2003.9\text{mW}/\text{cm}^2$ as it is transmitted through the $100\mu\text{m}$ layer of photopolymer. This results in a reflection with intensity of $15028.9\text{mW}/\text{cm}^2$ incident on the resin tank's PDMS window (interface 4-3) at an angle of 10.5° and producing a reflection coefficient of 0.029. The resulting secondary reflectance will have intensity of $43.0\text{mW}/\text{cm}^2$, which at 50mm/s scan speed delivers an exposure of $0.14\text{mJ}/\text{cm}^2$. The exposure of the secondary reflection will be two orders of magnitude less than the critical energy of cure. Therefore, the influence of secondary reflections is considered negligible in this application.

5.1.6. Refraction

As described in section 3.2.6.1, refraction can adversely affect the accuracy of the beam and lateral precision of the construction. The modelled cumulative distortion due to refraction (δK_{xt}) across the build area, is shown in Figure 5.30. The magnitude of the distortion increases progressively towards the extremities of the build area as the angle of incidence increases.

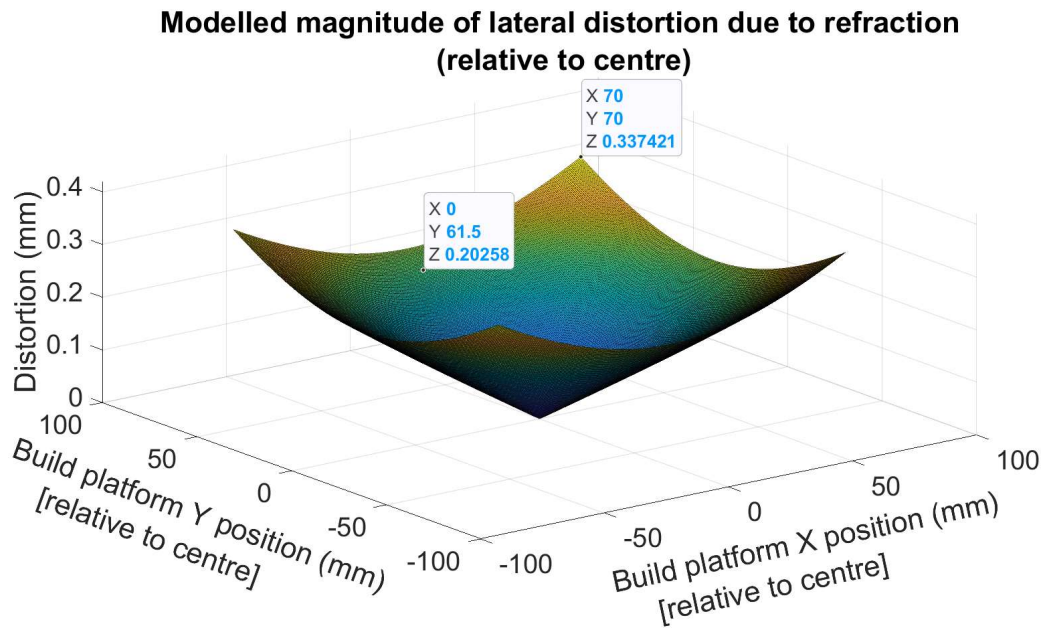


Figure 5.30: Modelled magnitude of lateral distortion across the build area of the Form 2

The measured distortion laterally across the build area is included in Table 4.15, (section 4.1.3.5). To isolate the distortion due to refraction from other factors in the measured results (Table 4.15), the experiment described in section 3.3.5, was conducted on the Formlabs Form 2 and 3 machines, and the results compared in figure (Figure 5.31).

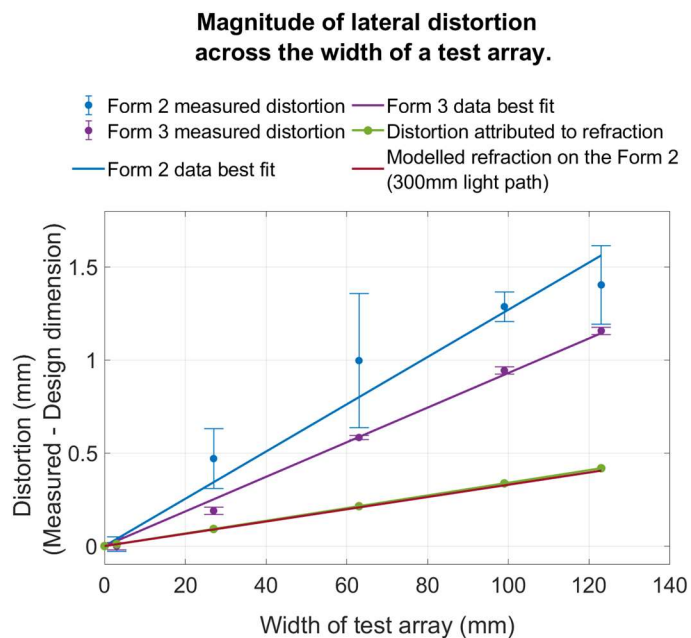


Figure 5.31: Measured and modelled distortion profiles for the Form 2 and the Form 3 SLA machines with refraction deduced from measurements.

Both the Form 2 and Form 3 machines exhibit lateral distortion. The cause of the lateral distortion in the Form 3 (Figure 5.31) is attributed to the file conversion tolerance [178] within the control software which is common to both machines. This is

because the Form 3 benefits from equipment to maintain a normal angle of incidence during construction and thereby eliminates refraction. Therefore, the difference between the measured values recorded using the Form 3 (Table 4.16) and those obtained from the Form 2 (Table 4.15), is attributed to refraction. By applying linear regression to the measured Form 2 and Form 1+ results (4.1.3.5), the distortion attributed to refraction is obtained (Figure 5.31).

This provides the magnitude of lateral distortion across the full width (123mm) of the test array calculated at 0.41mm. This is consistent with modelled value at the corresponding point (X: 61.5mm [relative to centre], Y: 0mm) in Figure 5.30 of 0.20mm which equates to 0.41mm across a 123mm dimension. Modelling predicts the lateral distortion from refraction to increase to 0.67mm at the longest (diagonal) dimension (198mm) of the build area.

5.1.7. Tolerances with ellipticity, divergence and steps

By applying Equation 3.26 to a laser path length of 300mm, the increase in the beam's width at the extremity of a square build area is shown in Figure 5.32. This shows a significant increase in the spot size once the length of the build area increases above approximately 100 μ m. The increase in beam width is dominated by the influence of ellipticity. Therefore, to reduce the AOI and the variation across the build area, it is beneficial to elongate the light path. This has been achieved with the use of the main mirror (Figure 3.9) in the case of the Formlabs equipment investigated in this study. To minimise the CLW and the corresponding MFS, the beam should be focussed on the photopolymer's surface.

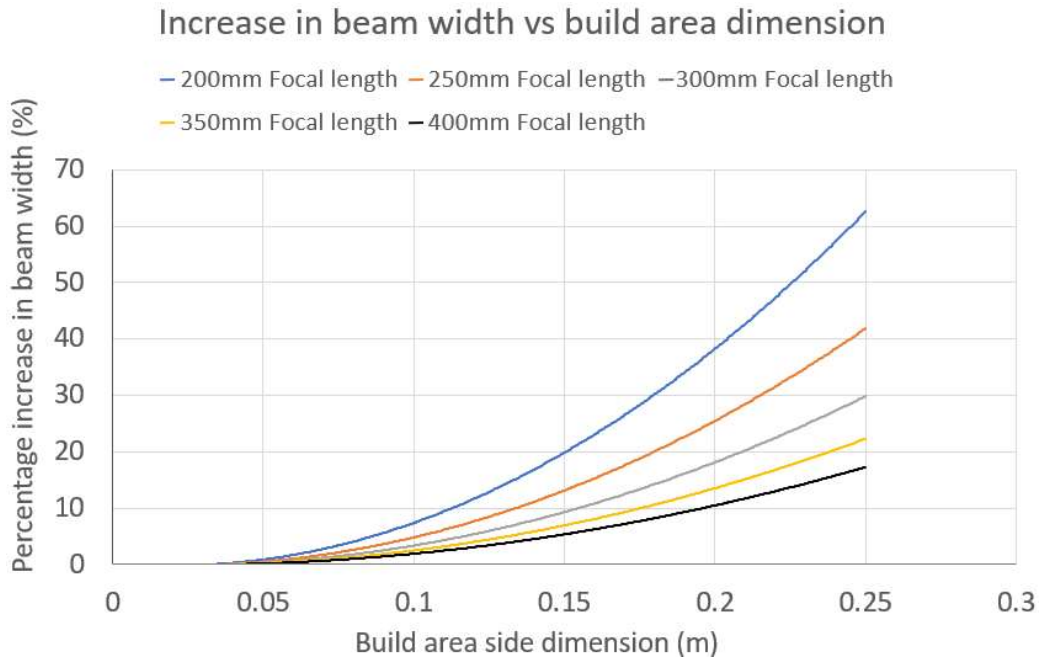


Figure 5.32: The increase in beam width due to ellipticity and divergence as a function of the build area dimension.

5.1.7.1. Optimising focus to reduce divergence.

The beam can be further optimised by focussing it on a midpoint between the extremity of the build area and the centre as shown in (Figure 5.33). Thereby reducing the extension to the light path at the extremity and the associated loss in focus.

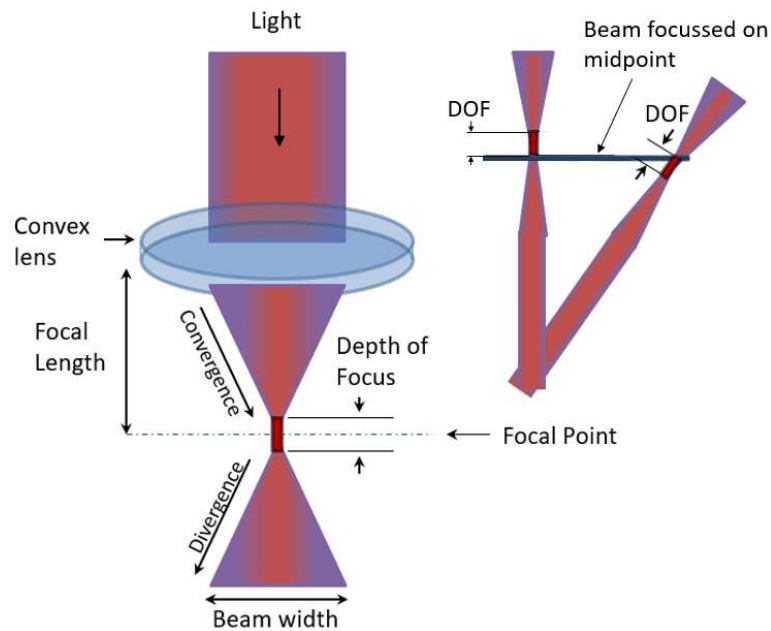


Figure 5.33: Focal length of a laser and optimal point of focus.

Figure 5.34 show the variation in the CLW across the build area using the optimised focal point for the Form 1+, and Form 2. The benefit compared to a beam focussed on the centre of the build area is demonstrated in Figure 5.34.

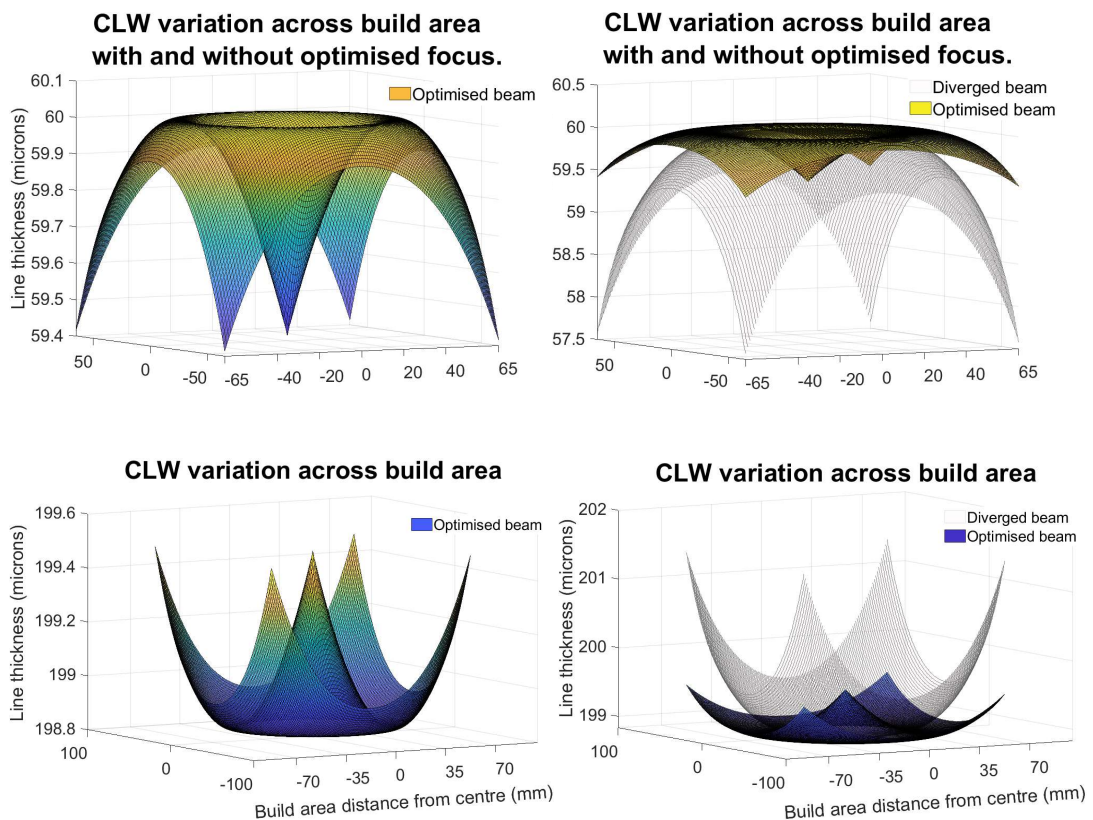


Figure 5.34: CLW with optimised focus.

[Top left] CLW from the Form 1+ beam optimised for focus.

[Top right] CLW from the Form 1+ beam with and without optimisation.

[Bottom left] CLW from the Form 2 beam optimised for focus (with MFLS and superposition).

[Bottom right] CLW from the Form 2 beam with and without optimisation (with MFLS and superposition).

By using the MATLAB programme (A1 Table 4.1) developed in section 3.2.7.2, the maximum build dimension to maintain the beam within the depth of focus (section 2.7.1) can be determined. To maintain a typical DOF equating to an 1% increase in the beam dimension, the above optimisation allows the length of the build platform to be doubled with a corresponding increase in area.

5.1.7.2. Manufacturing tolerances

The size of the inter-layer steps (3.2.3) for given operating conditions and the maximum layer thickness which can be applied before a defined manufacturing tolerance is exceeded have been modelled using Equation 3.32. To comply with the 50 μ m design tolerances for the package in Figure 1.2 using the case R1 parameters (Table 5.7), the MLT has been calculated to be 163.8 μ m. Similarly, the number of first layer scans applied to a

construction, would need to be considered to avoid the resulting meniscus described in section 5.1.4.2, exceeding design tolerances. However, it is envisaged the requirement for MFLS will be removed by treating the silicon nitride substrate as discussed in section 5.2.8.3.

As explained in section 3.2.2, the beam dimensions for a given exposure, determine the CLW and ability to meet manufacturing tolerances. These are relatively insensitive to dimensional changes in the beam waist. For instance, applying equation (Equation 3.20) to the Form 2 (R2 parameters) shows the beam waist would need to increase by 38.2% (from 118.9 μm to 164.3 μm) to exceed a 50 μm tolerance.

However, as already shown (Figure 5.32), the increase in beam dimensions due to ellipticity and divergence, increases disproportionately with distance. By applying an iterative process in MATLAB to combine the effects of D&E, it has been calculated that the maximum build area side length could be increased to 274mm until a 50 μm tolerance is exceeded.

The relationship between the CLW, tolerance and the corresponding exposure, is now used to identify the exposure limits for the operating window (Figure 5.35) in which to optimise the build process in section 5.1.8.

5.1.8. Construction Optimisation

Stereolithography has a lower throughput than alternative conventional techniques such as injection moulding. Consequently, the technology has often been applied to the manufacture of limited quantities or bespoke items rather than mass production. The process for maximising the build area to benefit the associated scale of production, while complying with tolerances, has been described in section 5.1.7.2. Here, the process to reduce the build time is discussed.

In a typical SLA process, the delay time between layers significantly influences the duration of a construction. Therefore, by orientating the part and maximising the layer thickness as described in section 5.1.7.2, the number of layers can be minimised, with a potentially substantial reduction in build time.

Using Equation 3.31 describing build time as a function of a part's geometry (section 3.2.12), hatch spacing, scan speed, and layer thickness, allows the corresponding exposure, with the effects of superposition and D&E (section 3.2.6), to be quantified. The relationship between build time, geometry (R_{az}), and exposure is mapped in Figure 5.35 for the Form 1 parameters in Case R1 (Table 5.7). This shows how the build time increases as a construction of given volume becomes proportionally taller and the exposure increases (i.e., applying MFLS, or reducing scan time or hatch spacing).

Build time vs shape geometry and delivered exposure

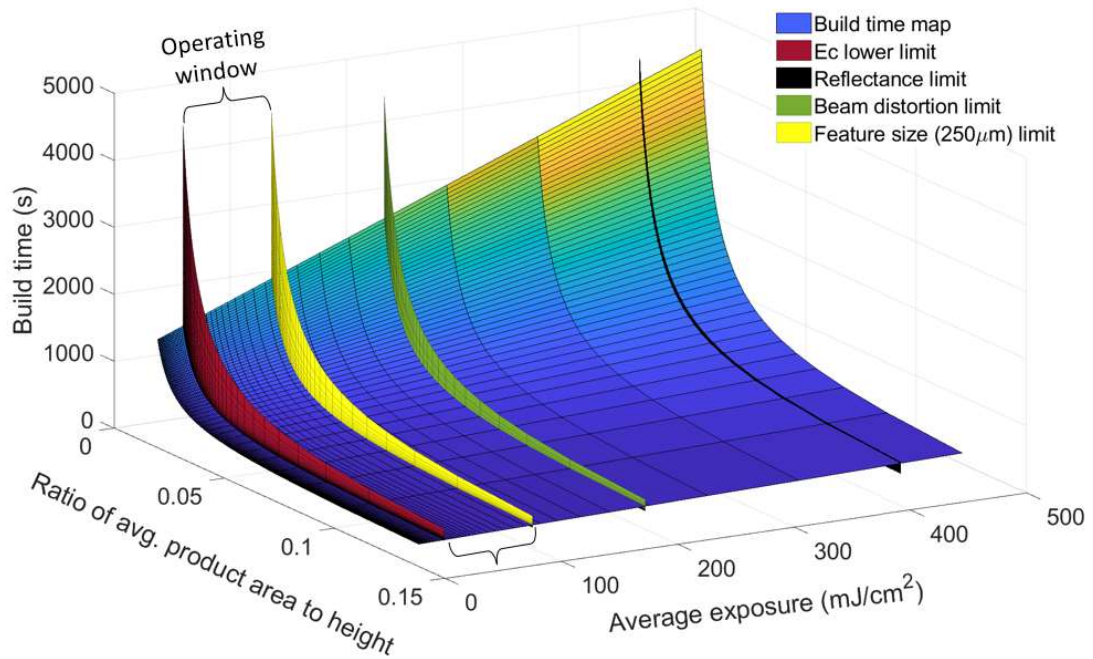


Figure 5.35: Build time operating window for optimisation using Case R1 parameters.

It is then possible to apply the upper exposure limits at which distorting effects will compromise the ability to comply with tolerances. The exposure limits include those associated with the onset of spurious curing from distortion in the beam (section 5.1.4.1), reflectance (section 5.1.5.3), and the CLW to achieve the required MFS (section 5.1.3). In the above example the MFS was set to $250\mu\text{m}$. Conversely, the minimum exposure limit is set at that recommended [9] to suitably cure the photopolymer of double the E_c (delivered at the layer depth). These exposure limits then define the operating window in which the machine parameters can be optimised to minimise build time (i.e., by increasing scan speed).

In this example (Figure 5.35) the upper exposure limit (yellow) is dictated by that which can achieve the minimum feature size of $250\mu\text{m}$. The model then identifies the hatch spacing can be increased to $140\mu\text{m}$ from $90\mu\text{m}$ (Case R1) to maintain the variation in exposure within defined limits of 3% ([9] (section 2.6)). This allows the build time for a 10mm cube to be reduced by 26.3% from 50:22 minutes to 37:08 minutes at the low scan speed of 50mm/s. A similar reduction of 26.6% was produced when comparing the construction time of the geometry with the same hatch spacings in Formlabs' preform build preparation software.

5.1.8.1. Optimisation of gas sensor

The optimisation process is now applied to the construction of the gas sensor package in appendix A, using the Form 1 machine. Reorientating the construction of the package from an upright position to a horizontal orientation will reduce the number of construction layers from 48 to 15 and the corresponding construction time by 65%. A review of the part's drawing (Appendix A) identifies a required MFS of $350\mu\text{m}$, and a maximum tolerance in the z-plane of $50\mu\text{m}$ and $100\mu\text{m}$ in the X-Y. Modelling the construction using the R1 parameters (Table 5.7) with a $50\mu\text{m}$ layer thickness, produces the operating window shown in Figure 5.36 with exposure limits between $36\text{mJ}/\text{m}^2$ and $219\text{mJ}/\text{cm}^2$ in which to optimise the build with the upper limit dictated by the distortion present in the beam (section 5.1.4.1). The limitations due to the relatively large MFS requirement and spurious curing from reflectance occur at $578\text{mJ}/\text{cm}^2$ and $439\text{mJ}/\text{cm}^2$ respectively. This allows the hatch spacing to be increased from $90\mu\text{m}$ to $139\mu\text{m}$ while complying the 3% variation (section 2.6) in lateral exposure due to superposition. Applying the increased hatch spacing will allow a further 5% reduction in construction time from 139s to 132s. The maximum spot size increase (relative to centre) while complying with the $100\mu\text{m}$ tolerance is 27.3% (section 3.2.7.2). The corresponding maximum build area in which to scale production while complying with the defined tolerance is calculated to be 566cm^2 (238mm side length).

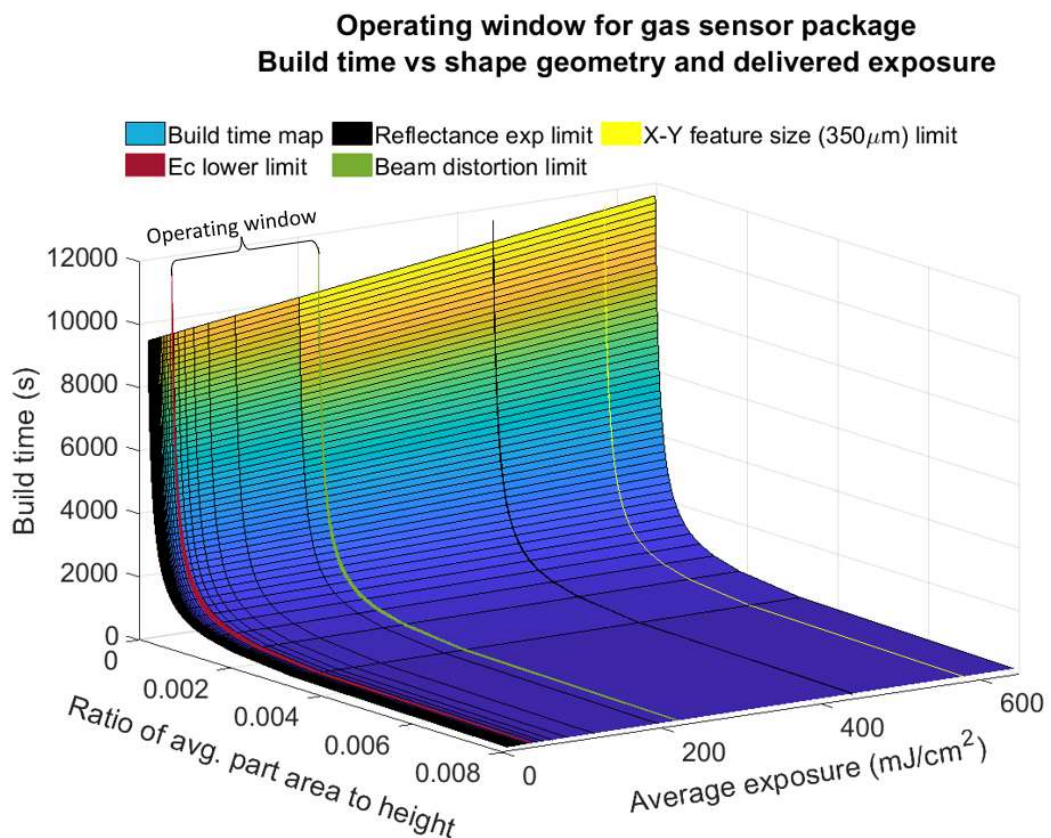


Figure 5.36: Operating window for gas sensor package

5.1.9. Mitigation and correction

In addition to the optimisation methods to reduce beam distortion discussed in section 5.1.7.1 and those to optimise the construction process in 5.1.8, additional methods to mitigate distorting effects are discussed in the following sections.

5.1.9.1. Angle of incidence

The reflection coefficient (section 3.2.10) is sensitive to the angle of incidence which in turn is dictated by the beam path length.

Figure 5.37 shows the reflectance coefficient for light (405nm) incident on silicon nitride submerged in FLC photopolymer increases with the AOI, from 0° to 90°. There is no critical angle for silicon nitride in this application due to the refractive index being greater than that of the photopolymer.

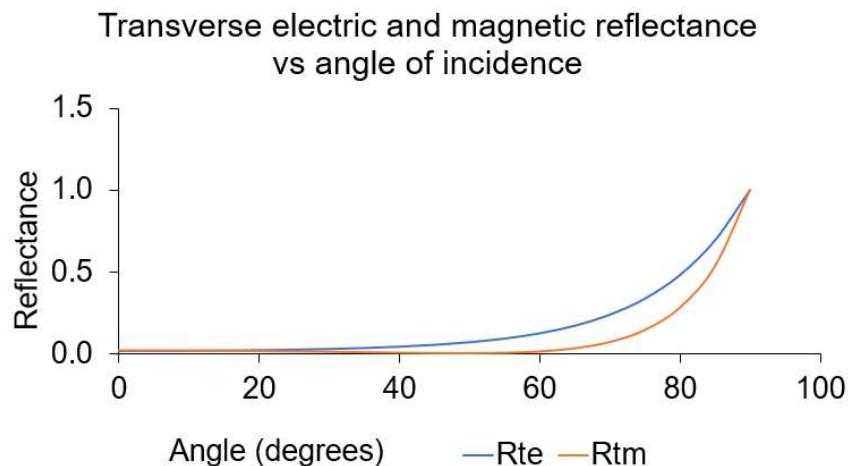


Figure 5.37: Transverse electric and magnetic reflectance of 405nm light incident on a silicon nitride wafer.

For the Formlabs equipment used in the current investigation, the greatest AOI formed between the galvanometer and the extremity of the build area (300mm path) is approximately 10 degrees. The path length is therefore important in reducing reflectance and other distorting effects (i.e., ellipticity and refraction) associated with the AOI. For the example material of aluminium possessing a lower refractive index ($n=0.5$) than the photopolymer with a path length below ~ 145 mm would result in the beam being incident above the critical angle ($\sim 19^\circ$) and total reflection. For these reasons, it is desirable to extend the path length which is achieved in the Formlabs equipment using the main mirror (Figure 3.9).

From the current investigation, it has been identified that mirror could be developed further with a parabolic profile to correct for the AOI formed between the galvanometer and the mirror. This would maintain a normal angle of incidence across the build area. By incorporating the main mirror into the reflectance model (B1 Table 4.1), the beam’s AOI on the mirror, and the corresponding angle of that surface required to reflect the beam normal to the build area, has been calculated. This process is applied to each cell of the MATLAB matrix and interpolated to produce the required corrective mirror profile. An example output of this process is shown in Figure 5.38.

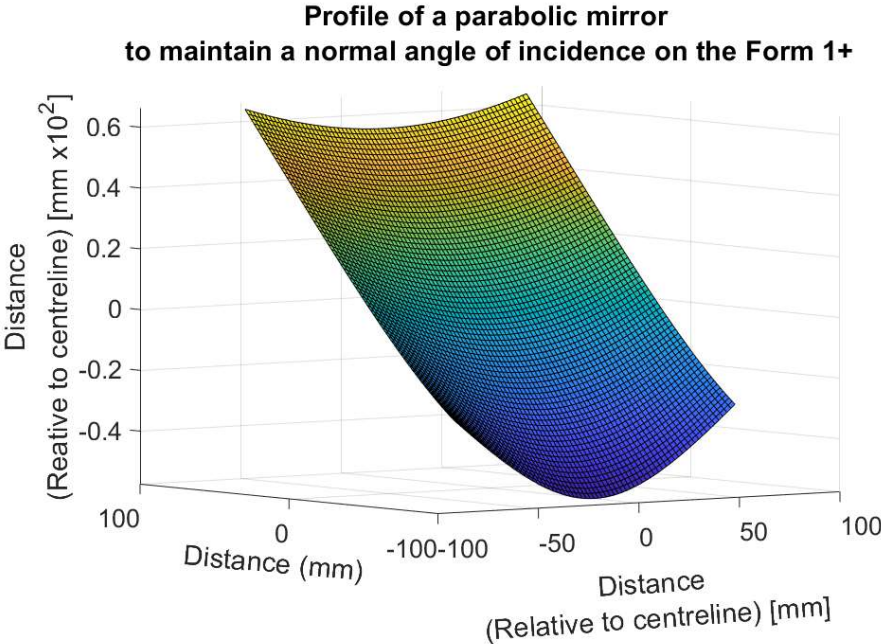


Figure 5.38: The profile of a parabolic mirror to maintain a normal angle of incidence for the geometry of the Form 1 machine.

5.1.9.2. Anti-reflective coatings

As described in section 1.4, it is common practice in photolithography to apply anti-reflective coatings. Applying the design rules described by Okonkwo et al [179], for the properties of the materials and beam parameters in the current application (section 3.1), the coating specification in Table 5.10 has been identified for silicon nitride in SLA.

Anti-reflective coating for silicon nitride for use in SLA	
Refractive index of photopolymer	1.54
Refractive index of silicon nitride	2.1
SLA Laser wavelength	405nm
Refractive index of anti-reflective coating for silicon nitride	1.78
Thickness of anti-reflective coating	56.98 (and multiples thereof)

Table 5.11: Specification for an anti-reflective coating to be applied to silicon nitride for use in SLA at 405nm.

The use of anti-reflective coatings in SLA has not been investigated for the reasons explained in section 3. However, it remains a topic for potential further investigation.

5.1.9.3. Material modification

Due to reflectance being a function of the dissimilarity between the refractive indices of contiguous media, if these refractive indices were equal, no reflectance would occur. This could be applied to an SLA process by modifying the refractive index of the photopolymer using the process described by Taormina et al [119].

5.1.9.4. Control logic compensation

Alternatively, by mapping the combined effects of distortion, as done in Figure 5.15, the control logic can be programmed with an algorithm to adjust the power setpoint of the beam and the corresponding exposure according to its location on the build area. The beam power correction coefficient is obtained by dividing the design power required to achieve the desired CLW (Equation 3.6) by the power required to construct the CLW of as-built test pieces and applying regression analysis. An example of such an algorithm for the Form 2 to correct the measured distortion in Figure 5.16, to achieve a consistent target 250 μ m CLW across the whole build area, is shown in Figure 5.39. In this example, Y is the power correction coefficient and X is distance (from centre) in the build area. This can be adjusted for different target CLW, and substrate materials to compensate for the cumulation of distorting effects.

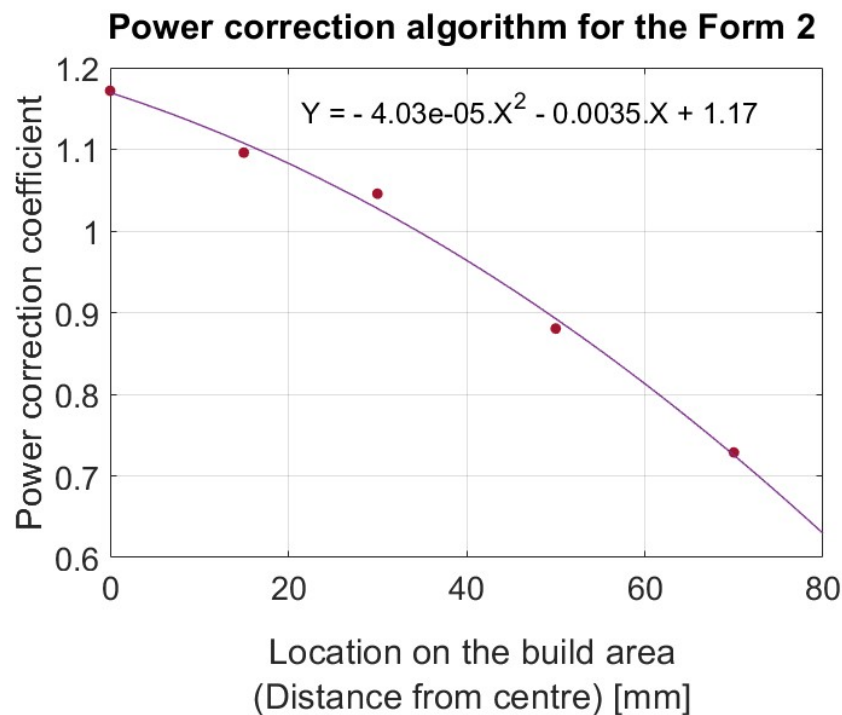


Figure 5.39: Beam power correction algorithm for the Form 2.

5.1.10. Distorting effects summary

To address the concerns associated with constructing directly onto silicon nitride (section 1.5) the potential for reflectance to produce spurious curing in the SLA process was investigated. To support this, the distorting effects of reflectance, refraction, divergence and ellipticity, which all occur at oblique angles, have been modelled. The D&E models were calibrated against as-built constructions and compared with the measured lateral distortion profile across the build area of a Form 2 SLA machine. This identified an additional and significant distorting mechanism is active at high exposures, which was attributed to reflectance. At assumed default operating parameters, modelling indicates that LSC due to reflectance is possible on the Form 2 machine.

The investigation identified that spurious curing from reflectance can be significant at high exposures and particularly when applying the common practice of repeated first layer scans to promote adhesion. This is a concern for the application in the current study because of the intention to construct SLA products directly onto a silicon nitride substrate.

Further experimentation on a Form 1+ machine produced unusually wide products due to low intensity distortions in the beam identified by profiling the laser. Spurious curing occurs when the photopolymer is sufficiently exposed to the distorted portion of the beam for curing to ensue. This explained the behaviour of the beam and the cure patterns produced at high exposures, but the method is unsuitable for accurate quantified analysis. Additionally, the distorted beam does not conform to a Gaussian profile at high exposures which makes Gaussian based models inapplicable. Consequently, a dedicated reflectance test where test pieces are constructed on to a prepared unreflective substrate, in parallel to the reflective substrate of interest was devised. This normalises the samples for the effects of D&E as well as environmental conditions and provides the distortion directly attributable to reflectance. This method confirmed the production of LSC from reflectance. The measured magnitude of the LSC followed a relationship with exposure corresponding to that predicted by modelling. The potential for reflectance from silicon nitride to produce LSC is significant but dependent upon a number of variables within the SLA process, the properties of the photopolymer, and the substrate.

During the investigation the potential for distortion from the characteristics of refraction and overexposure were also quantified. The latter together with a calibrated model for divergence and ellipticity have been used to identify limits at which manufacturing tolerances can be complied with. These limits are then used to define an operating window in which the construction process can be optimised for time and scale.

Several potential methods for further investigation to mitigate reflectance and other distorting effects which occur at oblique angles of incidence have been identified. These include the optimisation of the beam's focus to reduce divergence and the design of a parabolic mirror to maintain a normal angle of incidence onto the build area. Lastly, a process to produce an algorithm specific to a given SLA application, to compensate for the combined effects of distortion using as-built measurements, has been developed.

5.2. Adhesion discussion

“By definition ‘additive’ manufacture involves sticking things together. A sound knowledge of what helps and hinders the creation of strong interfaces will always be required.”

Professor Steven Abbott, (2020) [57].

This section discusses the results pertaining to adhesion presented in section 4.2 which were produced using the experimental methodology described in section 3.4.

5.2.1. Surface roughness

From the LEP (Equation 2.12), the minimum pore size which can be penetrated for a given photopolymer and conditions can be calculated. Influencing factors (section 2.4.4) are the atmospheric pressure, the head of pressure generated by the liquid (which is added to the atm pressure) and the IFT of the liquid. It is posited the substrate pores are irregular and therefore have a geometry factor (β) of <1 [103] with an assumed value of 0.9. This indicates that for the IFT of FLC photopolymer and its contact angle on silicon nitride (Table 4.28), at atmospheric pressure, the minimum pore size (β assumed = 0.9) which can be filled by a 100 micron pressure head (equal to a default SLA layer thickness) is $0.21\mu\text{m}$. Consequently, the surface pores on silicon nitride (Table 4.29) are considered too small for the photopolymer to penetrate and bond via structural mechanisms such as mechanical interlocking, as the resin solidifies during curing. Therefore, such mechanisms are dismissed for the application of constructing SLA parts onto polished silicon nitride. Conversely, FLC photopolymer has the potential to penetrate (Table 5.12) the pores present on the relatively rough surface of aluminium (rms roughness = $0.52\mu\text{m}$), and the build platform (rms roughness = $2.6\mu\text{m}$). Additionally, the photopolymer may also penetrate the larger pores present on polycarbonate which has a rms roughness of $0.02\mu\text{m}$ but a peak size of $0.94\mu\text{m}$. Consequently, FLC photopolymer is considered capable of producing structural

interactions following curing on the polycarbonate and aluminium surfaces. However, the quality of contact at smaller pores will be reduced due to the ‘lotus effect’ (section 2.4.4) impacting the SFE mechanism.

Minimum photopolymer-pore entry size	
Substrate	Minimum pore size (µm) which can be filled by FLC photopolymer (β = 0.9)
Polycarbonate	0.24
Aluminium	0.24
Silicon nitride	0.21

Table 5.12: Minimum substrate pore size which can be penetrated by FLC photopolymer.

5.2.2. Photopolymer characterisation

For reasons explained in section 3.4.2, (Figure 4.5) the change in SFE, elastic modulus, and Poisson’s ratio, were measured at regular intervals during the curing process to characterise how these properties may change. Poisson’s ratio and SFE were found to be uninfluenced by post build curing. Conversely, the tensile strength of the material (Figure 4.5) increased substantially with PBC. Elastic modulus also increases significantly (Figure 4.5) up to a knee point at 8 minutes of curing and continues to increase at a much-reduced rate thereafter.

The profile of elastic modulus can be divided into two stages, with each described using linear regression. The first stage, up to 8 minutes of cure is described by Equation 5.1.

$$\frac{E_{t_1} - E_{t_0}}{480} t + E_0 = E_t$$

Equation 5.1: Change in elastic modulus with time up to 8 minutes.

Where E is elastic modulus, t is time (seconds), t₀ is before PBC and t₁ is 8 mins of post build curing.

The second stage from 8 up to 30 minutes is described by Equation 5.2.

$$\frac{E_{t_2} - E_{t_1}}{1320} \cdot (t - t_1) + E_{t_1}$$

Equation 5.2: Change in modulus from 8 to 30 minutes.

5.2.3. Tensile adhesion tests of SLA products with curing.

The tensile test results of SLA sample pieces constructed onto polycarbonate and aluminium are shown in Figure 4.7 and Figure 4.8 (section 4.2.2) respectively with supporting data in Appendix G (section 7.5.1). Both sets of results consistently show an initial increase in the maximum strength of adhesion for a given period of PBC up to approximately 8 minutes. A high degree of scatter is present in experiments on both substrate materials. In the case of polycarbonate, the quality of adhesion becomes more susceptible to failure at reduced forces with progressive PBC beyond 8 minutes. Moreover, the adhesion of some test pieces to aluminium and PC substrates, when cured for 8 minutes and longer, was insufficient for testing. The high failure rate and variation in adhesive strength with PBC necessitated the further investigation discussed in the following sections (5.2.4 to 5.2.7).

5.2.4. Comparison of separation force with Kendall's model

Kendall's idealised model (Equation 2.8) is used to provide the maximum separation force achievable from the WoA generated under a tensile test.

By applying other measured parameters (WoA, elastic modulus and Poisson's ratio) and the contact area of the test piece to Kendall's model, a marginal increase in the adhesive strength (Table 5.13) due to the change in modulus from 0.43N for a green part to 0.57N after 8 minutes of PBC is predicted on aluminium, and similarly with polycarbonate (Table 5.13).

Kendall's tensile separation force attributable to SFE		
	Aluminium substrate (N)	Polycarbonate substrate (N)
Green part (E = 0.39 GPa)	0.43	0.40
Cured part (8 mins E = 0.69 Gpa)	0.57	0.53

Table 5.13: Predicted separation force for 1mm² SLA test pieces on aluminium and polycarbonate substrates calculated using Kendall's [65] model.

The measured strength of adhesion on these substrates (Figure 4.7 and Figure 4.8) substantially exceeds the maximum attributable to SFE. Therefore, SFE is discounted as the dominant mechanism.

To satisfy the tensile test requirements of MIL-STD-883 (table 2027-2) for a 1mm² sample piece, a separation force of 7.97N would be required. To achieve this from surface energy alone, the SFE of the substrate would need to be increased by two orders of magnitude. This is vastly greater than the 75% increase achieved in a dedicated study into surface

treatments, including silicon nitride by Barhoumi et al [93] (section 2.4.4) and considered unrealistic. Consequently, alternative methods to enhance adhesion are explored.

As mentioned in section 2.4.2.3, the mechanisms of intermingling [63] and entanglement [63] between an SLA polymer and silicon nitride are considered infeasible. Therefore, the relatively high adhesive strength between the acrylate SLA product and the substrate suggests a chemical bond mechanism.

5.2.5. Shear tests with frustum test pieces and progressive curing

As with the tensile tests, the maximum recorded adhesive shear strength increased substantially on PC with even limited (2 minutes) of PBC. A clear trend between the maximum adhesive strength and PBC is apparent with test pieces constructed onto the more consistent (Table 4.27) surface of silicon nitride (washed with acetone and IPA). It was concluded that the adhesion tests conducted by applying a shear force (section 3.4.5) provided much more consistent results than tensile tests. Consequently, the shear test and equipment set up was used for further investigation.

5.2.6. Increase in adhesive strength with curing.

As mentioned in section 2.4.5, it is common practice in SLA to increase first layer exposure to promote adhesion to the substrate. The measured initial increase in adhesive strength with post build curing consistently occurs in both tensile (Figure 4.27, Figure 4.7 and Figure 4.8) and shear tests (Figure 4.10 and Figure 4.11).

The trend in the maximum recorded adhesive strength in tensile tests follows the elastic modulus. Increasing the elastic modulus to approach that of the substrate will improve the transfer of stress through the interface with the substrate (section 2.4.1), reducing stress concentrations at the interface and the susceptibility to crack propagation.

According to Kendall [65] (section 3.4.2) the increasing modulus with cure will increase the potential energy for a given load. However, the strength of adhesion in a tensile test has a quadratic relationship with the elastic modulus (Equation 2.8) which was measured to increase from 0.39 GPa to 0.69 GPa (Figure 4.5) between 0 and 8 minutes of PBC. This increased modulus would be expected to increase the required separation force by up to ~33% ($\sqrt{1.77}$). In practice, the maximum adhesive strength recorded over the same period more than doubled on aluminium, and silicon nitride, and increased by nearly a factor of four on PC (Table 5.14).

Maximum adhesive strength recorded in tensile tests with, and without curing			
Substrate	Green part (0 mins)	8 minutes of PBC	Percentage change
Aluminium	15.2	57.3	277.0%
PC	8.8	42.4	384.6%
Silicon nitride	8.6	28.3	230.8%

Table 5.14: Maximum adhesive strength recorded in tensile tests after PBC.

The potential for structural mechanisms and mechanical interlocking between the SLA polymer and substrates of aluminium, and PC has been identified previously (section 5.2.1). The strength of any structural bond will increase with the stiffness and tensile strength (Figure 4.5) of the polymer as it cures. However, the relationship between adhesive strength and curing is also evident in shear tests with silicon nitride (Figure 4.11) on which structural bonding of the SLA polymer has been dismissed (section 5.2.1).

Therefore, the variation in elastic modulus is indicative of the overall exposure with an exposure-dependent adhesion mechanism considered to be operating in parallel. The adhesive strength of the SLA polymer to silicon nitride being enhanced with PBC (section 5.2.3) indicates the chemical bonding mechanism is activated by exposure to UV light. This mechanism is potentially supported by the formation of free radicals via the photoinitiator, with such activation processes commonly applied to UV-adhesives [57].

The chemical bonding mechanism is also attributed to increasing the maximum separation force up to approximately 8 minutes of PBC on aluminium and polycarbonate (Figure 4.7 and Figure 4.8). However, the potential for prolonged further curing to cause embrittlement of the joint will increase susceptibility to cracking and a reduction in the work of adhesion as discussed further in section 5.2.7.3.

The concept of a chemical bond mechanism is consistent with de Gennes principle. When applied to a polymer on a metal substrate [57] (section 2.1), this describes the WoA as a function of the density of the bonds between the polymer and the substrate, the strength of those bonds, and the length of the polymer chain. A polymer chain with a high contour length (Figure 2.7) will require more energy to stretch it until one of the attachment points fail, than a shorter one. During the early stages of curing, the length of the chains and the corresponding contour length increases. However, as cross-linking progresses, the contour length decreases, the material becomes stiffer, and the elastic energy which they can store (WoA) is reduced.

De Gennes equation is described [63] as a generalisation and to use it to calculate the WoA would require the extremely difficult measurement of its individual variables and attempts to measure the energy absorbed have been described in the literature [63] as “ambiguous”. However, Abbott has approximated [57] the WoA from chemical bonding to be 100 times

that of SFE which, when entered into Kendall's model (Equation 2.8), provides a separation force in the same order of magnitude as the maximum forces measured and supports the theory of chemical bonding being the dominant mechanism.

Consequently, the increase in the maximum adhesion recorded between an SLA polymer and silicon nitride (Figure 4.11 and Figure 4.27) with progressive curing, is attributed in part to an increase in the modulus of the polymer and to a greater extent progressively actinically activated chemical bonding.

5.2.7. Shrinkage and strain

It is known an SLA polymer piece will shrink during initial crosslinking and subsequent PBC. The shrinkage of the FLC photopolymer used in the current study has been measured at 0.45% after 20 minutes PBC (Figure 4.16). For a free-standing test piece, the stresses generated during shrinkage are relieved by the contraction of the test piece resulting in strain (Figure 5.40).

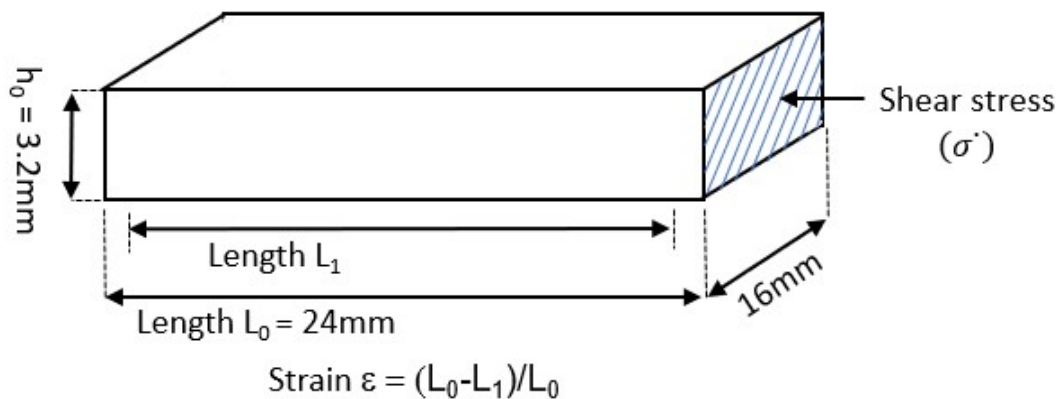


Figure 5.40: Lateral strain from shrinkage and the resulting stress plane.

When an SLA product is constructed onto a rigid substrate, subsequent shrinkage will result in residual stresses at the interface (Figure 5.41). With the SFE mechanism, it is possible for slippage [63] to occur where a material will re-attach (“heal”) to the substrate at a different location. Whereas in a chemical bonding mechanism, molecules in the polymer will be attached at specific site on the substrate resulting in stresses cumulating at the interface during PBC as shown in Figure 5.41.

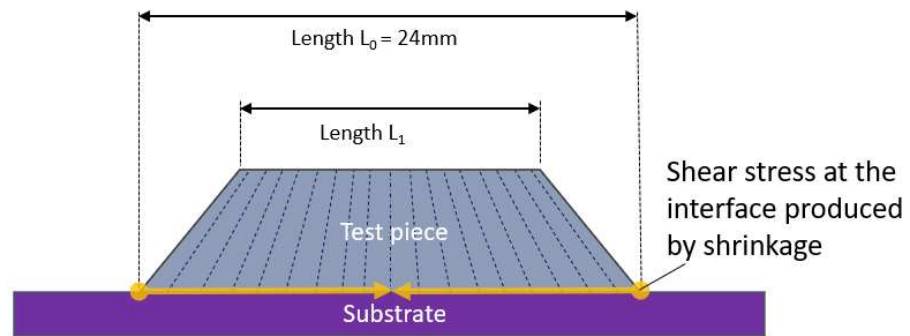


Figure 5.41: Shear stress from shrinkage at the interface with the substrate.

Conversely, SLA constructions are free to shrink in the vertical plane, which avoids residual stresses in this direction and are thereby assumed to be negligible.

The influence of shrinkage and the associated stress generated during curing is not considered in the adhesion models by de Gennes, and Kendall as discussed in section 2.1. Internal stress is described by Abbott [57] as “the enemy of all adhesion” because it will contribute to the applied force to initiate and propagate cracking. To further investigate the contribution of shrinkage to residual stress, the experiment described in section 3.4.2.7 was conducted to record the strain and calculate the corresponding stresses produced during the curing process. The analysis process summarised in Figure 5.42 will be followed.

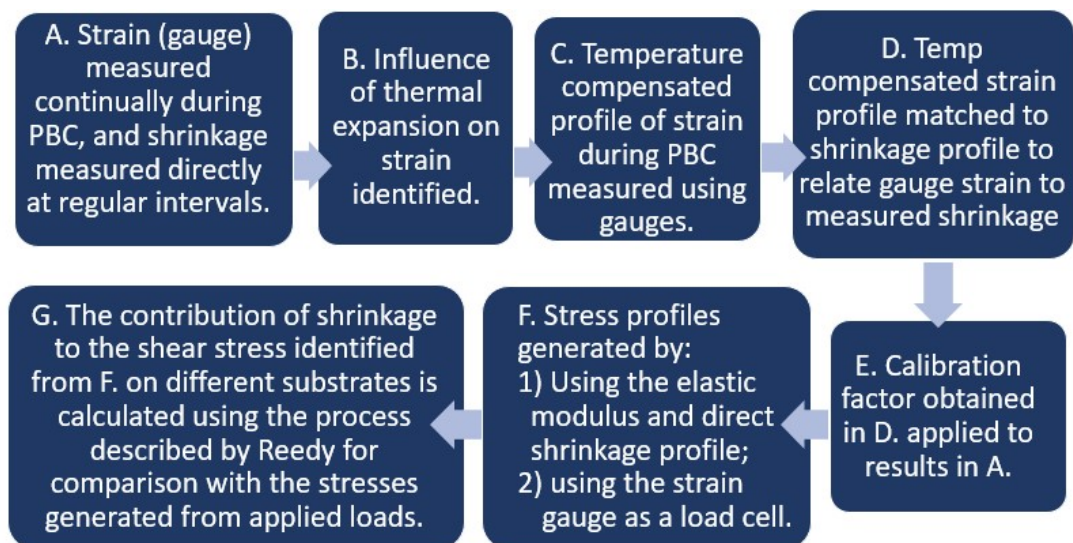


Figure 5.42: Process flow to calculate and compare the stresses generated from shrinkage to those generated from applied test loads.

5.2.7.1. Profiling strain

The strain from shrinkage measured manually (Figure 4.16) has been related to the average compensated gauge profile in Figure 5.43 [top] which shows the two trends to be consistent. The ratio of percent shrinkage to the gauge reading (a.u.) was then calculated at each PBC measurement point in Figure 5.43 [bottom].

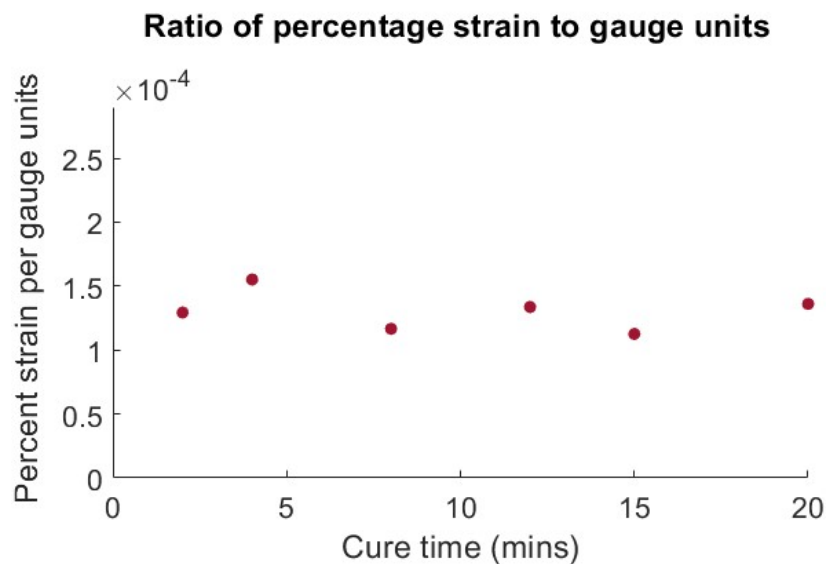
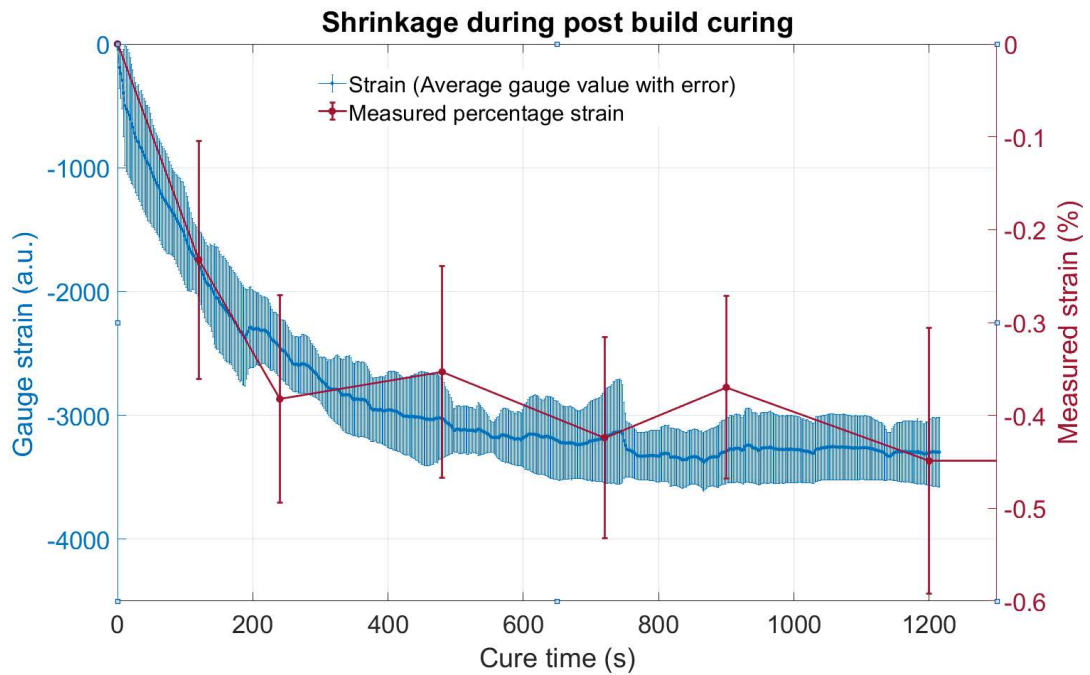


Figure 5.43: Gauge strain vs manually measured strain.
 [Top] Strain gauge values and manually measured strain (%) against cure time.
 [Bottom] Ratio of strain units (gauge) per one percent manually measured strain (Appendix G section 7.5.3.).

This ratio remains consistent ($\text{STDV } 1.505 \times 10^{-5}$) for the duration of PBC which provides confidence in the reliability of using the embedded gauges in the described arrangement. After 20 minutes (1200s) of PBC, shrinkage of the product is considered complete as shown by the levelling of the gradient in the recorded strain (Figure 5.43 top). The percentage strain per gauge unit after this period is $1.36 \times 10^{-4} \% / \text{a.u.}$ This value is used for calibrating the gauge output to produce a continuous profile of the percentage strain during PBC in Figure 5.44. By quantifying the strain profile for the SLA material (FLC) during PBC, the

shrinkage factor in the machine's control logic (Appendix F) can be adjusted for a given PBC period. This will achieve more accurate final constructions, reduce distortion, and the required manufacturing tolerances.

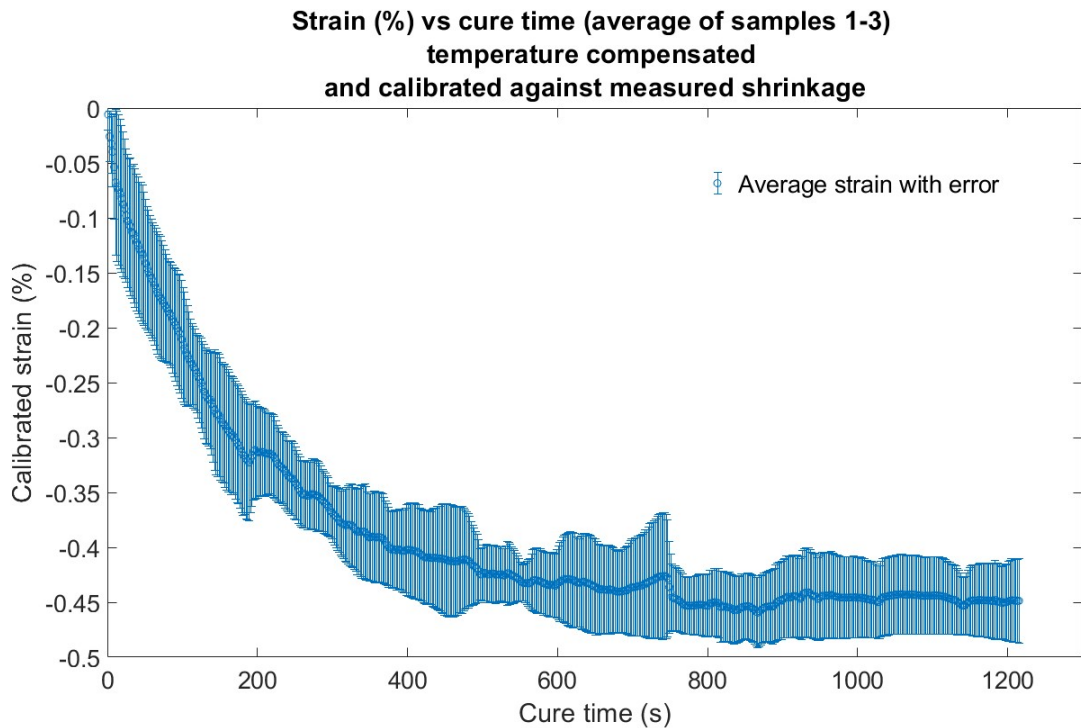


Figure 5.44: Strain (%) compensated for temperature and calibrated using measured shrinkage vs cure time

For completeness the gauge output coefficient has also been applied to the uncompensated strain readings in (Appendix G Figure G1.3).

5.2.7.2. Stress from dissimilar materials and shrinkage during curing

From characterising the strain due to shrinkage (section 5.2.7.1), and the material characteristics (Poisson's ratio and elastic modulus), the corresponding stress generated can be estimated. When doing so, it is also important to consider how the modulus changes during curing as this will result in a proportional decrease in the measured strain produced for a given stress loading. Any mismatch between the elastic modulus of the test piece and the substrate will result in stress concentrations at the interface, increasing the susceptibility to cracking and low force failure, as experienced by several authors in section 2.4.1. This is the result of stresses being transferred more freely across interfaces between materials with similar elastic moduli [59].

Professor Abbott [63], when discussing tensile test systems, explains their complexities with stresses applied in one direction producing strains in another due to Poisson's

principle. Using this principle and a simplification of the tensile test system, Reedy [180] generates an approximate expression (Equation 5.3) to describe the in-plane (shear) stress at the interface between a test piece and the substrate with dissimilar moduli.

$$\dot{\sigma} = \nu_2 \left(1 - \frac{E_2 \nu_1}{E_1 \nu_2} \right) \bar{\sigma}$$

Equation 5.3: Reedy's [180] expression for in-plane (shear) stress at the centre of the interface layer as a function of the applied tensile stress.

Where $\dot{\sigma}$ is the shear stress at the centre of the interface layer, $\bar{\sigma}$ is the applied tensile stress, E_1 and E_2 are the elastic modulus of the substrate and the test piece respectively, with corresponding Poisson's ratios of ν_1 and ν_2 .

Applying the materials properties (section 3.1) of the SLA polymer, PC, silicon nitride and aluminium to Reedy's expression (Equation 5.3), the in-plane shear stress resulting from a given tensile load on silicon nitride, and Aluminium is calculated to be 19% greater than PC for a green test piece. Silicon nitride and aluminium give comparable results due to their comparatively high elastic moduli (section 3.1).

Moreover, the calculated shear stress associated with PC is significantly reduced as the modulus of the test piece increases towards that of the substrate with curing, resulting in the stress on aluminium and silicon nitride being 43% and 45% greater respectively than PC after prolonged PBC (15 minutes).

In addition to the stress from the applied load, there will also be that due to shrinkage. This results from the shrinking bulk material adhered to the substrate, being unable to move laterally (Figure 5.41). It has been attempted to calculate the magnitude of this stress using the embedded strain gauges as load cells by calibrating them against a 10N load as described in section 3.4.2.7. The calibration process was performed on a green part. Therefore, the calibration factor obtained is corrected for the change in modulus during curing at 1 second increments, using the profiles described by Equation 5.1 and Equation 5.2, to give corrected strain from Equation 5.4.

$$\varepsilon_c = (\varepsilon_{10t} - \varepsilon_{10t-1}) \frac{E_t}{E_{t_0}} + \varepsilon_{10t-1}$$

Equation 5.4: Gauge strain corrected to compensate for the change in modulus during PBC.

Where ε_{10} is the strain gauge reading calibrated against a 10N force, E_t is the modulus at time t (seconds) and ε_c is the cumulated strain gauge reading corrected for modulus. The recorded gauge strain can then be related to a force and converted to stress using the CSA of

the test piece ($5.12 \times 10^{-5} \text{ m}^2$) in the shear plane to produce the corresponding stress profile (Figure 5.45) with and without temperature compensation.

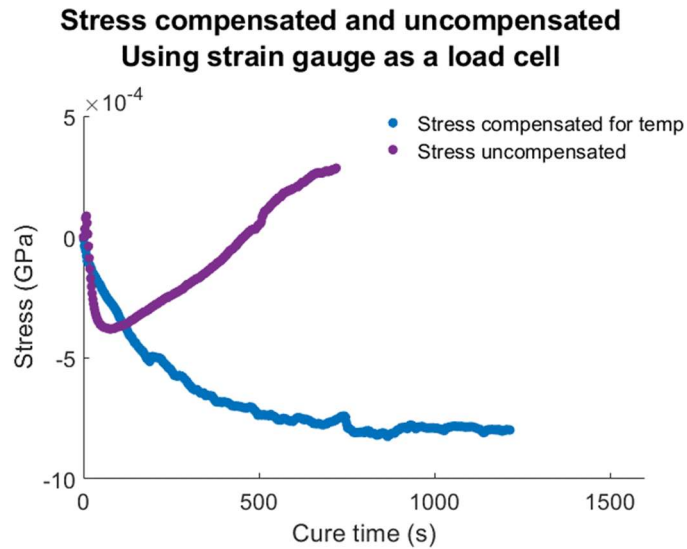


Figure 5.45: Stress recorded by using the strain gauge as a load cell, with PBC time dependent elastic modulus, uncompensated and compensated for temperature.

The calculated stress from shrinkage is compared to the stress at failure from shear tests (MIL-STD-883) on silicon nitride after an advanced period of PBC (8 minutes), in Table 5.15. By calculating the average stress from shrinkage, the total shear force exerted on the cross-section of the test pieces has been calculated to be 5.2N. This is significant (~29%) when compared (Table 5.15) to the average MIL-STD-883 shear test separation force of 18.2N (8 mins PBC) on silicon nitride and will contribute to crack initiation and propagation.

The contribution to the separation of shear test pieces (MIL-STD-883) from shrinkage.	
	Silicon nitride
Average measured separation force (shear) (MIL-STD-883, 8 mins PBC) (N)	18.2
Shear stress (σ) from measured separation force (MIL-STD-883, 8 mins PBC) (MPa)	2.7
Calculated shear stress (σ_s) from shrinkage (MPa)	0.78
Equivalent shear force to generate shear stress (N)	5.24

Table 5.15: Average separation force and stress from testing (MIL-STD-883) and calculated equivalent shear force required to generate the same magnitude of stress.

It is assumed the shear modulus of the FLC photopolymer is equal to its tensile modulus. By entering the calculated shear stresses from shrinkage (Table 5.15) into Reedy's equation (Equation 5.3), the equivalent tensile force required to generate a shear stress of the same

magnitude, with different substrates is calculated (Table 5.16). These are compared with the calculated (Equation 5.3) shear stresses produced at failure after a period of PBC (10 minutes of PBC) from tensile tests. The results for this period of PBC were used for comparison due to the low forces recorded on PC after longer periods as discussed in section 5.2.7.3. This analysis finds the tensile force at failure generates an approximate shear stress at the interface of 29.6MPa and 20.7MPa on aluminium and PC respectively, compared to a measured shear stress from shrinkage of 0.78MPa. This indicates the contribution of shrinkage to the stress at failure in a tensile test is low (<4%). This assumes the forces are evenly distributed across the joint and does not consider the influence of localised stress concentrations within it.

The contribution to the separation of tensile test pieces from shrinkage.		
Substrate	Aluminium	Polycarbonate
Avg. measured tensile separation force (N)	74.6	42.4
Avg. tensile stress $\bar{\sigma}$ from measured separation force. (MPa)	74.6	42.4
Calculated (Reedy) shear stress ($\hat{\sigma}$) from tensile load (MPa)	29.6	20.74

Table 5.16: Average tensile stress calculated from the measured separation force during tensile adhesion tests (1mm²) and the corresponding shear stress calculated using Reedy's equation for different substrates.

5.2.7.3. Causes of low force failure and variance

It is apparent that the strength of adhesion is sensitive to a high number of variables. Consequently, adhesion tests, particularly tensile tests are susceptible to a correspondingly high variation in their results. Professor Abbott [63] explains; "The problem is that the fracture mechanics of a butt joint [tensile test] are so complex that finding simple rules is not possible". Indeed, Kendall's model (Equation 2.8), although used by Abbott [57], [63] is based on an idealised system with perfect contact, no contamination, perfect alignment and without the influence of shrinkage. Moreover, the model is based on an energy balance, using the elastic modulus to calculate the energy stored by the system when exposed to a tensile force and does not consider localised stress concentrations.

In addition to commonly influencing factors, it has been demonstrated (section 5.2.7.2) that in SLA there are additional active mechanisms, significantly shrinkage and the variation in elastic modulus during curing.

The measured maximum separation force on aluminium is substantially greater than on PC (Figure 4.7 and Figure 4.8). Examination of the interface between a sectioned SLA polymer and a PC substrate using microscopy in section 4.2.5, was inconclusive as to the presence of mechanical interactions between the materials. However, aluminium, has a greater propensity to support mechanical interlocking, as discussed in section 5.2.1. For the

practice of increasing first layer exposure to benefit adhesion, the substrate should be sufficiently rough to allow liquid photopolymer to penetrate surface pores and establish mechanical interlocking, while possessing chemistry capable of supporting a suitable surface attachment mechanism. Both properties are afforded by the aluminium oxide surface of the build platform as reported in Table 4.29 and section 2.4.5 respectively.

Mechanical interlocking may also be benefitted by the lateral stress generated by shrinkage (Table 5.15), serving to lock the polymer into the substrate pores. Given the natural variation in the size and geometry of the pores formed on the surfaces of the substrates used, they can be expected to vary greatly, and so too can their influence on the strength of adhesion. For this reason, the benefit provided by increasing first layer exposure to enhance adhesion (section 2.4.5) will be specific to the substrate material with potentially significant variation between similar materials.

De Gennes principle describes the WoA from a chemical bonding mechanism to be proportional to the density of attachment points at the interface, and the strength of individual bonds. Aluminium has the potential to support the chemical adhesion mechanism described by Kim [71] (section 2.4.5) with a dissociation energy between the resulting Al-N interfacing bond of 297kJ/mol. Without knowing the product of the chemical mechanism with PC, a direct comparison cannot be made. However, a comparably weaker chemical bond across the interface with polycarbonate would contribute to the lower strength of adhesion measured. There is also the potential for an increased density of attachment sites (i.e., surface hydroxyl groups) on aluminium. However, the density of attachment sites can also reduce the average displacement length and the corresponding contour length of the material as discussed in section 2.4.2.5 which relates to the third component of de Gennes principle. A reduction in the contour length will reduce the strain at failure and the propensity for the material to dissipate energy. Therefore, it is hypothesised that the greater measured (Figure 4.8) adhesive strength on aluminium compared to PC (Figure 4.7) is attributable to the combined benefit provided by the mechanical and chemical mechanisms described. The discussed potential benefits of these to adhesion onto aluminium outweigh that provided by the increasing similarity in elastic modulus and the transfer of stress across the interface between the photopolymer and the PC substrate during curing, resulting in the greater separation force recorded.

It is also hypothesised that the increased occurrence of low force failures recorded on PC after prolonged periods of cure (>10 minutes), is attributable to the reducing propensity of the SLA polymer to dissipate energy as the contour length reduces (5.2.6), and the progressive cumulation of stress due to shrinkage at the interface.

5.2.7.4. Variation in adhesion

The consistency of the substrates as indicated by the standard variation using DSA (Section 3.4.2.10) demonstrate the combined variation in surface properties, including surface energy, surface roughness, and potential contamination. They also demonstrate the benefit afforded by sample preparation from solvent cleaning and polishing (aluminium). Griffiths law [58] describes how cracking will originate from the largest defect. A common source of defects in SLA is from the presence of entrapped gas often introduced during the construction process by the motion of the recoating blade. SEM images of the surface of SLA samples constructed following a period of approximately 14 hours during which the photopolymer was undisturbed and allowed to settle, and a second sample immediately following two hours of continual operation are shown in Figure 4.19. In the latter case, the volume and size of the surface defects is substantially greater and attributed to the increased presence of entrapped gas. The formation and size of the resulting bubbles is extremely difficult, if not impossible to reliably predict. Consequently, entrapped gas presents a significant and unpredictable variable which influences the consistency of adhesion in the tests conducted in this study and in practice.

Although measures were taken to align tensile test pieces with the applied force (section 3.4.4), even minor misalignment will amplify stress concentrations resulting in failure at reduced force. Consequently, any variation in the accuracy of alignment between test pieces will have a corresponding influence on the consistency of the results.

The influence of exposure on adhesion, either on the first layer (section 2.4.5) or the bulk body (i.e., during PBC), has been reported (section 5.2.6). Slight variations in the delivered exposure across the build area in laser SLA machines used in this study have also been identified (sections 5.1.4.3 and 5.1.5). Consequently, the location of construction will influence on the strength adhesion and introduce variance, particularly for green parts (without PBC).

Despite the high variance in the results, a clear trend of increasing adhesive strength with a limited period of PBC between 2 and 8 minutes is apparent (5.2.6). Methods to further enhance adhesion are now discussed.

5.2.8. Enhancing the adhesion of SLA to substrates

From the investigation performed, the dominant adhesive mechanism between an SLA polymer and silicon nitride is hypothesised to be chemical bonding (section 5.2.4) with dissipation acting to mitigate crack initiation and propagation. These mechanisms will now be explored, with the aim to promote adhesion to an extent compliant with MIL-STD-883K.

The addition of CSR and varying lateral exposure via the methods described in sections 3.4.6.2 and 3.4.6.3 respectively are intended to increase energy dissipation to mitigate crack initiation and propagation. The intended benefit is to reduce low force failures resulting in an increased average separation force with a lower variance.

5.2.8.1. CSR

SLA Frustum test pieces dosed with CSR were constructed using the method described in section 3.4.6.2 with the aim of promoting energy dissipation. The influence on adhesion was tested by applying a shear force, the results of which are shown in section 4.2.7.1.

An increased failure rate of constructions when using elevated CSR concentrations was observed. This is attributed to the required delay time to allow the photopolymer to settle and be recoated between layers being insufficient (section 2.5.2) and impacting the quality of the first layer bond with the substrate. Additionally, the addition of the CSR impacts the D_p of the photopolymer evidenced by its opaque appearance, reducing the overall exposure. The effect of this will be greatest at the deepest depth of each layer, which for the first layer will be at the interface with the substrate. Additionally, the D_p will affect the CLW, the step size and the ability to meet tolerances as discussed in sections 3.2.1 and 3.2.3. It was attempted to quantify the impact on D_p by using the equation derived by Taormina [119] (section 2.5.2) for which the scattering parameters are required. In an effort to obtain these, the work by Small et al [181] was reviewed which revealed the scattering parameters for the particles were sensitive to the particle diameter. For the material being used, this is wide ranging (section 3.1). Taormina's equation is also highly sensitive, because it uses a quadratic function of the difference in refractive indices between the photopolymer and the CSR. Since both materials used in the current study share the same refractive index of 1.52 (section 3.1), this gives an unrealistically high value. Consequently, it was concluded that a valid prediction of the CSR material's (Paraloid-BTA-751U) impact on the penetration depth, could not be made for this application.

No significant difference in the strength of adhesion of frustum shear test pieces (Figure 4.21) with the addition of CSR and constructed onto PC, was measured in proportions of 5% and 7.5% v/v. When added in increased proportions of 15% v/v, the separation force was significantly less at cure times up to 15 minutes at which point a comparable strength of adhesion to untreated photopolymer was measured. At the highest proportion in which the CSR was used of 25% v/v, the strength of adhesion was comparable to that of the 15% v/v mixture up to 8 minutes of cure. After a prolonged cure period of 30 minutes, the strength of adhesion of the 25% v/v test pieces remained significantly lower than untreated photopolymer. It was at extended periods of cure that the greatest influence of CSR would

be expected by providing greater energy dissipation to compensate for the reduced contour length of the polymer chains and increased rigidity. It is concluded that the addition of the Paraloid™ CSR to the FLC photopolymer did not benefit the adhesive strength of FLC to PC.

Potential explanations for this include the reported impact on penetration depth reducing exposure at the interface and impacting the ability of the photopolymer to bond with the substrate. However, although this may contribute to the increased build failure rate when using CSR, it would be expected to be compensated for by samples which were exposed to PBC. Paraloid CSR material was selected for its acrylate (styreneacrylate) shell and anticipated affinity with the FLC acrylate photopolymer. However, it is possible the CSR did not sufficiently bond with the bulk material. If so, crack energy generated under testing, would continue to propagate through the unbonded CSR/SLA polymer interface (Figure 2.8), as opposed to being dissipated by the rubber core [57]. To investigate this further, samples containing CSR were embrittled using liquid nitrogen and sectioned using the method described in section 3.4.3.4. The resulting fragments were examined using SEM as shown in Figure 4.23 and optical microscopy in Figure 4.24. High magnification SEM images of individual CSR particles before being mixed with the photopolymer, are shown in Figure 4.22 for comparison. All the sectioned images show the presence of CSR particles exposed at the surface of the fracture which is clearest on the SEM images (Figure 4.23). This indicates the shells may have introduced a weakened interface around which the crack energy applied during sectioning has propagated. Whereas if the CSR had bonded with the bulk material, the crack face would be expected to circumnavigate the particles and not contain CSR particles.

Due to the CSR itself being incapable of forming a bond with the substrate by any means other than through the relatively weak mechanism of SFE, the addition of the material will serve to dilute the photopolymer. This will impact the quality of contact between the monomers of the resin and the active sites on the substrate. Moreover, if not bonded effectively with the bulk SLA material, the CSR particles will act as defects sites in accordance with Griffiths law and serve to reduce the crack initiation energy. Examining the interface of constructions containing CSR using optical microscopy, and the method described in section 3.4.6.2, identified the presence of individual particles with inconsistencies around their boundary (Figure 4.25) which is more pronounced with higher proportions of CSR added.

Therefore, it is the failure for the CSR to bond with the bulk material, resulting in the particles diluting the photopolymer and acting as defect sites, which is attributed to the reduction in adhesion measured at proportions greater than 7.5% v/v.

Although the addition of CSR proved ineffective in this instance, the mechanism of dissipation cannot be discounted as an effective means to promote adhesion.

5.2.8.2. Varying lateral exposure and curing to promote dissipation.

The exposure across a cylindrical test piece (Figure 3.36) was varied using the method described in section 3.4.6.3. As with the addition of CSR, the aim of varying the exposure is to promote the dissipation of energy and increase the resilience of the part to crack failure. If successful, an increased average shear strength and a reduction in low force failures would be expected. The measured peak adhesion (section 4.2.7.2 Figure 4.26) of the test piece constructed with varied exposure is lower and within 13% of the pieces with standard exposure. Additionally, varying the cure laterally introduces much more variation into the results as shown by the standard deviation increasing from 20.3 for the standard cure test pieces to 90.6 for the test pieces with variable cure. Post build curing was not applied to the test pieces as this would remove the contrast in exposure generated.

However, given the benefit to adhesion previously identified (section 5.2.5) by even a limited period of PBC, it may be beneficial if the peak exposure, and the corresponding contrast in the SLA process, could be increased. By generating well bonded regions from high exposure interspersed with more flexible areas, potentially greater energy dissipation could be achieved. This could potentially be accomplished by adjusting the scan speed in the ITLM.py script which would require further work, or using an alternative and more powerful open source SLA system.

As well as reducing stress concentrations, Vu [77] and Fitton [76] describe other potential benefits to varying elastic modulus through exposure such as the construction of flexible joints and products with different textures. The method developed for this study (section 3.4.6.3) to vary exposure laterally using commercially available desktop SLA equipment, also provides the ability to investigate these concepts for future work.

5.2.8.3. Application of a monolayer

To promote chemical bonding (section 5.2.4), the density of active hydroxyl sites on the substrate surface was promoted using plasma treatment and subsequently applying a monolayer of TMSPMA using the method described in section 3.4.6.1. The silicon in the monolayer forms a covalent bond with the substrate via the hydroxyl groups and the

methacrylate tail of the TMSPMA has the capacity to crosslink with the acrylate SLA photopolymer. Constructions onto treated and untreated substrates were then tested for comparison.

The average adhesive strength (Figure 4.27) of tensile tests without PBC on untreated silicon nitride was 7.8N compared to 12.6N for the treated substrate. After 8 minutes of PBC, the average adhesive strength on the treated substrate was increased to 44.9N compared to 24.8N on the untreated substrate.

The tensile tests on the treated substrate showed the bond strength to be substantially enhanced (Figure 4.27) and more significantly, promoted to an extent above the tensile strength of the polymer. The majority of the green test pieces, and all pieces exposed to PBC, constructed onto the treated substrates experienced cohesive failure (Figure 5.46). This was demonstrated by the crack face being in the stem of the test pieces as shown in Figure 4.29 and the observations in Figure 5.47 to Figure 5.49, instead of at the interface (Figure 4.28) with untreated substrates.

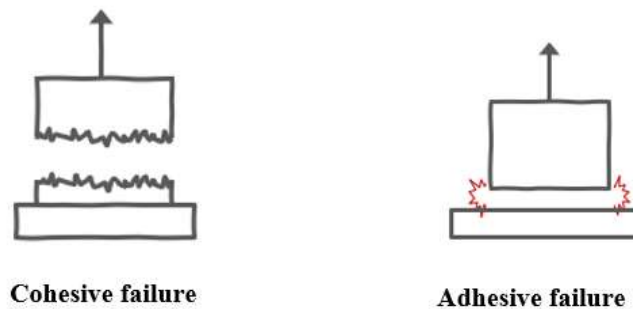


Figure 5.46: Adhesive vs Cohesive failure

Observations of retained material and fracture points following tensile adhesion testing on treated silicon nitride.



Figure 5.47: Green stumps after tensile testing on treated silicon nitride.



Figure 5.48: Stumps after tensile testing with 2 minutes PBC on treated substrate.



Figure 5.49: Stumps after tensile testing with 8 minutes PBC on treated substrate.

The tensile strength of the SLA polymer increases with PBC (Figure 4.5) due to the progressive cross-linking of polymer chains. Consequently, the tensile test results on treated substrates (Figure 4.27), reflect the cohesive strength of the material, and its relationship with PBC.

Shear tests were conducted following the method described in section (3.4.5.2) to test compliance with MIL-STD-883K which requires a separation force of 49N (section 3.4.5.2). The average separation force (Figure 4.30) without PBC on the treated substrate was 33.4N compared to 3.3N for untreated silicon nitride. After 2 and 8 minutes of PBC, the average adhesive strength on the treated substrate was increased to 100.2N and 93.3N respectively, with a minimum recorded separation force of 62.3N. Therefore, by applying the described treatment process (section 3.4.6.1) to a silicon nitride substrate, in conjunction with PBC, the strength of adhesion with the acrylate based FLC photopolymer can be promoted to an extent compliant with the requirements of MIL-STD-883 and satisfying one of the current study's primary objectives (section 1.5).

5.2.9. Adhesion summary

Through laboratory experimentation, the strength of adhesion of a commercially available SLA photopolymer onto polished silicon nitride substrates has been quantified. Additional testing to characterise the change in adhesive strength with post build curing has been conducted. The strain and corresponding stress produced from shrinkage during the PBC process has been measured in-situ using a dedicated experiment. In turn, the contribution to the shear force from shrinkage on a MIL-STD-883 test piece has been calculated to be 5.2N which is significant when compared to the measured force at failure of 18.2N (after PBC).

By following and developing the work of others, methods to improve the adhesion of SLA products to silicon nitride through the dissipation mechanism have been attempted. These include varying the elastic modulus of the SLA product through greyscale curing, and the addition of core shell rubber to the photopolymer. However, when tested, neither of these methods significantly increased the quality of adhesion.

Following further investigation, the dominant adhesion mechanism between SLA and silicon nitride has been concluded to be chemical bonding. The strength of adhesion between SLA constructions and silicon nitride was successfully enhanced by silanizing the substrate using oxygen plasma and the application of a TMSPMA monolayer. This bonds covalently with the substrate while the methacrylate tail cross-links with the bulk polymer. When the process is applied in conjunction with post build curing, the resulting bond strength has been found to be greater than the cohesive strength of the material. The enhanced adhesion has also been measured to comply with the requirements of the industry standard MIL-STD-883K. In doing so, one of the primary aims of the study has been achieved.

5.3. Discussion of inserting multiple geometries into the SLA process.

This section discusses the results and observations (section 4.3) from the investigation into inserting multiple stacked components into the SLA process to generate a 3D electronic package.

5.3.1. Step III Stage A: Stacked module concept.

The module concept (section 3.5.2.1 Step III: stage A.) demonstrates the ability to construct SLA packages directly onto silicon nitride. The substrate can be pre-treated as described in

section 5.2.8.3 to improve the bond between the two materials. The dowel concept to produce a tight fit, required a significant force to mate the modules together but firmly secured them once compressed. However, components cannot be inserted into the package during construction which results in the cavity being open (Figure 4.31) to permit geometries to be inserted after construction. This could be sealed after insertion by manually filling the cavity with photopolymer and applying PBC. When doing so, the part would need to be suitably orientated to avoid the photopolymer from flowing from the cavity. The product also highlights the difficulty with connecting inserted components electrically which prompted the module approach to provide access between each layer. Consequently, the concept requires multiple constructions to form a package. These issues can be mitigated by introducing the ability to insert components and wiring directly into the package during construction. Fine wire with diameter less than a single layer (100µm) can be inserted into the build without clashing, and be encapsulated by the subsequent SLA layer, thus removing the requirement for lateral vias. Therefore, the method described in section 3.5.2.2, to insert components directly into the package during construction was developed and discussed in the following section (5.3.2).

5.3.2. Step III Stage B: Inserting multiple stacked components.

The python interaction described in section 3.5.2.2 allows large geometries to be inserted at a predetermined layer within the package and during construction. This was initially demonstrated by inserting a micro-LED directly onto a build platform and onto silicon nitride in Figure 4.33, and later with the use of through vias (Figure 3.43) to accommodate wire runs. The inserted components were subsequently illuminated to prove the concept. The concept was further demonstrated by inserting a large LDR component (Figure 4.34) into a free-standing package with vertically orientated vias and wire runs. To allow the wire legs of the component to extend beneath the package, standard SLA supports were used as they are purposefully designed with a small contact area for easy removal.

The micro-LED and LDR inserts differ to the work previously referred to by Tiedje [10] as that was to encapsulate a component directly onto the build platform. The process described permits geometries to be inserted at any layer within the construction. Moreover, it also permits multiple components to be inserted and stacked vertically, in a single build.

To demonstrate this and the ability to insert complex geometries featuring a varying cross sectional area (section 2.2), the semi-conductor package (Figure 3.39) and the piston geometry (Figure 3.38) were selected (section 3.5.1). The adaptor packages were successfully inserted by following the process described in section 3.5.2.2. and proves the concept for inserting multiple large complex geometries.

5.3.3. Step IV: Connecting inserted components to form an SLA structural electronic package.

The final step was to insert multiple electrical components (large-LED, strain gauge and an LDR), with wire runs for electrical connections by following the method in 3.5.3. An insert (Figure 4.38 Stage B) was used to accommodate an offset wire run and serve as a single adaptor piece for the large-LED. Affixing the crimp fittings to the inserted wire (Figure 4.38 Stage C) formed an effective solderless connector. To these the LDR was subsequently attached allowing its electrical terminals to be vertically offset from the component. The connection was tested by increasing the light exposure to the LDR and recording the output (Figure 4.39) which showed a consistent response. Entrapped gas between the insert and the package housing is observable (Figure 4.39) which is attributed to the clearance between the two parts.

Manually installing the wire runs in combination with the adaptor pieces and the insertion process described in method 3.5.2.2, to embed and connect multiple large or complex geometries, allows structural electronics to be formed using the single AM process of SLA. This has been demonstrated with a proof of concept shown in Figure 4.39. The process is considered an effective and reliable alternative to using hybrid systems described in section 2.1 and meets objective no. 4 (section 1.5) of the current study.

5.3.4. Inserting geometries summary

To demonstrate the insertion of large and complex components, an example piston geometry and a semi-conductor package were constructed using SLA. Both the inserts fit the criteria for complex geometries, necessitating a two-part adaptor piece. Previous work has been furthered to insert multiple complex geometries into the body of an SLA construction. This was achieved by establishing a python interaction with a Form 1+ SLA machine to pre-programme the build process to pause at the required layers, activate a peel process and raise the platform to a required height.

The package was designed to have a clearance with the insert of 300µm. The surface of the adaptor piece was manually coated with liquid photopolymer prior to insertion. This forms a continuous joint between the insert and the package during post build curing and promotes suction to secure the insert while inverted until the subsequent layer has been applied to encapsulate the insert. Additionally, interconnectors have successfully been fitted as a means of connecting components electrically. This demonstrates a concept for constructing 3D electronic modules via the single AM process of SLA.

Chapter 6.

6. Findings and Conclusions

There is a paucity of information relating to the influence of reflectance in the SLA process. Therefore, to address concerns regarding the potential for reflectance (section 5.1.5) from silicon nitride to produce spurious curing, a model has been generated to predict the occurrence and magnitude of the characteristic together with other distorting effects. However, as with reflectance, the characteristics of divergence, ellipticity (section 5.1.4.3) and refraction (section 5.1.6) also occur at oblique angles and their magnitude influenced by the angle of incidence. Modelling identified that distortion due to divergence and ellipticity will be minor across the size of the build area (up to 140mm x 140mm) used. However, the relationship between the build area and the distortion is not linear which has implications for the scalability of production. Consequently, the maximum build dimensions which can be used before the combined influence of distorting effects compromises the ability to meet manufacturing tolerances (section 5.1.7.2) is incorporated within the model. It has also been demonstrated through modelling (section 5.1.7.1), that by adjusting the focal point of beam, divergence and the corresponding distortion can be reduced by up to 50%. Additionally, by characterising the relationship between distortion and the angle of incidence, an algorithm has been generated (section 5.1.9.4) to compensate for the change in CLW by modulating the power according to the build area location.

An experiment has been devised (section 3.3.6.3) to isolate and quantify the production of spurious curing due to reflectance from other distorting characteristics related to the AOI. In parallel, a model has been generated (section 3.2.10) to predict the onset and magnitude of spurious curing from reflectance depending on operating parameters and machine geometry. This was identified to be at exposures corresponding to scan speeds below 200mm/s for the Form 1+ equipment. Unusually wide CLW were produced at these speeds which are associated with low intensity distortions in the beam (section 5.1.4.1) manifesting as spurious cure at high exposures. This precluded accurate direct comparison between the measured and modelled results. However, the trend identified from modelling was replicated in the results of experimentation with reflectance being insufficiently powerful at speeds above 200mm/s to initiate curing.

Spurious curing from reflectance is greatest at oblique angles when the reflected exposure is above the critical energy of cure. This typically occurs during the application of MFLS (section 5.1.4.2) and the associated overexposure can often result in first layer distortions in the form of menisci. The application of MFLS is necessary to secure the construction to the

substrate and is not a concern with constructions mounted on supports. However, the aim of the current study requires construction directly on to silicon nitride. Therefore, it is envisaged that promoting adhesion to the substrate by applying the monolayer process discussed will sufficiently secure the part without MFLS and reduce the reflectance to below the critical energy of cure.

The influence of refraction at oblique angles of incidence has been modelled to result in a reduction in accuracy of 0.67mm across the diametric points of the Form 2 build area and validated (section 5.1.6) with as-built measurements. This and other distorting effects (reflectance, divergence, and ellipticity) can be mitigated with the use of a parabolic mirror (section 5.1.9.1) to maintain the beam at normal incidence to the substrate. A model to design the surface profile of such a device for different machine geometries has been generated as described in section 5.1.9.1.

Through further modelling, the exposure limits at which the onset of spurious curing and distortion occur can be calculated. This identifies the boundaries of an operating window (section 5.1.8) within which the construction process can be optimised for scale and time. The construction time is reduced by identifying the maximum hatch spacing permitted with consideration to the influence of superposition, to comply with a user defined maximum variation in exposure. This process has potential for significant savings in construction time with a reduction of over 26% demonstrated for an example 10mm cube. Additionally, by quantifying the shrinkage profile for the SLA material (FLC) during PBC, the shrinkage factor in the machine's control logic (Appendix F) can be adjusted for a given PBC period. This allows for more accurate products and reduced design tolerances.

From a review of literature (chapter 2), potential methods to promote adhesion of SLA photopolymer to different substrate materials with an emphasis on silicon nitride, have been identified. These were investigated using purpose designed experiments to quantify their effectiveness with the aim being to satisfy the requirements of the MIL-STD-883 standard [83].

To support the study, the active adhesion mechanisms were explored to identify which dominates for each material. This required characterising the properties of the photopolymer (section 3.4.2) to compare the measured adhesive strength with established models, and empirical observations. As part of the investigation (section 5.2.2), the solidified photopolymer's surface energy and Poisson's ratio after progressive periods of post build curing were measured and identified the characteristics to be uninfluenced by the process. From this investigation it is concluded that an acrylate SLA photopolymer is

compatible for construction onto silicon nitride (section 5.2.2) with chemical bonding being the dominant adhesion mechanism (section 5.2.6).

Residual stress and its potential to initiate and propagate cracking is widely reported to contribute to adhesion failure. Therefore, the strain and the associated stress generated by shrinkage during post-build curing was measured using embedded strain gauges. This stress was compared to that measured at separation during adhesion tests (section 5.2.7) on a MIL-STD-883 test piece constructed onto silicon nitride with PBC. The shear stress from shrinkage was found to contribute approximately 29% of the force at failure. Consequently, mitigating shrinkage will also benefit adhesion and offers potential avenue for further work.

Methods investigated to promote adhesion through energy dissipation included the addition of core shell rubber (section 5.2.8.1) to the photopolymer and varying the SLA product's elastic modulus (section 5.2.8.2) through greyscale exposure. The latter required a new process developing to generate suitable test pieces. This was devised by combining a series of existing python scripts to provide instruction to a Form 1+ SLA machine. However, laboratory testing did not identify any significant benefit to the strength adhesion from greyscale exposure nor the addition of CSR. Conversely, by applying post build curing (section 5.2.6) to promote the mechanism of entanglement, and plasma treatment in conjunction with the application a monolayer (TMSPMA), were found to significantly promote the strength of adhesion. By combining these processes, the strength of adhesion can be reliably enhanced (section 5.2.8.3) to an extent compliant with the stated industry standard.

By building on prior work, and the application of design rules, a process for inserting large and complex geometries has been demonstrated (section 5.3) using a Form 1+ SLA machine. This was achieved by establishing a python interaction (section 3.5.2.2) with the machine which allowed the construction to be interrupted at a pre-determined layer. A peel and platform raise process is then initiated to allow access to the part and insertion of an appropriate adaptor piece, determined according to the criterion value (section 2.2). A clearance of 300 μ m was identified to provide a suitable fit to hold the adaptor piece while the construction process was interrupted. The build process can then be resumed on demand. Subsequently, a proof of concept for constructing 3D electronic packages incorporating multiple stacked components using inserts and SLA alone, has been demonstrated (section 5.3.3).

Furthermore, from the investigations reported, a strategy to overcome the challenges associated with constructing electronic packages directly onto silicon nitride can be proposed. This would firstly involve coating the substrate with the TMSPMA as described

in section 5.2.8.3. This will serve to promote adhesion of the SLA polymer to the substrate, and to an extent compliant with the MIL-STD-883 standard. In doing so the requirement for multiple first layer scans, and the associated distorting effects, can be removed. The SLA construction could then proceed with improved accuracy by modulating the beam power across the build area as described in section 5.1.9.4. This will allow the dimensions of the build area and scale of production to be maximised. Electrical components incorporated into suitable adaptor pieces and housings to minimise cavities, can then be inserted into the build process as described in section 5.3.4. Lastly, by mapping the SLA construction using the process described in section 5.1.8, would allow the operating parameters to be optimised to reduce the overall construction time while complying with manufacturing requirements and tolerances.

The findings described above, and the work reported in the previous chapters has filled the knowledge gaps detailed in section 2.8 required to satisfy the aims of the study (section 1.5), with areas for future work identified. It is concluded that it is feasible to construct electronic packages using SLA onto silicon nitride while complying with manufacturing tolerances and the adhesive requirements of the relevant industry standard. Methods to achieve these aims have been demonstrated, together with mitigating measures and how the process can be optimised.

6.1. Further work

Areas identified for potential further investigation are discussed below.

- **The influence of shrinkage on adhesion.**

Shrinkage has been identified to generate stress at the interface with the substrate (section 5.2.7.2) and contribute to the separation force. Therefore, measures to mitigate shrinkage (section 2.7.3) have the potential to benefit adhesion and is an area for potential further investigation.

- **Testing of parabolic mirror.**

Further work is required to construct the parabolic mirror designed to maintain a normal angle of incidence throughout the build area as described in section 5.1.9.1. This would permit the effectiveness of the device at reducing the distorting effects due to refraction, divergence, ellipticity, and reflectance to be tested.

- **Build time optimisation.**

To quantify the required exposure delivered during the construction process to promote the adhesion of the constructed part to the substrate to an extent compliant

with MIL-STD-883K [83] will require further investigation. The results from that investigation would identify an increased minimum exposure limit for the operating window in Figure 5.35.

- **Further validation of the reflectance model.**

Due to the Form 1+ beam not conforming to a Gaussian profile at high exposures, it has not been possible to validate all aspects of the Gaussian based reflectance model. The trend identified is consistent with the measured results, with the difference between the modelled and measured values attributed to beam distortion. The model is physics based and the most likely cause for error is from differences between the input parameters and the material properties (i.e., refractive index, E_c , and D_p) and operating parameters (i.e., beam intensity at the print plane) used in practice. To accurately calibrate the reflectance model, test pieces constructed with known machine, substrate and photopolymer parameters will be required.

- **Validation of control logic compensation.**

The process described in section 5.1.9.4 to modulate the beam power according to its point of incidence on the build area has the potential to compensate for the combined influence of distorting effects. This would allow the CLW to be maintained constant at all locations within the build area. However, further work is required to validate the process. This would require accurately measuring the as-built dimensions of test pieces at different locations and the ability to vary the beam power, either between constructions or ideally according to location. The measured as-built dimensions of uncompensated test pieces, and compensated test pieces could then be compared with the design dimensions.

- **Cure from diffuse reflectance.**

One of the aims of this study is to investigate reflectance from polished silicon nitride. This has been calculated 5.1.5.3 to produce specular reflectance which has been modelled. However, extensive spurious cure resulting from diffuse reflections from the rough surface of the aluminium build platform on the Form 2 has also been identified. Such reflections will not maintain the Gaussian profile of the incident beam. Therefore, Gaussian based models, including superposition, are not applicable to diffuse reflections. Consequently, further work would be necessary to characterise and predict the impact of diffuse reflectance.

References

- [1] A. Agrawal, "Interfacial tension," Massachusetts Institute of Technology education website. Accessed: Sep. 19, 2023. [Online]. Available: <https://web.mit.edu/nmf/education/wettability/interfacial.html>
- [2] A. J. Lopes, E. MacDonald, and R. B. Wicker, "Integrating stereolithography and direct print technologies for 3D structural electronics fabrication," *Rapid Prototyp J*, vol. 18, no. 2, pp. 129–143, 2012, doi: 10.1108/13552541211212113.
- [3] C. Qingzhou, "60 Years of Photoresist Materials," Polymer Solutions for Electronics Consulting LLC. [Online]. Available: <https://www.polymersolutionsfe.com>
- [4] K. E. G. Dienel, B. Van Bochove, and J. V. Seppälä, "Additive Manufacturing of Bioactive Poly(trimethylene carbonate)/ β -Tricalcium Phosphate Composites for Bone Regeneration," *Biomacromolecules*, 2019, doi: 10.1021/acs.biomac.9b01272.
- [5] P. N. Bernal *et al.*, "Volumetric Bioprinting of Complex Living-Tissue Constructs within Seconds," *Advanced Materials*, vol. 31, no. 42, 2019, doi: 10.1002/adma.201904209.
- [6] "Align Q3 2019 Coporate Fact Sheet," Align Technology Inc. [Online]. Available: <https://www.aligntech.com/>
- [7] M. Guertin, C. Hull, and H. Nguyen, "Patent US6399010, Method and apparatus for stereolithographically forming three dimensional objects with reduced distortion." 1999.
- [8] "Texas Instrument DLP™ System Optics," *Product Application Report DLPA022*, no. July. pp. 1–26, 2010.
- [9] P. Jacobs, *Fundamentals of Stereolithography*. 1992.
- [10] T. Tiedje, S. Lungen, M. Schubert, M. Luniak, K. Nieweglowski, and K. Bock, "Will Low-Cost 3D Additive Manufactured Packaging Replace the Fan-Out Wafer Level Packages?," *Proceedings - Electronic Components and Technology Conference*, pp. 1065–1070, 2017, doi: 10.1109/ECTC.2017.276.
- [11] N. Hopkinson and P. Dickens, "Analysis of rapid manufacturing - Using layer manufacturing processes for production," *Proc Inst Mech Eng C J Mech Eng Sci*, vol. 217, no. 1, pp. 31–40, 2003, doi: 10.1243/095440603762554596.

- [12] L. A. Tse, P. J. Hesketh, D. W. Rosen, and J. L. Gole, "Stereolithography on silicon for microfluidics and microsensor packaging," *Microsystem Technologies*, vol. 9, no. 5, pp. 319–323, 2003, doi: 10.1007/s00542-002-0254-y.
- [13] A. Kataria and D. W. Rosen, "Building around inserts: Methods for fabricating complex devices in stereolithography," *Rapid Prototyp J*, vol. 7, no. 5, pp. 253–261, 2001, doi: 10.1108/13552540110410459.
- [14] B. K. Tehrani, R. A. Bahr, W. Su, B. S. Cook, and M. M. Tentzeris, "E-band characterization of 3D-printed dielectrics for fully-printed millimeter-wave wireless system packaging," *IEEE MTT-S International Microwave Symposium Digest*, pp. 1756–1759, 2017, doi: 10.1109/MWSYM.2017.8058985.
- [15] Y. Luo, Z. Ji, M. C. Leu, and R. Caudill, "Environmental performance analysis of solid freeform fabrication processes," *IEEE International Symposium on Electronics and the Environment*, no. February, pp. 1–6, 1999, doi: 10.1109/isee.1999.765837.
- [16] G. Aspar *et al.*, "3D Printing as a New Packaging Approach for MEMS and Electronic Devices," *Proceedings - Electronic Components and Technology Conference*, no. 1, pp. 1071–1079, 2017, doi: 10.1109/ECTC.2017.119.
- [17] G. E. Moore, "Cramming more components onto integrated circuits," *Electronics, Volume 28, April 19, 1965*, vol. 38, no. 8, 1965.
- [18] Y. C. Lee, R. Ramadoss, and N. Hoivik, "Introduction to MEMS packaging," *Mems Packaging*, pp. 1–29, 2018, doi: 10.1142/9789813229365_0001.
- [19] H. Gong, M. Beauchamp, S. Perry, A. T. Woolley, and G. P. Nordin, "Optical approach to resin formulation for 3D printed microfluidics," *RSC Adv*, vol. 5, no. 129, pp. 106621–106632, 2015, doi: 10.1039/c5ra23855b.
- [20] B. K. Tehrani, B. S. Cook, and M. M. Tentzeris, "Post-process fabrication of multilayer mm-wave on-package antennas with inkjet printing," *IEEE Antennas and Propagation Society, AP-S International Symposium (Digest)*, vol. 2015-October, pp. 607–608, 2015, doi: 10.1109/APS.2015.7304690.
- [21] B. K. Tehrani, S. A. Nauroze, R. A. Bahr, and M. M. Tentzeris, "On-package mm-wave FSS integration with 3D-printed encapsulation," *2017 IEEE Antennas and Propagation Society International Symposium, Proceedings*, vol. 2017-Janua, pp. 9–10, 2017, doi: 10.1109/APUSNCURSINRSM.2017.8072047.

- [22] S. Jangam, A. A. Bajwa, K. K. Thankkappan, P. Kittur, and S. S. Iyer, "Electrical Characterization of High Performance Fine Pitch Interconnects in Silicon-Interconnect Fabric," *Proceedings - Electronic Components and Technology Conference*, vol. 2018-May, pp. 1283–1288, 2018, doi: 10.1109/ECTC.2018.00197.
- [23] A. A. Bajwa *et al.*, "Heterogeneous Integration at Fine Pitch ($\leq 10 \mu\text{m}$) Using Thermal Compression Bonding," *Proceedings - Electronic Components and Technology Conference*, pp. 1276–1284, 2017, doi: 10.1109/ECTC.2017.240.
- [24] S. Jangam, "Heterogeneous Integration on Silicon-Interconnect Fabric using fine-pitch interconnects," 2020.
- [25] "Texas Instruments HDC302x Gas Sensor Technical data sheet," no. 1, p. 51, 2021.
- [26] A. Macleod, *Thin-Film Optical Filters, Fifth Edition*. 2018.
- [27] F. L. Pedrotti, L. M. Pedrotti, and L. S. Pedrotti, "Introduction to Optics," *Introduction to Optics*, 2017, doi: 10.1017/9781108552493.
- [28] L. Lu, J. Y. H. Fuh, A. Y. C. Nee, E. T. Kang, T. Miyazawa, and C. M. Cheah, "Origin of shrinkage, distortion and fracture of photopolymerized material," *Mater Res Bull*, vol. 30, no. 12, pp. 1561–1569, 1995, doi: 10.1016/0025-5408(95)00118-2.
- [29] V. Palazzi *et al.*, "3-D-Printing-Based Selective-Ink-Deposition Technique Enabling Complex Antenna and RF Structures for 5G Applications up to 6 GHz," *IEEE Trans Compon Packaging Manuf Technol*, vol. 9, no. 7, pp. 1434–1447, 2019, doi: 10.1109/TCPMT.2019.2919187.
- [30] T. Tiedje, S. Lungen, K. Nieweglowski, and K. Bock, "Will 3D-semiadditive packaging with high conductive redistribution layer and process temperatures below 100°C enable new electronic applications?," *2018 7th Electronic System-Integration Technology Conference, ESTC 2018 - Proceedings*, pp. 6–10, 2018, doi: 10.1109/ESTC.2018.8546450.
- [31] G. Fei, T. Wei, Q. Shi, Y. Guo, H. Oprins, and S. Yang, "Preliminary study on hybrid manufacturing of the electronic-mechanical integrated systems (EMIS) via the LCD stereolithography technology," *Solid Freeform Fabrication 2019: Proceedings of the 30th Annual International Solid Freeform Fabrication Symposium - An Additive Manufacturing Conference, SFF 2019*, pp. 2028–2036, 2019.

- [32] J. Li *et al.*, “Hybrid additive manufacturing of 3D electronic systems,” *Journal of Micromechanics and Microengineering*, vol. 26, no. 10, 2016, doi: 10.1088/0960-1317/26/10/105005.
- [33] T. Ackstaller, L. Lorenz, K. Nieweglowski, and K. Bock, “Combination of Thick-Film Hybrid Technology and Polymer Additive Manufacturing for High-Performance Mechatronic Integrated Devices,” *Proceedings of the International Spring Seminar on Electronics Technology*, vol. 2019-May, pp. 1–6, 2019, doi: 10.1109/ISSE.2019.8810205.
- [34] L. Lorenz, T. Ackstaller, and K. Bock, “Stereolithographic printed polymers on ceramic for 3D-opto-MID,” p. 12, 2020, doi: 10.1117/12.2554997.
- [35] B. K. Tehrani, R. A. Bahr, W. Su, B. S. Cook, and M. M. Tentzeris, “E-band characterization of 3D-printed dielectrics for fully-printed millimeter-wave wireless system packaging,” *IEEE MTT-S International Microwave Symposium Digest*, pp. 1756–1759, 2017, doi: 10.1109/MWSYM.2017.8058985.
- [36] B. Tehrani, R. Bahr, D. Revier, B. Cook, and M. Tentzeris, “The Principles of ‘Smart’ Encapsulation: Using Additive Printing Technology for the Realization of Intelligent Application-Specific Packages for IoT, 5G, and Automotive Radar Applications,” *Proceedings - Electronic Components and Technology Conference*, vol. 2018-May, pp. 111–117, 2018, doi: 10.1109/ECTC.2018.00025.
- [37] E. MacDonald *et al.*, “3D printing for the rapid prototyping of structural electronics,” *IEEE Access*, vol. 2, no. December, pp. 234–242, 2014, doi: 10.1109/ACCESS.2014.2311810.
- [38] J. Persad and S. Rocke, “A Survey of 3D Printing Technologies as Applied to Printed Electronics,” *IEEE Access*, vol. 10, no. December 2019, pp. 27289–27319, 2022, doi: 10.1109/ACCESS.2022.3157833.
- [39] Formlabs, “Form 1+ User manual,” pp. 1–8, [Online]. Available: <https://formlabs.com/media/upload/Form-1-plus-overview-US.pdf>
- [40] Y. Y. Chiu and J. H. Chang, “The algorithm of on line insert packaging fabrication in stereolithography,” *Proceedings of the 2005 IEEE International Conference on Mechatronics, ICM '05*, vol. 2005, pp. 487–491, 2005, doi: 10.1109/ICMECH.2005.1529306.
- [41] Y. S. Liao, H. C. Li, and M. T. Chen, “The study of rapid prototyping process with embedded functional inserts,” *J Mater Process Technol*, vol. 192–193, no. 1, pp. 68–74, 2007, doi: 10.1016/j.jmatprotec.2007.04.042.

- [42] Formlabs, “Form 2 Desktop Stereolithography 3D Printer Installation and Usage Instructions.” 2018.
- [43] B. Malengier, C. Hertleer, L. Cardon, and L. van Langenhove, “3D Printing on Textiles: Testing of Adhesion,” *Journal of Fashion Technology & Textile Engineering*, vol. s4, no. October, 2018, doi: 10.4172/2329-9568.s4-013.
- [44] T. Grothe, B. Brockhagen, and J. L. Storck, “Three-dimensional printing resin on different textile substrates using stereolithography: A proof of concept,” *J Eng Fiber Fabr*, vol. 15, 2020, doi: 10.1177/1558925020933440.
- [45] S. J. Orfanidis, “Electromagnetic waves and Antennas,” *Media*, vol. 2, pp. 525–570, 2008, [Online]. Available: <http://www.ece.rutgers.edu/~orfanidi/ewa/>
- [46] C. Sun, N. Fang, D. M. Wu, and X. Zhang, “Projection micro-stereolithography using digital micro-mirror dynamic mask,” *Sens Actuators A Phys*, vol. 121, no. 1, pp. 113–120, 2005, doi: 10.1016/j.sna.2004.12.011.
- [47] M. Nixon, B. Redding, A. A. Friesem, H. Cao, and N. Davidson, “Efficient method for controlling the spatial coherence of a laser”.
- [48] K. Luke, O. Yoshitomo, L. Michael, G. Alexander, and L. Michal, “Broadband mid-infrared frequency comb generation in a Si₃N₄ microresonator,” *Opt Lett*, vol. 40, no. 21, pp. 4823–4826, 2015, doi: 10.1364/oe.463312.
- [49] Y. Ning, “Process Parameter Optimization for Direct Metal Laser Sintering (DMLS),” *PHD Thesis*, p. 167, 2005.
- [50] J. Bennett, “Measuring UV curing parameters of commercial photopolymers used in additive manufacturing,” *Addit Manuf*, vol. 18, pp. 203–212, 2017, doi: 10.1016/j.addma.2017.10.009.
- [51] T. Chartier *et al.*, “Fabrication of millimeter wave components via ceramic stereo and microstereolithography processes,” *Journal of the American Ceramic Society*, vol. 91, no. 8, pp. 2469–2474, 2008, doi: 10.1111/j.1551-2916.2008.02482.x.
- [52] A. Zhakeyev, J. Tobin, H. Wang, F. Vilela, and J. Xuan, “Additive manufacturing of photoactive polymers for visible light harvesting,” *Energy Procedia*, vol. 158, pp. 5608–5614, 2019, doi: 10.1016/j.egypro.2019.01.579.
- [53] F. Schneider, J. Draheim, R. Kamberger, and U. Wallrabe, “Process and material properties of polydimethylsiloxane (PDMS) for Optical MEMS,” *Sens Actuators A Phys*, vol. 151, no. 2, pp. 95–99, 2009, doi: 10.1016/j.sna.2009.01.026.

- [54] M. Polyanskiy, “refractiveindex.info.” [Online]. Available: <https://refractiveindex.info/?shelf=other&book=air&page=Ciddor>
- [55] T. a Trezza and J. M. Krochta, “Heterogeneity of Biopolymer Coatings,” *J Appl Polym Sci*, vol. 79, no. 12, pp. 2221–2229, 2001.
- [56] B. Duncan, “Developments in testing adhesive joints,” *Advances in Structural Adhesive Bonding*, pp. 389–436, 2010, doi: 10.1533/9781845698058.3.389.
- [57] S. Abbott, *Sticking together: The science of adhesion*. 2020.
- [58] A. A. Griffiths, “The phenomena of rupture and flow in solids,” 1920. doi: 10.1098/rsta.1921.0006.
- [59] K. Kendall, “The adhesion and surface energy of elastic solids,” *J Phys D Appl Phys*, vol. 4, no. 8, pp. 1186–1195, 1971, doi: 10.1088/0022-3727/4/8/320.
- [60] T. L. Gordon and M. E. Fakley, “The influence of elastic modulus on adhesion to thermoplastics and thermoset materials,” *Int J Adhes Adhes*, vol. 23, no. 2, pp. 95–100, 2003, doi: 10.1016/S0143-7496(02)00064-7.
- [61] H. R. Newby, Bi-min Zhang; Chaudhury, Manoj K; Brown, “Macroscopic Evidence of the Effect of Interfacial Slippage on Adhesion.” 1995.
- [62] X. Wang, D. Tan, X. Zhang, Y. Lei, and L. Xue, “Effective elastic modulus of structured adhesives: From biology to biomimetics,” *Biomimetics*, vol. 2, no. 3, 2017, doi: 10.3390/biomimetics2030010.
- [63] S. Abbott, *ADHESION SCIENCE Principles and Practice*. 2015.
- [64] T. Winkler, “Determining the surface tension of liquids by measurements on pendant drops,” *Technical Note*, vol. 49, no. 40, pp. 1–5, 2010.
- [65] K.Kendall, *Molecular adhesion and its applications; The Sticky Universe*. 2001.
- [66] Inseto, “Technical data sheet for silicon nitride wafer.” 2021.
- [67] R. P. Wool, “Polymer Entanglements,” *Macromolecules*, vol. 26, no. 7, pp. 1564–1569, 1993, doi: 10.1021/ma00059a012.
- [68] N. S. Mpofo, J. I. Mwasiagi, L. C. Nkiwane, and D. Njuguna, “Use of regression to study the effect of fabric parameters on the adhesion of 3D printed PLA polymer onto woven fabrics,” *Fashion and Textiles*, vol. 6, no. 1, 2019, doi: 10.1186/s40691-019-0180-6.

- [69] R. Hashemi Sanatgar, C. Campagne, and V. Nierstrasz, "Investigation of the adhesion properties of direct 3D printing of polymers and nanocomposites on textiles: Effect of FDM printing process parameters," *Appl Surf Sci*, vol. 403, pp. 551–563, 2017, doi: 10.1016/j.apsusc.2017.01.112.
- [70] Formlabs, "Clear resin material safety data sheet."
- [71] J. Kim, J. Cho, and Y. S. Lim, "Bonding of urethane reactants to aluminum surface," *J Mater Sci*, vol. 40, no. 11, pp. 2789–2794, 2005, doi: 10.1007/s10853-005-2409-6.
- [72] J. Luo *et al.*, "Relative abundance of subsurface hydroxyl and molecular water species in silicate and aluminosilicate glasses," *J Non Cryst Solids*, vol. 510, no. October 2018, pp. 179–185, 2019, doi: 10.1016/j.jnoncrysol.2019.01.012.
- [73] G. F. Tjandraatmadja, L. S. Burn, and M. J. Jollands, "The effects of ultraviolet radiation on polycarbonate glazing," *Proc. 8th International Conf. On Durability of Building and Construction Materials, Vancouver, Canada*, vol. 30, pp. 884–898, 1999.
- [74] G. J. Lake and A. G. Thomas, "The strength of highly elastic materials," *Proc R Soc Lond A Math Phys Sci*, vol. 300, no. 1460, pp. 108–119, 1967, doi: 10.1098/rspa.1967.0160.
- [75] K. Ebe, H. Seno, and K. Horigome, "UV curable pressure-sensitive adhesives for fabricating semiconductors. I. Development of easily peelable dicing tapes," *J Appl Polym Sci*, vol. 90, no. 2, pp. 436–441, 2003, doi: 10.1002/app.12673.
- [76] M. D. Fitton and J. G. Broughton, "Variable modulus adhesives: An approach to optimised joint performance," *Int J Adhes Adhes*, vol. 25, no. 4, pp. 329–336, 2005, doi: 10.1016/j.ijadhadh.2004.08.002.
- [77] I. Q. Vu, L. B. Bass, C. B. Williams, and D. A. Dillard, "Characterizing the effect of print orientation on interface integrity of multi-material jetting additive manufacturing," *Addit Manuf*, vol. 22, no. February, pp. 447–461, 2018, doi: 10.1016/j.addma.2018.05.036.
- [78] X. Chen, I. A. Ashcroft, C. J. Tuck, Y. F. He, R. J. M. Hague, and R. D. Wildman, "An investigation into the depth and time dependent behaviour of UV cured 3D ink jet printed objects," *J Mater Res*, vol. 32, no. 8, pp. 1407–1420, 2017, doi: 10.1557/jmr.2017.4.

- [79] X. Kuang *et al.*, “Grayscale digital light processing 3D printing for highly functionally graded materials,” *Sci Adv*, vol. 5, no. 5, pp. 1–10, 2019, doi: 10.1126/sciadv.aav5790.
- [80] D. Tomicic, “Adhesion measurements of positive photoresist on sputtered aluminium surface,” *Science And Technology*, 2002.
- [81] W. K. Szeto, M. Y. Xie, J. K. Kim, M. M. F. Yuen, P. Tong, and S. Yi, “Interface failure criterion of button shear test as a means of interface adhesion measurement in plastic packages,” *International Symposium on Electronic Materials and Packaging, EMAP 2000*, pp. 263–268, 2000, doi: 10.1109/EMAP.2000.904165.
- [82] S. Lungen, T. Tiedje, K. Meier, K. Nieweglowski, and K. Bock, “Reliability of 3D additive manufactured packages,” *2018 7th Electronic System-Integration Technology Conference, ESTC 2018 - Proceedings*, 2018, doi: 10.1109/ESTC.2018.8546417.
- [83] “MIL-STD-883K Department of defense, test method standard for microcircuits.” 2016.
- [84] E. Skliutas, S. Kasetaitė, L. Jonušauskas, J. Ostrauskaite, and M. Malinauskas, “Photosensitive naturally derived resins toward optical 3-D printing,” *Optical Engineering*, vol. 57, no. 04, p. 1, 2018, doi: 10.1117/1.oe.57.4.041412.
- [85] Aculon, “Hydrophilic Aluminium coatings.” Accessed: Nov. 01, 2022. [Online]. Available: <https://www.aculon.com/hydrophilic-aluminum/>
- [86] S. S. Voyutskii and V. L. Vakula, “The role of diffusion phenomena in polymer-to-polymer adhesion,” *J Appl Polym Sci*, vol. 7, no. 2, pp. 475–491, 1963, doi: 10.1002/app.1963.070070207.
- [87] M. Korger, J. Bergschneider, M. Lutz, B. Mahltig, K. Finsterbusch, and M. Rabe, “Possible applications of 3D printing technology on textile substrates,” *IOP Conf Ser Mater Sci Eng*, vol. 141, no. 1, 2016, doi: 10.1088/1757-899X/141/1/012011.
- [88] T. Koziar, C. Döpke, N. Grimmelsmann, I. Juhász Junger, and A. Ehrmann, “Influence of fabric pretreatment on adhesion of three-dimensional printed material on textile substrates,” *Advances in Mechanical Engineering*, vol. 10, no. 8, pp. 1–8, 2018, doi: 10.1177/1687814018792316.
- [89] T. Koziar, T. Blachowicz, and A. Ehrmann, “Adhesion of three-dimensional printing on textile fabrics: Inspiration from and for other research areas,” *J Eng Fiber Fabr*, vol. 15, 2020, doi: 10.1177/1558925020910875.

- [90] “Silicon Nitride Wafers Explained.” Accessed: Dec. 15, 2019. [Online]. Available: <https://www.universitywafer.com/sin.html#:~:text=Silicon nitride wafers can be,%2C oxidation%2C and mechanical shock.>
- [91] M. S. Ismai, R. W. Bower, J. L. Veteran, and O. J. Marsh, “Silicon Nitride Direct Bonding,” *Electron Lett*, vol. 26, no. 14, pp. 1045–1046, 1990, doi: 10.1049/el:19900677.
- [92] P. R. Scheeper, J. A. Voorthuyzen, W. Olthuis, and P. Bergveld, “Investigation of attractive forces between PECVD silicon nitride microstructures and an oxidized silicon substrate,” *Sens Actuators A Phys*, vol. 30, no. 3, pp. 231–239, 1992, doi: 10.1016/0924-4247(92)80126-N.
- [93] H. Barhoumi, A. Maaref, and N. Jaffrezic-Renault, “Experimental study of thermodynamic surface characteristics and pH sensitivity of silicon dioxide and silicon nitride,” *Langmuir*, vol. 26, no. 10, pp. 7165–7173, 2010, doi: 10.1021/la904251m.
- [94] S. I. Raider, R. Flitsch, J. A. Aboaf, and W. A. Pliskin, “Surface Oxidation of Silicon Nitride Films,” *J Electrochem Soc*, vol. 123, no. 4, pp. 560–565, 1976, doi: 10.1149/1.2132877.
- [95] C. Koch and T. Rinke, “Chapter 01 MicroChemicals ®-Fundamentals of Microstructuring(SUBSTRATE PREPARATION)”, [Online]. Available: www.microchemicals.com/downloads/application_notes.html
- [96] U.Okoroanyanwu, *Chemistry and Lithography*. 2010.
- [97] J. Berthier, “Theory of Wetting,” *Micro-Drops and Digital Microfluidics*, pp. 7–73, 2013, doi: 10.1016/b978-1-4557-2550-2.00002-x.
- [98] S. P. Lee, H. W. Kang, S. J. Lee, I. H. Lee, T. J. Ko, and D. W. Cho, “Development of rapid mask fabrication technology for micro-abrasive jet machining,” *Journal of Mechanical Science and Technology*, vol. 22, no. 11, pp. 2190–2196, 2008, doi: 10.1007/s12206-008-0607-2.
- [99] G. Wolansky and A. Marmur, “Apparent contact angles on rough surfaces: The Wenzel equation revisited,” *Colloids Surf A Physicochem Eng Asp*, vol. 156, no. 1–3, pp. 381–388, 1999, doi: 10.1016/S0927-7757(99)00098-9.
- [100] A. Marmur, “Wetting on hydrophobic rough surfaces: To be heterogeneous or not to be?,” *Langmuir*, vol. 19, no. 20, pp. 8343–8348, 2003, doi: 10.1021/la0344682.

- [101] D. M. Lopes, S. M. M. Ramos, L. R. de Oliveira, and J. C. M. Mombach, “Cassie-Baxter to Wenzel state wetting transition: A 2D numerical simulation,” *RSC Adv*, vol. 3, no. 46, pp. 24530–24534, 2013, doi: 10.1039/c3ra45258a.
- [102] A. Rudawska, *Assessment of surface preparation for the bonding/adhesive technology*. 2019. doi: 10.1016/b978-0-12-817010-6.00009-6.
- [103] M. Rezaei, D. M. Warsinger, J. H. Lienhard V, M. C. Duke, T. Matsuura, and W. M. Samhaber, “Wetting phenomena in membrane distillation: Mechanisms, reversal, and prevention,” *Water Res*, vol. 139, pp. 329–352, 2018, doi: 10.1016/j.watres.2018.03.058.
- [104] B. Khatri, M. Frey, A. Raouf-Fahmy, M. V. Scharla, and T. Hanemann, “Development of a multi-material stereolithography 3D printing device,” *Micromachines (Basel)*, vol. 11, no. 5, 2020, doi: 10.3390/mi11050532.
- [105] Y. M. Huang and C. P. Jiang, “On-line force monitoring of platform ascending rapid prototyping system,” *J Mater Process Technol*, vol. 159, no. 2, pp. 257–264, 2005, doi: 10.1016/j.jmatprotec.2004.05.015.
- [106] F. Liravi, S. Das, and C. Zhou, “Separation force analysis and prediction based on cohesive element model for constrained-surface Stereolithography processes,” *CAD Computer Aided Design*, vol. 69, pp. 134–142, 2015, doi: 10.1016/j.cad.2015.05.002.
- [107] Y. Kanamori, J. Sato, T. Shimano, S. Nakamura, and K. Hane, “Polymer microstructure generated by laser stereo-lithography and its transfer to silicon substrate using reactive ion etching,” *Microsystem Technologies*, vol. 13, no. 8–10, pp. 1411–1416, 2007, doi: 10.1007/s00542-007-0380-7.
- [108] S. C. O. Dufaud, H. Le Gall, “Stereolithography of Lead Zirconate titanate for MEMS,” *Smart sensors, actuators and MEMS*, pp. 28–37, 2003.
- [109] D. R. L. Tse, H. Noh, “Fabrication of Chemical Sensor Packaging with SLA.” 2001.
- [110] P. J. H. A. Choudhury, “A novel method for stereolithography alignment of MEMS structures,” 2003.
- [111] B. Goubault *et al.*, “A New Microsystem Packaging Approach Using 3D Printing Encapsulation Process,” *Proceedings - Electronic Components and Technology Conference*, vol. 2018-May, no. Figure 5, pp. 118–124, 2018, doi: 10.1109/ECTC.2018.00026.
- [112] Y. Ohkubo, K. Endo, and K. Yamamura, “Adhesive-free adhesion between heat-assisted plasma-treated fluoropolymers (PTFE, PFA) and plasma-jet-treated

polydimethylsiloxane (PDMS) and its application,” *Sci Rep*, vol. 8, no. 1, pp. 1–11, 2018, doi: 10.1038/s41598-018-36469-y.

[113] S. Zips *et al.*, “Direct Stereolithographic 3D Printing of Microfluidic Structures on Polymer Substrates for Printed Electronics,” *Adv Mater Technol*, vol. 4, no. 3, pp. 1–5, 2019, doi: 10.1002/admt.201800455.

[114] M. Kellermeier *et al.*, “Towards additive manufacturing of dielectric accelerating structures,” *J Phys Conf Ser*, vol. 1596, no. 1, 2020, doi: 10.1088/1742-6596/1596/1/012020.

[115] ASTM International, “ASTM D648 - 18 Standard Test Method for Deflection Temperature of Plastics Under Flexural Load in the Edgewise Position,” *ASTM Standards*, no. April, p. 14, 2018, doi: 10.1520/D0648-18.1.

[116] B. S. I. Gibson, D. W. Rosen, *Additive Manufacturing Technologies*. 2010. doi: 10.1007/978-3-662-53120-4_16866.

[117] F. Zhang *et al.*, “Multi-branched benzylidene ketone based photoinitiators for multiphoton fabrication,” *Addit Manuf*, vol. 16, pp. 206–212, 2017, doi: 10.1016/j.addma.2017.06.008.

[118] B. Adzima, “The Ember Printer: An Open Platform for Software, Hardware, and Materials Development,” *UV&EB WEST Conference, Redondo Beach, CA*, 2015.

[119] G. Taormina, C. Sciancalepore, M. Messori, and F. Bondioli, “3D printing processes for photocurable polymeric materials: technologies, materials, and future trends,” *J Appl Biomater Funct Mater*, vol. 16, no. 3, pp. 151–160, 2018, doi: 10.1177/2280800018764770.

[120] C. Koch and T. Rinke, “Exposure - Basics of Microstructuring,” Microchemicals.Gmbh. [Online]. Available: <https://www.microchemicals.net/>

[121] A. Sakly, S. Kenzari, D. Bonina, S. Corbel, and V. Fournée, “A novel quasicrystal-resin composite for stereolithography,” *Mater Des*, vol. 56, pp. 280–285, 2014, doi: 10.1016/j.matdes.2013.11.025.

[122] Y. Li *et al.*, “Isotropic stereolithography resin toughened by core-shell particles,” *Chemical Engineering Journal*, vol. 394, no. March, p. 124873, 2020, doi: 10.1016/j.cej.2020.124873.

[123] S. J. Leigh, C. P. Purssell, J. Bowen, D. A. Hutchins, J. A. Covington, and D. R. Billson, “A miniature flow sensor fabricated by micro-stereolithography employing a

magnetite/acrylic nanocomposite resin,” *Sens Actuators A Phys*, vol. 168, no. 1, pp. 66–71, 2011, doi: 10.1016/j.sna.2011.03.058.

[124] M. Gurr, D. Hofmann, M. Ehm, Y. Thomann, R. Kubier, and R. Mülhaupt, “Acrylic nanocomposite resins for use in stereolithography and structural light modulation based rapid prototyping and rapid manufacturing technologies,” *Adv Funct Mater*, vol. 18, no. 16, pp. 2390–2397, 2008, doi: 10.1002/adfm.200800344.

[125] W. L. Tsang and A. C. Taylor, “Fracture and toughening mechanisms of silica- and core-shell rubber-toughened epoxy at ambient and low temperature,” *J Mater Sci*, vol. 54, no. 22, pp. 13938–13958, 2019, doi: 10.1007/s10853-019-03893-y.

[126] E. Fantino *et al.*, “3D Printing of Conductive Complex Structures with in Situ Generation of Silver Nanoparticles,” *Advanced Materials*, vol. 28, no. 19, pp. 3712–3717, 2016, doi: 10.1002/adma.201505109.

[127] K. Ikuta, T. Ogata, M. Tsubio, and S. Kojima, “Development of mass productive micro stereo lithography (mass-IH process),” *Proceedings of the IEEE Micro Electro Mechanical Systems (MEMS)*, pp. 301–306, 1996, doi: 10.1109/memsys.1996.493998.

[128] K. S. Lee, R. H. Kim, P. Prabhakaran, D. Y. Yang, T. W. Lim, and S. H. Park, “Two-photon stereolithography,” *Journal of Nonlinear Optical Physics and Materials*, vol. 16, no. 1, pp. 59–73, 2007, doi: 10.1142/S021886350700355X.

[129] C. Schmidleithner and D. Kalaskar, “3D Printing,” in *3D Printing*, 2018.

[130] M. Wu, W. Zhao, Y. Tang, D. Li, and B. Lu, “A novel stereolithography technology with conventional UV light,” *Rapid Prototyp J*, vol. 7, no. 5, pp. 268–274, 2001, doi: 10.1108/EUM0000000006117.

[131] J. Ion, *Laser processing of engineering materials : principles, procedure and industrial application*. Oxford : Elsevier Butterworth-Heinemann, 2005.

[132] J.-H. Sim, E.-D. Lee, and H.-J. Kweon, “Effect of the laser beam size on the cure properties of a photopolymer in stereolithography,” *International Journal of Precision Engineering and Manufacturing*, vol. 8, no. 4, pp. 50–55, 2007.

[133] R. D. Goodwin and W. M. Haynes, “NBS Technical Note 1051,” 1982.

[134] M. Kovalev, I. Gritsenko, N. Stsepuro, P. Nosov, G. Krasin, and S. Kudryashov, “Reconstructing the Spatial Parameters of a Laser Beam Using the Transport-of-Intensity Equation,” *Sensors*, vol. 22, no. 5, 2022, doi: 10.3390/s22051765.

- [135] J. Smith, "M2 Factor (Quality Factor)." Accessed: Apr. 12, 2022. [Online]. Available: https://scitec.uk.com/lasers/m2_factor.php
- [136] B. Landoni, "How to evaluate a Stereolithographic 3D Printer," OpenElectronics. Accessed: May 12, 2022. [Online]. Available: https://www.open-electronics.org/how-to-evaluate-a-stereo-lithographic-3d-printers/?utm_content=buffer144eb&utm_medium=social&utm_source=facebook.com&utm_campaign=buffer
- [137] H. Theuss and K. Pressel, "Handbook of Silicon Based MEMS Materials and Technologies (Third Edition). Chapter 32: Three-dimensional integration of MEMS," T. Markku, P.-K. Mervi, P. Matthias, T. Horst, M. Teruaki, and V. Lindroos, Eds., 2020, pp. 691-706,.
- [138] J. S. Ullett, S. J. Rodrigues, and R. P. Chartoff, "Linear Shrinkage of Stereolithography Resins," *Development*, pp. 261–269.
- [139] W. Vinson, J. Allison, P. Jacobs, Crescenta, and D. Smalley, "Patent US5238639 - Method and apparatus for stereolithographic curl balancing." 1993.
- [140] C. Manners, K. Bhatia, and H. Nguyen, "US Patent 6649113 Method to reduce differential shrinkage in three-dimensional stereolithographic objects.,," 2003.
- [141] A. K. Patra, R. K. Afshar, J. M. Rowland, M. M. Olmstead, and P. K. Mascharak, "Properties of atoms, radicals, and bonds.,," *Angewandte Chemie - International Edition*, vol. 42, no. 37, pp. 4517–4521, 2003, doi: 10.1002/anie.200352070.
- [142] Formlabs, "Formlabs support webpage," Formlabs webpage.
- [143] GE, "Lexan 9030 Polycarbonate - Technical Properties and Product Data Sheet."
- [144] "The Engineering Toolbox." [Online]. Available: <https://www.engineeringtoolbox.com/>
- [145] A. Rakic, "Algorithm for the determination of intrinsic optical constants of metal films: application to aluminium." 1995.
- [146] A. Khan, J. Philip, and P. Hess, "Young's modulus of silicon nitride used in scanning force microscope cantilevers," *J Appl Phys*, vol. 95, no. 4, pp. 1667–1672, 2004, doi: 10.1063/1.1638886.
- [147] Filmetrics, "Refractive Index of Si3N4, Silicon Nitride, SiN, SiON." [Online]. Available: <https://www.filmetrics.com/refractive-index-database/Si3N4/Silicon-Nitride-SiN-SiON>

- [148] “Paraloid BTA-751U impact modifier certification of analysis, Dow Europe GMBH.” 2020.
- [149] P. Jacobs, “Fundamental processes,” in *Fundamentals of Stereolithography*, 1992, pp. 79–110.
- [150] B. Frantzdale, “Form 1+ Default control logic for Formlabs clear resin.” Formlabs, 2017. [Online]. Available: https://github.com/Formlabs/OpenFL/blob/master/Form_1%2B_FLGPCL02_100.ini
- [151] A. E. Siegman, *Lasers*. Herdon, Va. University Science Books, 1986.
- [152] C. Demaria, “Stereolithography.” The University of Pisa, 2015.
- [153] M. Hunziker and R. Leyden, “Basic Polymer Chemistry,” in *Fundamentals of Stereolithography*, 1992, p. 31.
- [154] O. Pütsch, A. Temmler, J. Stollenwerk, E. Willenborg, and P. Loosen, “Active optical system for laser structuring of 3D surfaces by remelting,” no. September, 2013, doi: 10.1117/12.2023306.
- [155] L. A. Johnson, “BURN-IN AND RELIABILITY TESTING,” *IEEE*, vol. 44, no. 2, 2006, doi: 10.1109/MCOM.2006.1593543.
- [156] M. P. Shuttleworth, “A Digital Manufacturing Process For Three-Dimensional Electronics,” 2020.
- [157] K. Kambly, “Characterization of Curing Kinetics and Polymerization Shrinkage in Ceramic-Loaded Photocurable Resins For Large Area Maskless Photopolymerization (Lamp),” *School of Mechanical Engineering*, vol. MS, p. 79, 2009, [Online]. Available: https://www.researchgate.net/publication/44131812_Characterization_of_curing_kinetics_and_polymerization_shrinkage_in_ceramic-loaded_photocurable_resins_for_large_area_maskless_photopolymerization_LAMP
- [158] V. S. D. Voet *et al.*, “Biobased Acrylate Photocurable Resin Formulation for Stereolithography 3D Printing,” *ACS Omega*, vol. 3, no. 2, pp. 1403–1408, 2018, doi: 10.1021/acsomega.7b01648.
- [159] M. Bragaglia, F. R. Lamastra, V. Cherubini, and F. Nanni, “3D printing of polybutadiene rubber cured by photo-induced thiol-ene chemistry: A proof of concept,” *Express Polym Lett*, vol. 14, no. 6, pp. 576–582, 2020, doi: 10.3144/expresspolymlett.2020.47.

- [160] K. C. Wu and J. W. Halloran, "Photopolymerization monitoring of ceramic stereolithography resins by FTIR methods," *J Mater Sci*, vol. 40, no. 1, pp. 71–76, 2005, doi: 10.1007/s10853-005-5689-y.
- [161] Lavachemist, "Z-Jog_052320." Github, 2020. [Online]. Available: <https://github.com/opensourcemanufacturing/OpenFL/tree/master/Community-PythonScripts/Scripts>
- [162] "Heat Distortion Temperature," Polymer Properties Database. [Online]. Available: <https://polymerdatabase.com/polymer physics/HeatDistortion.html>
- [163] Formlabs Inc., "Form Cure time and temperature settings," *Formlabs Inc.*, pp. 14–16, 2022, [Online]. Available: <https://s3.amazonaws.com/servicecloudassets.formlabs.com/media/Finishing/Post-Curing/115001414464-Form Cure Time and Temperature Settings/FormCurePost-CureSettings.pdf>
- [164] "Formlabs Formcure product description." [Online]. Available: <https://formlabs.com/store/post-processing/form-cure/>
- [165] Kruss, "Drop Shape Analysis System DSA100 Installation and Operation." 2010.
- [166] D. K. Owens, "Estimation of the surface free energy of polymers," *J Appl Polym Sci*, vol. 13, pp. 1741–1747, 1969.
- [167] P. Materials, E. I. Materials, P. Matrix, C. Materials, and P. Specimens, "Standard Test Method for Tensile Properties of Plastics 1," no. January 2004, pp. 1–15, 2006, doi: 10.1520/D0638-14.1.
- [168] Arduino, "Arduino reference libraries." [Online]. Available: <https://www.arduino.cc/en/reference/libraries>
- [169] ASTM International, "ASTM D1623-17 Standard Test Method for Tensile and Tensile Adhesion Properties of Rigid Cellular Plastics," *ASTM StandardsL*, 2017, doi: 10.1520/D1623-17.
- [170] A. K. Coker, "MECHANICAL SEPARATIONS," *Ludwig's Applied Process Design for Chemical and Petrochemical Plants*, pp. 371–443, Jan. 2007, doi: 10.1016/B978-075067766-0/50013-0.
- [171] B. Frantzdale and M. Keeter, "OpenFL: Hacking SL with the Form1+ API." 2016. [Online]. Available: https://formlabs.com/media/upload/Formlabs_OpenFL.pdf

- [172] “Lightburnsoftware.com.” Accessed: May 31, 2022. [Online]. Available: <https://lightburnsoftware.com/>
- [173] “Stratasy Solutions Ltd; Grabcad.” Accessed: Mar. 07, 2022. [Online]. Available: Grabcad.com
- [174] Y. S. Liao, H. C. Li, and M. T. Chen, “The study of rapid prototyping process with embedded functional inserts,” *J Mater Process Technol*, vol. 192–193, no. 1, pp. 68–74, 2007, doi: 10.1016/j.jmatprotec.2007.04.042.
- [175] “Sourcingmap.com.” Accessed: Apr. 09, 2021. [Online]. Available: sourcingmap.com
- [176] Microsoft, “GitHub.” [Online]. Available: Github.com
- [177] Formlabs, “Form 3 vs. Form 2: Comparing Formlabs Desktop 3D Printers.” [Online]. Available: <https://formlabs.com/uk/blog/form-3-form-2-3d-printer-comparison/>
- [178] “ASTM 52909-2019 Additive manufacturing — Test artifacts — Geometric capability assessment of additive manufacturing systems.” 2019. doi: 10.1520/52902-19.
- [179] U. C. Okonkwo, I. P. Okokpujie, J. E. Sinebe, and C. A. K. Ezugwu, “Comparative analysis of aluminium surface roughness in end-milling under dry and minimum quantity lubrication (MQL) conditions,” *Manuf Rev (Les Ulis)*, vol. 2, 2015, doi: 10.1051/mfreview/2015033.
- [180] E. D. Reedy, “Strength of butt and sharp-cornered joints,” *Adhesion Science and Engineering*, pp. 145–192, 2002, doi: 10.1016/b978-0-444-51140-9.50032-9.
- [181] A. Small, S. Hong, and D. Pine, “Scattering properties of core-shell particles in plastic matrices,” *J Polym Sci B Polym Phys*, vol. 43, no. 24, pp. 3534–3548, 2005, doi: 10.1002/polb.20624.
- [182] “Formlabs Technical Specifications.” [Online]. Available: <https://formlabs.com/uk/3d-printers/form-3/tech-specs/>
- [183] A. Goghari, “Fabricating a 3D Printed Sculpture to Withstand Times Square.” Accessed: Apr. 02, 2020. [Online]. Available: <https://formlabs.com/blog/fabricating-3d-printed-structure-withstand-times-square/>
- [184] Schott, “Optical glass data sheet.” [Online]. Available: https://refractiveindex.info/download/data/2017/schott_2017-01-20.pdf

[185] A. Bruner and J. Dudley, “UVEB Technology Article; Seeing clearly with 3D Printed Lenses,” Digital Factory, Formlabs.

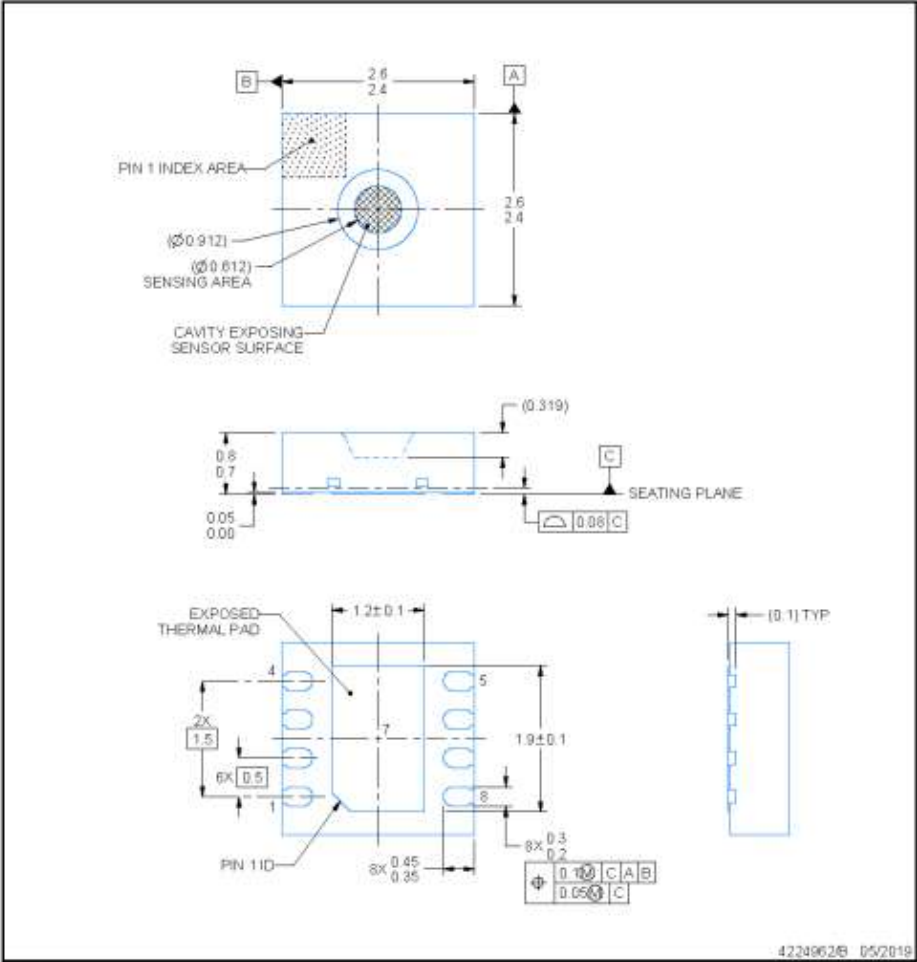
[186] “Strain gauge sensor,” Innovators guru. [Online]. Available:
<https://innovatorsguru.com/strain-gauge-sensor/>

[187] “How to Hookup BME280 Sensor to Arduino using I2C,” 2021. [Online]. Available: <http://cactus.io/hookups/sensors/barometric/bme280/hookup-arduino-to-bme280-barometric-pressure-sensor>

[188] Robotshop, “HX711 and a single strain gauge,” 2021. [Online]. Available:
<https://www.robotshop.com/community/forum/t/hx711-and-a-single-strain-gauge/48600>

Appendix A: Texas Instruments HDC302x Gas Sensor Drawing.

DEF0008A  **PACKAGE OUTLINE**
WSO8 - 0.8 mm max height
 PLASTIC SMALL-OUTLINE - NO LEAD



- NOTES:
1. All linear dimensions are in millimeters. Any dimensions in parenthesis are for reference only. Dimensioning and tolerancing per ASME Y14.5M.
 2. This drawing is subject to change without notice.
 3. The package thermal pad must be soldered to the printed circuit board for thermal and mechanical performance.
 4. The pick and place nozzle has to be between 0.915 and 1.875 mm.

Appendix B: Relevant standards

Relevant standards

- ISO 13445 (2006): Adhesives-Determination of Shear Strength of Adhesive Bonds between Rigid Substrates by the Block-Shear Method;
- ASTM 4541-17 (BS EN ISO 4624) Standard Test Method for Pull-Off Strength of Coatings Using Portable Adhesion Testers;
- ASTM D1623-17 standard Test Method for Tensile and Tensile Adhesion Properties of Rigid Cellular Plastics;
- ASTM D638-14 (2014): Standard Test Method for Tensile Properties of Plastics
- ASTM D 3163-01: Standard Test Method for Determining Strength of Adhesively Bonded Rigid Plastic Lap-Shear Joints in Shear by Tension Loading
- ASTM D 3983-98(2004): Standard Test Method for Measuring Strength and Shear Modulus of Nonrigid Adhesives by the Thick-Adherend Tensile-Lap Specimen
- ASTM D 4562-01: Standard Test Method for Shear Strength of Adhesives Using Pin-and-Collar Specimen
- ASTM D 5656-04: Standard Test Method for Thick-Adherend Metal Lap-Shear Joints for Determination of the Stress-Strain Behaviour of Adhesives in Shear by Tension Loading.
- PDISO/TR 11145-3:2004: Lasers and laser-related equipment — Test methods for laser beam widths, divergence angles and beam propagation ratios — Part 3: Intrinsic and geometrical laser beam classification, propagation, and details of test methods

Appendix C: Supporting adhesion principals.

C1: Lennard-Jones potential described by Kendall [65]

The following diagrams and description of the Lennard-Jones potential is taken directly from Kendall's book: Molecular adhesion and its applications [59].

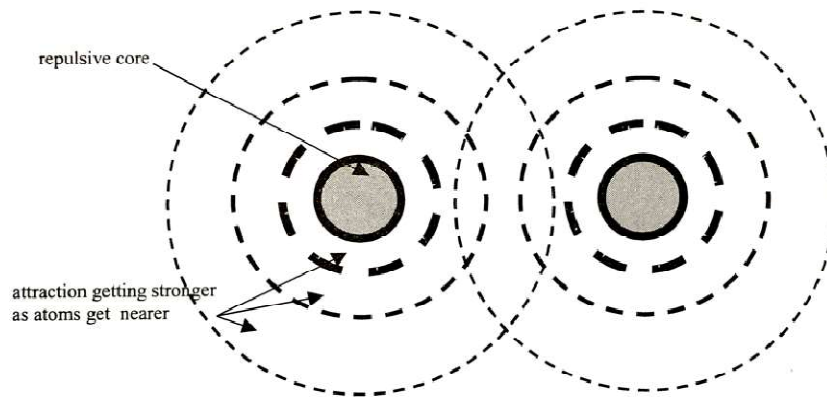


Figure C1.1: Diagram of two atoms being attracted towards each other: the attractions get stronger as the atoms approach, then a weak repulsion.

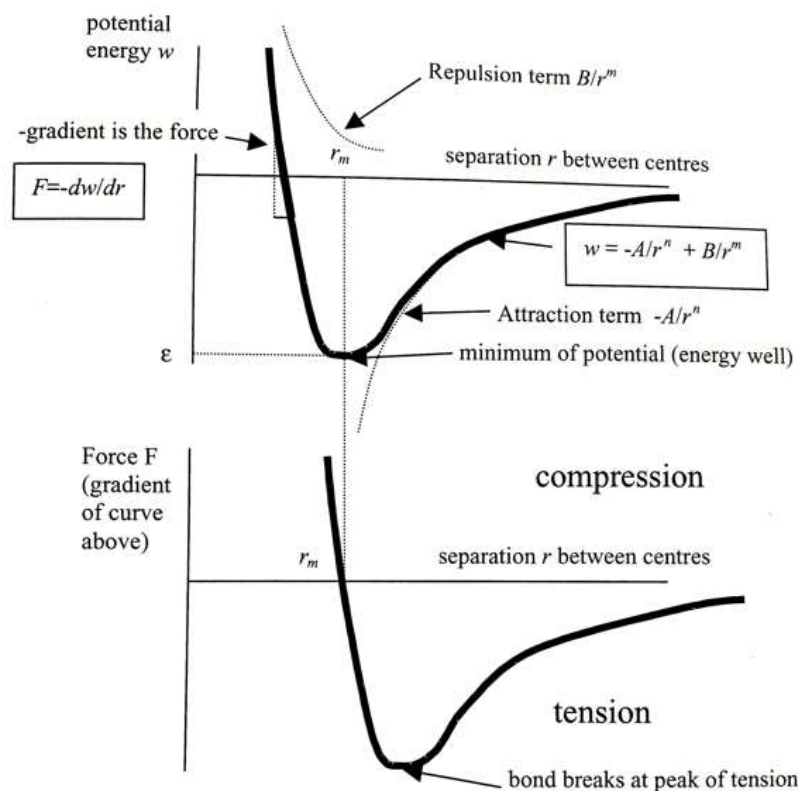


Figure 5.2. Curves showing the two-parameter model behavior: the energy is given in the top curve, and the force in the bottom curve. The equilibrium point is at the minimum of the energy curve.

Figure C1.2: Lennard-Jones potential as described by Kendall [68].

Where r_m is the equilibrium point where the compressive and tensile forces acting on the molecule are equal.

C2: The reaction mechanism between polyurethane and aluminium oxide can progress via two mechanisms described Kim [71].

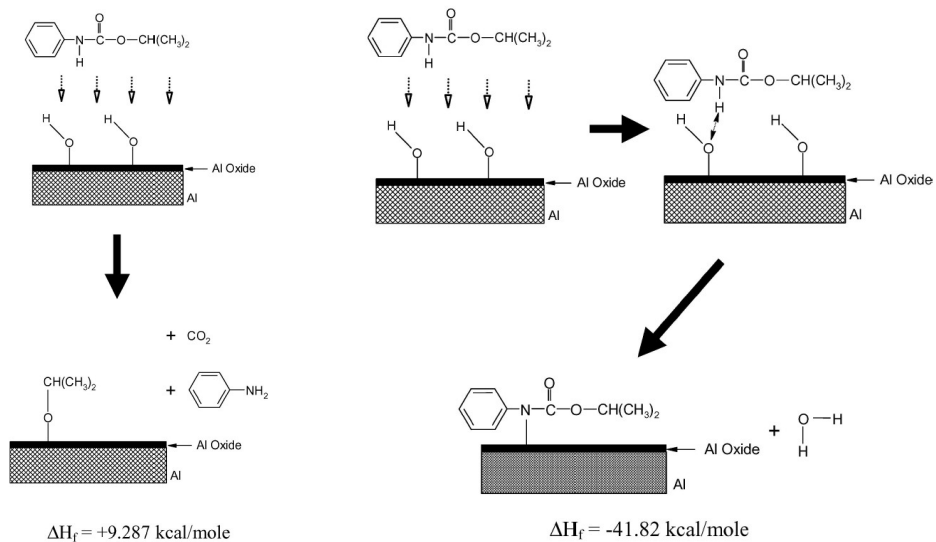
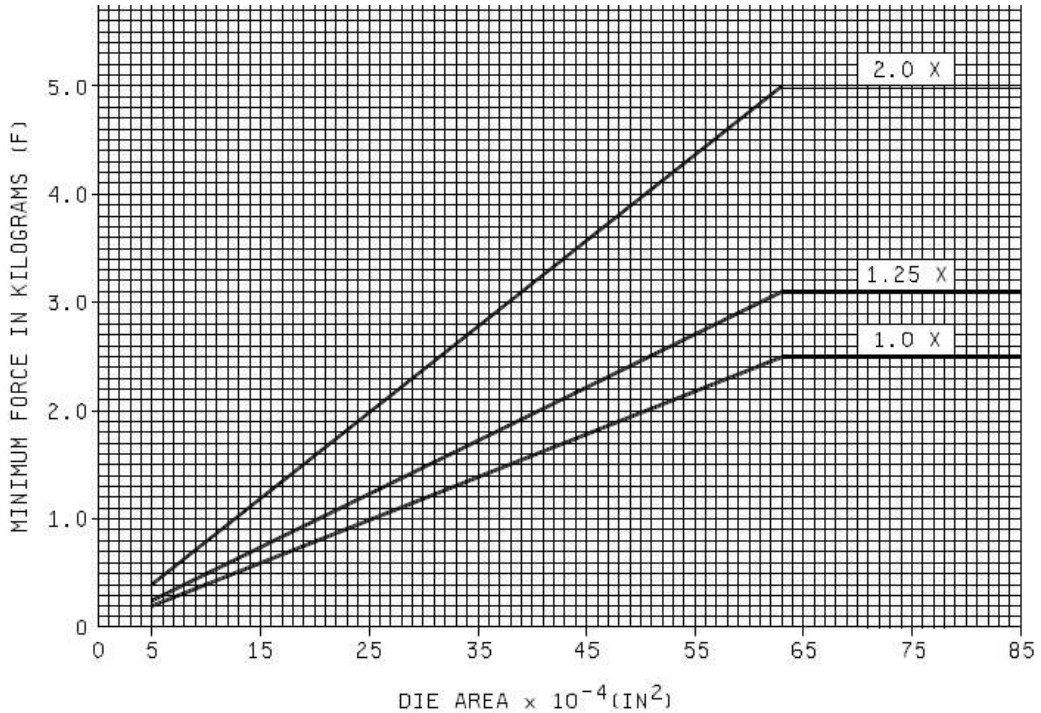


Figure C2.1: Bonding mechanisms of urethane to aluminium by Kim [71].

Two mechanisms of bonding between urethane and aluminium oxide: endothermic reaction evolving CO_2 and amine (Left) Exothermic condensation reaction evolving water (Right) by Kim [71].

Appendix D: MIL-STD-883K required attachment strength.



NOTES:

1. All die area larger than 64×10^{-4} (IN)² shall withstand a minimum force of 2.5 kg or a multiple thereof (see 3.2).
2. All die area smaller than 5×10^{-4} (IN)² shall withstand a minimum force (1.0X) of $0.04 \text{ kg}/10^{-4}$ (IN)² or a minimum force (2X) of $0.08 \text{ kg}/10^{-4}$ (IN)².

FIGURE 2019-4. Die shear strength criteria (minimum force versus die attach area).

Figure D1.1: Extract from standard MIL-STD-883K showing the required attachment strength according to contact area of the package.

The MIL-STD-883 test pieces used in the current study had a cross-sectional area of 5.1 mm^2 and therefore are required to withstand an upper limit of 49N.

Appendix E: Securing substrates to a build platform

Different methods to adhere glass and silicon substrates to the aluminium build platform of the Form 2 machine were considered. Initially two thin strips of tape approximately 7mm wide, with adhesive on both sides were placed onto the glass substrate (figure E1.1) which was then positioned with the taped face in contact with the build platform. This would allow the strips of tape to be easily cut with a blade from the side of the slide. First attempts found the tape would not adhere to the build platform. This was attributed to residual resin. Consequently, the platform was cleaned with acetone and the tape was found to adhere well. However, resin would seep between the slide and the build platform, and due to the transparency of the glass slide, would cure when exposed to the UV laser. This made the glass slide difficult to remove.

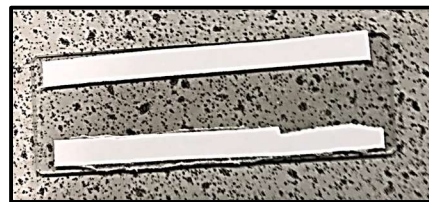


Figure E1.1: Slide with thin strips of tape attached.

A full strip of tape approximately 2mm narrower than the width of the slide was tried with the aim of preventing the seepage of resin between the platform and the slide. However, the resin still cured around the periphery of the tape, between the substrate and the build platform. Moreover, the tape is porous allowing for seepage of resin and curing during building. These slides were found to be significantly more difficult to remove than when adhered with thin strips (Fig. E1).

The glass was then secured on to the build platform by applying tape over the top surface of the glass slide. This combination was found easier to remove than the previous methods discussed due to resin being prevented from seeping between the substrate and the platform.

Subsequently, two glass slides were secured to the build platform using silicone. This was applied some days before use to allow time to cure and worked well with the glass slides being easy to remove using a blade.

Consideration was given to constructing a dedicated bracket to affix to the build platform to allow wafers to be slid in and out. However, affixing a bracket to the build platform into which a wafer could be located would be difficult for the following reasons:

- Some margin would need to be allowed in the z-axis to allow the wafer to be inserted into the mouth of the bracket. This is likely to result in some vertical movement of the wafer and allow seepage of resin between the wafer and the build platform, necessitating the bracket to have a spring mounting;
- Any bracket underarms supporting the wafer, would contact the upper surface of the resin tank and thereby introduce clash if greater than one layer thickness. The layer thickness would then be dictated by the dimensions of the bracket arms which would have to be less than 100 μ m and susceptible to breakage.
- Rubber banding was also considered; however these would not be sufficiently secure to withstand the stresses applied between layers when separating a build from the resin tank.

After reviewing the above methods, the use of electrical tape was chosen to affix substrates the build platform (Fig. E1.2).

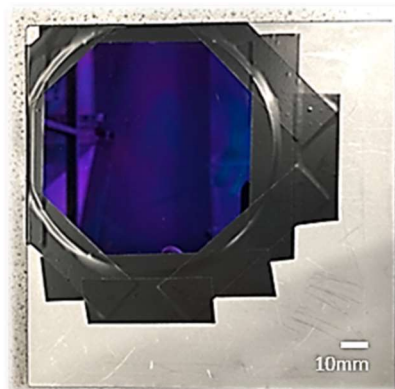


Figure E1.2: Wafer attached to the Form 2 build platform using electrical tape.

Appendix F: Form 1 default control logic

[perimeter]

basexyfeedrate = 800 ; Laser speed in mm/s for the perimeter of the base

baselaserpowermw = 49 ; Laser power in mW used for the perimeter of the base

modelxyfeedrate = 800 ; Laser speed in mm/s for the perimeter of the model.

modellaserpowermw = 48 ; Laser power in mW for the perimeter of the model (max: 62 mW for Form 1+)

supportxyfeedrate = 800 ; Laser speed in mm/s for the perimeter of the supports.

supportlaserpowermw = 53 ; Laser power in mW for the perimeter of the supports. (Max: 62 mW for Form 1+)

[PrintSettings]

SliceHeight = 0.1 ; The layer thickness in mm.

ScanlineSpacing = 0.09 ; Spacing of fill lines in mm.

InnerBoundaryOffset = 0.12

OuterBoundaryOffset = 0.03; Offset from model perimeter to outermost outline in mm

Xcorrectionfactor = 1.008 ; Scale factor for the x axis to account for shrinkage.
Ycorrectionfactor = 1.008 ; Scale factor for the y axis to account for shrinkage.
ScanlineBoundaryOffset = 0.03 ; Offset in mm from the innermost outline to the boundary of the fill. If this is zero, the fill touches the innermost outline; if this is positive it does not; if this is negative, the fill overlaps at least the inner outline.
OffsetsNum = 3 ; Number of outlines to draw. min: 0; max: unlimited

[Overview]

MaterialName = Clear

[laserRoutine]

firstlayerpasses = 10 ; The number of laser passes to do for layer 0 to attach to the build platform.

otherlayerpasses = 1 ; The number of laser passes to do for most layers

earlylayerpasses = 2 ; The number of laser passes to do for early layers as defined by earlytimesexpose.

[btwnLayerRoutine]

earlytimesexpose = 50 ; The number of layers that will be exposed earlylayerpasses times (excluding layer 0). That is, if earlytimesexpose is 3 and earlylayerpasses is 2, layer 0 will get firstlayerpasses passes, layer 1 and 2 will get 2 passes, and subsequent layers will get otherlayerpasses passes.

postlasercurewait = 1 ; Duration in seconds to wait from when the laser turns off until the motors start to move.

earlytimespeel = 22 ; The number of layers for which the p1 moves will be done. These are typically slower moves.

p1downvel = 1 ; Initial tilt speed in mm/s (at the tilt motor).

p1downmove = 10 ; Initial tilt distance in mm.

p1upvel = 4 ; Velocity of p1upmove in mm/s.

p1upmove = -10 ; Tilt up-move displacement in mm (should be negative).

p1upslowvel = 10 ; Velocity for p1upslowmove in mm/s.

p1upslowmove = -0.5 ; Additional up move in mm to overdrive into the hard stop. (Should be negative or zero.)

p2downvel = 1.5 ; Velocity of p2downmove in mm/s.

p2downmove = 7.5 ; After earlytimespeel, tilt distance in mm.

p2upvel = 10 ; Speed of p2upmove in mm/s.

p2upmove = -7.5 ; After earlytimespeel, un-tilt distance in mm. (should be negative.)

p2upslowvel = 10 ; Speed of p2upslowmove in mm/s.

p2upslowmove = -0.1 ; After earlytimespeel, overdrive distance into hard stop in mm. (Should be negative or zero.)

squishwaitmin_s = 0.25 ; Low end of the time in seconds we wait between finishing squishing and turning on the laser.

squishwaitmax_s = 2 ; High end of the time in seconds we wait between finishing squishing and turning on the laser.

[fill]

basexyfeedrate = 1500 ; Laser speed in mm/s used for filling the base (aka raft).

baselaserpowermw = 62 ; Laser power in mW used for filling the base (aka raft).

modelxyfeedrate = 1550 ; Laser speed in mm/s used for filling the model.

modellaserpowermw = 62 ; Laser power in mW for the model.

supportxyfeedrate = 1500 ; Laser speed in mm/s used for filling supports.

supportlaserpowermw = 62 ; Laser power in mW for filling supports.

Appendix G: Results data

7. Characterisation results data

The results of experimentation associated with characterisation of the photopolymer and substrate materials are shown below:

7.1 Elastic modulus

Elastic modulus (vertically built) tests to date (combined)			
Avg		GPa	Imperial (ksi)
0.394	Green (5-2-21)	0.38	55.6
	Green (18-2-21)	0.43	62.1
	Green (25-2-21)	0.34	48.7
	Green (26-2-21)	0.33	47.2
	Green (26-2-21)	0.43	62.1
	Green (9-3-21)	0.44	63.4
	Average	0.39	
0.56	4 mins post cure test 1 (5-2-21)	0.53	77.3
	4 mins post cure test 2 (5-2-21)	0.54	78.3
	4 mins (18-2-21)	0.56	81.3
	4 mins (26-2-21)	0.58	86.7
	4 mins (9-3-21)	0.59	85
	Average	0.56	
0.688	8 mins post cure test 1 (5-2-21)	0.68	99.2
	8 mins post cure test 2 (5-2-21)	0.68	98.9
	8 mins (25-2-21)	0.71	103.3
	8 mins (9-3-21)	0.69	99.8
	8 mins (23-3-21)	0.68	98.6
	Average	0.56	
0.712	15 mins (25-2-21)	0.67	97
	15 mins (25-2-21)	0.72	104
	15 mins (26-2-21)	0.75	109.2
	15 mins (26-2-21)	0.73	106
	15 mins (9-3-21)	0.69	100.7
	Average	0.69	
0.738	30 mins (18-2-21)	0.72	104.1
	30 mins (25-2-21)	0.74	106
	30 mins (26-2-21)	0.8	115.5
	30 mins (9-3-21)	0.73	106
	30 mins (9-3-21)	0.7	101.5
	Average	0.74	

Table G1.1: Change in elastic modulus with cure time.

7.2 Poisson's ratio and maximum force at break

Cure time (m)	Sample no.	Poisson's ratio	Avg Poisson's for cure time	Max breaking load for cure time (N)
0	1	0.42	0.41	462
0	2	0.40		
0	3	0.40		
4	1	0.39	0.38	1134
4	2	0.39		
4	3	0.38		
8	1	0.40	0.40	1302
8	2	0.42		
8	3	0.39		
12	1	0.38	0.40	1333
12	2	0.41		
12	3	0.40		
15	1	0.39	0.39	1326
15	2	0.39		
15	3	0.39		
		Average	0.40	

Table G1.2: Poisson's ratio and maximum force at break with cure time.

7.3 DSA results data

7.3.1 Pendant droplet results

FLC Pendant droplet IFT measurements					
Test no.	1	2	3	4	5
IFT (mJ/m ²)	30.39	29.42	30.53	29.09	30.2
Average IFT (mJ/m ²)	29.93				

Table G1.3: IFT calculation of Formlabs clear photopolymer using pendant drop shape.

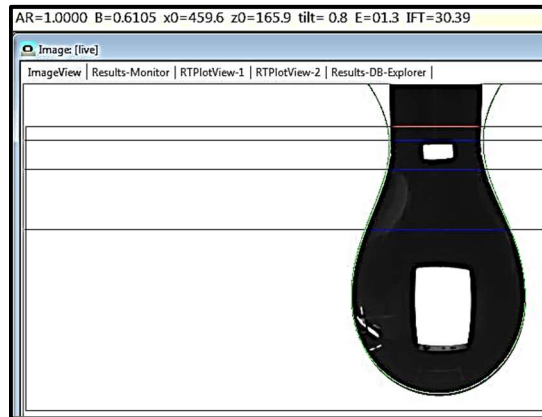


Figure G1.1: Pendant DSA test of FLC resin to determine IFT.

Water Pendant droplet IFT measurements					
Test no.	1	2	3	4	5
IFT (mJ/m ²)	71.81	73.18	72.77	72.66	71.36
Average IFT (mJ/m ²)	72.36				

Table G1.4: IFT calculation of water using pendant drop shape.

7.3.2 Contact angle results

Material	Water	
Substrate	Glass	
Pendant droplet IFT	72.36 mJ/m ²	
Sessile drop contact angle		
Test no.	Left contact angle	Right contact angle
1	31.3	32.2
2	31.5	32.3
3	30.2	30.0
4	32.9	33.1
5	31.5	32.0
Avg (L+R) =	31.75	

Table G1.5: Contact angle of FLC on glass

Material	FLC	
Substrate	Glass	
Pendant droplet IFT	29.93 mJ/m ²	
Sessile drop contact angle		
Test no.	Left contact angle	Right contact angle
1	33.7	33.2
2	33.2	33.7
3	36.3	37.3
4	35.6	36.4
5	36.3	36.2
Avg (L+R) =	35.2	

Table G1.6: Contact angle of FLC on glass

Material	Water	
Substrate	Si ₃ N ₄ wafer	
Pendant droplet IFT	72.36 mJ/m ²	
Sessile drop contact angle		
Test no.	Left contact angle	Right contact angle
1	43.2	43.2
2	43.8	43.8
3	43.2	43.2
4	44.7	44.7
5	43.89	43.89
Avg (L+R) =	43.76	

Table G1.7: Contact angle of water on a Si₃N₄ wafer

Material	Formlabs' clear photopolymer	
Substrate	Si ₃ N ₄ wafer	
Pendant droplet IFT	29.93 mJ/m ²	
Sessile drop contact angle		
Test no.	Left contact angle	Right contact angle
1	31.8	30.8
2	31.3	30.6
3	32.5	30.8
4	31.7	28.9
5	31.4	30.6
Avg (L+R) =	31.04	

Table G1.8: Contact angle of Formlabs' clear photopolymer on a Si₃N₄ wafer

Material	Formlabs' clear photopolymer
Substrate	Si ₃ N ₄ wafer
Pendant droplet IFT	29.93 mJ/m ²
Sessile drop contact angle	
Test no.	Contact angle
1	13.3
2	12.7
3	14.9
4	14.6
5	14.3
Avg =	31.04
STDV =	0.24

Table G1.9: Contact angle of Formlabs' clear photopolymer on PC washed with IPA.

Material	Formlabs' clear photopolymer
Substrate	Si ₃ N ₄ wafer
Pendant droplet IFT	29.93 mJ/m ²
Sessile drop contact angle	
Test no.	Contact angle
1	12.0
2	10.5
3	10.8
4	11.3
5	11.4
Avg =	11.2
STDV =	0.58

Table G1.10: Contact angle of Formlabs' clear resin on aluminium washed with acetone and IPA.

7.3.3 Surface free energy results

Green sample SLA slabs					
	Contact angle				
Sample no	1	2	3	4	5
Ethylene glycol	40.0	36.9	33.9	36.0	34.8
Deionised Water	62.9	61.2	62.2	59.5	59.3
SE-P (Surface)	24.5	25.1	19.6	28.5	27.6
SE-D (Surface)	14.1	14.8	20.4	13.0	13.9
SFE	40.3	40.0	40.0	41.5	41.6
Average SFE	40.93	Standard deviation			1.15

Table G1.11: Surface energy of green SLA slabs.

SLA slabs after 4 minutes of post build curing						
	Contact angle					
Sample no	1	2	3	4	5	6
Ethylene glycol	39.7	36.9	33.9	39.7	37.5	39.4
Deionised Water	60.0	61.2	62.2	65.2	64.2	64.3
SE-P (Surface)	31.9	25.1	19.62	18.6	18.6	20.3
SE-D (Surface)	9.9	14.8	20.39	18.9	19.8	17.5
SFE	41.74	39.96	40.01	37.43	38.4	37.8
Average SFE	39.39	Standard deviation			1.75	

Table G1.12: Surface energy of SLA slabs after 4 minutes of post build curing.

SLA slabs after 8 minutes of post build curing								
	Contact angle							
Sample no	1	2	3	4	5	6	7	8
Ethylene glycol	42.6	37.1	39.6	41.6	38.2	39.5	35.7	33.0
Deionised Water	65.5	60.4	62.1	65.1	62.5	58.5	58.4	57.6
SE-P (Surface)	21.1	27.4	26.0	20.9	23.35	35.0	31.1	30.1
SE-D (Surface)	15.5	13.2	13.2	16.1	15.6	8.5	11.6	13
SFE	36.6	40.7	39.3	37.0	39.0	43.5	42.7	43.1
Average SFE	40.21	Standard deviation			2.73			

Table G1.13: Surface energy of SLA slabs after 8 minutes of post build curing

SLA slabs after 12 minutes of post build curing						
	Contact angle					
Sample no	1	2	3	4	5	6
Ethylene glycol	40.4	36.4	36.1	37.5	38.7	41
Deionised Water	59.8	63.1	62.8	67.6	65.9	66.2
SE-P (Surface)	33.4	20.0	20.4	11.7	16.1	17.7
SE-D (Surface)	8.91	19.0	18.8	27.6	21.8	19.1
SFE	42.3	39.0	39.2	39.3	37.8	36.8
Average SFE	39.07	Standard deviation			1.87	

Table G1.14: Surface energy of SLA slabs after 12 minutes of post build curing

SLA slabs after 15 minutes of post build curing									
	Contact angle								
Sample no	1	2	3	4	5	6	7	8	9
Ethylene glycol	34.7	37.2	39.1	33.7	36.3	36.2	32.1	31.5	30.3
Deionised Water	62	60.9	59.6	61.4	56.3	61.6	59.8	58.5	57.1
SE-P (Surface)	20.9	26.3	32.2	21.3	37.9	23.4	23.5	26.2	38.5
SE-D (Surface)	19.0	14.0	9.9	19.0	8.1	16.4	17.8	16.0	14.8
SFE	39.8	40.2	42.1	40.3	46	39.7	41.3	42.2	43.4
Average SFE	41.67	Standard deviation			2.05				

Table G1.15: Surface energy of SLA slabs after 15 minutes of post build curing

Average SFE of all solidified polymer samples = 40.25 (STDV = 1.07)

SFE of aluminium				
	Contact angle			
Sample no	1	2	3	4
Ethylene glycol	51.7	41.2	42.6	42.3
Deionised Water	61.9	57.3	60	61.4
SE-P (Surface)	46.1	42.2	36.08	31.53
SE-D (Surface)	2.02	5.29	7.09	9.19
SFE	48.11	47.49	43.17	40.72
Average SFE	44.87	Standard deviation		3.53

Table G1.16: Surface energy of aluminium washed with acetone and IPA.

SFE of silicon nitride				
	Contact angle			
Sample no	1	2	3	4
Ethylene glycol	13.3	12.0	12.3	12.1
Deionised Water	43.2	43.8	43.2	44.7
SE-P (Surface)	52.23	49.75	51.62	47.28
SE-D (Surface)	7.12	8.10	7.41	9.03
SFE	59.34	57.85	59.04	56.30
Average SFE	58.13	Standard deviation		1.38

Table G1.17: Surface energy of a silicon nitride washed with acetone and IPA.

SFE of soda lime glass				
	Contact angle			
Sample no	1	2	3	4
Ethylene glycol	50.2	53.0	53.1	50.2
Deionised Water	68.5	66.5	67.6	64.3
SE-P (Surface)	23.39	33.49	30.35	35.4
SE-D (Surface)	10.68	5.01	6.15	5.15
SFE	34.08	38.49	38.5	40.55
Average SFE	37.41	Standard deviation		2.77

Table G1.18: Surface energy of a polycarbonate washed with IPA.

SFE of soda lime glass			
Sample no	Contact angle		
	1	2	3
Ethylene glycol	6.5	6.8	7.3
Deionised Water	28.5	29.4	27.6
SE-P (Surface)	90.16	88	92.37
SE-D (Surface)	0.52	0.67	0.39
SFE	90.68	88.67	92.78
Average SFE	90.70	Standard deviation	2.06

Table G1.19: Surface energy of a soda lime glass washed with acetone and IPA.

7.4 FTIR

FTIR (Combined area of peaks at 1637cm ⁻¹ and 1407cm ⁻¹ and normalised to the area of the 1701cm ⁻¹ peak)						
Cure time (m)	Sample no.				Average	STDV
	1	2	3	4		
Liquid resin	10.38	9.02	9.95	9.74	9.77	0.57
0	8.56	8.22	8.81	8.08	8.42	0.33
4	7.54	7.95	7.31	7.81	8.18	0.43
8	7.95	7.31	7.81	7.93	7.75	0.30
12	6.93	8.17	7.65	7.59	7.59	0.51
15	7.89	7.53	7.08	7.29	7.45	0.35
30	7.27	6.97	7.86	7.21	7.32	0.38

Table G1.20: Combined area of FTIR peaks at 1637cm⁻¹ and 1407cm⁻¹ wavenumbers normalised to the area of the peak at wavenumber 1701cm⁻¹ (C=O).

FTIR with increasing hatch spacing. Combined area of peaks at 1637cm ⁻¹ and 1407cm ⁻¹ and normalised to the area of the 1701cm ⁻¹ peak			
Hatch spacing (mm)	Combined Area (1637 + 1407)	Average area	STDV
0.02	7.4		
0.02	6.56		
0.02	7.26		
0.02	7.18	7.1	0.37
0.05	6.25		
0.05	8.07	7.16	1.29
0.1	8.51		
0.1	9.52	9.015	0.71
0.2	5.89		
0.2	8.41	7.15	1.78
0.4	8.7		
0.4	9.98		
0.4	7.65	8.78	1.17
0.6	10.39		
0.6	9.83	10.11	0.40

Table G1.21: FTIR measurements with increasing hatch spacing.

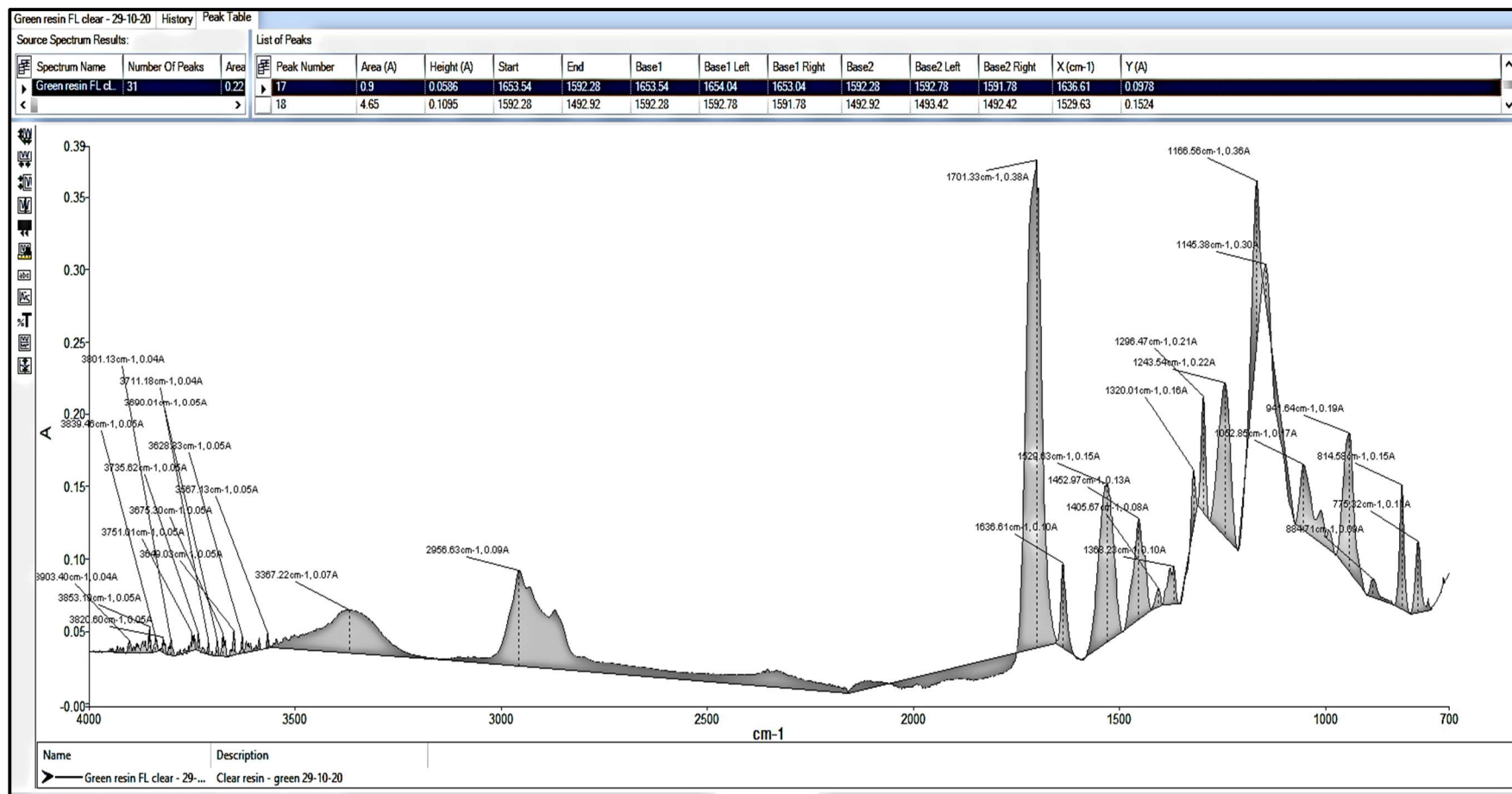


Figure G1.2: Example absorbance vs wavenumber profile for Formlabs' clear photopolymer

7.5 Adhesion results data

Raw data and additional supporting experimental results pertaining to the adhesion investigation are included below.

7.5.1 Tensile adhesion tests (Texture analyser)

Aluminium cured on frame 1mm ² test piece																
Cure time (m)	Separation force (N)														Average	STDV
0	15.2	11.2	10.1	13.1	11.4	14.1	14.0	13.3	13.0	12.7	13.0	14.3	13.1	9.9	8.61	4.2
0	11.9	2.9	4.2	7.3	4.0	6.7										
4	31	35.9	31	28.1	21.8	41.7	41.8	48.7	41.5	42.85	44.57	47.28	27.96	31.5	37.36	7.62
4	40.2	33.3	40.4	39.5	48.1	28.1										
6	30.4	29.9	37.2	33.3	18.5	22.9	24.3	22.2	11.8	16.1	0.9	1.1	0.7	17.6	19.09	11.86
6	2.2	10.1	22.8	32.9	27.9											
8	1.8	1	1.1	1.4	5.06	5.05	4.86	7.17	4.63	1.3	0.5	2.25	0.64	9.5	13.85	19.75
8	1.6	0.2	50.0	39.6	42.2	39.8	46.5	1.1	3.3	4.0	1.4	57.3	52.3	2.3		
10	32.4	41.6	37.3	30.8	45.9	42.1	53.3	34.8	33.8	38.2	30.4	37.5	29.4	40.6	36.15	7.16
10	25.6	26.4	34.5													
12	34.2	55.4	74.6	56.4	55.5	40.2	59.2	51.1	41.7	45.1	53.7	50.9	32.7	50.1	47.17	12.31
12	48.8	39.9	45.8	44	43.8	58.1										
15	37.9	36.2	40.2	48.8	41.1										40.84	4.85

Table G1.22: Tensile adhesion test separation force on aluminium.

Polycarbonate cured on frame 1mm ² test piece																
Cure time (m)	Separation force (N)														Average	STDV
0	8.21	8.75	6.62	7											7.65	1.00
4	27	21.9	10.8	18.6	21.6	17.6	18.3	17.7	19.8	22.1					19.54	4.19
6	4.7	4.8	3.4	5.9	3.3	20.5	28.3	35.7							13.33	12.97
8	15.9	40.5	42.4	17.9	9.5	10.1	6.5	1.4	2.7	2.0	3.4	2.6	1.8	12.05	14.12	
10	12.6	11.1	4.2	1.5	1.9	1.9	1.9	1.9	1.6	16.5	18.3	7.0	33.2	9.31	9.69	
12	3.3	2.5	2.2	2.7	1.7	2.3	1.2								2.27	0.68
15	1.9	11.3	14.7	20.2	13.6	13.8	9.7								12.17	5.60

Table G1.23: Tensile adhesion test separation force on polycarbonate.

Separation force of 1mm ² tensile test pieces on untreated silicon nitride							
Cure time (m)	Separation force (N)					Average (N)	STDV
0	6.68	8.16	8.55			7.80	0.99
4	25.57	18.94	17.43	16.74		19.67	4.04
8	26.83	28.28	21.75	22.39		24.81	3.23

Table G1.24.1: Tensile adhesion test separation force on untreated silicon nitride

Separation force of 1mm ² tensile test pieces on treated silicon nitride							
Cure time (m)	Separation force (N)					Average (N)	STDV
0	14.72	11.12	11.93			12.59	1.89
4	37.01	31.48	36.12	36.31		35.23	2.53
8	44.74	44.99	46.65	44.48	42.57	44.69	1.46

Table G1.24.2: Tensile adhesion test separation force on treated silicon nitride.

7.5.2 Shear test data

Separation force of frustum shear test pieces on silicon nitride					
Cure time (m)	Separation force (N)			Average (N)	STDV
0	2.46	11.73	20.66	11.62	9.1
2	77.61	65.21		71.41	8.77
8	153.81	93.67	86.53	111.34	36.96
15	97.67	102.24	166.32	122.04	38.32

Table G1.25: Separation force for frustum test pieces constructed onto silicon nitride.

Separation force of frustum shear test pieces on silicon nitride								
Cure time (m)	Separation force (N)						Average (N)	STDV
0	1.3	0.56	3.3	1.3	17.5	2.9	4.5	6.4
2	69.6	74.0	48.2				63.9	13.8
4	42.8	81.5	36.5				53.6	24.4
8	79.3	46.27	40.21				55.27	21.1
15	35.53	58.82	61.51				51.95	14.3
30	35.18	38.44	31.8				35.1	3.3

Table G1.26: Separation force of frustum shear test piece on polycarbonate.

Separation force of MIL-STD-883K shear test pieces on untreated silicon nitride					
Cure time (m)	Separation force (N)			Average (N)	STDV
0	2.47	5.7	1.83	3.33	2.07
2	8.97	13.41	5.3	9.23	4.06
8	18.05	25.35	11.31	18.24	7.02

Table G1.27.1: Separation force of MIL-STD-883K shear test pieces on silicon nitride

Separation force of MIL-STD-883K shear test pieces on treated silicon nitride					
Cure time (m)	Separation force (N)			Average (N)	STDV
0	21.96	38.58	39.62	33.39	9.91
2	62.3	113.3	87.1	87.57	25.50
8	91.3	86.06	102.6	93.32	8.45

Table G1.27.2: Separation force of MIL-STD-883K shear test pieces on treated silicon nitride

Separation force of frustum shear test piece on glass with standard and varied exposure.					
	Separation force (N)			Average (N)	STDV
Standard exposure	259.18	221.14	227.65	235.99	20.35
Varied exposure	227.30	46.20	139.73	137.74	90.57

Table G1.28: Separation force of frustum shear test piece on glass with standard and varied exposure.

7.5.3 Shrinkage measurements

The shrinkage of standalone test pieces measured manually using the method described in section 3.4.2.8 and used for comparison with the compensated strain in section 5.2.7.1, are included in Tables G1.29 to G1.31.

Measured length and shrinkage (mm) for sample 1												
Cure time / measurement no.	0	2	4	8	12	15	20	25	30	35	40	45
1	24.14	24.09	24.05	24.05	24.04	24.1	23.99	24.05	24.02	24.05	24.07	24.03
2	24.13	24.07	24.06	24.03	24.01	24.05	24.02	24.05	23.99	24.05	24.06	24.02
3	24.11	24.11	24.08	24.05	24.02	24.02	24.01	24.02	23.99	24.06	24.06	24.01
4	24.17	24.13	24.05	24.07	24.02	24.05	24.02	24.07	24.03	24.07	24.06	24.02
5	24.17	24.1	24.06	24.04	24.03	24.05	24.01	24.06	24.03	24.05	24.07	24.04
Average	24.14	24.10	24.06	24.05	24.02	24.05	24.01	24.05	24.01	24.06	24.06	24.02
STDV	0.0261	0.0224	0.0122	0.0148	0.0114	0.0288	0.0122	0.0187	0.0205	0.0089	0.0055	0.0114
Shrinkage absolute (mm)		0.066	0.106	0.118	0.142	0.112	0.156	0.116	0.154	0.11	0.102	0.142

Table G1.29: Measured absolute shrinkage sample 1.

Measured length and shrinkage (mm) for sample 2												
Cure time / measurement no.	0	2	4	8	12	15	20	25	30	35	40	45
1	24.16	24.11	24.07	24.08	24.08	24.06	24.07	24.03	23.99	23.99	24.03	24.04
2	24.16	24.14	24.05	24.11	24.09	24.08	24.09	24.09	24.08	24.08	24.06	24.07
3	24.18	24.09	24.06	24.12	24.09	24.11	24.08	24.07	24.08	24.04	24.06	24.03
4	24.16	24.06	24.07	24.10	24.07	24.07	24.10	24.03	24.06	23.97	24.04	24.06
5	24.17	24.09	24.08	24.05	24.08	24.07	24.08	24.00	24.05	24.03	24.06	24.04
Average	24.17	24.10	24.07	24.09	24.08	24.08	24.08	24.04	24.05	24.02	24.05	24.05
STDV	0.0089	0.0295	0.0114	0.0277	0.0084	0.0192	0.0114	0.0358	0.0370	0.0432	0.0141	0.0164
Shrinkage absolute (mm)	0	0.068	0.1	0.074	0.084	0.088	0.082	0.122	0.114	0.144	0.116	0.118

Table G1.30: Measured absolute shrinkage sample 2.

Average measured length and shrinkage of samples (mm) 1 and 2.												
Cure time	0	2	4	8	12	15	20	25	30	35	40	45
Average length	24.16	24.10	24.06	24.07	24.05	24.07	24.05	24.05	24.03	24.04	24.06	24.04
STDV	0.022	0.025	0.012	0.031	0.032	0.026	0.041	0.027	0.035	0.034	0.013	0.018
Shrinkage absolute (mm)	0.000	0.067	0.103	0.096	0.113	0.100	0.119	0.119	0.134	0.127	0.109	0.130
Percentage of original length	0.00	0.23	0.38	0.35	0.42	0.37	0.45	0.45	0.51	0.48	0.41	0.49
STDV (% of orig length)	0.000	0.128	0.112	0.114	0.108	0.098	0.143	0.121	0.107	0.182	0.108	0.086

Table G1.31: Average of samples 1 and 2.

Ratio of manually measured shrinkage to recorded strain (gauge) with cure time	
Cure time (minutes)	Ratio of percentage measured shrinkage to recorded strain (gauge)
2	1.29×10^{-4}
4	1.55×10^{-4}
8	1.12×10^{-4}
12	1.34×10^{-4}
15	1.13×10^{-4}
20	1.36×10^{-4}
Standard deviation =	1.51×10^{-5}

Table G1.32: Ratio of manually measured shrinkage to recorded strain (gauge) with cure time.

7.5.4 Application of the shrinkage coefficient to uncompensated gauge readings

Using the same calibration process and manually measuring the shrinkage before and after each strain test shrinkage, the individual, and average (corrected) percentage strain profiles were generated for PBC without temperature compensation in Figure G1.3.

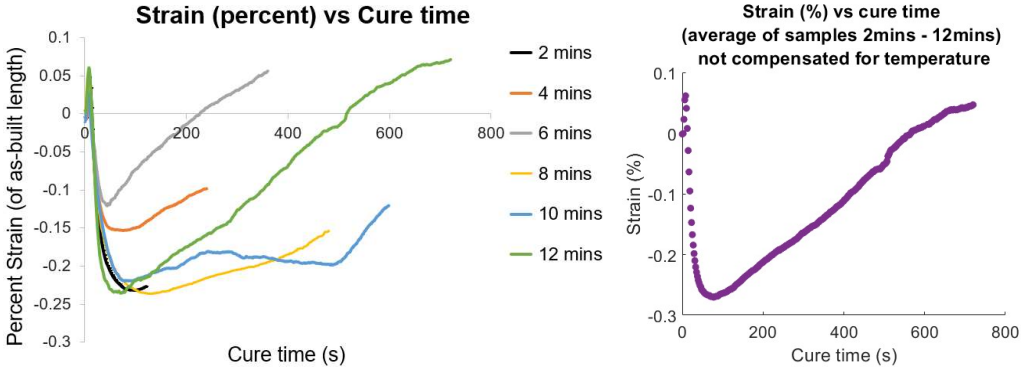
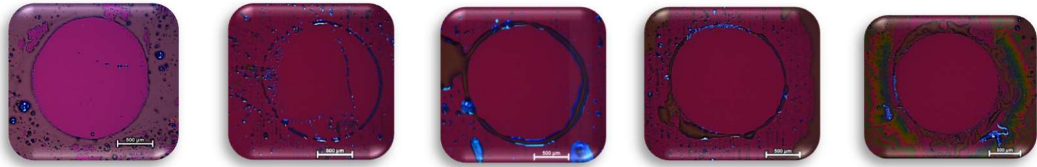


Figure G1.3: Uncompensated strain profiles

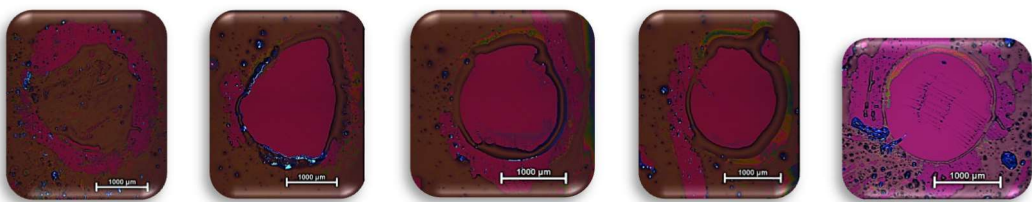
[Left] Strain (percent calibrated against measured as-built length) vs cure time for samples after different periods of cure. [Right] Average (corrected) strain (%) vs cure time for samples 2 mins - 12 min.

7.5.5 Tensile test footprints on untreated substrates.

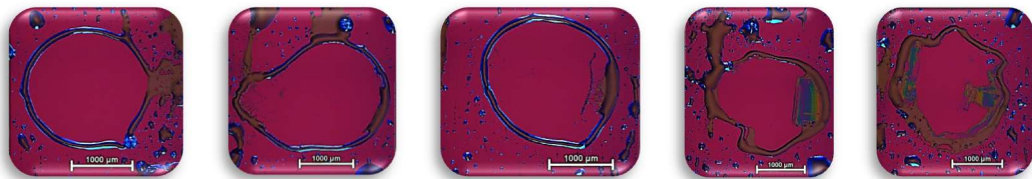
Further optical microscope images of the residue retained on untreated silicon nitride following tensile tests, after increasing periods of PBC are shown below.



Above: Footprint of green (no PBC) tensile test pieces on untreated substrate (500μm scalebars).



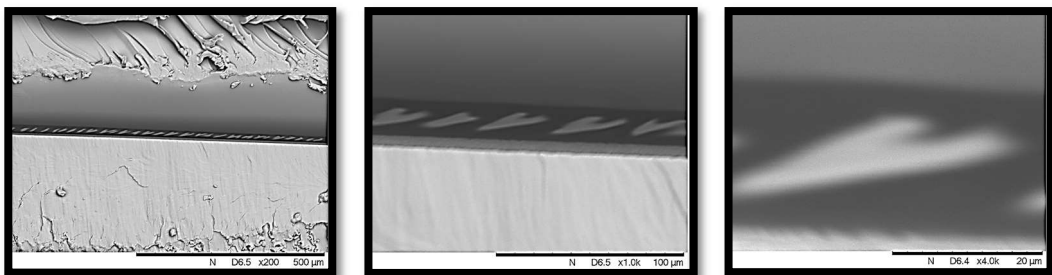
Above: Footprint of tensile test pieces on untreated substrate after 2 mins of curing (1000μm scalebars).



Above: Footprint of tensile test pieces on untreated substrate after 8 mins of curing (1000μm scale bars)

7.5.6 SEM images of a sectioned SLA-substrate interface.

SEM images in addition to those shown in section 4.2.5 of the sectioned interface between an SLA slab and polycarbonate are shown below.



Above: SEM images of SLA sample 2 interface (profile view) with SLA onto of PC (500x, 1000x and 4000x magnification from top left to right)

Appendix H: Model inputs and outputs

8. Reflectance and Refraction Model Inputs

Input	Default Value
Machine parameters	
Laser[42] operating wavelength	405nm
Form 2 Laser[182] spot size (FWHM)	140 μ m
Form 1+ Laser[182] spot size (FWHM)	155 μ m
Resin tank thickness	2mm
Refractive[183] index of Formlabs' (acrylic) resin tank	1.5
Extinction[147] coefficient of Formlabs' (acrylic) resin tank	5×10^{-8}
Refractive[147] index of Formlabs' glass window (@405nm)	1.53
Extinction[184] coefficient of glass window	9.055×10^{-9}
Refractive[147][54] index of air (@405nm)	1.53
Extinction coefficient of air	0
Form 1 laser power at print plane	From calibration process
Form 2 laser power at print plane	From calibration process
Hatch spacing	0.09 mm (Form 1)
Scan speed	800mm/s (Form 1)
First layer scans	10 (Form 1)
Layer thickness	100 μ m
Machine geometry	
Form 1 Build area	130mm x 130mm
Form 2 Build area	140mm x 140mm
Mirror dimensions	125mm x 105mm
Mirror angle to the horizontal	0.88 radians
Distance of centre of mirror to the build area	110mm
Distance of the centre of the mirror to the galvanometer mirror	190mm
Photopolymer properties	
Refractive index [185] of Formlabs' clear photopolymer	1.54
Penetration [50] depth (D_p)	192 μ m
Critical [50] energy of cure (E_c)	12.6mJ/cm
Silicon nitride	
Refractive index [147] of silicon nitride	2.1
RMS Surface roughness	0.001 μ m

Reflectance and Refraction Model Outputs

Media 1 = Air

Media 2 = Window beneath the resin tank

Media 3 = Resin tank base

Media 4 = Photopolymer

Media 5 = Silicon nitride wafer

Parameter	Units
The maximum power reflected from the interface at media 1/2:	mW/cm ²
The maximum power transmitted into media 2:	mW/cm ²
The maximum power attenuated through media 2 is:	mW/cm ²
The maximum power reflected from the interface at media 2/3:	mW/cm ²
The maximum transmitted power into media 3:	mW/cm ²
The maximum attenuated power through media 3:	mW/cm ²
The maximum power reflected from the interface at media 3/4:	mW/cm ²
The maximum power transmitted into media 4:	mW/cm ²
The maximum power attenuated through media 4:	mW/cm ²
The maximum power incident on media 5 wafer:	mW/cm ²
The maximum power reflected from media 5 wafer from a single pass:	mW/cm ²
Magnitude of potential spurious curing from reflectance of a single pass (without superposition) from surface 5:	μm
The maximum power reflected from media 5 wafer with superposition:	mW/cm ²
Magnitude of potential spurious curing from reflectance with superposition from surface 5:	μm
Magnitude of potential spurious curing from reflectance with superposition and repeat first layer passes from surface 5:	μm

Appendix I: Supporting diagrams.

11. Example images of drop shape analysis.

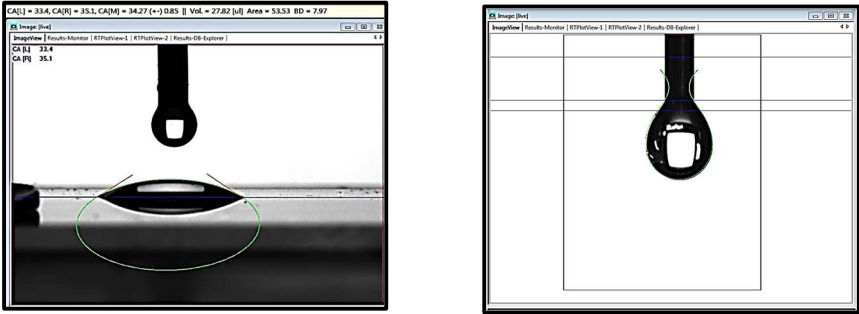


Figure I1 Example images of sessile (left) and pendent (right) droplet measurement.

12. CAD diagram of two-piece bespoke mounting bracket for adhesion shear test.

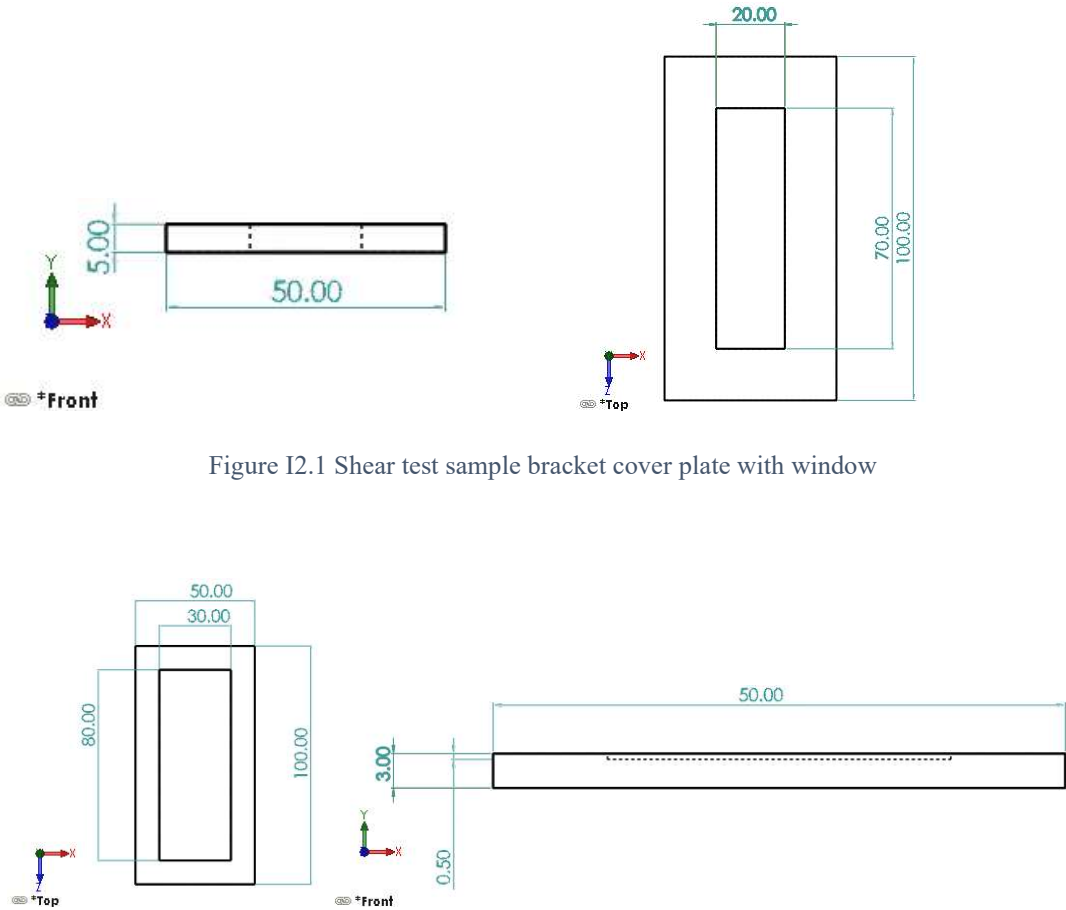


Figure I2.1 Shear test sample bracket cover plate with window

Figure I2.2 Shear test bracket back plate with recess.

I3. Wiring diagrams for strain sensors.

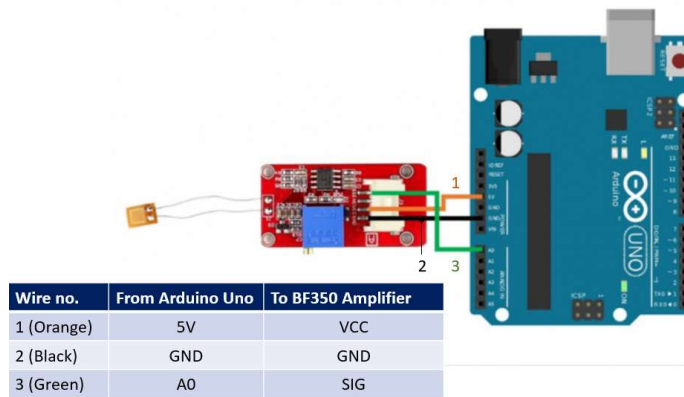


Figure I3.1: Wiring [168] schematic diagram for connecting a strain gauge and 3-pin amplifier module [186] to an Arduino Uno processor.

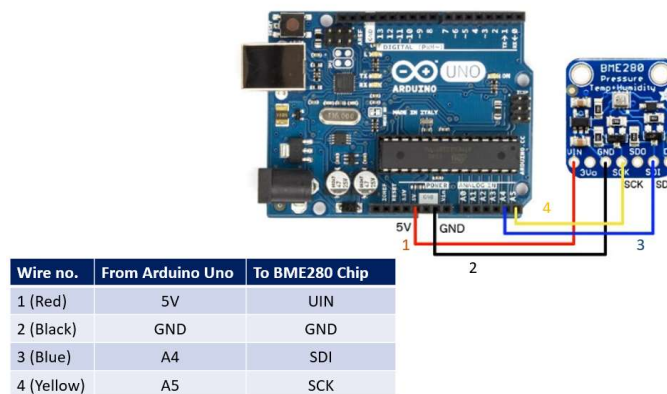


Figure I3.2: Wiring schematic diagram [168] for connecting BME280 chip [187] to Arduino Uno processor.

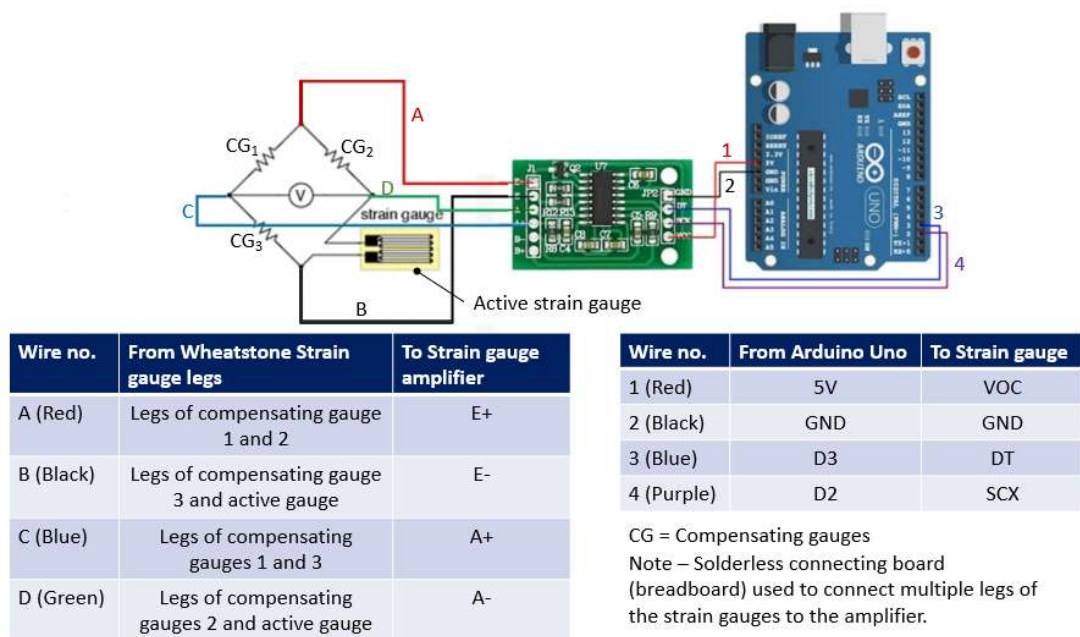


Figure I3.3: Wiring schematic diagram [168] for connecting a strain gauge and 4-pin amplifier module with Wheatstone bridge [188] to an Arduino Uno processor.

Breadboard connections

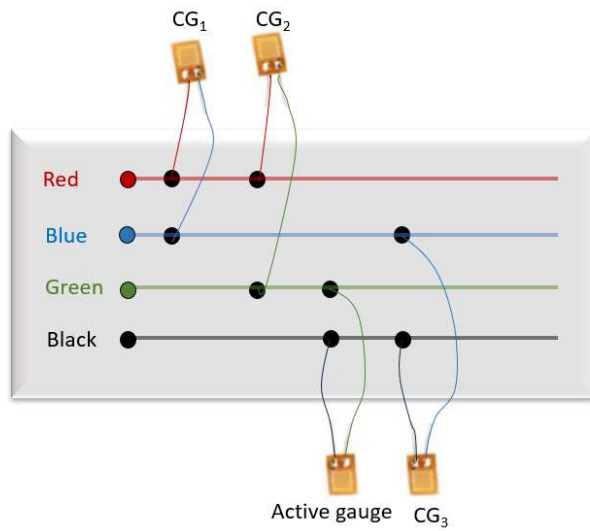


Figure I3.4 Breadboard connections between strain gauges and the amplifier.

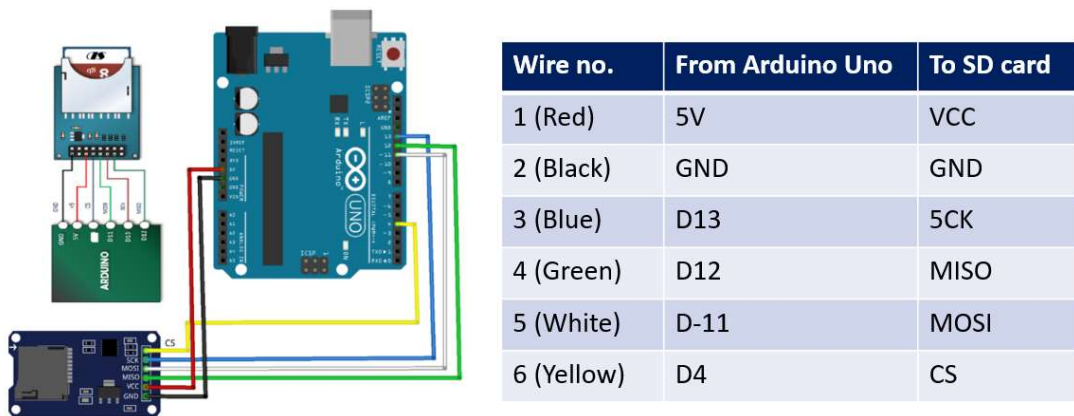


Figure I3.5: Wiring schematic diagram [29] for connecting an SD card for data logging to an Arduino Uno processor.

Appendix J: MATLAB scripts

Table of scripts

Note: The scripts are separated into two series; A and B. Each series are written to be run sequentially; they will not run out of sequence.

Script	Name	Comment
A1	Distortion with divergence and ellipticity.	Calculation of the magnitude of distortion due to divergence and ellipticity.
A2	Characterisation of distortion profiles.	Characterisation of the distorted beam profiles combined with the influence of superposition.
A3	Identification of operating window.	Applies the exposure limits for distorting effect for compliance with manufacturing tolerances to identify an operating window.
A4	Optimisation of SLA process and build time.	Reduces the hatch spacing to defined limits of variance in exposure with superposition and minimises build time.
B1	Refraction with Parabolic mirror.	Calculates the loss in accuracy due to refraction and the profile of a parabolic mirror to maintain a normal angle of incidence.
B2	Reflection	Calculates the magnitude of reflectance and the potential for lateral spurious curing, from a substrate with consideration to the SLA operating parameters, machine architecture, the refractive indices of the media within the light path and the properties of the substrate.

A1: Distortion with divergence and ellipticity

```
% Characterisation of SLA process
%
% Variables:
% Laser: FWHM = FWHM laser width,
% LP = Laser power at print plane,
% I0 = Peak intensity,
% I01D = The peak intensity of spot 1 diverged at the corner of the build
area
% I01DE = The peak intensity of diverged elliptical spot of beam 1 at the
corner of the build area
% AbI = Absolute intensity,
% APLS = Absolute Power through the laser spot
% FL = Focal length
% e2 = 1/e2 laser spot size
% WL = Wavelength in nm
% Emax0 = Maximum exposure
% EmaxD = Maximum exposure of diverged beam
% EmaxDE = Maximum exposure of diverged elliptical beam
%
% Minimum feature size (MFS):
% Rxy = Radius from the centre of the laser spot
% ResXY = XY MFS,
% ResZ = Z resolution,
% ReqRXY = Required MFS,
% ReqRZ = Required Z resolution
% BT = Build time
```

```

% RX = Radius in the X direction relative to the build platform centre,
% RY = radius in the Y dimension relative to the build platform centre.
% MBD = Maximum build diameter (based on laser focal length)
% TPLS = Total Proportion of the laser power through the laser spot
%
% REc = Radius of the laser spot with an intensity equal to the critical
cure energy of the resin
% MLTEc = Minimum cured line width
% Exp1 = Exposure according to scan speed 1
% RLT = Required layer thickness (microns)
% CLW0 = The cured line width based on the focussed beam properties
without divergence or ellipticity
% CLWD = The cured line width with divergence
% CLWDE = The cured line width with divergence and ellipticity
%
% Machine parameters:
% SS1 = Scan speed for profile 1,
% ST = Scan time
% HS = Line spacing,
% FLP = No. of first layer passes
%
% Resin properties:
% Ec = Critical cure energy
% Dp = Penetration depth,

clear all

% input the laser parameters
FWHM = input('Input laser FWHM spot size (microns): ');
LP = input('Input laser power (mW): ');
WL = input('laser wavelength (nm): ');

SS1 = input('Input scan speed (mm/s) default = 800: ');

% Enter the properties of the resin
Ec = input('Input the critical cure energy of the resin (mJ/cm^2): ');
Dp = input('Input the penetration depth of the resin (microns): ');

[RX,RY] = meshgrid(-600:5:600);
% Convert FWHM laser width to 1/e2 dimension (microns)
e2 = sqrt((FWHM^2)/(-2*log(0.5)));

% Calculate peak intensity from laser profile and power
I0 = LP*(2/(pi*(e2/10000)^2));

%Calculate the radius of the spot
Rxy = sqrt((RX.^2)+(RY.^2));

% Calculate the absolute intensity through the 1/e2 laser spot (Rxy) -
this is the beam intensity profile
AbI = I0.*exp((-2.*(Rxy./10000).^2)./(e2./10000)^2));
TPLS = exp((-2.*Rxy.^2)./(e2^2));

APLS = LP*(1-TPLS);

figure(1)
surf(RX,RY,AbI,'FaceLighting','gouraud',...
'MeshStyle','column',...
'SpecularColorReflectance',0,...

```

```

    'SpecularExponent',5,...
    'SpecularStrength',0.2,...
    'DiffuseStrength',1,...
    'AmbientStrength',0.4,...
    'AlignVertexCenters','on',...
    'LineWidth',0.2,...
    'FaceAlpha',0.25,...
    'FaceColor',[0.1 0.08 0.9],...
    'EdgeAlpha',0.4);
legend('Profile beam 1','Location','northeast')
title('Laser intensity vs Spot radius')
xlabel('Radius of laser spot (microns)')
zlabel('Intensity (mW/cm^{2})')

Emax0 = ((sqrt(2/pi))*((LP/1000)/(e2/1000000*SS1/1000)))*1000/100/100;
ST1 = Emax0/I0;
Exp1 = ST1.*AbI;

% Cured line width
CLW0 =
(sqrt(((log(sqrt(2/pi))*(LP/1000)/((e2/1000000)*(SS1/1000)*(Ec/1000*100*100
))))*((e2/1000000)^2))/2))*1000000*2;
fprintf('The cured line width and minimum achievable feature size for beam
profile 1 is: %.2f microns.\n',CLW0);

figure(2)
surf(RX,RY,Exp1,'FaceLighting','gouraud',...
'MeshStyle','column',...
'SpecularColorReflectance',0,...
'SpecularExponent',5,...
'SpecularStrength',0.2,...
'DiffuseStrength',1,...
'AmbientStrength',0.4,...
'AlignVertexCenters','on',...
'LineWidth',0.2,...
'FaceAlpha',0.25,...
'FaceColor',[0.1 0.08 0.9],...
'EdgeAlpha',0.4);
legend('Profile beam 1','Location','northeast')
title('Delivered exposure vs Spot radius')
xlabel('Radius of laser spot (microns)')
zlabel('Exposure (mJ/cm^{2})')

%Graph of Ec threshold
hold on
MEc = (RX-RX).*(RY-RY)+Ec;
surf(RX,RY,MEc,'LineWidth',0.1,...
'FaceAlpha',0.01,...
'EdgeAlpha',0.1,...
'FaceColor',[0.8,0.4,0.2]);
legend('Profile beam 1','Ec','Location','northeast')

CMP = input('Compare with a 2nd profile? (Y=1, N=0): ');
if CMP == 1
    FWHM2 = input('Input 2nd laser FWHM spot size (microns): ');
    LP2 = input('Input 2nd laser power (mW/cm^2): ');
    WL2 = input('laser wavelength (nm): ');

    %Enter 2nd resin properties

```



```

Ec2 = input('Input 2nd resin critical cure energy (mJ/cm^2): ');
Dp2 = input('Input 2nd resin penetration depth (microns): ');

%Enter the machine properties
SS2 = input('Input scan speed (mm/s) default = 800: ');

e22 = sqrt((FWHM2^2)/(-2*log(0.5)));

I02 = LP2*(2/(pi*(e22/10000)^2));

Rxy2 = sqrt((RX.^2)+(RY.^2));

AbI2 = I02.*exp((-2.*(Rxy2./10000).^2)./((e22/10000)^2));

TPLS2 = exp((-2.*Rxy2.^2)./(e22^2));

APLS2 = LP2*(1-TPLS2);
figure(1)
hold on
surf(RX,RY,AbI2,'SpecularExponent',1,...
     'SpecularStrength',1,...
     'DiffuseStrength',1,...
     'AmbientStrength',0.4,...
     'FaceColor',[1 0.4 0.6],...,
     'AlignVertexCenters','on',...
     'LineWidth',0.2,...
     'FaceAlpha',0.25,...
     'EdgeAlpha',0.4);
legend('Profile beam 1', 'Profile beam 2', 'Location', 'northeast')

% Emax for beam 2
Emax2 = ((sqrt(2/pi))*((LP2/1000)/(e22/1000000*SS2/1000)))*1000/100/100;

% Scan time beam 2
ST2 = Emax2/I02;

% Convert intensity to exposure for beam 2
Exp2 = AbI2.*ST2;

% Converting FWHM spot diameter to 1/Ec^2 radius
e22 = sqrt((FWHM2^2)/(-2*log(0.5)));

CLW2 =
(sqrt(((log(sqrt(2/pi))*(LP2/1000))/((e22/1000000)*(SS2/1000)*(Ec2/1000*100*
100))))*((e22/1000000)^2))/2))*1000000*2;
fprintf('The minimum line thickness and achievable feature size for beam
profile 2 is: %.2f microns.\n',CLW2);

figure(2)
hold on
surf(RX,RY,Exp2,'SpecularExponent',1,...
     'SpecularStrength',1,...
     'DiffuseStrength',1,...
     'AmbientStrength',0.4,...
     'FaceColor',[1 0.4 0.6],...,
     'AlignVertexCenters','on',...
     'FaceAlpha',0.25,...
     'LineWidth',0.2,...
     'EdgeAlpha',0.4);

```

```

legend ('Profile beam 1', 'Ec', 'Profile beam 2', 'Location', 'northeast')

elseif CMP == 0
    end

display ('Distortion due to laser profile 1 focal length')

% M2 = The M^2 laser beam quality 1 = a perfect beam
% M21YN indicates whether the M^2 laser quality is known
M21YN = input('Is the M^2 laser beam quality known? (Y = 1, N = 0)');
if M21YN == 1
    M2 = input('Input beam M^2 beam quality (1 = a perfect beam): ');
elseif M21YN == 0
    display ('The beam quality is assumed to be 1');
    M2 = 1;
end

% To calculate the distortion for given laser parameters and build area

% LPZ = Laser path length in Laser path length (to resin at centre of the
build platform).
% BASL = Build area (square) side length to be inputted in mm
% LPC = Total laser path length to the corner of the build area. Example
for a 130mm diameter square platform being =SQRT((65^2)+(65^2)) = 91.92mm
(opp). sqrt((91.92^2)+(250^2)) = 266.36
% ExtC = Extension to laser path to corner of the build area (LPC-LPZ)
% ExtE = Extension to the laser path to the edge of the build area (LPE-
LPZ)
% e2D = Diverged 1/e spot size in the corner of the build area
% PCISSD = The percentage increase in the laser spot size due to
divergence and the influence of focal length
% PCISSDE = The percentage increase in the laser spot size due to
divergence and ellipticity
% AbID = The absolute intensity of the laser spot at the extremity (i.e.,
in the corner) of the build area accounting for focus/divergence
% e2D = The 1/e2 spot size calculated from the diverged FWHM dimension

% REcD = Radius of 1/e2 diverged
% MLTEcD = Minimum line thickness 1/e2 diverged
% Exp1D = Exposure of beam 1 diverged

% DD = Distance of the photopolymer from the focal point (Divergence
Distance)
% DDe = Divergence distance to edge of build area
% Zr = Rayleigh length (meters)
% LFL = Laser focal distance

LPZ = input('Input the laser path length (mm) to centre of build area
(Form 1/2 default = 300): ');
LFL = input('Input the laser focal length (mm) (Form 1/2 default = 300):
');

BASL1 = input('Input build area dimension (side length in mm [e.g. Form 1
= 130]): ');
LPC = sqrt(((sqrt(((BASL1/2)^2)+((BASL1/2)^2)))^2)+(LPZ^2));
ExtC = LPC-LPZ;
ExtE = (sqrt((LPZ^2)+((BASL1/2)^2)))-LPZ;

DDe = LPZ-LFL+ExtE;

```

```

Zr = (pi*((e2/1000000)^2))/((M2*(WL/100000000)));

% Diverged beam waist 1/e2 at the corner of the build area and percentage
increase in spot size due to divergence at corner
DD = LPZ-LFL+ExtC;
e2D = ((e2/1000000)*sqrt(1+(((DD/1000)/(Zr))^2)))*1000000;
PCISSD = (e2D-e2)/e2*100;

% Emax at the corner of the build area
EmaxD = ((sqrt(2/pi))*((LP/1000)/(e2D/1000000*SS1/1000)))*1000/100/100;
CLWD = sqrt(2)*e2D*sqrt(log(EmaxD/Ec));

% AOI = Angle of incidence for ellipticity at the corner of the build area
AOIc = atan((sqrt(((BASL1/2)^2)+((BASL1/2)^2)))/LPZ);
% e2De = Diverged elliptical spot size at the corner of the build area
e2DE = e2D/cos(AOIc);
PCISSDE = (e2DE-e2)/e2*100;
EmaxDE = ((sqrt(2/pi))*((LP/1000)/(e2DE/1000000*SS1/1000)))*1000/100/100;
CLWDE = sqrt(2)*e2DE*sqrt(log(EmaxDE/Ec));

%The peak intensity of the diverged elliptical spot
I01DE = LP*(2/(pi*(e2DE/10000)^2));

% This is the diverged spot profile (using e2D)
% Calculate peak intensity from laser profile and power.
I01D = LP*(2/(pi*(e2D/10000)^2));

% Calculate the absolute intensity through the diverged spot (Rxy)
AbI1D = I01D.*exp((-2.*(Rxy./10000).^2)./(e2D/10000)^2);

% STD = Scan time (s) for diverged spot size
STD = EmaxD/I01D;

% Calculate the radius of the diverged 1/e2 laser spot which possesses
an exposure = Ec.
% Scan time calculated using diverged spot size.
REcD = sqrt((e2D^2*log((Ec/STD)/I01D))/-2);

% The minimum line thickness of the diverged spot for the given resin
MLTEcD = 2*REcD;

% Beam waist, Emax and cured line width at the edge of the build area
(i.e. position 70mm on Form 2):

% e2DEe = Diverged elliptical spot size at the edge of the build area
% AOIe = Angle of incidence for ellipticity at edge of the build area

e2De = ((e2/1000000)*sqrt(1+(((DDe/1000)/(Zr))^2)))*1000000;
PCISSDe = (e2De-e2)/e2*100;
EmaxDe = ((sqrt(2/pi))*((LP/1000)/(e2De/1000000*SS1/1000)))*1000/100/100;
CLWDe = sqrt(2)*e2De*sqrt(log(EmaxDe/Ec));

AOIe = atan((BASL1/2)/LPZ);
e2DEe = e2De/cos(AOIe);
PCISSDEe = (e2DEe-e2)/e2*100;
EmaxDEe =
((sqrt(2/pi))*((LP/1000)/(e2DEe/1000000*SS1/1000)))*1000/100/100;
CLWDEe = sqrt(2)*e2DEe*sqrt(log(EmaxDEe/Ec));

```

```

fprintf ('The 1/e2 diverged spot size at the corner of the build area
(microns) is: %.3f microns.\n',(e2D));
fprintf ('The 1/e2 diverged spot size will be increased by: %.3f
percent.\n', (PCISSD));
fprintf('The minimum line thickness and minimum achievable feature size at
the corner of the build area for the diverged profile of beam 1 is: %.2f
microns.\n',CLWD);

fprintf ('The 1/e2 diverged elliptical spot size at the corner of the
build area (microns) is: %.3f microns.\n',(e2DE));
fprintf ('The 1/e2 diverged elliptical spot size will be increased by:
%.3f percent.\n', (PCISSDE));
fprintf('The minimum line thickness and minimum achievable feature size at
the corner of the build area for the elliptical diverged profile of beam 1
is: %.2f microns.\n',CLWDE);

fprintf ('The 1/e2 spot size at the edge of the build area with divergence
(microns) is: %.3f microns.\n',(e2De));
fprintf ('The 1/e2 spot size at the edge of the build area will be
increased by: %.3f percent.\n', (PCISSDe));
fprintf('The minimum line thickness and minimum achievable feature size at
the edge of the build area for the diverged profile of beam 1 is: %.2f
microns.\n',CLWDe);

fprintf ('The 1/e2 spot size at the edge of the build area with divergence
and ellipticity (microns) is: %.3f microns.\n',(e2DEe));
fprintf ('The 1/e2 spot size at the edge of the build area will be
increased by: %.3f percent.\n', (PCISSDEe));
fprintf('The minimum line thickness and minimum achievable feature size at
the edge of the build area for the elliptical diverged profile of beam 1
is: %.2f microns.\n',CLWDEe);

%Figure of diverged beam intensity profile
figure(1)
hold on
surf(RX,RY,AbI1D,'FaceLighting','gouraud',...
'MeshStyle','column',...
'SpecularColorReflectance',0,...
'SpecularExponent',5,...
'SpecularStrength',0.2,...
'DiffuseStrength',1,...
'AmbientStrength',0.4,...
'AlignVertexCenters','on',...
'LineWidth',0.2,...
'FaceAlpha',0.25,...
'FaceColor',[0.9 0.08 0.1],...
'EdgeAlpha',0.4);
legend ('Profile beam 1', 'Profile beam 2', 'Profile beam 1 Diverged',
'Location', 'northeast')

% Exposure (mJ/cm2) = Scan time x Absolute Intensity
Exp1D = STD.*AbI1D;

% Figure of diverged beam's exposure profile
figure(2)
hold on
surf(RX,RY,Exp1D,'FaceLighting','gouraud',...

```

```

'MeshStyle', 'column', ...
'SpecularColorReflectance', 0, ...
'SpecularExponent', 5, ...
'SpecularStrength', 0.2, ...
'DiffuseStrength', 1, ...
'AmbientStrength', 0.4, ...
'AlignVertexCenters', 'on', ...
'LineWidth', 0.2, ...
'FaceAlpha', 0.25, ...
'FaceColor', [0.9 0.08 0.1], ...
'EdgeAlpha', 0.4);
legend('Profile beam 1', 'Profile beam 2', 'Profile beam 1 diverged',
'Location', 'northeast')
title('Laser exposure vs Spot radius')
xlabel('Radius of laser spot (microns)')
ylabel('Radius of laser spot (microns)')
zlabel('Exposure (mJ/cm2)')

% minimum line thickness across the build area
% BPX = Distance from the centre of the build platform in the X dimension
% BPY = Distance from the centre of the build platform in the Y dimension
% BPxy = Absolute distance from the centre of the build platform in the XY
plane
% LTBpxy = The minimum line thickness a given distance from the centre of
the build platform

% Meshgrid of a BASL1 x BASL1 build platform
[BPX, BPY] = meshgrid((-BASL1/2):1:(BASL1/2));

% Calculate the distance from the centre of the build platform in the X-Y
plane
BPxy = sqrt((BPX.^2)+(BPY.^2));

% Calculate the minimum line thickness at a given distance from the centre
of the build platform

% laser path to the corner of the build area (LPC1)
LPC1 = sqrt((BPxy.^2)+(LPZ.^2));
EXT = LPC1-LPZ;

% DD = Divergence distance to point in build area
DD = LPZ-LFL+EXT;

% The 1/e2 spot size at each location across the build area
e2Dxy = ((e2./1000000).*sqrt(1+(((DD./1000)./(Zr)).^2))).*1000000;

% CLW of diverged beam
BPxyEmaxD =
((sqrt(2./pi)).*((LP./1000)./(e2Dxy./1000000.*SS1./1000))).*1000./100./100
;
BPxyCLWD = sqrt(2).*e2Dxy.*sqrt(log(BPxyEmaxD./Ec));

hold on
figure(3)
surf(BPX, BPY, BPxyCLWD, 'FaceLighting', 'gouraud', ...
'MeshStyle', 'column', ...
'SpecularColorReflectance', 0, ...
'SpecularExponent', 5, ...
'SpecularStrength', 0.2, ...

```

```

'DiffuseStrength',1,...
'AmbientStrength',0.4,...
'AlignVertexCenters','on',...
'LineWidth',0.01,...
'FaceAlpha',0.01,...
'FaceColor',[0.8,0.4,0.2],...
'EdgeAlpha',0.1);
legend('Beam 1','Location','northeast')
title('Line thickness variation across build area due to divergence')
xlabel('Build area distance from centre (mm)')
ylabel('Line thickness (microns)')

% AOIE = Angle of incidence for ellipticity at target point in the build
area
BPxyAOIE = atan(BPxy./LPZ);

% Cured line width of diverged elliptical beam
BPxye2DE = e2Dxy./cos(BPxyAOIE);
BPxyEmaxDE =
((sqrt(2./pi)).*((LP./1000)./(BPxye2DE./1000000.*SS1./1000)))./10;
CLWDE = sqrt(2).*BPxye2DE.*sqrt(log(BPxyEmaxDE./Ec));

hold on
figure(4)
surf(BPX,BPY,CLWDE,'FaceLighting','gouraud',...
'MeshStyle','column',...
'SpecularColorReflectance',0,...
'SpecularExponent',5,...
'SpecularStrength',0.2,...
'DiffuseStrength',1,...
'AmbientStrength',0.4,...
'AlignVertexCenters','on',...
'LineWidth',0.01,...
'FaceAlpha',0.01,...
'FaceColor',[0.8,0.4,0.2],...
'EdgeAlpha',0.1);
legend('Beam 1','Location','northeast')
title('Line thickness variation across build area due to divergence and
ellipticity')
xlabel('Build area distance from centre (mm)')
ylabel('Line thickness (microns)')

% Optimisation of the focal length and laser spot:
% To minimise the variation in the spot size across the build area and the
minimum achievable line thickness. EXT is the extension in the laser path
length when aimed at the centre of the build area to its extremity.

% OLPZ1 = Optimised LPZ
% OEXT = Optimised extension
% DCCS = Scaler distance from centre of the build area to the corner
% EXTS = Scaler extension
% LPC1M = Matrix value of laser path length from source to a point in the
build area
% Prefix 0 = optimised

LPC1M = sqrt((BPxy.^2)+(LPZ.^2));
DCCS = sqrt(((BASL1/2)^2)+((BASL1/2)^2));
EXTS = sqrt((LPZ^2)+(DCCS^2))-LPZ;
OEXT = (-0.5*EXTS)+(EXTS.*BPxy./DCCS);

```

```

% Oe2Dxy = Optimised spot size for divergence
% The 1/e2 spot size of the optimised spot at each location across the
build area - this is based on the beam being focussed on the centre of the
build area
Oe2Dxy = ((e2./1000000).*sqrt(1+(((OEXT./1000)./(Zr)).^2))).*1000000;

% Calculate peak intensity from laser profile and power.
OBPxyI01D = LP.*(2./(pi.*(Oe2Dxy./10000).^2));

% The cure line width of the OPTIMISED diverged spot for the given resin
OBPxyEmaxD =
((sqrt(2./pi)).*((LP./1000)./(Oe2Dxy./1000000.*SS1./1000))).*1000./100./10
0;
OBPxyCLWD = sqrt(2).*Oe2Dxy.*sqrt(log(OBPxyEmaxD./Ec));

% optimise option Y/N
Opt = input('Optimise laser path length?: (Y=1 N=0)');
if Opt == 1

hold on
figure(3)
surf(BPX, BPY, OBPxyCLWD, ...
      'FaceAlpha', 0.75, ...
      'EdgeAlpha', 0.75);
legend('Beam 1', 'Optimised beam', 'Location', 'northeast')
title('Line thickness variation across build area')
xlabel('Build area distance from centre (mm)')
ylabel('Line thickness (microns)')

else
end

disp('Press enter to calculate the maximum build area to meet a defined
tolerance')
% Pause until key press added
for ind = 1
    pause;
end

% To calculate the maximum build area to meet a defined tolerance in the
minimum feature size

    % BTol = Allowable tolerance in the beam 1/e2 radius
    % BTolE2 = Allowable 1/e2 dimension in microns
    % MaxExt = Maximum allowable extension to the path of the laser
from the focal distance until divergence (without ellipticity) results in
the CLW being greater than the allowable minimum feature size (mm)
    % MaxHDCC = Max permitted horizontal distance from centre to the
corner of the build area based on the beam being focussed on the centre of
the build area (i.e. LPZ = LFL)
    % MaxHDCM = Maximum horizontal build platform dimension (square)
from centre of build area to midpoint of the edge (mm)
    % MaxHD = Maximum horizontal build platform dimension (square)
    % MaxA = Maximum allowable build area (cm^2)
    % Suffix E is for divergence with ellipticity
    Tol = input('Manufacturing tolerance (microns): ');

```

```

        BTol = input('Input maximum allowable tolerance of the beam 1/e2
radius (percentage): ');
        BTole2 = e2*(1+(BTol/100));

        % Max extension due to divergence only using Zr (Rayleigh length)
method
        MaxExt = (Zr*1000)*(sqrt(((1+(BTol/100))^2)-1));
        MaxHDCC = sqrt(((MaxExt+LPZ)^2-LPZ^2));
        MaxHDCM = sqrt(MaxHDCC^2/2);
        MaxHD = MaxHDCM*2;
        fprintf('The maximum side length of the build area (square)
limited by divergence to meet the allowable beam tolerance is: %.3f
mm.\n', (MaxHD));
        MaxA = (MaxHD/10)*(MaxHD/10);
        fprintf('The maximum allowable build area to meet tolerance due to
divergence is: %.3f cm^2.\n', (MaxA));

% Routine to calculate max side length to satisfy the tolerance with the
combined influence of divergence and ellipticity
% postscript 3 used for values in the routine

BASL3 = BASL1;
e2DE3 = e2DE;
if e2DE < ((BTol/100)+1)*e2
    while e2DE3 < ((BTol/100)+1)*e2
        BASL3 = BASL3 +1;
    LPC3 = sqrt(((sqrt(((BASL3/2)^2)+((BASL3/2)^2)))^2)+(LPZ^2));
    ExtC3 = LPC3-LPZ;

% Diverged beam waist 1/e2 at the corner of the build area and percentage
increase in spot size due to divergence at corner
DD3 = LPZ-LFL+ExtC3;
e2D3 = ((e2/1000000)*sqrt(1+(((DD3/1000)/(Zr))^2)))*1000000;
PCISSD3 = (e2D3-e2)/e2*100;

% AOIc = Angle of incidence for ellipticity at the corner of the build
area
AOIc3 = atan((sqrt(((BASL3/2)^2)+((BASL3/2)^2)))/LPZ);
e2DE3 = e2D3/cos(AOIc3);
% 0.99 used to continue iteration until the distorted (diverged
elliptical) spot is within 1% of the maximum spot size which can meet the
MFS
if e2DE3 > (((BTol/100)+1)*e2)*0.99
break
end
    end
else
end
fprintf('The maximum side length of the build area (square) limited by the
combined effects of divergence and ellipticity to meet the allowable beam
tolerance is: %.3f mm.\n', (BASL3));
% end of routine for calculating max dimension for diverged elliptical
spot

disp('Press enter to calculate cure profile')
% Pause until key press added
for ind = 1
    pause;
end

```



```

% Line z-profile and depth
% CD = Cure depth
Exp1 = ST1.*AbI;

% Cure depth of focussed beam
CD = Dp.*log(Exp1/Ec);
fprintf('The maximum depth of cure for beam profile 1 is: %.2f
microns.\n',max(max(CD)));

figure(5)
surf(RX,RY,CD,...
    'FaceColor',[0.7 0.08 1],...
    'FaceAlpha',0.2,...
    'EdgeAlpha',0.2);
title('Focussed beam cure profile')
xlabel('Beam radius (microns)')
ylabel('Build distance from centre (microns)')
zlabel('Depth of cure (microns)')
zlim([0,400])

% Extend the 2D (XZ) profile of the cure shape in the Y plane
% Suffix l is for line profile
% RX=RY with the radius in the diagonal plane will be equal to the lateral
plane (RX).

[RXl,RYl] = meshgrid(-175:5:400);
AbI1l = I0.*exp((-2.*(RXl./10000).^2)./((e2./10000).^2));
Exp1l = ST1.*AbI1l;
CDl = Dp.*log(Exp1l./Ec)+(RYl-RYl);

% linep input for line profile
linep = input('Add line profile? (Y=1, N=0): ');
if linep == 1

hold on
figure (5)
surf(RXl,RYl,CDl,...
    'FaceColor',[0.7 0.08 1],...
    'FaceAlpha',0.2,...
    'EdgeAlpha',0.2);

elseif linep == 0
end

% line profile cap due to layer thickness
RLT = input('Required layer thickness of build (microns) (Default = 50):
');

% Comparison of cure profiles
hold on
figure(7)
surf(RX,RY,CD,...
    'FaceColor',[0.7 0.08 1],...
    'FaceAlpha',0.2,...
    'EdgeAlpha',0.2);
title('Focussed beam cure profile with meniscus')
xlabel('Beam radius (microns)')

```

```

ylabel('Build distance from centre (microns)')
zlabel('Depth of cure (microns)')
zlim([0,RLT])
linep = input('Add line profile? (Y=1, N=0): ');
if linep == 1

hold on
figure (7)
surf(RX1,RY1,CD1,...
'FaceColor',[0.7 0.08 1],...
'FaceAlpha',0.2,...
'EdgeAlpha',0.2);

elseif linep == 0
end

% Calculation of step size between bottom and top of cure layers for I0
and initial laser parameters
% AbIr is the absolute intensity at radius r
% exp1r is the exposure at radius r
exp1r=(exp(RLT/Dp))*Ec;
ABIr=exp1r/ST1;
Step0 = (0.5*CLW0)-(0.5*(2*sqrt(((log(ABIr/I0))/-2)*e2DE^2)));
fprintf('The step at each side of each layer is: %.2f microns.\n',Step0);

% MLTss = Maximum layer thickness before step size exceeds manufacturing
tolerance for the diverged elliptical beam
MLTss = Dp*log(((ST1*I0)*(exp((((CLW0-Tol)/2)^2)/(e2DE^2))*-2))/Ec);
fprintf('The maximum layer thickness before the total step size (i.e.,
cumulative effect from both sides of the layer) exceeds manufacturing
tolerances is: %.2f microns.\n',MLTss);

% enter the no. of repeat first layer scans
FLS = input('Number of repeat first layer scans: ');

% Equivalent laser power delivered to first layer
LPM = FLS*LP;

% I0M = Equivalent intensity delivered for first layer scan (mW/cm2) for
the diverged elliptical beam
I0M = LPM*(2/(pi*(e2DE/10000)^2));

% AbIM Absolute intensity for the first layer for the diverged elliptical
beam
AbIM = I0M.*exp((-2.*(Rxy./10000).^2)./((e2DE/10000)^2));

% APLSM = Equivalent absolute power through the laser spot for the first
layer
APLSM = LPM*(1-TPLS);
Exp1 = ST1.*AbIM;

% CDM = depth of cure for the first layer due to repeat scans (i.e., which
forms the meniscus)
CDM = Dp.*log(Exp1./Ec);

% CDM cannot be greater than the first layer thickness because only have
repeat scans for the first layer
CDM(CDM>RLT)=RLT;

```

```

% Comparison of cure profiles
hold on
figure(7)

surf(RX,RY,CDM,...
     'FaceColor',[0.7 0.08 1],...
     'FaceAlpha',0.2,...
     'EdgeAlpha',0.2);
title('Beam cure profile')
xlabel('Beam radius (microns)')
ylabel('Build distance from centre (microns)')
zlabel('Depth of cure (microns)')
zlim([0,700])

```

A2: Characterisation of distortion profiles

```

% This script characterises the cure profile with the influence of
% superposition for the diverged elliptical beam generated in
% A1 which needs to be run prior to set the parameters.

e2 = e2DE; % from A1 for elliptical diverged beam at the corner of the
build area
I0 = I01DE; % from A1 for elliptical diverged beam
SS1 = input('Input scan speed (mm/s) default = 1000: ');
ST1=(sqrt(pi/2)*e2/1000000)/(SS1/1000);

LPZ = input('Input the laser path length (mm) to centre of build area
(Form 1/2 default = 300): ');
LFL = input('Input the laser focal length (mm) (Form 1/2 default = 300):
');
BASL1 = input('Input build area dimension (side length in mm [e.g. Form 1
= 130]): ');
LPC = sqrt(((sqrt(((BASL1/2)^2)+((BASL1/2)^2)))^2)+(LPZ^2));
ExtC = LPC-LPZ;
ExtE = (sqrt((LPZ^2)+((BASL1/2)^2)))-LPZ;
[BPX,BPY] = meshgrid((-BASL1/2):1:(BASL1/2));

% Calculate the distance from the centre of the build platform in the X-Y
plane
BPxy = sqrt((BPX.^2)+(BPY.^2));

% Calculate the minimum line thickness at a given distance from the centre
of the build platform
% LPC = Total laser path length to the corner of the build area.
LPC1M = sqrt((BPxy.^2)+(LPZ.^2));
Ext = LPC1M-LPZ;

%% Calculate build time and superposition
% HS1 = hatch spacing of scan pattern (beam 1) (microns)
% Exp1p = Exposure profile
HS1 = input('Input hatch spacing of beam profile 1 (microns): ');
[RX,RY] = meshgrid(-600:5:600);
Rxy = sqrt((RX.^2)+(RY.^2));
AbI1p = I0.*exp((-2.*(Rxy./10000).^2)./((e2./10000).^2));
Exp1p = ST1.*AbI1p;

[RX1,RY1] = meshgrid(-175:5:400);

```

```

AbI11 = I0.*exp((-2.*(RX1./10000).^2)./((e2./10000).^2));
Exp11 = ST1.*AbI11;
CD1 = Dp.*log(Exp11./Ec)+(RY1-RY1);

% X dimension of scan with superposition
XD1s = RX1+(6*HS1);

% superposition profiles
% RXLs = Radius in X dimension for line
% suffix s is for superposition profile
RXLs = RX1+HS1;
RXLs1 = RXLs+HS1;
RXLs2 = RXLs1+HS1;
RXLs3 = RXLs2+HS1;
RXLs4 = RXLs3+HS1;
RXLs5 = RXLs4+HS1;

% The below inputs for Lx, Ly, and Lz, assume that the part has been
optimally orientated already (i.e., orientated to give the minimum no. of
layers while accounting for any other build specific requirements such as
avoiding excessive contact area with the resin window).
Lx = input('Average length of build (mm): ');
Ly = input('Average width of build (mm): ');
Lz = input('Absolute height of build (mm): ');
RLT = input('Required layer thickness of build (microns) (Default = 50):
');

% DT1 = Delay time between layers
DT1 = input('Delay time between layers (s) including recoating (Default =
10 seconds): ');

% RT1 = Raster scan time for a single raster scan for profile 1
RT1 = (Lx*Ly)/(SS1*(HS1/1000));
fprintf('The scan time for a single raster for profile 1 is: %.2f
seconds.\n',RT1);

% Display the number of layers
fprintf('The build consists of %.0f layers.\n',RLT)

% TBT = Total build time
TBT = ((DT1+RT1)*(Lz/(RLT/1000)))/60;
fprintf('The total build time for profile 1 is: %.2f minutes.\n',TBT);

% Question to calculate superposition.
SupInp1 = input('Calculate superposition? (Y=1, N=0): ');
if SupInp1 == 1

figure(5)
surf(RX,RY,Exp1p,...
    'FaceColor',[0.7 0.08 1],...
    'FaceAlpha',0.2,...
    'EdgeAlpha',0.2);
title('Exposure profile')
xlabel('Beam radius (microns)')
ylabel('Build area distance from centre (mm)')
zlabel('Exposure (mJ/cm^{2})')
zlim([0.2,100])

% Add exposure due to superposition

```

```

ExpLPInp = input('Calculate exposure line profile? (Y=1, N=0): ');
if ExpLPInp == 1
    hold on
    figure (5)
    surf(RX1,RY1,Exp11,...
'FaceColor',[0.90 0.08 1],...
'FaceAlpha',0.2,...
'EdgeAlpha',0.2);
    zlim([0.2,110])
    title('Exposure profile')
xlabel('Build dimension (microns)')

elseif LineExp == 0
end

% LineExp input for superposition line profile
LineExps = input('Add repeat line profiles? (Y=1, N=0): ');
if LineExps == 1

    hold on
    figure (5)
    surf(RX1s,RY1,Exp11,...
'FaceColor',[1 0.18 1],...
'FaceAlpha',0.2,...
'EdgeAlpha',0.2);

    hold on
    figure (5)
    surf(RX1s1,RY1,Exp11,...
'FaceColor',[1 0.38 1],...
'FaceAlpha',0.2,...
'EdgeAlpha',0.2);

    hold on
    figure (5)
    surf(RX1s2,RY1,Exp11,...
'FaceColor',[1 0.58 1],...
'FaceAlpha',0.2,...
'EdgeAlpha',0.2);

    hold on
    figure (5)
    surf(RX1s3,RY1,Exp11,...
'FaceColor',[1 0.78 1],...
'FaceAlpha',0.2,...
'EdgeAlpha',0.2);

    hold on
    figure (5)
    surf(RX1s4,RY1,Exp11,...
'FaceColor',[1 0.88 1],...
'FaceAlpha',0.2,...
'EdgeAlpha',0.2);

    hold on
    figure (5)
    surf(RX1s5,RY1,Exp11,...
'FaceColor',[1 0.98 1],...
'FaceAlpha',0.1,...

```

```

        'EdgeAlpha',0.1);

% plane of Ec threshold
hold on
figure(5)
MEc2 = (RX1-RX1).*(RY1-RY1)+Ec;
surf(RX1s1,RY1,MEc2,'LineWidth',0.1,...
     'FaceAlpha',0.01,...
     'EdgeAlpha',0.1,...
     'FaceColor',[0.8,0.4,0.2]);

elseif LineExps == 0
end

display ('Calculating exposure due to superposition')

end

% CD1s = Cure depth with superposition for beam profile 1
% Zone of influence - Using the concept of "zone of influence", only scan
lines located such that absolute values of y +(-)nhs<2.146W0 are to be
considered.
% LZoI = No. of lines (in either direction orthogonal, and in addition to
the line of cure (y), within the "zone of influence" = 2.146*W0 where W0 =
E2
LZoI = floor((e2/10000)*2.146/(HS1/10000));
fprintf('The number of lines within the zone of influence are: %.0f
.\n',(LZoI));

% EpExpS2 = Peak exposure for a given scan line orthogonal to the line
being scanned
% EpExpS0 = Peak exposure with no additional lines within the zone of
influence
% REpEv = Ratio of peak to valley exposure
% Postscript no. in superposition refers to the scan line orthogonal to y,
m refers to minus.
% Therefore y0 is along the centre of the line being scanned.
% The valleys are an orthogonal distance of one half width of the hatch
spacing (HS1)
% EV (The valley occurs at the midpoint between adjacent lines so y =
0.5HS1.

% Maximum exposure at peak intensity for a single line scan (scaler)
Emax=I0*ST1;
fprintf('The peak exposure for an individual scan line is: %.3f
mJ/cm2.\n',(Emax));

% LZoI0
EpExpS0 = Emax*(exp((-2*((0-(0*(HS1/10000)))^2))/((e2/10000)^2)));
EPLZoI0 = EpExpS0;

% LZoI1
% Peaks
EpExpS1 = Emax*(exp((-2*((0-(1*(HS1/10000)))^2))/((e2/10000)^2)));
EpExpSm1 = Emax*(exp((-2*((0+(1*(HS1/10000)))^2))/((e2/10000)^2)));
EPLZoI1 = EpExpS0+EpExpS1+EpExpSm1;

% Valleys
EVExpS0 = Emax*(exp((-2*((0-(0.5*(HS1/10000)))^2))/((e2/10000)^2)));

```

```

EVExpSm1 = Emax*(exp((-2*((0+(0.5*(HS1/10000)))^2))/((e2/10000)^2)));
EVLZoI1 = EVExpS0+EVExpSm1;

% Ratio of Peaks to valleys
REpEv1 = EPLZoI1/EVLZoI1;

% LZoI2
EpExpS2 = Emax*(exp((-2*((0-(2*(HS1/10000)))^2))/((e2/10000)^2)));
EpExpSm2 = Emax*(exp((-2*((0+(2*(HS1/10000)))^2))/((e2/10000)^2)));
EPLZoI2 = EPLZoI1+EpExpS2+EpExpSm2;

EVExpS1 = Emax*(exp((-2*((0-(1.5*(HS1/10000)))^2))/((e2/10000)^2)));
EVExpSm2 = Emax*(exp((-2*((0+(1.5*(HS1/10000)))^2))/((e2/10000)^2)));
EVLZoI2 = EVLZoI1+EVExpS1+EVExpSm2;
REpEv2 = EPLZoI2/EVLZoI2;

% LZoI3
EpExpS3 = Emax*(exp((-2*((0-(3*(HS1/10000)))^2))/((e2/10000)^2)));
EpExpSm3 = Emax*(exp((-2*((0+(3*(HS1/10000)))^2))/((e2/10000)^2)));
EPLZoI3 = EPLZoI2+EpExpS3+EpExpSm3;

EVExpS2 = Emax*(exp((-2*((0-(2.5*(HS1/10000)))^2))/((e2/10000)^2)));
EVExpSm3 = Emax*(exp((-2*((0+(2.5*(HS1/10000)))^2))/((e2/10000)^2)));
EVLZoI3 = EVLZoI2+EVExpS2+EVExpSm3;

REpEv3 = EPLZoI3/EVLZoI3;

% LZoI4
EpExpS4 = Emax*(exp((-2*((0-(4*(HS1/10000)))^2))/((e2/10000)^2)));
EpExpSm4 = Emax*(exp((-2*((0+(4*(HS1/10000)))^2))/((e2/10000)^2)));
EPLZoI4 = EPLZoI3+EpExpS4+EpExpSm4;

EVExpS3 = Emax*(exp((-2*((0-(3.5*(HS1/10000)))^2))/((e2/10000)^2)));
EVExpSm4 = Emax*(exp((-2*((0+(3.5*(HS1/10000)))^2))/((e2/10000)^2)));
EVLZoI4 = EVLZoI3+EVExpS3+EVExpSm4;

REpEv4 = EPLZoI4/EVLZoI4;

% LZoI5
EpExpS5 = Emax*(exp((-2*((0-(5*(HS1/10000)))^2))/((e2/10000)^2)));
EpExpSm5 = Emax*(exp((-2*((0+(5*(HS1/10000)))^2))/((e2/10000)^2)));
EPLZoI5 = EPLZoI4+EpExpS5+EpExpSm5;

EVExpS4 = Emax*(exp((-2*((0-(4.5*(HS1/10000)))^2))/((e2/10000)^2)));
EVExpSm5 = Emax*(exp((-2*((0+(4.5*(HS1/10000)))^2))/((e2/10000)^2)));
EVLZoI5 = EVLZoI4+EVExpS4+EVExpSm5;

REpEv5 = EPLZoI5/EVLZoI5;

% LZoI6
EpExpS6 = Emax*(exp((-2*((0-(6*(HS1/10000)))^2))/((e2/10000)^2)));
EpExpSm6 = Emax*(exp((-2*((0+(6*(HS1/10000)))^2))/((e2/10000)^2)));
EPLZoI6 = EPLZoI5+EpExpS6+EpExpSm6;

```

```

EVExpS5 =Emax*(exp((-2*((0-(5.5*(HS1/10000)))^2))/((e2/10000)^2)));
EVExpSm6 =Emax*(exp((-2*((0+(5.5*(HS1/10000)))^2))/((e2/10000)^2)));
EVLZzoI6 = EVLZzoI5+EVExpS5+EVExpSm6;

REpEv6 = EPLZzoI6/EVLZzoI6;

if LZoI == 0
% There is no valley between lines for a single scan line
fprintf('No superposition will occur due to wide hatch spacing, the peak
exposure for an individual scan line is: %.3f mJ/cm2.\n',(EPLZzoI0));
Eavs = EPLZzoI0;

elseif LZoI == 1
fprintf('The peak exposure of superposition with +1/-1 scan line within
the zone of influence is: %.3f mJ/cm2.\n',(EPLZzoI1));
fprintf('The valley exposure of superposition with +1/-1 scan line within
the zone of influence is: %.3f mJ/cm2.\n',(EVLZzoI1));
fprintf('The ratio of peak to valley exposure with +1/-1 scan lines within
the zone of influence is: %.3f .\n',(REpEv1));

% LZ1Latpc = Percentage variation in the peak lateral exposure
LZ1Latpc = (EPLZzoI1-EVLZzoI1)/EPLZzoI1*100;
fprintf('The variation in the peak lateral exposure is: %.3f
percent.\n',(LZ1Latpc));
Eavs = (EPLZzoI1+EVLZzoI1)/2;

% Depth of cure with superposition
CD1s = Dp.*log(Eavs/Ec);
fprintf('The average depth of cure for beam profile 1 with superposition
is: %.2f microns.\n',(CD1s));

hold on
figure (5)
ExpLZI1 = (RX1-RX1).*(RY1-RY1)+EPLZzoI1;
surf(RX1s1,RY1,ExpLZI1,'LineWidth',0.1,...
'FaceAlpha',0.6,...
'EdgeAlpha',0.2,...
'FaceColor',[0.9,0.1,1]);
legend('Beam profile','Scanline 1','Scanline 2','Scanline 3',
'Scanline 4','Scanline 5','Scanline 6','Scanline 7','Ec',
'Superposition exposure','Location','northeast')

elseif LZoI == 2
fprintf('The peak exposure of superposition with +2/-2 scan line within
the zone of influence is: %.3f mJ/cm2.\n',(EPLZzoI2));
fprintf('The valley exposure of superposition with +2/-2 scan line within
the zone of influence is: %.3f mJ/cm2.\n',(EVLZzoI2));
fprintf('The ratio of peak to valley exposure with +2/-2 scan lines within
the zone of influence is: %.3f .\n',(REpEv2));
LZ2Latpc = (EPLZzoI2-EVLZzoI2)/EPLZzoI2*100;
fprintf('The variation in the peak lateral exposure is: %.3f
percent.\n',(LZ2Latpc));
Eavs = (EPLZzoI2+EVLZzoI2)/2;

% Depth of cure with superposition
CD1s = Dp.*log(Eavs/Ec);
fprintf('The average depth of cure for beam profile 1 with superposition
is: %.2f microns.\n',(CD1s));

```



```

hold on
figure (5)
ExpLZI2 = (RX1-RX1).*(RY1-RY1)+EPLZoI2;
surf(RX1s1,RY1,ExpLZI2,'LineWidth',0.1,...
     'FaceAlpha',0.6,...
     'EdgeAlpha',0.2,...
     'FaceColor',[0.4,0.1,1]);
legend('Beam profile', 'Scanline 1', 'Scanline 2', 'Scanline 3',
       'Scanline 4', 'Scanline 5', 'Scanline 6', 'Scanline 7', 'Ec',
       'Superposition exposure', 'Location', 'northeast')

elseif LZoI == 3
fprintf('The peak exposure of superposition with +3/-3 scan line within
the zone of influence is: %.3f mJ/cm2.\n',(EPLZoI3));
fprintf('The valley exposure of superposition with +3/-3 scan line within
the zone of influence is: %.3f mJ/cm2.\n',(EVLZoI3));
fprintf('The ratio of peak to valley exposure with +3/-3 scan lines within
the zone of influence is: %.3f .\n',(REpEv3));
LZ3Latpc = (EPLZoI3-EVLZoI3)/EPLZoI3*100;
fprintf('The variation in the peak lateral exposure is: %.3f
percent.\n',(LZ3Latpc));
Eavs = (EPLZoI3+EVLZoI3)/2;

% Depth of cure with superposition
CD1s = Dp.*log(Eavs/Ec);
fprintf('The average depth of cure for beam profile 1 with superposition
is: %.2f microns.\n',(CD1s));

hold on
figure (5)
ExpLZI3 = (RX1-RX1).*(RY1-RY1)+EPLZoI3;
surf(RX1s1,RY1,ExpLZI3,'LineWidth',0.1,...
     'FaceAlpha',0.6,...
     'EdgeAlpha',0.2,...
     'FaceColor',[0.9,0.1,1]);
legend('Beam profile', 'Scanline 1', 'Scanline 2', 'Scanline 3',
       'Scanline 4', 'Scanline 5', 'Scanline 6', 'Scanline 7', 'Ec',
       'Superposition exposure', 'Location', 'northeast')

elseif LZoI == 4
fprintf('The peak exposure of superposition with +4/-4 scan line within
the zone of influence is: %.3f mJ/cm2.\n',(EPLZoI4));
fprintf('The valley exposure of superposition with +4/-4 scan line within
the zone of influence is: %.3f mJ/cm2.\n',(EVLZoI4));
fprintf('The ratio of peak to valley exposure with +4/-4 scan lines within
the zone of influence is: %.3f .\n',(REpEv4));
LZ4Latpc = (EPLZoI4-EVLZoI4)/EPLZoI4*100;
fprintf('The variation in the peak lateral exposure is: %.3f
percent.\n',(LZ4Latpc));

% Depth of cure with superposition
Eavs = (EPLZoI4+EVLZoI4)/2;
CD1s = Dp.*log(Eavs/Ec);
fprintf('The average depth of cure for beam profile 1 with superposition
is: %.2f microns.\n',(CD1s));

hold on
figure (5)

```

```

ExpLZI4 = (RX1-RX1).*(RY1-RY1)+EPLZoI4;
surf(RX1s1,RY1,ExpLZI4,'LineWidth',0.1,...
     'FaceAlpha',0.6,...
     'EdgeAlpha',0.2,...
     'FaceColor',[0.9,0.1,1]);
legend('Beam profile','Scanline 1','Scanline 2','Scanline 3',
       'Scanline 4','Scanline 5','Scanline 6','Scanline 7','Ec',
       'Superposition exposure','Location','northeast')

elseif LZoI == 5
fprintf('The peak exposure of superposition with +5/-5 scan line within
the zone of influence is: %.3f mJ/cm2.\n',(EPLZoI5))
fprintf('The valley exposure of superposition with +5/-5 scan line within
the zone of influence is: %.3f mJ/cm2.\n',(EVLZoI5));
fprintf('The ratio of peak to valley exposure with +5/-5 scan lines within
the zone of influence is: %.3f .\n',(REpEv5));
LZ5Latpc = (EPLZoI5-EVLZoI5)/EPLZoI5*100;
fprintf('The variation in the peak lateral exposure is: %.3f
percent.\n',(LZ5Latpc));

% Depth of cure with superposition
Eavs = (EPLZoI5+EVLZoI5)/2;
CD1s = Dp.*log(Eavs/Ec);
fprintf('The average depth of cure for beam profile 1 with superposition
is: %.2f microns.\n',(CD1s));

hold on
figure(5)
ExpLZI5 = (RX1-RX1).*(RY1-RY1)+EPLZoI5;
surf(RX1s1,RY1,ExpLZI5,'LineWidth',0.1,...
     'FaceAlpha',0.6,...
     'EdgeAlpha',0.2,...
     'FaceColor',[0.9,0.1,1]);
legend('Beam profile','Scanline 1','Scanline 2','Scanline 3',
       'Scanline 4','Scanline 5','Scanline 6','Scanline 7','Ec',
       'Superposition exposure','Location','northeast')

elseif LZoI == 6
fprintf('The peak exposure of superposition with +6/-6 scan line within
the zone of influence is: %.3f mJ/cm2.\n',(EPLZoI6))
fprintf('The valley exposure of superposition with +6/-6 scan line within
the zone of influence is: %.3f mJ/cm2.\n',(EVLZoI6));
fprintf('The ratio of peak to valley exposure with +6/-6 scan lines within
the zone of influence is: %.3f .\n',(REpEv6));
LZ6Latpc = (EPLZoI6-EVLZoI6)/EPLZoI6*100;
fprintf('The variation in the peak lateral exposure is: %.3f
percent.\n',(LZ6Latpc));

% Depth of cure with superposition
Eavs = (EPLZoI6+EVLZoI6)/2;
CD1s = Dp.*log(Eavs/Ec);
fprintf('The average depth of cure for beam profile 1 with superposition
is: %.2f microns.\n',(CD1s));

hold on
figure(5)
ExpLZI6 = (RX1-RX1).*(RY1-RY1)+EPLZoI6;
surf(RX1s1,RY1,ExpLZI6,'LineWidth',0.1,...

```

```

    'FaceAlpha',0.6,...
    'EdgeAlpha',0.2,...
    'FaceColor',[0.9,0.1,1]);
legend ('Beam profile', 'Scanline 1', 'Scanline 2', 'Scanline 3',
'Scanline 4', 'Scanline 5', 'Scanline 6', 'Scanline 7', 'Ec',
'Superposition exposure', 'Location', 'northeast')
else
end

% For investigating reflectance, the line spacing for the perimeter has
% been set at 90 microns to be consistent with the bulk fill.
% Calculating the minimum line thickness corresponding to the peak
% exposure with superposition.

% EI0S = Equivalent peak beam intensity corresponding to superposition
if LZoI == 0
    EI0S = EPLZoI0/ST1;

elseif LZoI == 1
    EI0S = EPLZoI1/ST1;

elseif LZoI == 2
    EI0S = EPLZoI2/ST1;
    EI0Sm = EVLPZoI2/ST1;
    EI0Sa = ((EPLZoI2+EVLPZoI2)/2)/ST1;

elseif LZoI == 3
    EI0S = EPLZoI3/ST1;

elseif LZoI == 4
    EI0S = EPLZoI4/ST1;

elseif LZoI == 5
    EI0S = EPLZoI5/ST1;

elseif LZoI == 6
    EI0S = EPLZoI6/ST1;
else
end

% MLTEcS = Minimum line thickness achievable with superposition for Ec -
% when the exposure (=Ec/ST1) equals the critical cure energy
% REcS = Radius of cure when effective exposure with superposition becomes
% equal to the critical cure energy of the resin
REcS = sqrt(((e2^2)*log((Ec/ST1)/EI0S))/-2);
MLTEcS = 2*REcS;
fprintf('The maximum width of cure for defined perimeter scan conditions
is: %.2f microns.\n',MLTEcS);
fprintf('The maximum radius of cure for defined perimeter scan conditions
is: %.2f microns.\n',REcS);

```

A3: Identification of process window

```
% This script is used to optimise the build time using the parameters
% generated in the script A2 which needs to be run first.

% Build time (see notes for Lx, Ly, and Lz in previous scripts)
% Lx = Average length of build (mm)
% Ly = Average width of build (mm)
% Lz = Absolute height of build (mm)

% RAHR = Ratio of average raster scan area to the build part's total
height (Lz) with Lz having a minimum of 1 layer thickness (Has to be in
metres for the build time calculation to work)

% BY = RAHR
% BX = Exposure
% RT1 = Time for a single raster scan for profile 1
% DT1 = delay time
% RLT = Required layer thickness (minimum z-feature size)
% SS1 = Scan speed of profile 1
% HS1 = Hatch spacing of profile 1
% BT = Build time

% The range of RAHR, representative of typical constructions are
considered to be between 1mm and 30mm height
% The range of exposures representative of typical operating conditions
are up to 1000 mJ/cm2.

[BX,BY] = meshgrid(0.035:0.08:4);

% Eavs = The average exposure calculated using peak and valley
superposition values

SS1 = BX.*1000;
Lz = BY.*15;

% To round up the height of the build to the next increment of RLT to only
calculate whole layers and avoid build times corresponding to less than
one layer and calculations of fractions of a layer
Lz = ((ceil((Lz.*1000)./RLT)).*(RLT))./1000;
RAHR = (Lx./1000.*Ly./1000)./(Lz./1000);

% Creating a superposition matrix
e2 = e2DE;
I0 = I01DE;
% Calculate a value for LZOI for each cell in the matrix and then
calculate superposition for each of those cells
% ED = exposure distance
LZoI00 = floor(((e2./10000).*2.146./(HS1./10000)).*(SS1./SS1));
ED = (sqrt(pi/2)*e2);
Emax = I0.*(ED./1000000)./(SS1./1000);

EpExpS00 = Emax.*(exp((-2.*((0-(0*(HS1./10000))).^2))./((e2./10000).^2)));
EPLZoI00 = EpExpS00;

% Peaks
EpExpS10 = Emax.*(exp((-2.*((0-
(1.*(HS1./10000))).^2))./((e2./10000).^2)));
```

```

EpExpSm10 = Emax.*(exp((-
2.*((0+(1.*(HS1./10000))).^2))./((e2./10000).^2)));
EPLZoI10 = EpExpS00+EpExpS10+EpExpSm10;

% Valleys
EVEExpS00 = Emax.*(exp((-2.*((0-
(0.5.*(HS1./10000))).^2))./((e2./10000).^2)));
EVEExpSm10 = Emax.*(exp((-
2.*((0+(0.5.*(HS1./10000))).^2))./((e2./10000).^2)));
EVLZoI10 = EVEExpS00+EVEExpSm10;

% Ratio of Peaks to valleys
REpEv10 = EPLZoI10./EVLZoI10;

% LZoI2
EpExpS20 = Emax.*(exp((-2.*((0-
(2.*(HS1./10000))).^2))./((e2./10000).^2)));
EpExpSm20 = Emax.*(exp((-
2.*((0+(2.*(HS1./10000))).^2))./((e2./10000).^2)));
EPLZoI20 = EPLZoI10+EpExpS20+EpExpSm20;

EVEExpS10 = Emax.*(exp((-2.*((0-
(1.5.*(HS1./10000))).^2))./((e2./10000).^2)));
EVEExpSm20 = Emax.*(exp((-
2.*((0+(1.5.*(HS1./10000))).^2))./((e2./10000).^2)));
EVLZoI20 = EVLZoI10+EVEExpS10+EVEExpSm20;

REpEv20 = EPLZoI20./EVLZoI20;

% LZoI3
EpExpS30 = Emax.*(exp((-2.*((0-
(3.*(HS1./10000))).^2))./((e2./10000).^2)));
EpExpSm30 = Emax.*(exp((-
2.*((0+(3.*(HS1./10000))).^2))./((e2./10000).^2)));
EPLZoI30 = EPLZoI20+EpExpS30+EpExpSm30;

EVEExpS20 =Emax.*(exp((-2.*((0-
(2.5.*(HS1./10000))).^2))./((e2./10000).^2)));
EVEExpSm30 =Emax.*(exp((-
2.*((0+(2.5.*(HS1./10000))).^2))./((e2./10000).^2)));
EVLZoI30 = EVLZoI20+EVEExpS20+EVEExpSm30;

REpEv30 = EPLZoI30./EVLZoI30;

% LZoI4
EpExpS40 =Emax.*(exp((-2.*((0-(4.*(HS1./10000))).^2))./((e2./10000).^2)));
EpExpSm40 =Emax.*(exp((-
2.*((0+(4.*(HS1./10000))).^2))./((e2./10000).^2)));
EPLZoI40 = EPLZoI30+EpExpS40+EpExpSm40;

EVEExpS30 =Emax.*(exp((-2.*((0-
(3.5.*(HS1./10000))).^2))./((e2./10000).^2)));
EVEExpSm40 =Emax.*(exp((-
2.*((0+(3.5.*(HS1./10000))).^2))./((e2./10000).^2)));
EVLZoI40 = EVLZoI30+EVEExpS30+EVEExpSm40;

REpEv40 = EPLZoI40./EVLZoI40;

% LZoI5

```

```

EpExpS50 =Emax.*(exp((-2.*((0-(5.*(HS1./10000))).^2))./((e2./10000).^2)));
EpExpSm50 =Emax.*(exp((-
2.*((0+(5.*(HS1./10000))).^2))./((e2./10000).^2)));
EPLZoI50 = EPLZoI40+EpExpS50+EpExpSm50;

EVEpS40 =Emax.*(exp((-2.*((0-
(4.5.*(HS1./10000))).^2))./((e2./10000).^2)));
EVEpSm50 =Emax.*(exp((-
2.*((0+(4.5.*(HS1./10000))).^2))./((e2./10000).^2)));
EVLZoI50 = EVLZoI40+EVEpS40+EVEpSm50;

REpEv50 = EPLZoI50./EVLZoI50;

% LZoI6
EpExpS60 = Emax.*(exp((-2.*((0-
(6.*(HS1./10000))).^2))./((e2./10000).^2)));
EpExpSm60 = Emax.*(exp((-
2.*((0+(6.*(HS1./10000))).^2))./((e2./10000).^2)));
EPLZoI60 = EPLZoI50+EpExpS60+EpExpSm60;

EVEpS50 =Emax.*(exp((-2.*((0-
(5.5.*(HS1./10000))).^2))./((e2./10000).^2)));
EVEpSm60 =Emax.*(exp((-
2.*((0+(5.5.*(HS1./10000))).^2))./((e2./10000).^2)));
EVLZoI60 = EVLZoI50+EVEpS50+EVEpSm60;

REpEv60 = EPLZoI60./EVLZoI60;

if LZoI00 == 0
Eavs = EPLZoI00;
end

if LZoI00 == 1
Eavs = (EPLZoI10+EVLZoI10)./2;
end

if LZoI00 == 2
Eavs = (EPLZoI20+EVLZoI20)./2;
end

if LZoI00 == 3
Eavs = (EPLZoI30+EVLZoI30)./2;
end

if LZoI00 == 4
Eavs = (EPLZoI40+EVLZoI40)./2;
end

if LZoI00 == 5
Eavs = (EPLZoI50+EVLZoI50)./2;
end

if LZoI00 == 6
Eavs = (EPLZoI60+EVLZoI60)./2;
end

disp('Paused - press enter to continue')
% Pause until key press added
for ind = 1

```

```

        pause;
        disp(ind);
end

BT =
(RAHR.*((Lz./1000).^2))./((SS1./1000).*(HS1./1000000))./(RLT./1000000)+((D
T1.*((Lz./1000))./(RLT./1000000)));

figure(6)
surf(RAHR,Eavs,BT)
title('Build time vs shape geometry and laser exposure')
xlabel('RAHR')
ylabel('Average exposure (mJ/cm2)')
zlabel('Build time (s)')

disp('Paused - press enter to continue')

% Pause until key press added
for ind = 1
    pause;
end

% Graph of Ec threshold
% MEcBT = Minimum exposure threshold for build time (minimum exposure to
cure to the layer thickness + 10% margin)
% ExpCD = Required minimum exposure to cure the resin (for given Dp and
Ec) to the depth of 1 layer thickness*2 + 10% margin. The minimum exposure
is doubled to achieve 2*Ec on the far side of the constructed slice. This
is in accordance with Jacob's who recommends 2 x EC.

figure(6)
hold on
ExpCD = (Ec*exp(RLT/Dp))*2*1.1;
MEcBT = (RAHR-RAHR).*(Eavs-Eavs)+ExpCD;
surf(RAHR,MEcBT,BT,'LineWidth',0.1,...
    'FaceAlpha',0.4,...
    'EdgeAlpha',0.6,...
    'FaceColor',[1,0.4,0.8]);

% MExpRBT = Maximum exposure threshold for reflectance which has been
identified to correspond to a scan speed of 200mm/s (approximately
439mJ/cm2 for Case 1 parameters).
figure(6)
hold on
MExpRBT = (RAHR-RAHR).*(Eavs-Eavs)+439.1;
surf(RAHR,MExpRBT,BT,'LineWidth',0.1,...
    'FaceAlpha',0.6,...
    'EdgeAlpha',1,...
    'FaceColor',[0.6,0.2,1]);
legend('Build time','Ec lower limit','Reflectance exp limit',
'Location','northeast')

% MExpD is 219.6mJ/cm2 which corresponds to the exposure delivered by 7.2
scans at 400mm/s which is identified as the threshold where distortion of
the beam occurs
figure(6)
hold on

```

```

MExpD = (RAHR-RAHR).*(Eavs-Eavs)+219.6;
surf(RAHR,MExpD,BT,'LineWidth',0.1,...
     'FaceAlpha',0.6,...
     'EdgeAlpha',1,...
     'FaceColor',[0.6,0.2,1]);
legend('Build time','Ec lower limit','Reflectance exp limit','Beam
distortion limit','Location','northeast')

% MSTR = Minimum scan time to meet required feature size (s)
% MSSR = Minimum scan speed to meet required feature size (mm/s) this is
calculated from the maximum distorted beam size due to ellipticity and
divergence in script A2
% RR = Required feature size (line thickness)
% EavRS = Average exposure delivered at given hatch spacing and minimum
scan speed to achieve target feature size

% Calculates the maximum exposure which can be delivered while still
achieving the required feature size for which superposition is calculated
(planer).

RR = input('Required minimum X-Y feature size (microns): ');
MSTR = Ec/((exp((-2*((RR/2)^2))/(e2^2)))*I0);
MSSR = ((ED/1000000)/MSTR)*1000;

% O Suffix = Optimised
% R suffix = For calculating the exposure limit for feature size
% EP = Exposure peak
% EV (The valley occurs at the midpoint between adjacent lines so y =
0.5HS1.
% EpExpS0 = Peak exposure with no additional lines within the zone of
influence
% EpExpS1 = Peak exposure for a given scan line orthogonal to the line
being scanned
% REpEv = Ratio of peak to valley exposure
% Postscript no. in superposition refers to the scan line orthogonal to y,
m refers to minus.
% Therefore y0 is along the centre of the line being scanned.
% The valleys are an orthogonal distance of one half width of the hatch
spacing (HS1)
% LZoI = No. of lines either side of the target line which are within the
zone of influence
% SLZI = scan line number within zone of influence

% Updated Zone of influence - Using the concept of "zone of influence",
only scan lines located such that absolute values of y +(-)nhs<2.146W0
to be considered.
% LZoIO = No. of lines (in either direction orthogonal, and in addition to
the line of cure (y), within the "zone of influence" = 2.146*W0 where W0 =
E2

LZoIOR = floor((e2/10000)*2.146/(HS1/10000));
fprintf('The number of lines within the zone of influence, at the minimum
scan speed to achieve the required feature size, are: %.0f \n',(LZoIOR));

%EmaxR = Optimised Emax adjusted for minimum scan time to achieve required
feature size
EmaxR =I0*MSTR;

% LZoI0R

```



```

EpExpS0R = EmaxR*(exp((-2*((0-(0*(HS1/10000)))^2))/((e2/10000)^2)));
EPLZoI0R = EpExpS00;

% LZoI1R
% Peaks
EpExpS1R = EmaxR*(exp((-2*((0-(1*(HS1/10000)))^2))/((e2/10000)^2)));
EpExpSm1R = EmaxR*(exp((-2*((0+(1*(HS1/10000)))^2))/((e2/10000)^2)));
EPLZoI1R = EpExpS0R+EpExpS1R+EpExpSm1R;

% Valleys
EVEExpS0R = EmaxR*(exp((-2*((0-(0.5*(HS1/10000)))^2))/((e2/10000)^2)));
EVEExpSm1R = EmaxR*(exp((-2*((0+(0.5*(HS1/10000)))^2))/((e2/10000)^2)));
EVLZoI1R = EVEExpS0R+EVEExpSm1R;

% Ratio of Peaks to valleys
REpEv1R = EPLZoI1R/EVLZoI1R;

% LZoI2
EpExpS2R = EmaxR*(exp((-2*((0-(2*(HS1/10000)))^2))/((e2/10000)^2)));
EpExpSm2R = EmaxR*(exp((-2*((0+(2*(HS1/10000)))^2))/((e2/10000)^2)));
EPLZoI2R = EPLZoI1R+EpExpS2R+EpExpSm2R;

EVEExpS1R = EmaxR*(exp((-2*((0-(1.5*(HS1/10000)))^2))/((e2/10000)^2)));
EVEExpSm2R = EmaxR*(exp((-2*((0+(1.5*(HS1/10000)))^2))/((e2/10000)^2)));
EVLZoI2R = EVLZoI1R+EVEExpS1R+EVEExpSm2R;

REpEv2R = EPLZoI2R/EVLZoI2R;

% LZoI3
EpExpS3R = EmaxR*(exp((-2*((0-(3*(HS1/10000)))^2))/((e2/10000)^2)));
EpExpSm3R = EmaxR*(exp((-2*((0+(3*(HS1/10000)))^2))/((e2/10000)^2)));
EPLZoI3R = EPLZoI2R+EpExpS3R+EpExpSm3R;

EVEExpS2R = EmaxR*(exp((-2*((0-(2.5*(HS1/10000)))^2))/((e2/10000)^2)));
EVEExpSm3R = EmaxR*(exp((-2*((0+(2.5*(HS1/10000)))^2))/((e2/10000)^2)));
EVLZoI3R = EVLZoI2R+EVEExpS2R+EVEExpSm3R;

REpEv3R = EPLZoI3R/EVLZoI3R;

% LZoI4
EpExpS4R = EmaxR*(exp((-2*((0-(4*(HS1/10000)))^2))/((e2/10000)^2)));
EpExpSm4R = EmaxR*(exp((-2*((0+(4*(HS1/10000)))^2))/((e2/10000)^2)));
EPLZoI4R = EPLZoI3R+EpExpS4R+EpExpSm4R;

EVEExpS3R = EmaxR*(exp((-2*((0-(3.5*(HS1/10000)))^2))/((e2/10000)^2)));
EVEExpSm4R = EmaxR*(exp((-2*((0+(3.5*(HS1/10000)))^2))/((e2/10000)^2)));
EVLZoI4R = EVLZoI3R+EVEExpS3R+EVEExpSm4R;

REpEv4R = EPLZoI4R/EVLZoI4R;

% LZoI5
EpExpS5R = EmaxR*(exp((-2*((0-(5*(HS1/10000)))^2))/((e2/10000)^2)));
EpExpSm5R = EmaxR*(exp((-2*((0+(5*(HS1/10000)))^2))/((e2/10000)^2)));
EPLZoI5R = EPLZoI4R+EpExpS5R+EpExpSm5R;

EVEExpS4R = EmaxR*(exp((-2*((0-(4.5*(HS1/10000)))^2))/((e2/10000)^2)));

```

```

EVExpSm5R = EmaxR*(exp((-2*((0+(4.5*(HS1/10000)))^2))/((e2/10000)^2)));
EVLZoI5R = EVLZoI4R+EVExpS4R+EVExpSm5R;

```

```

REpEv5R = EPLZoI5R/EVLZoI5R;

```

```

% LZoI6

```

```

EpExpS6R = EmaxR*(exp((-2*((0-(6*(HS1/10000)))^2))/((e2/10000)^2)));
EpExpSm6R = EmaxR*(exp((-2*((0+(6*(HS1/10000)))^2))/((e2/10000)^2)));
EPLZoI6R = EPLZoI5R+EpExpS6R+EpExpSm6R;

```

```

EVExpS5R = EmaxR*(exp((-2*((0-(5.5*(HS1/10000)))^2))/((e2/10000)^2)));
EVExpSm6R = EmaxR*(exp((-2*((0+(5.5*(HS1/10000)))^2))/((e2/10000)^2)));
EVLZoI6R = EVLZoI5R+EVExpS5R+EVExpSm6R;

```

```

REpEv6R = EPLZoI6R/EVLZoI6R;

```

```

% For the purposes of investigating reflectance, the line spacing for the
perimeter has been set at 90 microns to be consistent with the bulk fill.
% Calculating the minimum line thickness corresponding to the peak
exposure with superposition.

```

```

if LZoIOR == 0
EavRS = EPLZoI0R;
VLE = EPLZoI0R;
end

```

```

if LZoIOR == 1
EavRS = (EPLZoI1R+EVLZoI1R)/2;
VLE = (REpEv1R-1)*100;
end

```

```

if LZoIOR == 2
EavRS = (EPLZoI2R+EVLZoI2R)/2;
VLE = (REpEv2R-1)*100;
end

```

```

if LZoIOR == 3
EavRS = (EPLZoI3R+EVLZoI3R)/2;
VLE = (REpEv3R-1)*100;
end

```

```

if LZoIOR == 4
EavRS = (EPLZoI4R+EVLZoI4R)/2;
VLE = (REpEv4R-1)*100;
end

```

```

if LZoIOR == 5
EavRS = (EPLZoI5R+EVLZoI5R)/2;
VLE = (REpEv5R-1)*100;
end

```

```

if LZoIOR == 6
EavRS = (EPLZoI6R+EVLZoI6R)/2;
VLE = (REpEv6R-1)*100;
end

```

```

fprintf('The average exposure delivered with superposition to achieve the
minimum feature size is (mJ/cm^2): %.2f .\n', (EavRS));

```

```

fprintf('The variation in lateral exposure is (percent): %.4f .\n',(VLE));

% MExpXYRBT = Maximum exposure threshold for XY feature size based at the
% calculated minimum scan speed required to achieve the minimum exposure
% corresponding to the given hatch spacing.
figure(6)
hold on
MExpXYRBT = (RAHR-RAHR).*(Eavs-Eavs)+EavRS;
surf(RAHR,MExpXYRBT,BT,'LineWidth',0.1,...
     'FaceAlpha',0.8,...
     'EdgeAlpha',1,...
     'FaceColor',[0.4,0.3,1]);
legend('Build time map','Ec lower limit','Reflectance exp limit','Beam
distortion limit','X-Y feature size exp limit','Location','northeast')

```

A4: Optimisation of SLA process and build time

```

% The A3_Build_time_optimisation_13_7_23 script needs running prior to
% this one to set the parameters. This script calculates the maximum
% exposure which can be delivered while still achieving the required
% feature size with the influence of superposition and the corresponding
% maximum hatch spacing which is permissible to maintain the variation in
% lateral exposure within defined limits.

```

```

% MSTR = Minimum scan time to meet required feature size (s)
% MSSR = Minimum scan speed to meet required feature size (mm/s)
% RR = Required feature size (minimum line thickness)
% EavRS = Average exposure delivered at given hatch spacing and minimum
% scan speed to achieve target feature size
% EmaxR = Emax corresponding to the max exposure to still be able to
% achieve the minimum feature size arrived at by adjusting for the minimum
% scan time

```

```

% The lower the value for feature size, the faster the scan speed (MSSR)
% will be and the lower the overall exposure due to superposition,
% potentially allowing a reduced hatch spacing.

```

```

% Ed is the exposure distance
% e2DE is the maximum size of the diverged elliptical spot at the
% extremity of the build area

```

```

e2 = e2DE;
I0 = I01DE;
RR = input('Required minimum X-Y feature size (microns): ');
MSTR = Ec/((exp((-2*((RR/2)^2))/(e2^2)))*I0);
ED =(sqrt(pi/2)*e2);
MSSR = ((ED/1000000)/MSTR)*1000;
EmaxR =I0*MSTR;

```

```

% 0 suffix = Optimised
% R suffix = For calculating the exposure limit for feature size
% EP = Exposure peak
% EV (The valley occurs at the midpoint between adjacent lines so y =
% 0.5HS2.
% EpExpS0 = Peak exposure for a single line within the zone of influence
% EpExpS1 = Peak exposure for a given scan line orthogonal to the line
% being scanned

```

```

% REpEv = Ratio of peak to valley exposure
% Postscript no. in superposition refers to the scan line orthogonal to y,
m refers to minus.
% Therefore y0 is along the centre of the line being scanned.
% The valleys are an orthogonal distance of one half width of the hatch
spacing (HS2)
% LZoI = No. of lines either side of the target line which are within the
zone of influence
% SLZI = scan line number within zone of influence

% Zone of influence - only complete scan lines located within the ZOI to
be used, therefore absolute values of y +(-)nhs<2.146W0 are taken.
% LZoIO = No. of lines (in either direction orthogonal, and in addition to
the line of cure (y), within the "zone of influence" = 2.146*W0 where W0 =
E2

% EavRSOH = Average exposure delivered optimised for minimum scan speed to
achieve target line width and maximum hatch spacing to achieve variation
in lateral exposure
% LET = Lateral exposure tolerance (%)
% VLE = Variation in lateral exposure (%)

LET = input('Input maximum permissible variation in lateral exposure (%):
');

% Optimisation of hatch spacing
Opthatch = input('Enter new values for hatch spacing or and variation in
lateral exposure? (Y=1, N=0): ');
if Opthatch == 1

% Hatch spacing (HS2) and VLE entered below can be a known value or any
value above LET. The programme will then calculate new values of VLE and
HS2.
HS2 = input('Input starting value for hatch spacing of scan pattern 1
(microns): ');
VLE = input('Input starting value for variation in lateral exposure VLE
(%): ');
else
end

% If function (if the permitted max variation in exposure is greater than
the calculated variation) to determine whether to run the while loop to
incrementally reduce the hatch spacing.
if LET<VLE

while LET<VLE

HS2 = HS2-1;

LZoIOR = floor((e2/10000)*2.146/(HS2/10000));
fprintf('The number of lines within the zone of influence, at the minimum
scan speed to achieve the required feature size, are: %.0f .\n',(LZoIOR));

EmaxR =I0*MSTR;

% LZoIOR
EpExpS0R = EmaxR*(exp((-2*((0-(0*(HS2/10000)))^2)))/((e2/10000)^2));
EPLZoIOR = EpExpS0R;

```

```

% LZoI1R
% Peaks
EpExpS1R = EmaxR*(exp((-2*((0-(1*(HS2/10000)))^2))/((e2/10000)^2)));
EpExpSm1R = EmaxR*(exp((-2*((0+(1*(HS2/10000)))^2))/((e2/10000)^2)));
EPLZoI1R = EpExpS0R+EpExpS1R+EpExpSm1R;

% Valleys
EVExpS0R = EmaxR*(exp((-2*((0-(0.5*(HS2/10000)))^2))/((e2/10000)^2)));
EVExpSm1R = EmaxR*(exp((-2*((0+(0.5*(HS2/10000)))^2))/((e2/10000)^2)));
EVLZoI1R = EVExpS0R+EVExpSm1R;

% Ratio of Peaks to valleys
REpEv1R = EPLZoI1R/EVLZoI1R;

% LZoI2
EpExpS2R = EmaxR*(exp((-2*((0-(2*(HS2/10000)))^2))/((e2/10000)^2)));
EpExpSm2R = EmaxR*(exp((-2*((0+(2*(HS2/10000)))^2))/((e2/10000)^2)));
EPLZoI2R = EPLZoI1R+EpExpS2R+EpExpSm2R;

EVExpS1R = EmaxR*(exp((-2*((0-(1.5*(HS2/10000)))^2))/((e2/10000)^2)));
EVExpSm2R = EmaxR*(exp((-2*((0+(1.5*(HS2/10000)))^2))/((e2/10000)^2)));
EVLZoI2R = EVLZoI1R+EVExpS1R+EVExpSm2R;

REpEv2R = EPLZoI2R/EVLZoI2R;

% LZoI3
EpExpS3R = EmaxR*(exp((-2*((0-(3*(HS2/10000)))^2))/((e2/10000)^2)));
EpExpSm3R = EmaxR*(exp((-2*((0+(3*(HS2/10000)))^2))/((e2/10000)^2)));
EPLZoI3R = EPLZoI2R+EpExpS3R+EpExpSm3R;

EVExpS2R = EmaxR*(exp((-2*((0-(2.5*(HS2/10000)))^2))/((e2/10000)^2)));
EVExpSm3R = EmaxR*(exp((-2*((0+(2.5*(HS2/10000)))^2))/((e2/10000)^2)));
EVLZoI3R = EVLZoI2R+EVExpS2R+EVExpSm3R;

REpEv3R = EPLZoI3R/EVLZoI3R;

% LZoI4
EpExpS4R = EmaxR*(exp((-2*((0-(4*(HS2/10000)))^2))/((e2/10000)^2)));
EpExpSm4R = EmaxR*(exp((-2*((0+(4*(HS2/10000)))^2))/((e2/10000)^2)));
EPLZoI4R = EPLZoI3R+EpExpS4R+EpExpSm4R;

EVExpS3R = EmaxR*(exp((-2*((0-(3.5*(HS2/10000)))^2))/((e2/10000)^2)));
EVExpSm4R = EmaxR*(exp((-2*((0+(3.5*(HS2/10000)))^2))/((e2/10000)^2)));
EVLZoI4R = EVLZoI3R+EVExpS3R+EVExpSm4R;

REpEv4R = EPLZoI4R/EVLZoI4R;

% LZoI5
EpExpS5R = EmaxR*(exp((-2*((0-(5*(HS2/10000)))^2))/((e2/10000)^2)));
EpExpSm5R = EmaxR*(exp((-2*((0+(5*(HS2/10000)))^2))/((e2/10000)^2)));
EPLZoI5R = EPLZoI4R+EpExpS5R+EpExpSm5R;

EVExpS4R = EmaxR*(exp((-2*((0-(4.5*(HS2/10000)))^2))/((e2/10000)^2)));
EVExpSm5R = EmaxR*(exp((-2*((0+(4.5*(HS2/10000)))^2))/((e2/10000)^2)));
EVLZoI5R = EVLZoI4R+EVExpS4R+EVExpSm5R;

```

```

REpEv5R = EPLZoI5R/EVLZoI5R;

% LZoI6
EpExpS6R = EmaxR*(exp((-2*((0-(6*(HS2/10000)))^2))/((e2/10000)^2)));
EpExpSm6R = EmaxR*(exp((-2*((0+(6*(HS2/10000)))^2))/((e2/10000)^2)));
EPLZoI6R = EPLZoI5R+EpExpS6R+EpExpSm6R;

EVEpS5R =EmaxR*(exp((-2*((0-(5.5*(HS2/10000)))^2))/((e2/10000)^2)));
EVEpSm6R =EmaxR*(exp((-2*((0+(5.5*(HS2/10000)))^2))/((e2/10000)^2)));
EVLZoI6R = EVLZoI5R+EVEpS5R+EVEpSm6R;

REpEv6R = EPLZoI6R/EVLZoI6R;

% The perimeter line spacing for experimentation has been set at 90
microns to be consistent with the bulk fill.
% Calculating the minimum line thickness corresponding to the peak
exposure with superposition.

if LZoIOR == 0
EavRSOH = EPLZoI0R;
VLE = EPLZoI0R;
end

if LZoIOR == 1
EavRSOH = (EPLZoI1R+EVLZoI1R)/2;
VLE = (REpEv1R-1)*100;
end

if LZoIOR == 2
EavRSOH = (EPLZoI2R+EVLZoI2R)/2;
VLE = (REpEv2R-1)*100;
end

if LZoIOR == 3
EavRSOH = (EPLZoI3R+EVLZoI3R)/2;
VLE = (REpEv3R-1)*100;
end

if LZoIOR == 4
EavRSOH = (EPLZoI4R+EVLZoI4R)/2;
VLE = (REpEv4R-1)*100;
end

if LZoIOR == 5
EavRSOH = (EPLZoI5R+EVLZoI5R)/2;
VLE = (REpEv5R-1)*100;
end

if LZoIOR == 6
EavRSOH = (EPLZoI6R+EVLZoI6R)/2;
VLE = (REpEv6R-1)*100;
end

if LET > VLE
break
end
end

```

```

% Minimum hatch spacing to meet required maximum variation in lateral cure
MHS2 = HS2;

fprintf('The calculated variation in lateral exposure is (percent): %.2f
.\n',(VLE));
fprintf('The maximum hatch spacing to meet the required variation in
lateral exposure and the minimum scan speed to achieve the required
feature size is (microns): %.1f .\n',(MHS2));
fprintf('The minimum exposure to meet required variation in lateral
exposure, while complying with the required feature size is (mJ/cm^2):
%.1f .\n',(EavRSOH));

% MExpXYRBT = Maximum exposure threshold for XY feature size based on the
calculated minimum scan speed required to achieve the minimum exposure
corresponding to the given hatch spacing.
figure(6)
hold on

MExpXYRBT = (RAHR-RAHR).*(Eavs-Eavs)+EavRSOH;
surf(RAHR,MExpXYRBT,BT,'LineWidth',0.1,...
'FaceAlpha',0.8,...
'EdgeAlpha',1,...
'FaceColor',[0.4,0.3,1]);
legend('Build time','Ec lower limit','Reflectance exp limit','X-Y
feature size exp limit','Location','northeast')

else
disp('The variation in lateral exposure is within tolerance')
end

```

B1: Refraction with Parabolic mirror

```

close all;
%
[PlatX,PlatY] = meshgrid(-70:2:70);
Int = 5;
%
% PlatX = Form 2 build platform dimensions = 140mm
% PlatY = Form 2 build platform dimensions = 140mm
% PlatZ = Dimension of galvanometer mirror beneath build platform (mm)
% LambdaUV = Wavelength of UV light (nm)
%
% media 1 = air
% KM2 = Thickness of media 2 = glass window (mm)
% KM3 = Thickness of media 3 = acrylic resin tray window (mm)
% LT = Thickness of media 4 = resin build layer thickness (microns)
% n1 = refractive index of media 1 (air)
% n2 = refractive index of media 2 (glass)
% n3 = refractive index of media 3 (acrylic resin tray base)
% n4 = refractive index of media 4 (resin)
% n5 = refractive index of media 5 (Silicon nitride wafer)
%
prompt = 'Enter wavelength of light (Form2 = 405nm)? ';
LambdaUV = input(prompt);
prompt = 'What is the thickness of the medium 2 (glass window Form 2 =
3mm) (mm)? ';

```

```

KM2 = input(prompt);
prompt = 'What is the thickness of the medium 3 (resin tank window i.e.
7mm) (mm)? ';
KM3 = input(prompt);
prompt = 'What is the build layer thickness applied (microns)? ';
LT = input(prompt);
%
% Mirror
% Assumed alignment of the centre of the mirror and the centre of the
build platform in the Z-axis and the centreline of the mirror/galvanometer
in the x-axis
%
% ML = Mirror length (measured)
% MW = Mirror width (measured)
% ZMT = Vertical distance from top of mirror to window
% ZMB = Vertical distance from bottom of mirror to window
% XLM = Horizontal distance from the galvanometer to the mirror
(estimated)
% AOM = Angle of mirror to the horizontal
%
prompt = 'Enter the length of the main mirror (Form 1 = 125mm)';
ML = input(prompt);
prompt = 'Enter the width of the main mirror (Form 1 = 105mm)';
MW = input(prompt);
prompt = 'Enter the vertical distance from top of mirror to window (Form 1
= 70mm)';
ZMT = input(prompt);
prompt = 'Vertical distance from bottom of mirror to window (Form 1 =
110mm)';
ZMB = input(prompt);
prompt = 'Enter the distance from the mirror to the galvanometer (Form 1 =
190mm)';
XLM = input(prompt);
AOM = asin((ZMB-ZMT)/ML);

fprintf('The length of the mirror is: %.2f mm.\n',ML);
fprintf('The width of the mirror is: %.2f mm.\n',MW);
fprintf('The angle of the mirror to the horizontal is: %.2f
radians.\n',AOM);
%
% Xi = Horizontal distance in the X axis of the point of incidence from
the centre of the build platform
% Zc = Height of window above centre point of mirror
% Xlc = Horizontal distance (along x-axis) of the lens from the centre
point of the mirror
% KFar = Furthest point of the platform from the galvanometer mirror (mm)
% AOIpx = Angle of incidence on window in x-axis
% AOImx = Angle of incidence on mirror in x-axis
% Xim = Point of incidence on mirror from centre (in the X-axis)
% POImx = Point of incidence on mirror from centre (absolute - in the
plane of the mirror)
% LMu = Length of mirror used
% PlatZ = Distance of the build plate centre point from the centre of the
mirror
%
Xi = PlatX;
Zc = ZMT+(sin(AOM)*(ML/2));
Xlc = XLM+((ML/2)*cos(AOM));
PlatZ = (Xlc+Zc)+KM2+KM3+(LT/1000);

```



```

AOIpx = atan(Xi./PlatZ);
AOImx = (90/180*pi)+AOIpx-(2.*AOM); % relative to the horizontal
Xim = PlatX;
POImx = Xim./(cos(AOM));
LMu = (max(max(POImx)))*2;
fprintf('The length of the mirror utilised is: %.2f mm.\n',LMu);
%
% Yi = Horizontal distance in the X axis of the point of incidence from
the centre of the build platform
% AOIPy = Angle of incidence on window in y-axis
% AOImy = Angle of incidence on mirror in y-axis
% Yim = Point of incidence on mirror from centre (in the Y-axis)
% POImy = Point of incidence on mirror from centre (absolute - in the
plane of the mirror)
% WMu = Length of mirror used

Yi = PlatY;
AOIPy = atan(Yi./PlatZ);
AOImy = AOIPy;
Yim = Yi-(tan(AOIPy)*Zc);
POImy = Yim;
WMU = (max(max(POImy)))*2;
fprintf('The width of the mirror utilised is: %.2f mm.\n',WMU);
POIpxy = sqrt((PlatX.^2)+(PlatY.^2));
AOIpxy = atan(POIpxy./PlatZ);
AOImxyc = Xim+Xlc;
AOImxyd = AOImxyc.*tan(AOImx);
AOImxye = AOImxyc./cos(AOImx);
AOImxyb = AOImxye./cos(AOImy);
AOImxy = acos(AOImxyc./AOImxyb);
POImxy = POIpxy-(tan(AOIpxy).*Zc);
AOICmxy = (((90/180*pi)-(AOImxy))./2);
AOIC2 = (45/180*pi)-AOICmxy+AOM; %This is the profile of the corrective
mirror in situ (i.e. with 45 degrees at the centre)
AOIC4 = AOM-AOICmxy; %This is the corrected profile of the mirror on the
flat relative to the horizontal - gives 0 radians at the centre.
AOIC8 = 5.*tan(AOIC4);
AOIC9 = 5.*tan((AOIC2));

n1 = 1.0003;
prompt = 'What is the refractive index of medium 2 (Form 2 = glass = 1.53,
Form 1 = air = 1.0003? ';
n2 = input(prompt);
n3 = 1.447;
n4 = 1.5403;
prompt = 'What is the refractive index of the substrate (@405nm Si3N4 =
2.1 aluminium = 0.50047)? ';
n5 = input(prompt);
KFar = (sqrt((PlatX.^2)+(PlatY.^2)+(PlatZ.^2)));

if n5<n4
Crit5 = asin(n5/n4);

else
    Crit5 = 90*pi/180;
end
%
% FIRST REFRACTION
% Theta2 = angle of incidence on media 2

```

```

% TranTheta12 - angle of transmission from media 1 into 2
% Kx2 = horizontal distance of the unrefracted beam from origin (mm) at
% exit of media 2
% Kxd2 = horizontal distortion (absolute) at exit of media 2
%
Theta2 = acos(PlatZ./KFar);
TranTheta12 = asin(n1.*sin(Theta2)./n2);
Kx2 = KM2*tan(TranTheta12);
Kxd2 = tan(Theta2)*KM2-(tan(TranTheta12)*KM2);
%
% SECOND REFRACTION
% Theta3 = angle of incidence on media 3
% TranTheta23 - angle of transmission from media 2 into 3
% Kxd3 = horizontal distortion (absolute) at exit of media 3
% DCum3 = Cumulative horizontal distortion at exit of media 3
%
Theta3 =(pi/2)-(pi-(pi/2)-TranTheta12);
TranTheta23 = asin(n2*sin(Theta3)/n3);
Kxd3 = tan(Theta3)*KM3-(tan(TranTheta23)*KM3);
DCum3 = Kxd2 + Kxd3;
%
% THIRD REFRACTION
% Theta4 = angle of incidence on media 4
% TranTheta34 = angle of transmission from media 3 into 4
% Kxd3 = horizontal distortion (absolute) at exit of media 4
% DCum3 = Cumulative horizontal distortion at exit of media 4
%
Theta4 = (pi/2)-(pi-(pi/2)-TranTheta23);
TranTheta34 = asin(n3*sin(Theta4)/n4);
Kxd4 = tan(Theta4)*(LT/1000)-(tan(TranTheta34)*(LT/1000));
DCum4 = DCum3+Kxd4;
%
Theta5 = (pi/2)-(pi-(pi/2)-TranTheta34);
%
% Theta5max = maximum incident angle on surface 5
%
Theta5max = max(max(Theta5));
if Theta5max > Crit5
    display ('There is light incident on surface 5 above the critical
angle')
end
%
CritLim45 = n4*sin(Theta5)/n5;
CritLim45(CritLim45>1)=1;
TranTheta45=asin(CritLim45);
%
surf(PlatX,PlatY,A0IC8');
figure(5)
colormap parula
title('Profile of parabolic mirror relative to the incident light')
xlabel('Build platform X plane position (mm)')
ylabel('Build platform Y plane position mm')
zlabel('Profile of mirror (mm)')

hold off
surf(PlatX,PlatY,DCum4');
colormap parula
legend('Distortion mm','Location','NorthEast')
title('Horizontal Distortion Due to Refraction (relative to centre)')

```

```

xlabel('Build platform X plane position mm')
ylabel('Build platform Y plane position mm')
zlabel('Distortion mm')
%
hold off

% Distortion is relative to centre so Abdist = Dcum4*1
Abdist = DCum4*1;
surf(PlatX,PlatY,Abdist');
colormap parula
legend('Distortion mm','Location','NorthEast')
title('Horizontal Distortion Due to Refraction (relative to centre)')
xlabel('Build platform X plane position mm')
ylabel('Build platform Y plane position mm')
zlabel('Distortion mm')

%
fprintf('The X dimension of the build platform is: %.2f
mm.\n',max(abs(max(abs(PlatX)))));
fprintf('The Y dimension of the build platform is: %.2f
mm.\n',max(abs(max(abs(PlatY)))));
fprintf('The effective linear light path (galvanometer to platform) in the
z axis is: %.2f mm below the build
platform.\n',max(abs(max(abs(PlatZ)))));
fprintf('The furthest point on the build platform from the galvanometer
mirror is: %.2f mm.\n',max(abs(abs(max(KFar)))));
fprintf('The thickness of medium 2 is: %.2f mm.\n',KM2);
fprintf('The thickness of medium 3 is: %.2f mm.\n',KM3);
fprintf('The build layer thickness is: %.2f microns.\n',LT);
fprintf('The refractive index of media 1 is: %.2f \n',n1);
fprintf('The refractive index of media 2 is: %.2f \n',n2);
fprintf('The refractive index of media 3 is: %.2f \n',n3);
fprintf('The refractive index of media 4 is: %.2f \n',n4);
fprintf('The refractive index of media 5 is: %.2f \n',n5);
fprintf('The wavelength of the light is: %.2f nm.\n',LambdaUV);
%
fprintf('The greatest angle of incidence on to media 2 is: %.2f
radians.\n',max(abs(abs(max(Theta2)))));
fprintf('The greatest angle of incidence on to media 3 is: %.2f
radians.\n',max(abs(abs(max(Theta3)))));
fprintf('The greatest angle of incidence on to media 4 is: %.2f
radians.\n',max(abs(max(abs(Theta4)))));
fprintf('The greatest angle of incidence on to media 5 is: %.2f
radians.\n',max(abs(max(abs(Theta5)))));
fprintf('The greatest angle of transmission in to media 2 is: %.2f
radians.\n',max(abs(max(abs(TranTheta12)))));
fprintf('The greatest angle of transmission in to media 3 is: %.2f
radians.\n',max(abs(max(abs(TranTheta23)))));
fprintf('The greatest angle of transmission in to media 4 is: %.2f
radians.\n',max(abs(max(abs(TranTheta34)))));
fprintf('The greatest angle of transmission in to media 5 is: %.2f
radians.\n',max(abs(max(abs(TranTheta45)))));
%
fprintf('The greatest deviation due to refraction through medium 2 is:
%.2f mm.\n',max(abs(max(abs(Kxd2)))));
fprintf('The greatest deviation due to refraction through medium 3 is:
%.2f mm.\n',max(abs(max(abs(Kxd3)))));
fprintf('The greatest cumulative deviation due to refraction at the exit
of medium 3 is: %.2f mm.\n',max(abs(max(abs(DCum3)))));

```

```

fprintf('The greatest deviation due to refraction through medium 4 is:
%.3f mm.\n',max(abs(max(abs(Kxd4)))));
fprintf('The greatest cumulative deviation due to refraction at the exit
of medium 4 is: %.3f mm.\n',max(abs(max(abs(DCum4)))));
%

```

B2 Reflection

```

% This script calculates the magnitude of reflectance and its potential to
% produce spurious curing using parameters defined in
% B1_Refraction_with_mirror which needs to be run first.
%
% REFLECTION AT AN OBLIQUE ANGLE
%
% VARIABLES
% c = speed of light (299272458 m/s)
% AoR = Angle of Reflection (from media no.)
% FSI = Free Space Impedance (ohms)
% Imp = Impedance of media (ohms)
% rte = reflection coefficient (electric wave)
% rtm = reflection coefficient (magnetic wave)
% tte = transmission coefficient (electric wave)
% ttm = transmission coefficient (magnetic wave)
% Rte = Reflectance coefficient (electric wave)
% Rtm = Reflectance coefficient (magnetic wave)
% OR = Overall reflectance (electric and magnetic - assumed incident light
is circularly polarised (50/50 te/tm).
% Tte = Transmittance coefficient (electric wave)
% Ttm = Transmittance coefficient (magnetic wave)
% OT = Overall transmittance (electric and magnetic wave - assumed
circularly polarised)
% k0 = Wave number
% PL = Phase loss
% Aac = Attenuation of amplitude coefficient
% Apc = Attenuation of power coefficient
% Abc = Absorption coefficient
% PAC = Power absorption coefficient
% oIP = Oblique model incident power on a surface before reflection
% oTP = Oblique model Transmitted power from media after reflection before
attenuation
%
% AP = Attenuated Power through a media
% PT = Total Power (A check calc to ensure it adds up to 1)
% PPP = Power at the print plane
% oRP = Reflected Power (oblique model) of media
% oRE = Reflected Energy (oblique model) of media
% SC = Spurious curing depth (microns)
% SCs = Spurious curing depth (microns) with superposition
% SCsfls = Spurious curing depth (microns) with the influence of first
layer scans
% ET = Exposure Time (s)
% Ec = Critical cure energy (mJ/cm2)
% PD = Penetration depth (microns)
% hs = Hatch spacing (microns)
%
FSI = 376.73;
c = 299272458;
%

```



```

% PAA2 = Phase attenuation (amplitude/energy) of media 2
% PAP2 = Phase attenuation (power) of media 2
% AC2 = Absorption coefficient media 2
% PAC2 = Power absorption coefficient media 2
% Media 2-3 (glass to acrylic)
% fUV = Frequency of UV light
%
AoR23 = -Theta3;
Imp3 = FSI./n3;
rte23 = (Imp3.*cos(Theta3)-
Imp2.*cos(TranTheta23))./((Imp3.*cos(Theta3))+(Imp2.*cos(TranTheta23)));
rtm23 = (Imp3.*cos(TranTheta23)-
Imp2.*cos(Theta3))./((Imp3.*cos(TranTheta23))+(Imp2.*cos(Theta3)));
tte23 = 1+rte23;
ttm23 = (1+rtm23).*(cos(Theta3)./cos(TranTheta23));
Rte23 = rte23.^2;
Rtm23 = rtm23.^2;
OR23 = 0.5.*Rte23+0.5.*Rtm23;
Tte23 = (tte23.^2).*(Imp2./Imp3).*cos(TranTheta23)./cos(Theta3);
Ttm23 = (ttm23.^2).*(Imp2/Imp3).*cos(TranTheta23)./cos(Theta3);
OT23 = 0.5.*Tte23+0.5.*Ttm23;

Xc2 = 0;
PL2 = Xc2.*k0.*KM2./1000.*cos(Theta2);
PAA2 = exp(-PL2);
PAP2 = PAA2.^2;
fUV = c./(LambdaUV./1000000000);
AC2 = 4.*pi.*fUV.*Xc2./c.*cos(Theta2);
PAC2 = exp(-AC2.*KM2./1000);
TotalP23 = OT23+OR23;
%
% oTP2 and oRP23 are calculated after oTP4 and oRP45
AoR34 = -Theta4;
Imp4 = FSI./n4;
rte34 = (Imp4.*cos(Theta4)-
Imp3.*cos(TranTheta34))./((Imp4.*cos(Theta4))+(Imp3.*cos(TranTheta34)));
rtm34 = (Imp4.*cos(TranTheta34)-
Imp3.*cos(Theta4))./((Imp4.*cos(TranTheta34))+(Imp3.*cos(Theta4)));
tte34 = 1+rte34;
ttm34 = (1+rtm34).*(cos(Theta4)./cos(TranTheta34));
Rte34 = rte34.^2;
Rtm34 = rtm34.^2;
OR34 = 0.5.*Rte34+0.5.*Rtm34;
Tte34 = (tte34.^2).*(Imp3./Imp4).*cos(TranTheta34)./cos(Theta4);
Ttm34 = (ttm34.^2).*(Imp3./Imp4).*cos(TranTheta34)./cos(Theta4);
OT34 = 0.5.*Tte34+0.5.*Ttm34;
Xc3 =(0.008+0.002)./2./100000;
PL3 = Xc3.*k0.*KM3./1000.*cos(Theta3);
PAA3 = exp(-PL3);
PAP3 = PAA3.^2;
fUV = c./(LambdaUV./1000000000);
AC3 = 4.*pi.*fUV.*Xc3./c.*cos(Theta3);
PAC3 = exp(-AC3.*KM3./1000);
TotalP34 = OT34+OR34;
%
% oTP3 and oRP34 are calculated after oTP4 and oRP45
%
AoR45 = -Theta5;
Imp5 = FSI./n5;

```

```

rte45 = (Imp5.*cos(Theta5)-
Imp4.*cos(TranTheta45))./((Imp5.*cos(Theta5))+(Imp4.*cos(TranTheta45)));
rtm45 = (Imp5.*cos(TranTheta45)-
Imp4.*cos(Theta5))./((Imp5.*cos(TranTheta45))+(Imp4.*cos(Theta5)));
tte45 = 1+rte45;
ttm45 = (1+rtm45).*(cos(Theta5)./cos(TranTheta45));
Rte45 = rte45.^2;
Rtm45 = rtm45.^2;
OR45 = 0.5.*Rte45+0.5.*Rtm45;
Tte45 = (tte45.^2).*(Imp4./Imp5).*cos(TranTheta45)./cos(Theta5);
Ttm45 = (ttm45.^2).*(Imp4./Imp5).*cos(TranTheta45)./cos(Theta5);
OT45 = 0.5.*Tte45+0.5.*Ttm45;
%
Xc4 = 9.055./1000000000;
%
% The peak power intensity incident at surface 4 (resin) at the centre of
the spot (i.e., the maximum power intensity I0)
oTP4 = PI;

% Subscript s refers to the influence of superposition
oTP4s = PIs;
TotalP45 = OT45+OR45;
oRP45 = oTP4.*OR45;
oRE45 = oRP45.*ET;
%
oTP3 = oTP4./(1-(1-PAP3)-OR34);
AP45 = oTP4-(PI/(exp(LT/PD)));
%
AP34 = (oTP3).*(1-PAP3);
oRP34 =(oTP4.*OR34)./(1-OR34);
%
oTP2 = oTP3./(1-(1-PAP2)-OR23);
AP23 = (oTP2).*(1-PAP2);
oRP23 = (oTP3.*OR23)./(1-OR23);
%
oRP12 = (oTP2.*OR12)./(1-OR12);
oTP1 = oTP2+oRP12;
%
% Reflected energy from substrate accounting for attenuation through the
resin based on penetration depth
oIP5 = oTP4-AP45;
oRP5 = oIP5.*OR45;
oRE5 = oRP5.*ET;
%
% Reflected energy from substrate with superposition
oIP5s =((1./exp(1)).^((LT./cos(Theta5))./PD)).*(oTP4s);
oRP5s = oIP5s.*OR45;
oRE5s = oRP5s.*ET;
%
%Spurious curing without superposition
SC = PD.*log(oRE5./Ec);
SC(SC<0)=0;

% The horizontal component of the spurious cure resulting from the
reflection from medium 5 = SCH
SCH = SC.*sin(Theta5);
%
% Spurious curing with superposition
SCs = PD.*log(oRE5s./Ec);

```

```

% Vertical component of incident power = oIP5sV
% Vertical component of incident exposure = oIE5sV
% Vertical component of reflected exposure = oRE5sV
oIP5sV = oIP5s.*cos(Theta5);
oIE5sV = oIP5sV.*ET;
% If the reflection coefficient is negative, destructive interference will
% occur at normal angles of incidence, so the reflectance coefficient is set
% to negative for the analysis of the vertical component at normal angles of
% incidence (i.e., at the centre of the build area).
en = round((sqrt(numel(oIE5sV)))/2);
OR45v = OR45;
if rtm45(en,en) < 0
OR45v = OR45-(2.*OR45);
else
end
% The difference between the CLW from the vertical component of the
% reflected exposure and the CLW from the incident exposure gives the
% spurious cure
oRE5sV = oIE5sV.*OR45v;
CLWVIs = sqrt(2).*LSSe2.*sqrt(log(oIE5sV./Ec));
CLWVRs = sqrt(2).*LSSe2.*sqrt(log((oIE5sV+oRE5sV)./Ec));

DCLWRv = CLWVRs-CLWVIs;

% Influence of incident and reflected exposure at the CENTRE of the build
% area
% en gives the number of elements in a row of the square array. The
% following process is used to give the value at the centre of the array. In
% the event the array is an even number, rounding gives the next value up.
en = round((sqrt(numel(oIE5sV)))/2);
% Incident exposure at the central locations (i.e., normal angle of
% incidence.) = IEC
IEC = oIE5sV(en,en);
OR45vc = OR45;
if rtm45(en,en) < 0
OR45vc = OR45-(2.*OR45(en,en));
else
end

% oRE5sVc is the reflected exposure at the centre of the build area
oRE5sVc = IEC*OR45vc(en,en);
% Sum of reflected and incident exposure in the vertical plane accounting
% for destructive or constructive interference = oRV
oR5Vc = IEC+oRE5sVc;
% The cured line width from the incident and reflected exposure (with
% superposition) in the vertical plane at the centre of the build area =
% CLWVRsc
% The cured line width from the incident exposure (with superposition) in
% the vertical plane at the centre of the build area = CLWVIsC
CLWVIsC = sqrt(2).*LSSe2.*sqrt(log(oIE5sV(en,en)/Ec));
CLWVRsc = sqrt(2).*LSSe2.*sqrt(log(oR5Vc/Ec));

% The difference in the CLW due to the interaction of the reflected
% component in the vertical plane with consideration to whether it is
% constructive or destructive = DCLWR
DCLWRc = CLWVRsc-CLWVIsC;

```



```

% The horizontal component of the spurious cure with superposition
resulting from the reflection from medium 5 = SCsH
SCsH = SCs.*(sin(Theta5));
%
% Spurious curing with superposition and repeat first layer scans.
SCsfls = PD.*log(oRE5s./Ec)+(PD.*log(FLS));
SCsfls(SC<0)=0;
% The horizontal component of the spurious cure resulting from the
reflection from medium 5 = SCH
SCsflsH = SCsfls.*sin(Theta5);

%hold on;
figure(2)
surf(PlatX,PlatY,SCsflsH');
colormap parula
legend('Spurious curing \mum','Location','NorthEast')
title('Spurious Curing due to reflectance with SP and repeat scans')
xlabel('Build area location (X-Distance from centre) (mm)')
ylabel('Build area location (Y-Distance from centre) (mm)')
zlabel('Spurious curing \mum')
%
%hold on;
figure(3)
surf(PlatX,PlatY,DCLWRv');
colormap parula
legend('Spurious curing \mum','Location','NorthEast')
title('Spurious Curing due to vertical component of reflectance with SP
and repeat scans')
xlabel('Build area location (X-Distance from centre) (mm)')
ylabel('Build area location (Y-Distance from centre) (mm)')
zlabel('Spurious curing from vertical component of reflection \mum')
%
fprintf('The maximum intensity within the laser spot is: %.2f
mW/cm2.\n',Emax);
%
fprintf('The maximum power reflected from the interface at media 1/2 is:
%.2f mW/cm2.\n',max(max(oRP12)));
fprintf('The maximum power transmitted into media 2 is: %.2f
mW/cm2.\n',max(max(oTP2)));
fprintf('The maximum power attenuated through media 2 is: %.2f
mW/cm2.\n',max(max(AP23)));
%
fprintf('The maximum power reflected from the interface at media 2/3 is:
%.2f mW/cm2.\n',max(max(oRP23)));
fprintf('The maximum transmitted power into media 3 is: %.2f
mW/cm2.\n',max(max(oTP3)));
fprintf('The maximum attenuated power through media 3 is: %.2f
mW/cm2.\n',max(max(AP34)));
%
fprintf('The maximum power reflected from the interface at media 3/4 is:
%.2f mW/cm2.\n',max(max(oRP34)));
fprintf('The maximum power transmitted into media 4 is: %.2f
mW/cm2.\n',max(max(oTP4)));
fprintf('The maximum power attenuated through media 4 is: %.2f
mW/cm2.\n',max(max(AP45)));
%
fprintf('The maximum power incident on media 5 wafer (without
superposition) is: %.2f mW/cm2.\n',max(max(oIP5)));

```

```

fprintf('The maximum power reflected from media 5 wafer from a single scan
without superposition is: %.2f mW/cm2.\n',max(max(oRP5)));
fprintf('The reflectance of a single scan without superposition from
surface 5 has the potential to produce up to %.3f microns (magnitude) of
spurious curing.\n',max(max(SC)));
fprintf('The reflectance of a single scan without superposition from
surface 5 has the potential to produce up to %.3f microns of spurious
curing laterally.\n',max(max(SCH)));
%
fprintf('The maximum power reflected from media 5 wafer with superposition
is: %.2f mW/cm2.\n',max(max(oRP5s)));
fprintf('The reflectance with the influence of superposition from surface
5 has the potential to produce up to %.3f microns (magnitude) of spurious
curing.\n',max(max(SCs)));
fprintf('The reflectance with the influence of superposition from surface
5 has the potential to produce up to %.3f microns of spurious curing
laterally.\n',max(max(SCsH)));
fprintf('The reflectance with the influence of superposition and repeat
first layer scans from surface 5 has the potential to produce up to %.3f
microns (magnitude) of spurious curing.\n',max(max(SCsfls)));
fprintf('The reflectance with the influence of superposition and repeat
first layer scans from surface 5 has the potential to produce up to %.3f
microns of spurious curing laterally.\n',max(max(SCsflsH)));
fprintf('The result of interference between the vertical components of the
incident and reflected beams at the centre of the build are with
superposition and repeat first layer scans from surface 5 has the
potential to influence the CLW by %.3f microns.\n',max(max(DCLWRc)));
fprintf('Reflectance from surface 5 has the potential to influence the CLW
by a maximum MAGNITUDE of %.3f microns.\n',max(max(abs(DCLWRv))));
%
fprintf('max angle of reflectance %.2f.\n',min(min(AoR45)));
%
% The following script applies the Bennet-Porteous model to analyse the
effect of Surface Roughness
%
% SR = RMS Surface Roughness (nm)
% RCsr = Reflectance coefficient for surface roughness
% SCsr = Magnitude of spurious curing accounting for surface roughness
with superposition
% SCsHr = The magnitude of the lateral component of spurious curing from
the substrate with superposition
%
prompt = 'Enter the rms surface roughness of the substrate (medium 5 -
e.g. Silicon nitride = 2.5nm, Aluminium = 1118.89nm)? ';
SRs = input(prompt);
RCsr = exp(-(((4.*pi.*SRs.*cos(Theta5))./LambdaUV).^2));
SCsr = PD.*log((RCsr.*oRE5s)./Ec);
SCsr(SCsr<0)=0;
%
if SCsr>0
fprintf('Due to the surface roughness, the MAGNITUDE of specular
reflectance from surface 5 will be sufficient to produce up to %.2f
microns of spurious curing.\n',max(max(SCsr)));
else
fprintf('The exposure from specular reflectance is not sufficient to
initiate curing.\n');
end
%
SCsHr= SCsr.*sin(Theta5);

```

```

fprintf('The reflectance with the influence of superposition from surface
5 has the potential to produce up to %.3f microns of spurious curing
laterally.\n',max(max(SCsHr)));
%
%Graphs
hold off;
surf(PlatX,PlatY,SCsHr');
colormap parula
title('Lateral Spurious Curing With Smooth and Rough Surface')
xlabel('Build platform X plane position mm')
zlabel('Lateral spurious curing \mum')
%
hold on;
surf(PlatX,PlatY,SCsH');
colormap parula
legend('Lateral spurious curing with rough surface \mum','Lateral spurious
curing with smooth surface \mum','Location','NorthEast')
view(45,10)

```